MMSE Vol.3

ISSN 2412-5954

SCIENTIFIC PERIODICALS

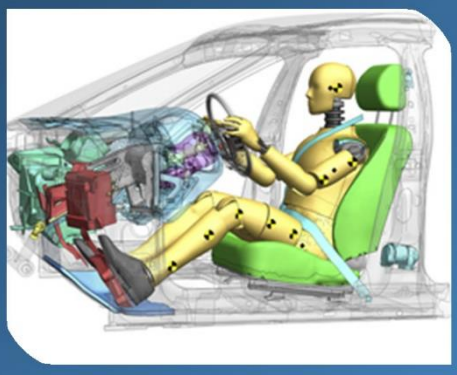
#3
2016

MECHANICS, MATERIALS SCIENCE & ENGINEERING







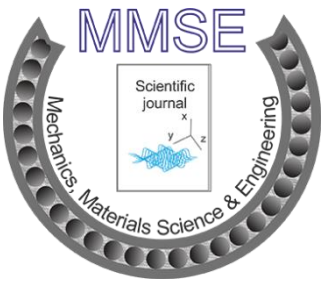


OPEN ACCESS

WWW.MMSE.XYZ

Sankt Lorenzen 36, 8715, Sankt Lorenzen, Austria

Mechanics, Materials Science & Engineering Journal



March 2016

Mechanics, Materials Science & Engineering Journal (MMSE Journal) is journal that deals in peer-reviewed, open access publishing, focusing on wide range of subject areas, including economics, business, social sciences, engineering etc.

MMSE Journal is dedicated to knowledge-based products and services for the academic, scientific, professional, research and student communities worldwide.

Open Access model of the publications promotes research by allowing unrestricted availability of high quality articles.

All authors bear the personal responsibility for the material they published in the Journal.

The Journal Policy declares the acceptance of the scientific papers worldwide, if they passed the peer-review procedure.

Editor-in-Chief Mr. Peter Zisser

ISSN 2412-5954

e-ISSN 2414-6935

Design and layout: Mechanics, Materials Science & Engineering Journal, www.mmse.xyz

Technical support: hotmail@mmse.xyz

©2016, Magnolithe GmbH

© Copyright, by the authors

CONTENT

I. Materials Science. MMSE Journal Vol. 3……6

Characterization and Thermo – Elasto – Viscoplastic Modelling of Cunip Copper Alloy in Blanking Process 7

Technology of Modifying a Machine Element 14

II. Mechanical Engineering & Physics. MMSE Journal Vol. 3 19

Modeling of Heat Transfer and Self-Heating Phenomenon In Materials With High Dissipation 20

Rolling Contact Fatigue Life Evaluation Using Weibull Distribution 28

The Boltzmann Equation Of Phonon Thermal Transport Solved In the Relaxation Time Approximation – I – Theory 34

Elements of Calculus Quaternionic Matrices And Some Applications In Vector Algebra And Kinematics 46

The Boltzmann Equation Of Phonon Thermal Transport Solved In the Relaxation Time Approximation – II – Data Analysis 57

Automation of Analysis And Structural-Parametric Synthesis of Planetary Gearboxes With Two Degrees Of Freedom 67

Intellectual Drive With Electric Engines On a Stock Car 81

A Numerical-Analytical Approach to the Analysis of Non-Stationary Temperature Fields in Multiply-Connected Solids 90

Modeling Curvilinear Motion of Tracked Vehicle with the Dual-Flux Electromechanical Turning Mechanism 107

A Fast Algorithm to Solve Nonlinear Hypersingular Integral Equations Arising in a Crack Problem 120

A Virtual Stage-Gate Approach to Developing Injection Moulds for Polymer-Based Drug-Delivery Systems 135

IV. Electrical Complexes and Systems. MMSE Journal Vol. 3 148

Secondary Power Resources of the Fuel and Energy Complex in Ukraine……149

VI. Power Supply Technologies. MMSE Journal Vol. 3 155

Monitoring of the thermal state of induction motors with low quality power supply 156

VII. Environmental Safety. MMSE Journal Vol. 3 163

Nasal Bone Fractures In Children And Adolescents. Patient Demographics, Etiology of The Fracture and Evaluation of Plain Film Radiography as a Diagnostic Method in Children's Clinical University Hospital 164

New Basis Points of Geodetic Stations for Landslide Monitoring 171

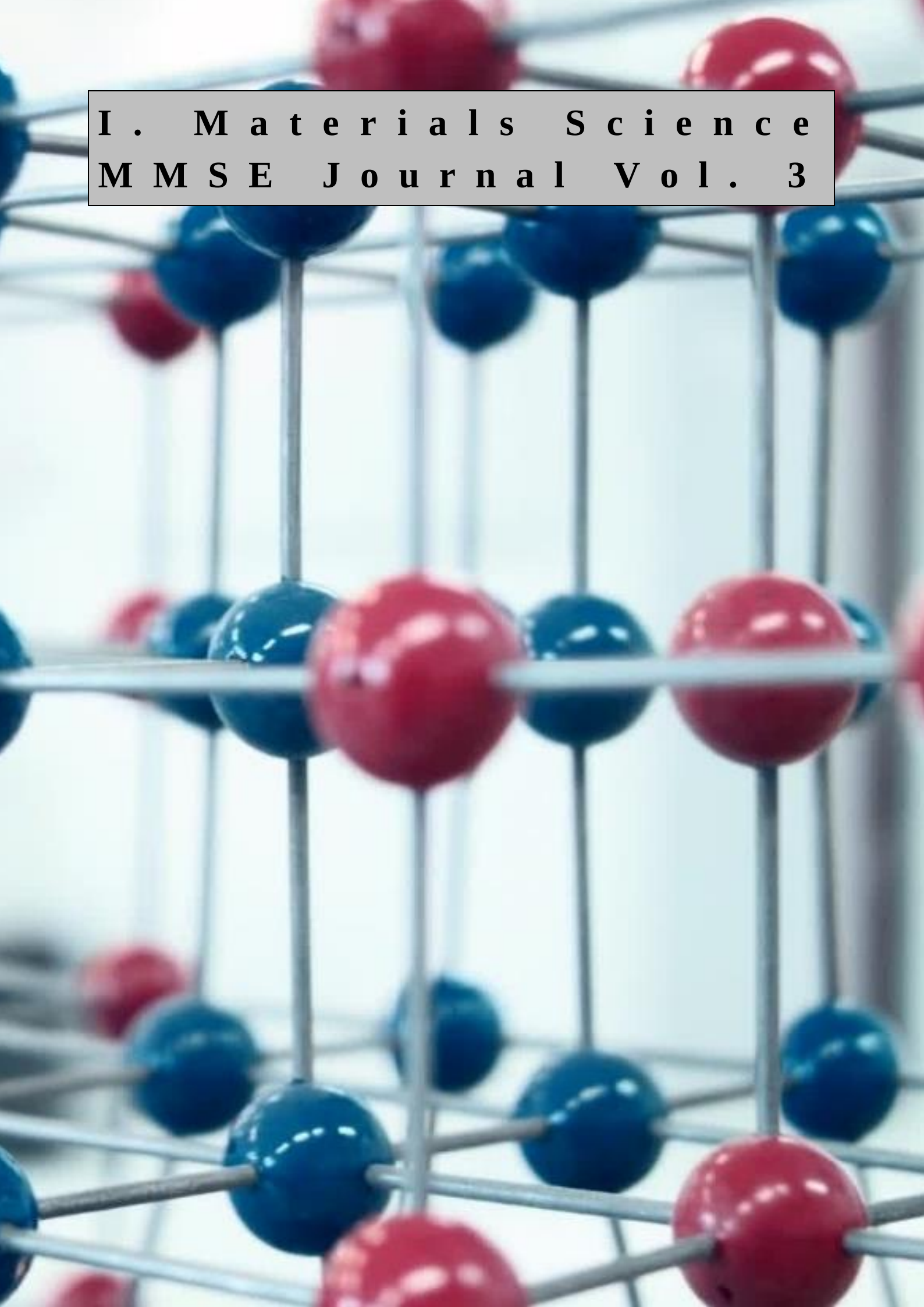
IX. Economics & Management. MMSE Journal Vol. 3 178

The Current State of Taxation and Regulation of Land Plot Size of Industrial Areas in Ukraine ..179

X. Philosophy of Research and Education. MMSE Journal Vol. 3 185

Physics and Optics in Dante's Divine Comedy 186

A Matlab Toolbox For Grey Clustering Probability Model Of Postgraduate's Innovative Ability 193



I. Materials Science MMSE Journal Vol. 3

Characterization and Thermo – Elasto – Viscoplastic Modelling of Cunip Copper Alloy in Blanking Process

A. Touache[1], S. Thibaud[2], J. Chambert[2], P. Picart[2]

1 – Mechanical Engineering Laboratory, Faculté des Sciences et Techniques, Sidi Mohammed Ben Abdellah University, Fez, Morocco

2 – Institute FEMTO-ST, Applied Mechanics Laboratory, University of Franche-Comté, 24 rue de l'Epitaphe, 25000 Besançon, France



DOI **10.13140/RG.2.1.3289.0645**

Keywords: strain rate/temperature sensitivity, blanking process, copper alloys, FEM

ABSTRACT. Numerical simulations of blanking process are performed to investigate CuNiP copper alloy behavior under blanking conditions. Numerical simulations are mostly dependant of a correct modeling of the material behavior with thermo-mechanical sensitivity. A thermo-mechanical characterization by a set of uniaxial tensile tests at different temperatures and strain rates is presented. A thermo – elasto - viscoplastic approach was investigated to propose the mechanical behavior model based on a phenomenological way in the framework of the thermodynamic of irreversible processes. This model is implemented in finite element software untitled "Blankform" dedicated to the numerical simulation of precision blanking operations and developed at the Applied Mechanics Laboratory. Numerical results are presented and compared with experiments.

1. Introduction. In precision blanking for very thin sheet about 0.254mm thickness, accurate predictions of maximal blanking load and cut edge profile are essential for designers and manufacturers. A finite element code untitled Blankform [1-2] has been developed at the Applied Mechanics Laboratory to simulate the blanking operation from elastic deformation to the complete rupture of the sheet.

In blanking operation like many metal forming processes the material undergoes very large strains, high strain rates and significant variations in temperature. So to obtain an acceptable prediction of the maximal blanking load by FEM simulation, it needs an adapted model for mechanical behavior which takes into account large strains, strain rate and thermal effects. In this paper, a specific thermo-elasto-viscoplastic modelling has been developed for CuNiP copper alloy used for manufacturing electronic components by high precision blanking.

In first, tensile tests are carried out at room temperature with various strain rates. The temperature distribution in the specimen is observed using a thermal CCD camera. Then a second set of tensile tests are carried out in various isothermal conditions. Considering locally the temperature evolution as a function of the strain rate, the analysis of the tensile curves obtained for these experiments allows to propose a new thermo-elasto-viscoplastic modelling for a copper alloys. The identification of the associated material parameters is investigated and presented. The proposed mechanical behavior is implanted in the finite element code Blankform. Finally the capability of the new modelling to predict the maximum blanking force is presented and discussed.

2. Experiments. To study strain rate sensitivity, tensile tests are performed at room temperature with four strain rates: $2 \cdot 10^{-3}s^{-1}, 4 \cdot 10^{-3}s^{-1}, 8 \cdot 10^{-3}s^{-1}$ and $9 \cdot 10^{-2}s^{-1}$. During each tests, a thermal camera allows the measurement of the heating in the specimen due to the mechanical energy dissipation. The second set of tests is performed at a constant strain rate ($2 \cdot 10^{-3}s^{-1}$) with three different temperatures T=20 °C, 50°C and 150 °C.

Even the strain rate and thermal effects are strongly coupled two sets of experiments are carried out to investigate separately the strain rate and temperature effects on the flow stress. The strain rate range investigated by experiments is lower than those observed in industrial blanking process (about 10 s^{-1}). The extension of the modelling in term of large strain rate domain is made by introducing a Johnson-Cook-like modelling [2]. The stress/strain curves obtained for the first (various strain rates) and second set (various temperatures) of experiments are shown respectively on figures 1 and 2.

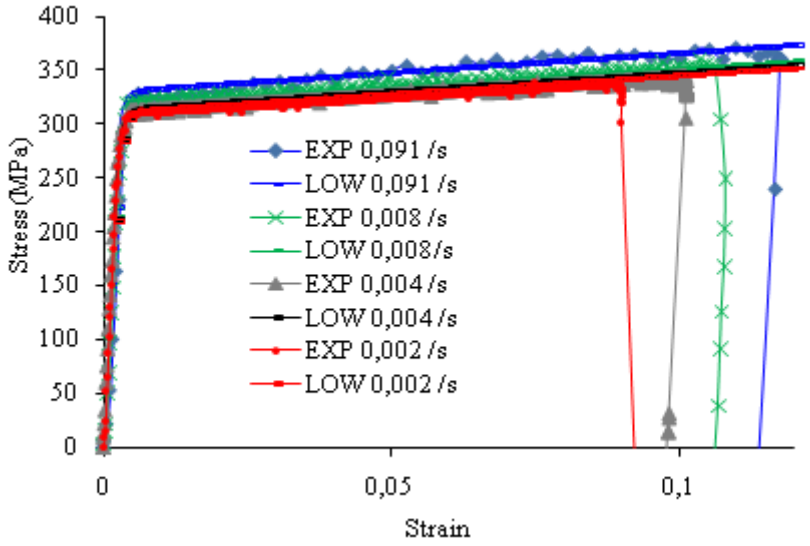


Fig. 1. Stress-strain curves with different strain rates at room temperature (20 °C)

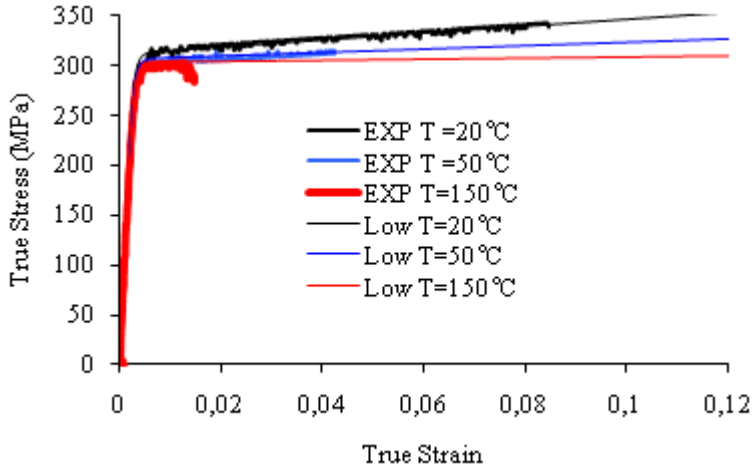


Fig. 2. Stress/Strain curves with different temperatures ($\dot{\varepsilon}$=2.1 10-3 s^{-1}).

The flow stress decreases with temperature increasing and increases with strain rate increasing. Furthermore the deformation at rupture decreases with temperature increasing and increases with strain rate increasing. For tensile tests achieved at a temperature below 150 °C show a fast decreasing of the stress flow. The rupture of specimens appears quickly. The testing device does not allow test in the range of strain rates corresponding to industrial blanking conditions. However these tests show the influence of strain rate and temperature on the mechanical behavior of CuNiP copper alloy.

The mean heating of the specimen due to the strain rate evolution which was calculated by thermal camera is presented on figure 3. The heating increases with the strain rate. So the mechanical modeling should take in account temperature and strain rate coupling.

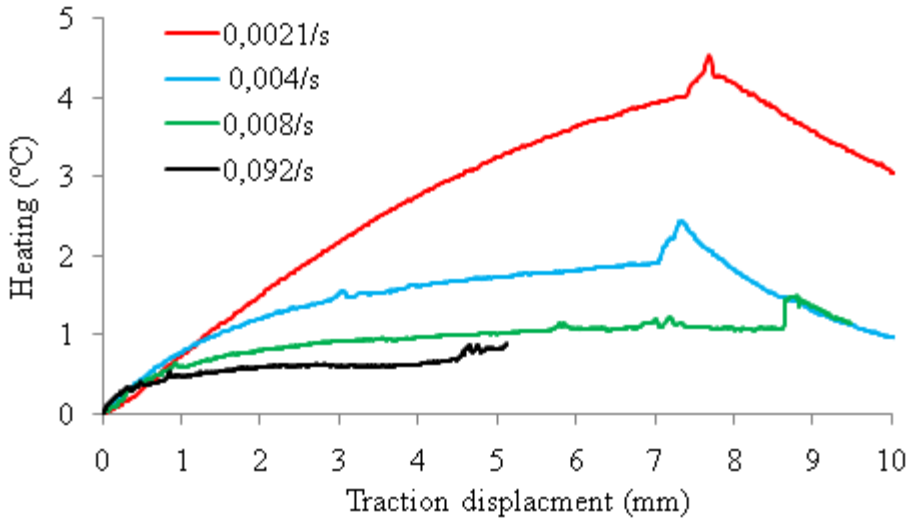


Fig. 3. Specimen heating for different strain rates (20 °C).

3. Modeling. A number of models of thermo-elasto-viscoplastic behavior, for example the models of Johnson-Cook, Prandtl-Ludwik, Zener-Holomon and Armstrong-Zerilli [4], these models were generally developed for mechanical behavior at very high strain rate so higher than speeds in blanking process which are about $10s^{-1}$. We will propose a new model as well as possible reproducing experimental tests and the sensitivities at the strain rate and temperature. We propose following multiplicative low for predicting the thermo-elasto-viscoplastic yield stress:

$$\sigma_0 = \left(\sigma_y + Q\left(1 - e^{-b\varepsilon^{vp}}\right) + \frac{K_0}{T}\varepsilon^{vp}\right)\left(1 + a_\vartheta ln\left(1 + \frac{\dot{\varepsilon}^{vp}}{\varepsilon_0}\right)\right)e^{\alpha/T}\,. \qquad (1)$$

With: σ_0 the equivalent stress, ε^{vp} the equivalent strain, T the temperature, $\dot{\varepsilon}^{vp}$ the strain rate and σ_y, Q, b, K_0, a_ϑ, ε_0 and α are material hardening parameters.

The first exponential term makes possible to take into account the beginning of the hardening curve as well as the quasi-saturation of this one. The second linear represents the slope of the curve. The term in 1/T represents the fall of the hardening curve with the rise in the temperature. The strain rate influence is proposed according to a term in logarithm. It makes possible to formulate saturation effect of strain rate. Finally a term proportional to exponential of the reverse of the temperature represents saturation and softening due to the temperature.

At low velocity, the term of strain rate in equation (1) tend to one. In first, we set σ_y at the yield point at ambient temperature. The use of a genetic algorithm allows parameter identification with the experimental results at imposed temperatures and strain rate. The results of this inverse identification are listed in table 1. Experimental and predicted stress flow curves are in good agreements (see figure 1 and 2)

Table 1. Identified material parameters for CuNiP copper alloy.

Material parameters	Value
E (MPa) Young's modulus	99500
ν (MPa) Poisson's ratio	0,31
σ_y (MPa) Yield stress	199
Q (MPa)	97
b	1300
K_0 (MPa.°C^{-1})	8200
a_ϑ	0,02
ε_0 (s^{-1})	2.1 10^{-3}
α (°C^{-1})	0,9

4. Numerical Implementation

To take into account temperature and strain rate effects observed during tensile tests, a phenomenological modeling is proposed. A like-plasticity model described by the way of the Von-Mises criterion:

$$f = \frac{1}{2}\,\underline{\sigma}:\underline{\underline{P}}:\underline{\sigma} - \frac{1}{3}\,\sigma_0^2\ . \tag{2}$$

Where f is the yielding surface, $\underline{\sigma}$ is the Cauchy stress tensor, $\underline{\underline{P}}$ is the 4th order deviatoric tensor and σ_0 the flow stress.

We consider that the blanking process is carried out in adiabatic conditions. With these assumptions, the local heating is simply computed from the strain and stress state by:

$$\frac{\partial T}{\partial t} = \frac{\xi}{\rho C_v}\underline{\sigma}:\underline{\dot{\varepsilon}}^{vp}\ . \tag{3}$$

With ρ, C_v and ξ are respectively the density, the specific heat and the transfer coefficient of the material. The parameter ξ permits to take into account the heating. The values of these parameters are given by literature in table 2.

Table 2. Identified material parameters for CuNiP copper alloy.

Material properties	**Value**
ρ (kg.m^{-3}) Density	8900
C_v (J.kg^{-1}.°C^{-1}) Specific heat	22,32
ξ	0,05

In the finite element software Blankform, equation (3) is not strongly coupled with the mechanical solution. The temperature is computed after loading increment by resolution of equation (3).

The new modelling is implanted in Blankform software by a standard numerical procedure as presented in [5]. This software allows the numerical simulation of 2D problems including large strains and inelastic materials. The time integration is based on an implicit algorithm. To solve the equilibrium and the non linear constitutive equations, a Newton Raphson method is used.

5. Blanking FEM simulation. The blanking test geometry is described on figure 4 and table 3. Sliding contact conditions are assumed between tools and specimen. The simulation has been performed in 2D plane strain conditions. The initial mesh is made up 3118 triangular 3 nodes elements with one integration point.

In blanking process a localized shear band appears between the punch and die. This band presents locally very significant values of the equivalent plastic strain about 4 at a punch penetration of 50%. To reduce the influence of the mesh distortion, a global periodic remeshing of the specimen is generated after every 5% of punch penetration. The average size of the elements in the band of shearing is about 1.3% of the thickness.

Table 3.Geometric parameters of the blanking test

	Value (mm)
Punch width	*1.7*
Hole die width	*1.72*
Punch radius	*0.01*
Die radius	*0.01*
Punch-die clearance	*0.01*
Specimen thickness	*0.2*

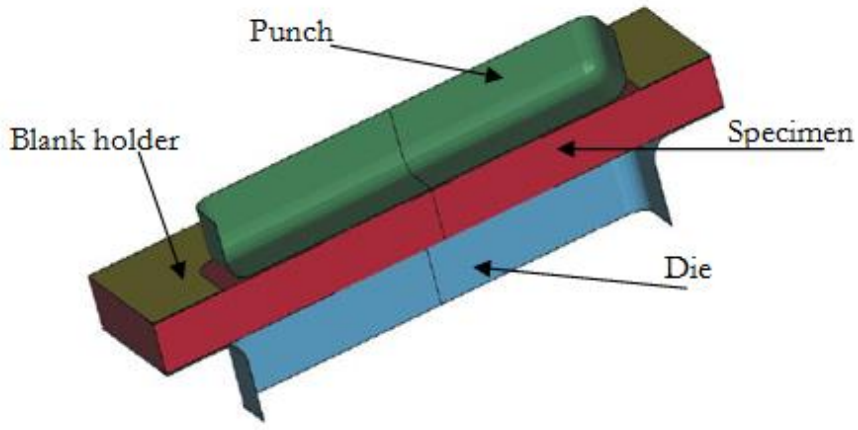
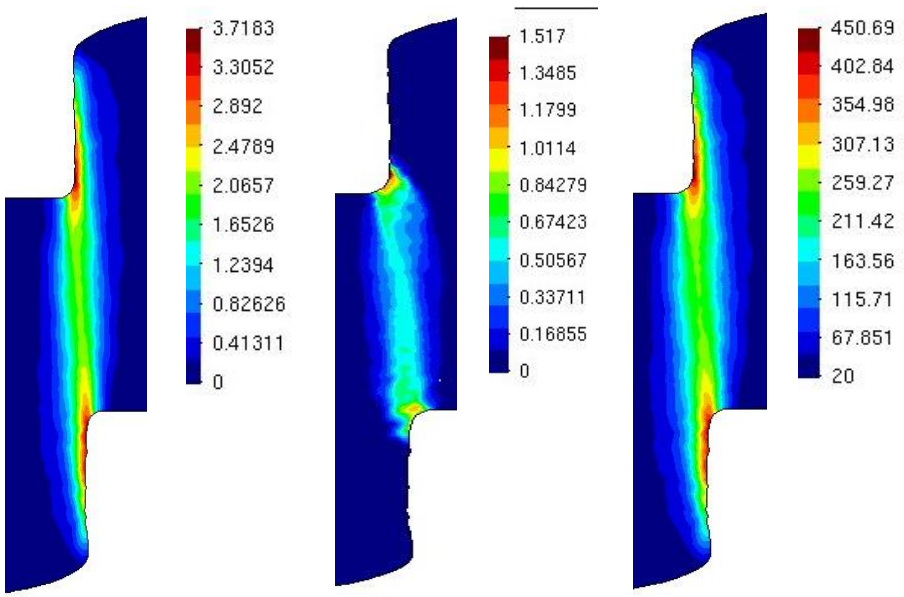


Fig. 4. Schematic description of the blanking operation.

6. Results. Fig. 5, a presents the equivalent strain according to the penetration of the punch. We observe a band of localized plastic deformations. This band is located between the cutting edges of the punch and the die. In the centre of the band, the equivalent deformation is approximately 4 if the punch penetration is 47%. The temperature increases up to 215 °C (see fig. 5, c) near punch and die corners and the strain rate is about $1.5s^{-1}$ (see fig. 5, b).

In the tensile tests carried out to characterize the behavior, the values of the strain, strain rate and temperature are much lower than the values is thus to check obtained in blanking FEM simulation. The validity of the thermo-elasto-viscoplastic law used in this range of deformation is thus to check. For that we have to compare numerical results and experimental blanking test.

Figure 6 gives experimental and numerical load-displacement curves for two different punch speed 0.1 mm.s^{-1} and 6 mm.s^{-1}. The prediction of the blanking load curve is rather correctly carried out until the initiation of the phase of cracking. This difference can be explained because in the proposed model we do not taking into account the damage phenomena [6]. The relative error on the maximum value of the blanking load is about 2.3 % which is very acceptable (see table 4).



(a) *(b)* *(c)*

Fig. 5. Field of the equivalent deformation (a), strain rate in s^{-1}(b) and temperature in °C (c) in the shear band.

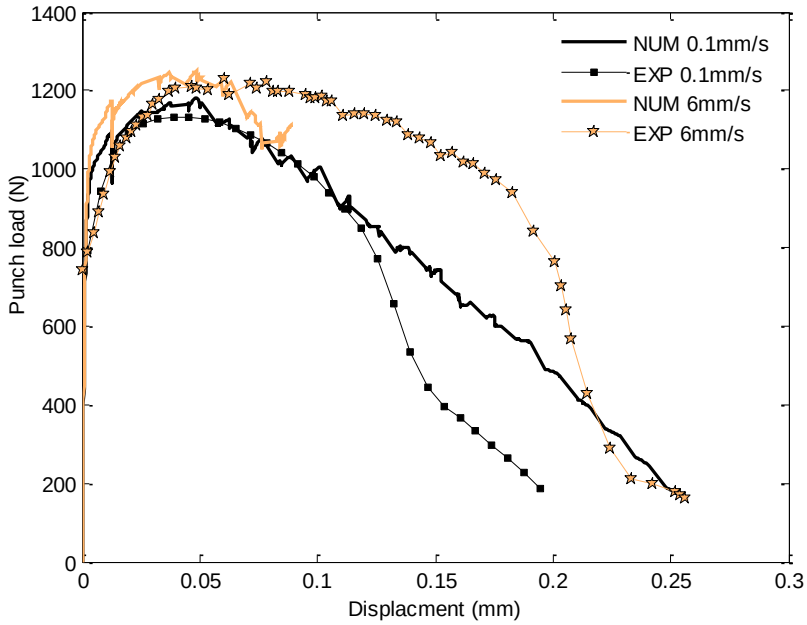


Fig. 6. Experimental and predicted load/displacement curves

Table 4. Experimental and predicted maximal blanking load for tow value of punch speed

Punch speed	*Numeric (N)*	*Experiment (N)*	*Error (%)*
0.1mm/s	*1163*	*1136*	*+2.3%*
6mm/s	*1227*	*1200*	*+2.2%*

6. Conclusion. The thermo–elasto–viscoplastic behaviour of the CuNiP copper alloy was characterized by the use of a set of tensile tests at imposed strain rates and temperatures. A multiplicative behaviour law is proposed to take into account the material sensitivity at the strain rate and the temperature. After having identified by genetic algorithm the parameters of the proposed law, it was implemented in the computer finite elements software Blankform. The application in simulation of the blanking process shows that the thermo-elasto-viscoplastic model for the CuNiP copper alloy allows a correct prediction of the sensitivity of the maximum blanking load at versus punch speed. However, it will be necessary to validate the experimental step for the characterization of the sensitivity at the speed and the temperature on other copper alloys in order to improve the proposed thermo – elasto – viscoplastic model for similar coppers alloys.

References

[1] V. Lemiale, Contribution à la modélisation et à la simulation numérique du découpage des métaux, PhD Thesis, University of Franche-Comté (2004), France [in french].

[2] A. Touache, "Contribution à la caractérisation et à la modélisation de l'influence de la vitesse et de la température sur le comportement en découpage de tôles minces", Ph.D. Thesis, Université de Franche-Comté, France, December (2006) [in French].

[3] G.R. Johnson, W.H. Cook, A constitutive model and data for metals subjected to large strains, High Strain Rates and High Temperature, In 7th International Symposium on Ballistics, The Netherlands, 1983.

[4] M. Micunovic, M. Radosavljevic, C. Albertini, M. Montagnani, Viscoplastic behaviour of damaged AISI 316H from dynamic experiments, Facta Universtatis, Vol. 2 n° 10: 1299-1317, 1997.

[5] J.C. Simo, T.J.R. Hugues, Computational Inelasticity, Springer Verlag Edition (1998).

[6] Hambli R., Comparison between Lemaitre and Gurson damage models in crack growth simulation during blanking process, International Journal of Mechanical Sciences, 43: 2769-2790, 2001.

Technology of Modifying a Machine Element

R. P. Didyk[1,a], R. S. Puhach[2,b]

1 – Dr. Sci. (Tech.), Professor, State Higher Educational Institution "National Mining University", Dnepropetrovsk, Ukraine

2 – Postgraduate, State Higher Educational Institution "National Mining University", Dnepropetrovsk, Ukraine

a – didyk@nmu.org.ua

b – dracov-pugach@yandex.ua

DOI **10.13140/RG.2.1.1561.7683**

Keywords: basis points, landslide processes, local geodetic network, recalculation of coordinates, the coordinate system.

ABSTRACT. For the first time, products of serpentine decomposition have been identified on the basis of fundamental structural research. These products form a protective ceramic metal layer on the metallic surface. During sliding contact surfaces is formed on a protective layer having anti unique characteristics. There is a restoration of the functional state of the friction surface of the unit due to the initiation of self-organizing processes. Results of industrial tests prove the high effectiveness of the use of natural minerals as machine elements modifiers. They allowed making the service life of mining and metallurgical equipment 2,5 - 5 times longer because of the reduction or elimination of repair works and increase in functional properties of engineering products.

Introduction. Methods of strengthening machine element surfaces subjected to friction are based on various physical, chemical and mechanical processes, resulting in the increase in wear resistance, strength, hardness and corrosion resistance, which ensures a specified service life and minimization of energy losses during the friction unit operation.

Since there is no universal way of strengthening tribological units, it is important to consider the factors specific for each single case: for example, the allowable distortion of machine elements, the occurrence and type of residual stresses, the impact of technological environment, ecological and financial parameters. Some strengthening methods are widely known: chemical and thermal treatment, diffusion, surfacing, chemical deposition from gas medium, implantation, thermal vacuum methods, ion plasma methods and laser methods. A detonation method allows obtaining coatings with enhanced operational properties. Each of the above methods has its advantages, disadvantages and a particular field of application [1].

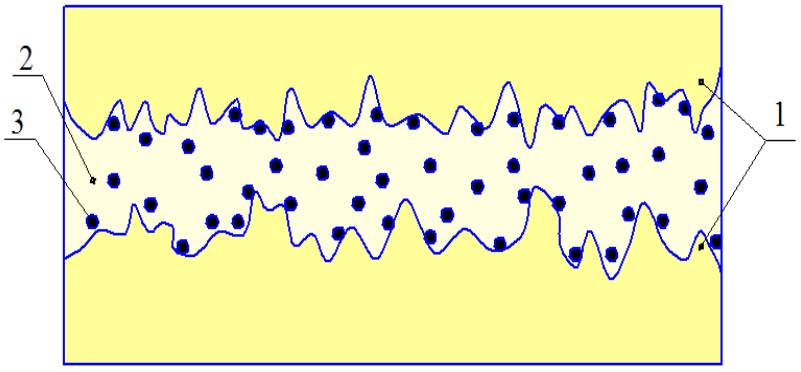
The new direction in solving this problem is the mechano-chemisty influence of tribotechnical powdercompositions - geomodifiers of friction (GMF) - on the working surfaces of machine elements.

Research results. High loads, extreme speed, a wide temperature range and the presence of aggressive media determine new requirements for the performance and operation of friction units of modern mining and metallurgical equipment. To ensure the efficient work of gears, rolling contact bearings, skid bases, cam shaft mechanisms, guide members, sealing elements, junctures, locks and docking devices, it is necessary to create special self-lubricating materials and coatings, friction modifiers, durable coatings with high chemical resistance and new ways of friction unit treatment.

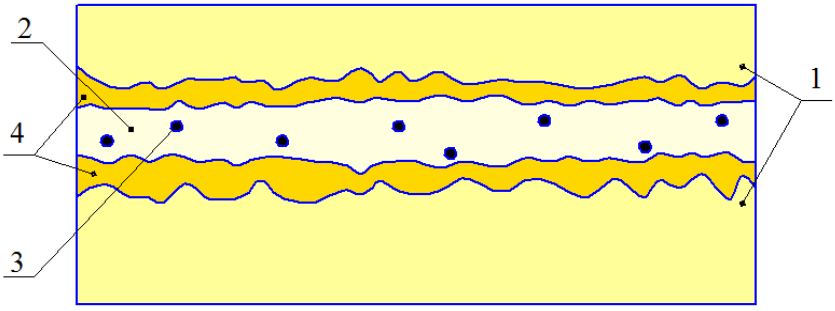
The result of the received mechanoactivation effect became apparent at the following stages of the technological process of friction geomodifier manufacturing. Fine dispersed powders (0.5 - 1 μm) having been crushed in a special manner and having passed the mechanoactivation stage, are brought

into a friction area with the lubricant, where they make structural modifications in the friction surface in a favorable way for tribotechnics.

The principles of creating nanomaterial on the basis of natural materials have been developed to enhance wear resistance and tribological properties of heavily duty units, in particular in a case of extreme conditions. The article has investigated the technology of activation less slip in the area of surface matching where dispersed micro- and nanoparticles of geomodifiers on the basis of SiO_2 , Al_2O_3 are involved. The perfect property of the rolling of spherical nanoparticles with slipping has been found out when there is a relative motion of the surfaces of pairs elements on ceramics in the intermediate layer of ceramic particles. The relevant feature of implementing the effect of the activationless functioning of nanomodifier particles in the area of moveable surface matching is 90% amorphization of components (SiO_2, Al_2O_3). The amorphization is formed at the stage of running in the surfaces, creating flat-topped micro relief in tribocoupling and achieving sizes of inactivated particles in the process of dispersing nano quantities. The content of ceramics in nanoparticles in the lubricant comprises 7-10% of the total volume of oil and allows particles not only to penetrate into the dimples of microgeometry of mating pairs surfaces (fig. 1,a), but also to continuously migrate in suspension in oil (fig. 1, b), acting as bearing microballs. It has been revealed that on the surface of tribocontact, the microrelief with new properties is gradually formed. These properties are completely coordinated with the features of the self- organization of surface matching systems. In extreme conditions of uncontrolled workflow, a quasi-protective layer of residual ceramic nanoparticles contained in geomodifiers provide the short-term antiwear effect in case in case the lubrication is absent [2].



a)



b)

Fig.1. Operation of mating pairs: a – introduction of particles into the cavities geomodifiers friction surface roughness details; b – exchange particles geomodifiers friction between the rubbing surfaces of parts prior to formation wear resistant layer; 1 – mating surfaces; 2 – lubricant; 3 – geomodifier of friction; 4 – wear resistant film

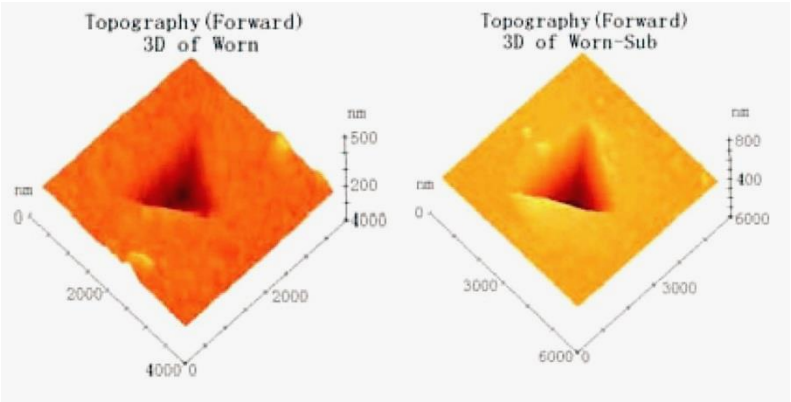
As a result, of the mechanism of action studies GMF is as follows: during operation of the friction assembly formed by friction surfaces on the defective layer of metal. GMF particles are introduced into the friction zone having weak abrasive properties, this layer is removed at the same time split up between the friction surfaces, reducing its abrasiveness. Later, in the process of hardening the friction occurs at the Turn of friction and further splitting GMF particle planes of contact. On the surface layer of the cermet is formed. A characteristic feature of the friction process, GMF is its ability to self-regulation due to the simultaneous passage of the processes in the two contact surfaces under the influence of the same load. Diffusion in a GMF solid surface is slower, resulting in a complete equalization of the microhardness of the surface layers of the contacting parts. Changes that occur in this case, lead to an increase in linear dimensions of parts. The process of increasing the linear dimensions is also self-adjusting, as continues until until you have selected the existing gaps.

Studies have been conducted in steel samples containing 0.5% C and 1.1% Cr, on the friction machine for 100 hours of continuous operation, for "by the roller pad" scheme. As lubricants used in the cases of the first oil and the other oils with the addition of GMF. The composition of GMF included 33% SiO2; 2,5% Al2O3; 4% Fe2O3; 35% MgO.

The process of self-organization consists in a hereditary “memory” of material. Included in the structure of a powder, *A1* and *Fe* are catalysts of pyrolytic carbon formation along the borders of grains up to as subsurface layer, and the basic composition of GMF modifies the boundary layer with a high degree of available bonds attaching the “lost” material from the dispersion environment.

Studies rubbing surfaces after treatment showed GMF, GMF components that diffuse into the surface layers of the metal and form a new layer, which is a solution phase GMF components constituting the steel. The penetration depth is 30 - 50 μm.

Research microhardness treated GMF metal surfaces at different depths it possible to establish a certain relationship. The hardness of the modified surface of the surface layer significantly exceeds the initial hardness. Figure 2 is a photomicrograph of a trace of the indenter, hardness (load of 20 μN) in the process of determining the microhardness of the sample steel surface. Clearly visible differences in the size and depth of indentation pyramids that corresponds to an increase in the microhardness of 1.5 times.

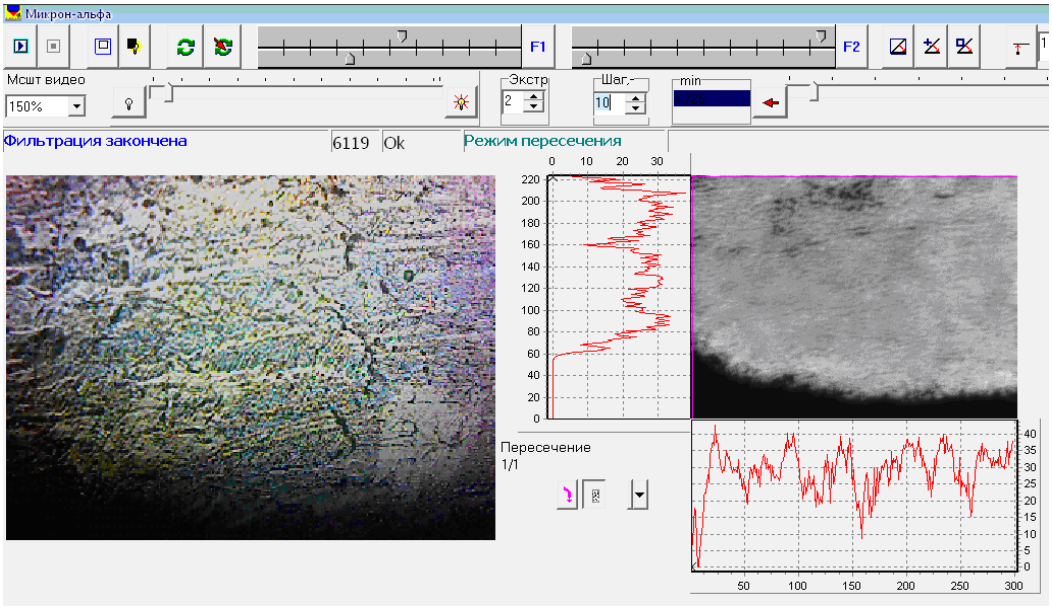


a) *b)*

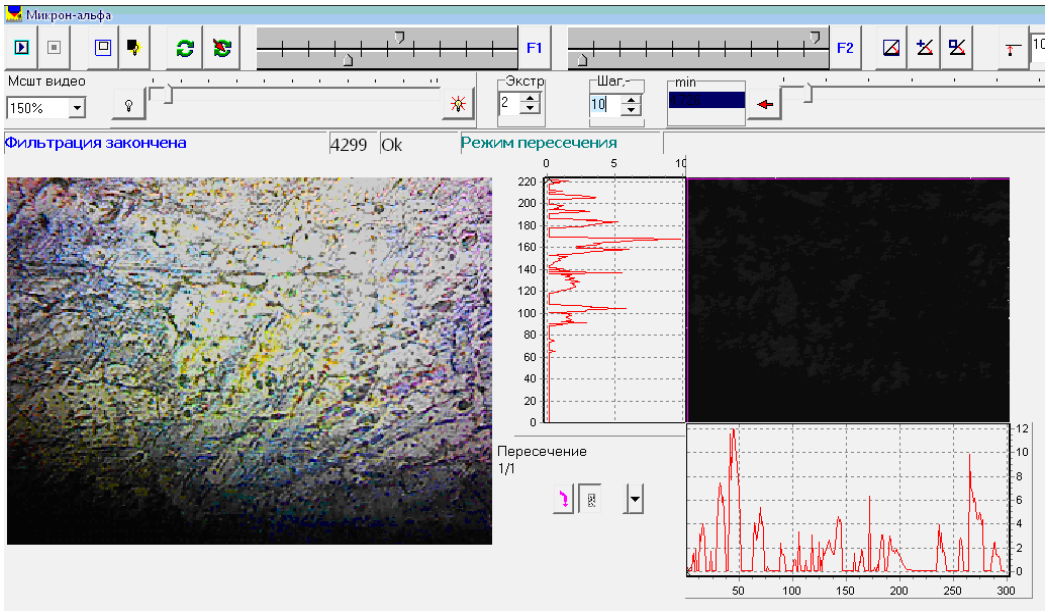
Fig. 2. The microhardness of the surface layer: and - after the use of lubrication oil; b - after the addition of the friction zone GMF

Measurement was performed on the surface microprofile profilometer «Micron-alpha» and shown in Figure 3, it has been found the change of surface roughness. The roughness on the surface of all investigated parameters undergoes positive changes arising surface leveling, reduced the number of

critical peaks and troughs surface irregularities, all of which contribute to an increase in contact area between the rubbing parts. Table 1 shows the average data on the measurement of the surface roughness of the test samples that indicate a decrease in the roughness of 2 times.



a)



b)

Fig. 3. Surface profilograms steel: a - after using oil lubrication; b - after the addition of the friction zone GMF

Endurance tests were conducted for 100 hours by measuring the mass of the worn parts every 5 hours. Figure 4 shows a wear steel using two different lubricants. As can be seen in the test sample, which is added to the friction zone GMF first 20 hours of an intensive wear, due to the micro grinding surface of the part and its alignment, the negative values in the figure indicate the restoration of the worn surface GMF elements. Thus, new reduced metal layer arises on the workpiece surface.

Table 1. The average data for the measurement of surface roughness

Data	After working in the oil lubrication, μm	After working in the oil lubrication with the addition of GMF, μm
Rz	6,51	2,908
Ra	8,05	3,938
R	0,097	1,026
H	16,2	6,128

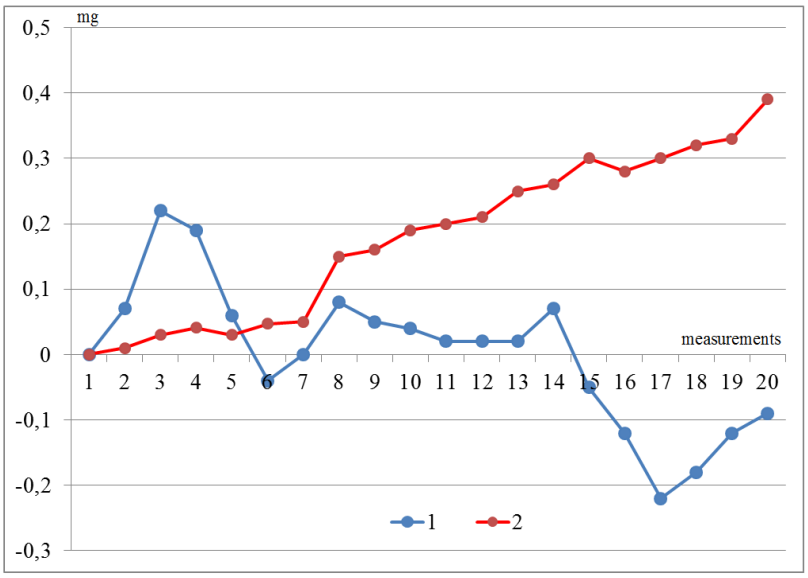


Fig. 4. Metal wear schedule: 1 - after adding GMF friction zone; 2 - after the use of oil lubrication

Summary. The study found that on the surface of the layer formed by the continuous restoration, reaching the size of 30 - 50 μm. After treatment, the roughness decreases by 2 times, which leads to the creation of favorable form microscopic irregularities with greater bearing area shares. The studies found a decrease in the average coefficient of friction by 10 ... 15% when the temperature drops in the contact zone in an average of 15 ... 20%.

A distinctive feature of GMF is an opportunity not only significantly reduce the wear and tear, but also to restore the functional state of the worn surfaces of friction units of machines and mechanisms at the expense of self-organizing initiation triboprocesses towards the restoration of physical bonds with the surface layer of the fine among the main material in the lubricating medium mechanism.

The use of GMF as the compositions for worn out friction units' recovery, without operating equipment being shut down, allows essential reduction in maintenance costs related to machinery and equipment repair, reduction in power consumption, an increase in a service life of machinery and mechanisms.

References

[1] Didyk R.P. New technology recovery units of friction and surface modification of machine parts, Proc. Scien. tr., Kiev, CHSM NASU,2003, pp. 23-27.

[2] R.P. Didyk, R.S. Puhach, V.A. Kozechko. New technology of modifying a machine element surface in an attempt to overcome the tribological barrier, State Higher Educational Institution "National Mining University", Dnepropetrovsk, 2015 №5 (149) pp. 59 - 63.

II. Mechanical Engineering & Physics

MMSE Journal Vol. 3



Modeling of Heat Transfer and Self-Heating Phenomenon In Materials With High Dissipation

Irina Viktorova[1, a] & Michael A. Bates [2, b]

1 – Department of mathematical sciences, Clemson university, Clemson, USA, SC

2 – Department of mechanical engineering, Clemson, USA, SC

a – iviktor@clemson.edu

b – mabates@clemson.edu



DOI **10.13140/RG.2.1.2198.3761**

Keywords: viscoelasticity, Volterra integral equation, Fourier equation, Maxwell-Cattaneo equation, self heating phenomenon, differential equations.

ABSTRACT. In engineering mechanics, the properties of many materials are significantly dependent on temperature thus emphasizing the importance of the consideration of heat generation due to the influence of mechanical vibrations. Such considerations will lead to the development of a model predicting the point of catastrophic thermal failure, known as heat explosion, through the development of a model considering the loss of energy by means of internally generated heat and the transfer of such heat through implementation of the Fourier Law of Cooling. The Maxwell-Cattaneo model of heat transfer is applied. This allows for the investigation of a more realistic heat transfer equation. Finally, the model will be discretized, and solutions will be compared.

Introduction. In engineering mechanics, many material properties are highly dependent on temperature. This serves to highlight the importance of considering all aspects of heat introduction into a mechanical system. One commonly ignored source of heat is the influence of self-heating due to mechanical vibrations, specifically, cyclic loadings. While this may seem to be, and is in fact, negligible in many situations in which adequate heat transfer out of the system is allowed, the results of such self-heating can be catastrophic in adiabatic or nearly adiabatic conditions leading to disastrous and catastrophic thermal failure known as heat explosion. Even when there is minimal risk of heat explosion from self-heating, failure to consider this internal heat generation may result in undesirable or unpredictable material behavior under mechanical vibrations or cyclic loading conditions.

1. The Stress-Strain Relationship. In order to examine this self-heating phenomenon, the underlying physical principles behind the system must first be briefly examined. When an object is placed under a load, thus inducing a stress σ, deformation of that body results. This deformation is known as strain denoted by [1]. In the linear region of the stress-train diagram, deformation is not permanent. This is referred to as elastic deformation. However, once a critical value of strain is reached, a portion of the resulting strain results in permanent deformation of the body. This is known as plastic deformation. The resulting input energy required to inflict this strain, is given as the area under the stress strain curve. Simply stated, the stress as a function of strain in the elastic region is given as:

$$\sigma = E\varepsilon, \tag{1.1}$$

where E is the modulus of elasticity, also known as Youngs Modulus.

This constant of proportionality describes the slope of the elastic region of the stress strain relationship. For many materials including viscoelastic materials, this relationship is not strictly linear. This results in the creation of a hysteresis loop between the loading and unloading curves of the stress-strain diagram. Referring back to our previous assertion that the energy required to impose this strain is the area under the stress-strain curve, it is obvious that this hysteresis loop dictates a loss in energy in the system.

Given the law of conservation of energy, it is impossible for this energy to simply be lost. Instead, a large portion of this mechanical energy is converted into heat, approximately 70-80 with the remaining energy being converted into entropy within the atomic structure of the material. Such changes are manifested as changes in dislocation boundaries etc. By finding the difference in area under the loading, and unloading curves, and applying this to a heat transfer equation, the temperature at any point in a body can be predicted under cyclic load influences.

Heat Explosion. *When a material on which cyclic stress are imposed is sufficiently thermally insulated such that adiabatic or near adiabatic conditions are maintained, the results can be catastrophic. Since heat is not allowed to escape, the temperature will continue to rise with each successive stress cycle resulting in a massive temperature rise that ultimately results in catastrophic thermal failure known as heat explosion.*

When a material surface lacks sufficient thermal insulation to be considered adiabatic, the surface is said to be dissipative, or highly dissipative depending on the level of insulation. This will result in moderate temperature increases due to cyclic stress imposition compared to the model in which such self-heating effects are not considered. Consideration of these aforementioned effects prove to be of significant consequence when examining the mechanical behavior of the material.

Analysis. While there are several different models for the propagation of heat through a material, the selection of such an equation will greatly affect the accuracy of your model. There are two classical approaches to modeling heat propagation, the Fourier equation and the Maxwell-Catteneo Equation. Each model can be used to produce accurate solutions; however the accuracy of the Fourier model has come into question and has the model itself has actually been broken in certain situations. However, the Fourier equation will prove to be much easier to solve, particularly when the non-homogeneous case is considered (Fig. 1).

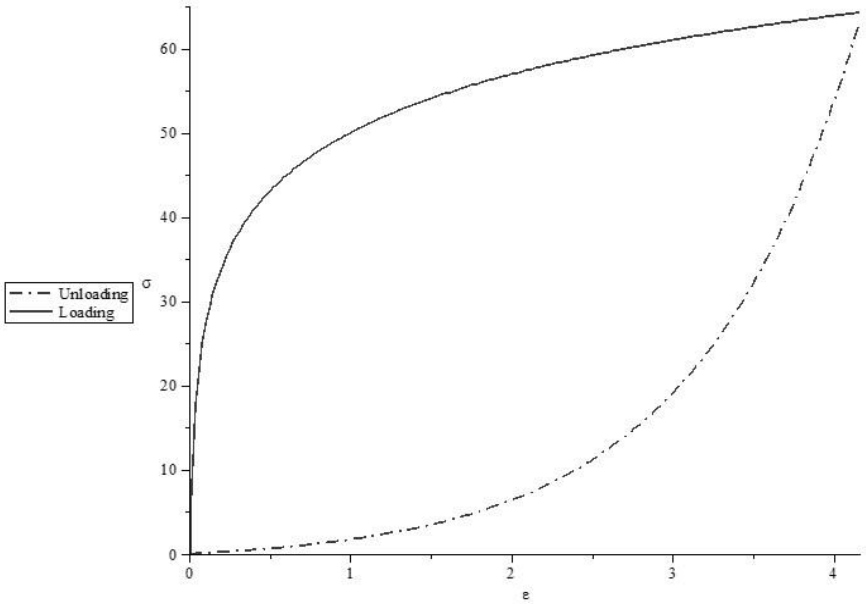


Fig. 1. Hysteresis loop in the stress-strain graph indicates a loss of energy from between the loading and unloading curves

2. The Fourier Law of Conduction. *Perhaps the most commonly used model for heat propagation through a solid is Fouriers law of heat conduction which can be shown by*

$$\frac{\partial T(x,t)}{\partial t} = \frac{\partial T(x,t)}{\partial x} + w, \tag{2.1}$$

where $T(x,t)$ represents the temperature at a given point, x and time, t in the material, W represents the work done on the material in each cycle [4]

While this model may prove to be an effective in many applications, there are some very real limitations that must be considered. Perhaps the biggest limitation is illustrated by the very nature of the equation itself. The Fourier equation, Eq. (1.1), is by definition a first-order partial differential equation of the parabolic form. This allows for an infinite velocity of heat transfer through the material. This is rather unrealistic in real life, as the velocity of heat propagation through the material must be limited to some finite value. Secondly, recent research suggests that Fouriers equation breaks down at grating spacing of about 5 microns, thus predicting a slower rate of heat propagation than is actually occurring [2]. While the Fourier equation does have shortcomings, there are benefits of modeling with this equation. It is a first order PDE which is easily solvable using many numerical methods and by separation of variables [1]. Applying initial value conditions which bound the distribution to an initial temperature of 100 degrees and holding the ends of the rods to a constant zero degrees, the following temperature distribution is obtained (Fig. 2):

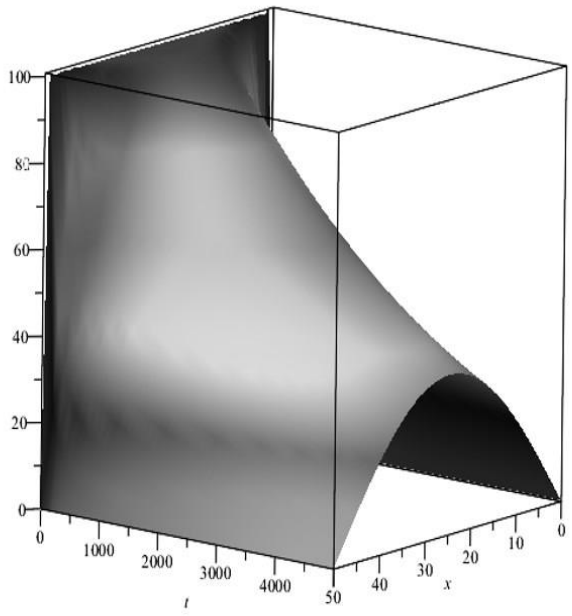


Fig. 2. Homogenous case of Fourier's Law of Conduction

The Maxwell-Catteneo Equation. *Another proven model for heat transport is the Maxwell-Catteneo model which is given as:*

$$\tau \frac{\partial^2 T(x,t)}{\partial t^2} + \frac{\partial T(x,t)}{\partial t} = K \frac{\partial^2 T(x,t)}{\partial x^2} + W. \tag{2.2}$$

From this equation, two things are immediately obvious. It is a second order partial differential equation of the hyperbolic form [4]. Unlike the Fourier law, this limits the velocity of heat propagation through the material to a finite value which is indicative of the actual system. Secondly, this equation has not been shown to break down at smaller grate spacing like the Fourier model. However, finding a solution to this equation will prove to be more difficult as an analytical solution is not as easily obtained as the reduced differential transform method (RDTM) must be used in much the same way it is applied to the well-known telegraph equation.

3. Development of the heat equation. In order to determine the governing equations for self-heat generation, the area within the hysteresis loop must be calculated. We will consider the method proposed below [2]. While there are many stress-strain relationships that model viscoelastic behavior, the Volterra model serves as the most accurate model for this scenario. The Volterra equation is given as

$$\phi(\epsilon) = \sigma + \int_0^t K(\tau - t)\sigma(t) f[T(t)T(\tau)]d\tau, \tag{3.1}$$

where the function $K(t-\tau)$ is the viscoelastic kernel given by

$$K(t-\tau) = k/(t-\tau)^{\alpha}. \tag{3.2}$$

And the imposed stress function, $\sigma(t)$ is given by

$$\sigma(t) = \sigma_0 + \sigma_1 cos(\theta). \tag{3.3}$$

Examining Eq. (6) implies a sinusoidal application of stress of amplitude σ_1 centered around an average stress level of σ_0. Applying the Voltera model, the area under the hysteresis loop, Q_0 is given as

$$Q_0 = \frac{\omega}{2\pi}\left\{\frac{2\sigma_0\sigma_1}{E} - \left[\frac{\sigma_0\sigma_1 k\omega}{E(1-\alpha)}\int_{-\frac{\pi}{\omega}}^{0} t^{(1-\alpha)}\sin(\omega t)dt + \frac{{\sigma_0}^2 k\pi \sin\left[\frac{1}{2}\pi(1-\alpha)\Gamma(1-\alpha)\right]}{2E\omega^{(1-\alpha)}}\right]\right\} \tag{3.4}$$

However, all energy loss is not transformed into heat. Instead, a portion of the energy contributes to internal entropy generation, creation of dislocation boundaries, and other structural changes in the material. Therefore, a constant of proportionality, is introduced and the final expression for the internal heat generation is given by

$$D_{in} = \frac{\mu\omega Q_0 T^{\gamma}}{\xi 2\pi}, \tag{3.5}$$

where μ typically lies between 0.7 and 0.8.

However, we must also consider heat dissipation from the surface of the rod such that μ typically lies between 0.7 and 0.8. However, we must also consider heat dissipation from the surface of the rod such that

$$D_{out} = -\beta(T - T_0), \tag{3.6}$$

where T_0 is the ambient temperature.

Finally, combining these equations we obtain the expression for total heat evolution into/out of the material

$$D(T) = Q_1\left(\frac{T}{T_0}\right)^{\gamma} - \beta_0\left(\frac{T}{T_0} - 1\right), \tag{3.7}$$

where the expression Q_1 is given by

$$Q_1 = \frac{\mu\omega Q_0 T_0{}^{\gamma}}{\xi 2\pi}. \tag{3.8}$$

And the expression β_0 is defined $\beta_0 = \beta T_0$ where β is the heat transfer coefficient.

Application of the self-heating model to the heat equations. From this model for the internal heat generation and dissipation of heat from the surface has been developed, it can be applied to the both the Fourier and Maxwell-Catteneo heat transfer equation to create a model for the temperature in the rod at any given point and time.

4. Application of self-heating model to the Fourier Law of Conduction. *By applying the self-heating model, Eq (3.8) to the Fourier Law of Heat Conduction, the following nonhomogenous equation was obtained*

$$\frac{\partial T(t,x)}{\partial t} - \alpha\frac{\partial^2 T(x,t)}{\partial x^2} = \frac{D(T)}{\rho c}, \tag{4.1}$$

and holding all parameters constant except for the angular frequency ω, the following isochronic diagram of the temperature distribution for angular frequencies of 10, 20, 30 and 40 was obtained numerically. From this plot it is readily apparent that as the angular frequency of the load application increases, the temperature at any given point and time also increases. While the temperature does continue to decrease as time progresses, there is a definite temperature elevation that corresponds to the increase in angular frequency of the applied stress. This is consistent with the underlying physical system (Fig. 3).

Application of self-heating model to the Maxwell-Catteneo Model. *When the self heating model is applied to the Maxwell-Catteneo equation, the non-homogenous solution is obtained as follows:*

$$\tau\frac{\partial^2 T}{\partial t^2}+\frac{\partial T}{\partial t}=K\frac{\partial^2 T}{\partial x^2}+\frac{D(t)}{\rho c}. \tag{4.2}$$

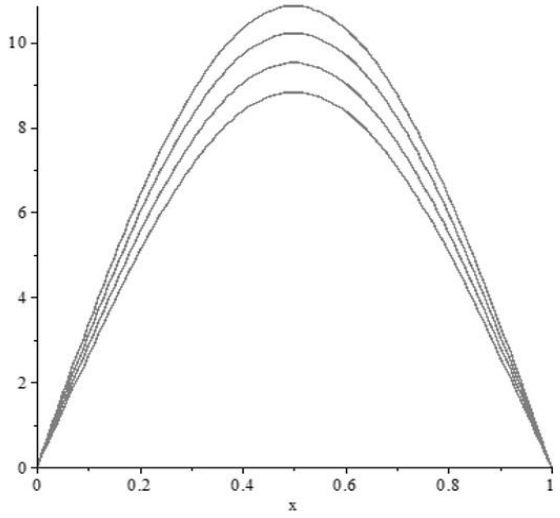


Fig. 3. Isochronic temperature versus position distribution for decreasing angular frequencies

Obtaining accurate solutions to the Maxwell-Catteneo model presents many more challenges. The most obvious is that it is a second order, non-homogenous hyperbolic partial differential equation which cannot be solved by most analytical techniques. Furthermore, many equation solvers such as those found in Maple cannot solve this type of equation analytically or numerically. In addition, it is difficult to define a fourth boundary condition necessary for solving the equation. Therefore, this solution must be obtained numerically or by other analytical methods such as the reduced differential transform method (Srivastava, 2013). As we continue our research, our aim is to develop methods of solving this equation to create a model that more accurately represents the self-heating phenomenon than Fouriers Law of conduction.

5. Development of Nodal Equations. Applying a nodal energy balance to node *i* the following expression is obtained

$$\dot{Q}_{i-1\to i}+\dot{Q}_{i+1\to i}+\dot{Q}_{int}=mc\frac{\partial T(x,t)}{\partial t}. \tag{5.1}$$

It can be shown that the first order derivative with respect to time and the first order derivative with respect to the spacial variable x can be is approximated using the following expressions

$$\frac{\partial T(x,t)}{\partial t}=\frac{T_i^{n+1}-T_i^n}{\Delta t}, \tag{5.2}$$

$$\frac{\partial T(x,t)}{\partial x}=\frac{T_[i+1]^n-T_i^n}{\Delta x}. \tag{5.3}$$

Next, the total energy entering and exiting the node through conduction is given by Fourier's Law of Conduction:

$$\dot{Q} = kA_c \frac{\partial T(x,t)}{\partial x}. \tag{5.4}$$

Substituting Eqs.(2, 3, 4) into Eq. 2 yields

$$\dot{Q}_{int}(t) + kA_c \left[\frac{T_[i-1]^n - T_i^n}{\Delta x}\right] + kA_c \left[\frac{T_[i+1]^n - T_i^n}{\Delta x}\right] = \rho c A_c \Delta x \left[\frac{T_[i]^{n+1} - T_i^n}{\Delta t}\right]. \tag{5.5}$$

To calculate the temperature at node *i* time *n* + 1, Eq. (5.4) must be solved for T_i^{n+1}. This yields the following expression for T_i^{n+1} in terms of the thermal conductivity, *k*, the material density, ρ, the cross sectional area of the rod, A_c, the thermal diffusion, α and the respective time and spacial steps, Δt and Δx

$$T_i^{n+1} = \frac{\dot{Q}_{int}(t)}{\rho c \Delta x A_c} + \frac{kA_c \Delta t}{\rho c A_c \Delta x}\left[\frac{T_{i-1}^n - T_i^n}{\Delta x}\right] + \frac{kA_c \Delta t}{\rho c A_c \Delta x}\left[\frac{T_{i+1}^n - T_i^n}{\Delta x}\right] + T_i^n. \tag{5.6}$$

Simplifying Eq. (5.2) yields the following expression

$$T_i^{n+1} = \dot{Q_{int}} \frac{\Delta t}{\rho c \Delta x A_c} + \frac{\alpha \Delta t}{\Delta x^2}\left[T_{i+1}^n - 2T_i^n + T_{i-1}^n\right] + T_i^n, \tag{5.7}$$

where the thermal diffusivity, α is given by $\alpha = \frac{k}{\rho c_p}$ and c_p is the specific heat capacity of the material at constant pressure.

6. Initial and boundary conditions. Therefore, in accordance with Eq. (5.7) the temperature at any node at any time step can be specified provided that the temperature at the end nodes and the temperatures at the previous time step are known. These requirements specify our boundary conditions. The first initial condition is:

$$T(x,0) = T_0. \tag{6.1}$$

This initial condition specified in Eq. (6.1) specifies that at any spacial coordiante, at initial time t=0, the temperature, T will be some initial value T_0. Next the temperatures at the end points are held constant. Consider the finite rod of length L. Holding each end at a constant temperature yields the following boundary conditions:

$$T(0,t) = T_1,$$
$$T(L,t) = T_1. \tag{6.2}$$

with the intial and boundary conditions specified, they can be initialized in the temperature distribution matrix, and the temperature at all other nodes and time steps is calculated in accordance with Eq.(5.7).

Solution. When Eq. (5.7) is applied to the initial and boundary conditions specified in Eq. (6.2), the following temperature distribution is obtained below in Fig. 4.

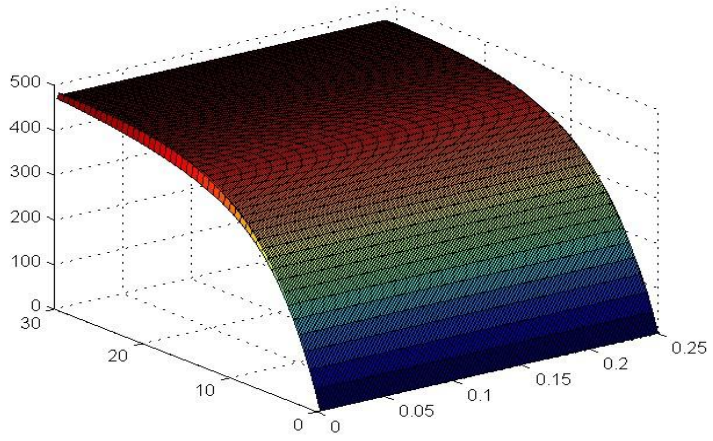


Fig. 4. Temperature distribution

Summary. In engineering mechanics, many material properties are highly dependent on temperature. This emphasizes the importance of consideration of all sources of heat both externally and internally generated. Such considerations led to the development of a model to predict the self-heating of viscoelastic materials due to mechanical vibrations modeled by the imposition of cyclic loadings on a viscoelastic rod. Such self-heating is manifested physically by an increase of temperature across the rod. However, to study this self-heating phenomenon, it is important to first consider the model with which heat transfer is modeled. Traditionally, Fourier's Law of heat conduction has been used. In recent years however, research from MIT suggested that Fourier's model may not be accurate when considering very small time intervals. This has led to the development of the Maxwell-Catteneo model for self-heating described above. As we continue our research, we plan to continue developing the Maxwell-Catteneo model, develop an experimental test plan, and ultimately compare the relative accuracy of the Fourier and Maxwell-Catteneo models developed in this paper.

References

[1] Gilbert R.P., Hsiao G.C., 2003. *Maple Projects for Differential Equations*. Prentice-Hall.

[2] Paste D.A., 2014. A collaborative effort breaks fourier's law.

[3] Srivastava V.K., 2013. The telegraph equation and its solution by reduced differential transform method. *Modelling and Simulation in Engineering*.

[4] Viktorova I., 1981. The dependence of heat evaluation on parameters of cyclic deformation process. *Mechanics of Solids*.

[5] Viktorova I., 1984. Self-heating of inelastic composites under cyclic deformation. *Mechanics of Solids*, 83, 1–58.

Rolling Contact Fatigue Life Evaluation Using Weibull Distribution

Semrád K.[1, a], Čerňan J.[1, b], Draganová K.[1, c]

1 – Department of Aviation Technical Studies, Technical University of Kosice, Faculty of Aeronautics, Slovakia

a – karol.semrad@tuke.sk

b – jozef.cernan@tuke.sk

c – katarina.draganova@tuke.sk



DOI **10.13140/RG.2.1.3338.9849**

Keywords: MS Excel, Weibull Distribution, Contact Fatigue Damage, Rolling Contact Fatigue, AXMAT, RMAT, Survival Probability, Sintered Materials, Hertzian Contact Stresses, Finite Element Method – FEM.

ABSTRACT. Surfaces subjected to rolling and sliding contacts may suffer from contact fatigue. This text deals with solid mechanic aspects of contact fatigue including the description of experimental study on contact fatigue. This document describes the methodology used in MS Excel for evaluation of component survival probability by Weibull distribution in application for evaluation of contact fatigue survival probability.

Introduction. Contact stresses and deformations are those that have their origin in the mutual contact of objects, realized by tiny contact areas. Principles of the contact mechanics can be applied for example for calculation of contact stresses between teeth of gear sets, within roller bearings, between the wheel and a rail of rail vehicles, etc. When two solid bodies are brought into a contact, the deformation occurs at or very close to the areas of the true contact, so we have to consider that the stress is three-dimensional. The Hertzian contact stresses (pressures) have a local character and that is the reason why their values, together with the distance from the contact area, decrease rapidly. Stresses that occur, when solving contact tasks, cannot be considered as the linear function of loads, because with the change of the load power, dimensions of the contact area are also different [1].

In the reliability engineering, failure analysis and survival analysis many statistical methodologies are used. In the article measured data were analysed using the Weibull distribution that is a continuous probability distribution, the gradients of which directly inform us about the shape and scale parameters corresponding to the characteristic life and failure rate of the specimen. Methodology for the Weibull distribution calculation in the commonly used MS Excel environment is also described.

Rolling Contact Fatigue. Considering one surface moving over the other in a rolling motion, the rolling element produces subsurface stresses. The effect of cyclically repeated contact stresses on the surface layer of solid parts are becoming visible, after certain time of running, when local subsurface cracks propagates and defects, commonly called pits, are formed. The process of pitting effect creation is the function of contact stresses, mechanical properties of material, surface roughness, internal stress distribution in layers close to the surface, condition of material microstructure – homogeneity and level of pollution, fibres orientation and sliding direction, attributes of used grease, direction and size of rolling. The inevitable condition and the main cause of pitting creation is the cyclical change of contact stress and is based on the fact that there is a relationship (similar to Wöhler curve diagram shown in Fig. 1) between the contact stress change amplitude and the number of cycles until the damage [1].

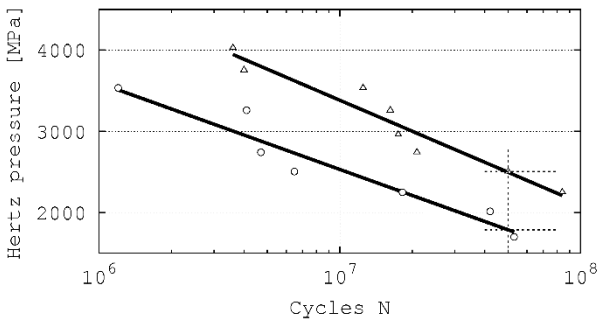


Fig. 1 Wöhler Curve Diagram

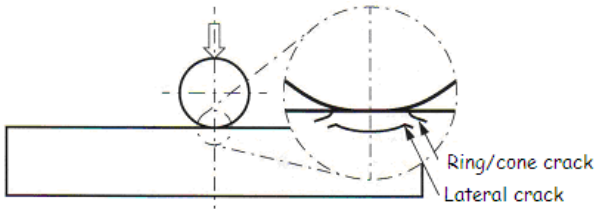


Fig. 2 Mechanism of Rolling Contact Fatigue

The whole process of the contact fatigue is the result of simultaneous effect of the rolling contact and material status. Considering enlarging and spreading of contact cracks, cracks have to form or already exist in the material structure (Fig. 2). In the first case, formation of micro-cracks mostly on two phases of boundary areas with considerable specific differences and acting like stress concentrators when loaded can be expected. Besides this, the high cyclic contact fatigue can evocate all by itself (in extreme testing conditions) phase transformations and so places with different structure and properties when compared to the main structure. In the second case, we are talking about a priori cracks, integrals or pores of a specific shape, which are able to grow immediately after loading (in certain conditions). Creation of the contact fatigue phenomenon does not occur in the whole specimen, only in the areas under the surface, where maximal shear stress is applied. However, the surface is sensitive, too, for example according to the strain energy hypothesis, the level of stress has the same value only if the friction factor reaches f=0,1. Of course, destruction can happen also by spreading of the fatigue cracks from the surface with existing defects, such as damaged surface, corrosion, low hardness or thick carbides [1].

Experimental Equipments. Equipment called AXMAT (Fig. 3 and 4) is designed for testing of flat circular specimen when verifying material resistance against the contact fatigue, to clarify the problem of rolling contact itself from material, tribological and lubrication point of view, between rolling parts. Maximal contact stress according to the point contact of the two - spheres theory, one with $R_2=\infty$, another $R_1=R$: contact of sphere and flat plane, is equals to:

$$\sigma_{\max} = 0{,}388.\sqrt[3]{4\,F\,\frac{E_1^2.E_2^2}{(E_1+E_2)^2}\cdot\frac{1}{R^2}}\,, \tag{1}$$

where E_1, E_2 are the Young´s modules of contact parts materials and F is the loading power.

The dangerous place, from the strain point of view, is the point which lies on the connection of the spheres´ centres and its distance from the contact plane is equal to the half of the contact area radius. Maximal shear stress equals to:

$$\tau_{\max} \cong 0{,}31.\sigma_{\max}. \tag{2}$$

Flat, circular, ring-like shaped specimen with given dimensions is pressed by the rotating axial bearing ring, using standardized bearing balls which are situated between the specimen and the bearing [2].

The next testing equipment type RMAT gives us ability to try fatigue strength of materials under contact stress when rolling. Specimen of cylindrical shape with given dimensions is rolled by two rotating discs, also with given shapes, while one of discs also presses the specimen [2].

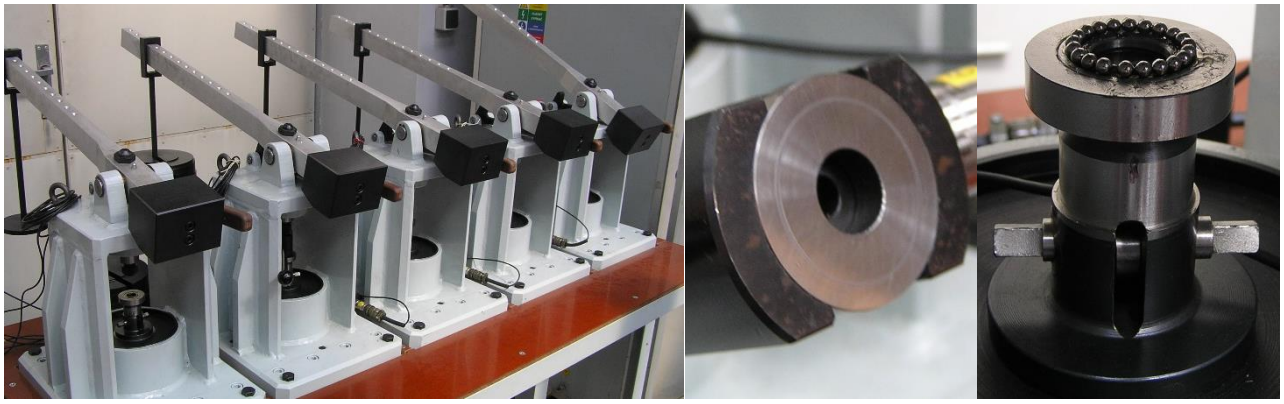


Fig. 3 AXMAT Experimental Equipment

Data Evaluation. In conditions of our department, AXMAT testing device was used to analyse formation of pitting damage at specimens made from sintered powders with adequate surface treatment, as part of the VEGA project No. 1/0464/08 - Tribological aspects of sintered materials damage with the emphasis on contact fatigue and wear out. Specimen provings run on using the testing device with chosen load level and are finished by pitting or by achieving 500 hours run out without break. Using this result, it is possible to create a relation between contact stresses and the number of cycles until pitting occurs (Fig. 1). In the specific case, the specimen was manufactured from sintered powder, alloyed 1,5Cr and 0,5Mo with the addition of 0,3C, die-pressed using 600 MPa pressure and temperature of 1120 °C for the period of ½ hrs. The surface of the specimen was subsequently subjected to abrasion and plasma nitriding at the temperature of 520 °C for the period of 7 hrs. For plotting the survival probability a set of 10 same material specimens are used. Time or the number of cycles until pitting damages appear under identical load conditions is recorded. In this case, the contact pressure is 1500 MPa. The results are evaluated by the Weibull distribution that shows the relation between the percentual survival probability and the number of cycles (Fig. 8). Using processed diagrams we are able to define L_{10}, L_{50}, L_{90} levels for 10, 50 and 90 % survival probability value, respectively [2].

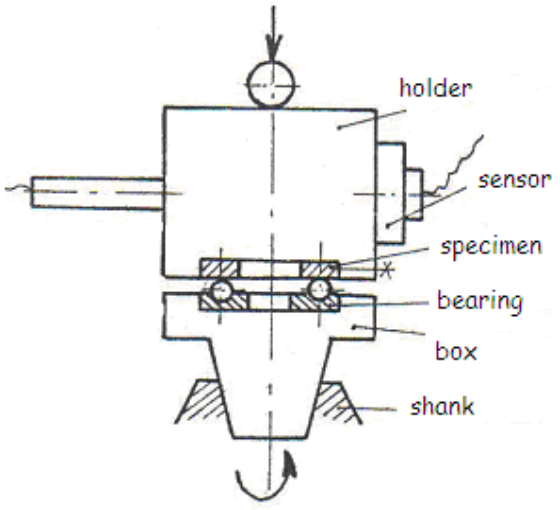


Fig. 4 AXMAT Design

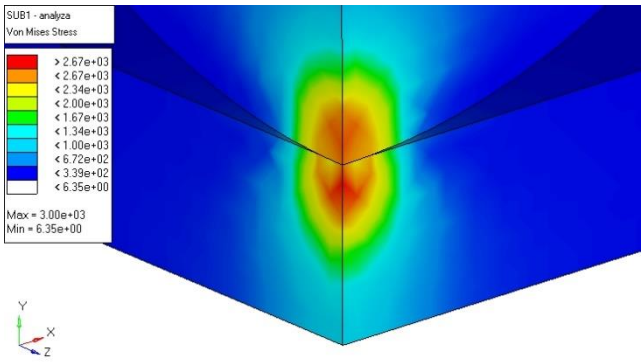


Fig. 5 FEM Analysis

As a control for calculate the maximum stresses by (1) and (2) we used the stress calculation using the finite element method (FEM). It gives a graphic picture of the stress distribution in the interesting area (Fig. 5).

	A	B	C	D	E	F
1	**Design Cycles**	**Rank**	**Median Ranks**	**1/(1-Median Rank)**	**ln(ln(1/(1-Median Rank)))**	**ln(Design Cycles)**
2	5 300 000	1	0.067307692	1.072164948	-2.663843085	15.48321738
3	5 828 000	2	0.163461538	1.195402299	-1.72326315	15.57818445
4	6 700 000	3	0.259615385	1.350649351	-1.202023115	15.71761808
5	10 000 000	4	0.355769231	1.552238806	-0.821666515	16.11809565
6	25 930 000	5	0.451923077	1.824561404	-0.508595394	17.07091116
7	38 319 000	6	0.548076923	2.212765957	-0.230365445	17.46145641
8	57 800 000	7	0.644230769	2.810810811	0.032924962	17.87249933
9	86 800 000	8	0.740384615	3.851851852	0.299032932	18.27911718
10	89 300 000	9	0.836538462	6.117647059	0.593977217	18.30751205
11	164 500 000	10	0.932692308	14.85714286	0.992688929	18.91842113
12						
13	**Coefficients**	**Beta/Alpha**				
14	0.826	0.826				
15	-14.631	49282275.97				
16						
17	**Cycles**	**Surv.Prob.**				
18	0	1.0000				
19	10 000 000	.7650				
20	20 000 000	.6220				
21	30 000 000	.5150				
22	40 000 000	.4310				
23	50 000 000	.3635				

Fig. 6 Preparing Data for Weibull Analysis in the MS Excel

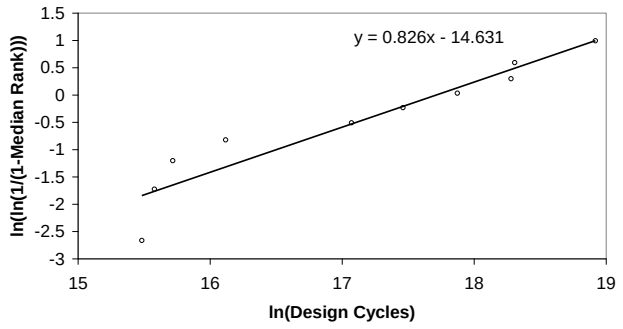


Fig. 7 Linear Fit Plot

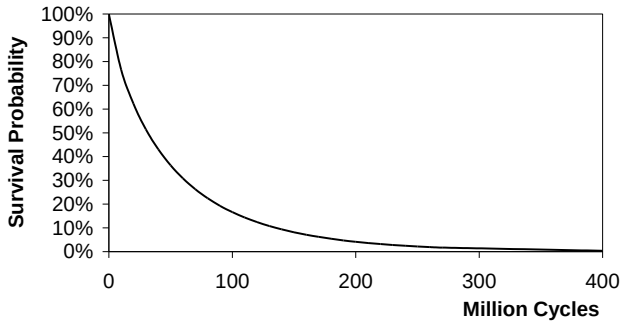


Fig. 8 Survival Graph

Weibull analysis in MS Excel. Modelling the data using Weibull analysis by MS Excel requires some preparation [3]. Open MS Excel and fill the cells (Fig. 6):

1. In cell A1 type the label Design Cycles. Enter the failure cycles data into cells A2:A11 from lowest to highest.

2. In cell B1 type the label Rank. In cells B2:B11 type the integers 1 – 10.

3. In cell C1 type the label Median Ranks. In cell C2 enter the formula:

=((B2–0.3)/(10+0.4)). Next copy cell C2 down through cell C11. Note that in the formula for median ranks the 10 is the total number of design units tested.

4. In cell D1 type the label 1/(1–Median Rank). Then in D2 enter the formula:

=1/(1–C2). Copy cell D2 down through cell D11.

5. In cell E1 type the label ln(ln(1/(1–Median Rank))). In cell E2 type the formula: =LN(LN(D2)). Copy cell E2 down through cell E11.

6. In cell F1 type the label ln(Design Cycles). In cell F2 type the formula: =LN(A2). Copy cell F2 down through cell F11.

After the processed data visualisation (column E vs. column F) we can expect a straight line (Fig. 7). By performing a simple linear regression we can obtain parameters: α - Characteristic Life, which is a measure of the scale, or spread, in the distribution of data and β - Shape Parameter, which indicates whether the failure rate is increasing. When the linear regression is performed, the estimate for the Weibull β parameter comes directly from the slope of the line. The estimate for the α parameter has to be calculated as:

$$\alpha = e^{-\left(\frac{b}{\beta}\right)}. \tag{3}$$

7. In cell A13 type the label Coefficients. Enter the coefficients from the linear regression formula: y=0,826x–14,631 into cells A14, A15; where A15 is the *b* coefficient in formula (3). In this case *b* = –14,631.

8. In cell B13 type the label Beta/Alpha. In cell B14 enter the formula: =A14 and In cell B15 enter the formula: =EXP(–A15/A14).

The formula for reliability assuming a Weibull distribution is:

$$R(t) = e^{-\left(\frac{x}{\alpha}\right)^{\beta}}, \tag{4}$$

where *x* is the time (or number of cycles) until failure.

9. In cell A17 type the label Cycles and In cells A18:A46 type the values 0 – 400 million in increments of 10 000 000.

10. In cell B17 type the label Survival Probability. In cell B18 type the formula:

=1–WEIBULL(A18;B$14;B$15;TRUE). Copy cell B18 down through cell B46.

The result is the Survival Graph (Fig. 8). The data in column A(Cycles) vs. column B(Survival Probability) can be plotted in percentages [4].

Summary. The results of L_{10}, L_{50}, L_{90} levels for 10, 50 and 90 % survival probability value for our specimens made from sintered powders are:

L_{10} = 130 000 000 cycles, L_{50} = 31 000 000 cycles, L_{90} = 3 000 000 cycles.

Sintered materials with their specific structure (presence of pores) have different reaction on behaving in such conditions as presented. With respect to this fact and to reality of large boom in the sintered part production and their application in the automobile industry, there is an objective need for basic research and systematic monitoring of the attributes that do influence durability and life-time of such strained materials. The Weibull distribution's strength is in its versatility. Depending on the parameter's values, the Weibull distribution can approximate an exponential, normal or skewed distribution. The Weibull distribution's virtually limitless versatility is matched by Excel's countless capabilities.

References

[1] K. Semrád, V. Zahradníček, Experimental Study on Contact Fatigue. In: Acta Avionica, vol. XI, no. 18, p. 97-100. Faculty of Aeronautics, Technical University of Kosice, 2009. ISSN 1335-9479.

[2] K. Semrád, R. Zahradníček, Using MS Excel for Evaluation of Component Survival Probability. In: ICMT´11: International Conference on Military Technologies 2011, Brno, Czech Republic, 10 to 11 May, 2011, p. 551-556. Faculty of Military Technology, University of Defence in Brno, 2011. ISBN 978-80-7231-788-2.

[3] E. Ostertagová, Probability and Mathematical Statistics with examples (in Slovak). Elfa Košice, 2005, p. 123. ISBN 80-8086-005-X.

[4] William W. Dorner, Using Microsoft Excel for Weibull Analysis. In: Quality Digest Magazine, January 1999, Best Access Systems, Indianapolis, USA, URL: http://www.qualitydigest.com/jan99/html/body_weibull.html

The Boltzmann Equation Of Phonon Thermal Transport Solved In the Relaxation Time Approximation – I – Theory

Amelia Carolina Sparavigna[1]

1 – Department of Applied Science and Technology, Politecnico di Torino, Italy


DOI **10.13140/RG.2.1.1001.1923**

Keywords: Thermal Conductivity, Phonons, Boltzmann Equation.

ABSTRACT. The thermal transport of a dielectric solid can be determined by means of the Boltzmann equation regarding its distribution of phonons subjected to a thermal gradient. After solving the equation, the thermal conductivity is obtained. A largely used approach for the solution is that of considering a relaxation time approximation, where the collisions of phonons are represented by relaxation times. This approximation can be questionable, but its use is able of providing reliable information on thermal conductivity and on the role of impurities and lattice defects in the thermal transport. Here we start a discussion on the thermal conductivity in dielectric solids. The discussion is divided in two parts. In the first part, which is proposed in this paper, we analyse the Boltzmann equation and its solution in the relaxation time approximation. In a second part, which will be the subject of a next paper, we will show comparison of calculated and measured thermal conductivities.

Introduction. The thermal transport of dielectric solids can be determined, in a semiclassical approach, by means of the Boltzmann equation, a well-known equation of statistical mechanics used to describe a system not in thermodynamic equilibrium [1-3]. In the case of a dielectric solid, the system is an assembly of phonons, quasiparticles originated from quantization of lattice vibrations, subjected to a thermal gradient. The Boltzmann equation contains a non-equilibrium distribution $g(\mathbf{r},\mathbf{k},t)$, in which arguments $(\mathbf{r},\mathbf{k},t)$ are position, wave-vector and time for the considered particles. The problem of transport is solved when distribution $g(\mathbf{r},\mathbf{k},t)$ is determined and, from it, the thermal conductivity evaluated.

Solving the Boltzmann equation to have the phonon non-equilibrium distribution is a non-trivial task. In particular, it requires the evaluation of phonon scattering mechanisms, which are rendering the equation an integro-differential equation [4-14]. A simple approach to the solution is that of using the relaxation time approximation. This approximation can be questionable because it is not considering the real microscopic properties of the lattice [6,7]; however, its use is able of providing good information on thermal conductivity and on the role impurities and defects in thermal transport. For this reason, the use of relaxation time approximation for solving the Boltzmann equation is an approach, which is still largely used.

The core of a relaxation time approximation is the following. Let us have a particle or a quasi-particle, a phonon for instance, that in the time interval *dt*, is subjected to a collision with probability $\mathrm{d}t/\tau$. We can assume that the time parameter τ is depending on the phonon properties: $\tau = \tau(\mathbf{r},\mathbf{k})$. We assume the variation of the distribution be given by:

$$\mathrm{d}g(\mathbf{r},\mathbf{k},t) = g(\mathbf{r},\mathbf{k},t+\mathrm{d}t) - g(\mathbf{r},\mathbf{k},t) = \frac{\mathrm{d}t}{\tau(\mathbf{r},\mathbf{k})}\, g^{o}(\mathbf{r},\mathbf{k})\,. \qquad (1)$$

In Eq.1, $g^o(\mathbf{r},\mathbf{k})$ is the equilibrium Bose-Einstein distribution. Approximation (1) tells that we assume, for solving the Boltzmann equation, that the distribution of phonons emerging from collisions does not depend on the non-equilibrium distribution $g(\mathbf{r},\mathbf{k},t)$, which we have before the collision. This assumption is reasonable if we are not too far from equilibrium.

As told previously, the relaxation time approximation is still largely used and therefore its discussion can be relevant for researchers who are investigating the thermal transport of solids. Here, we propose a first paper where we discuss how the thermal conductivity of a dielectric solid is determined from the Boltzmann equation. In a next paper, we will continue our analysis, comparing the thermal conductivity evaluated using the relaxation time approximation to experimental data.

Boltzmann equation and thermal conductivity. Phonons, such as electrons, move changing their position and momentum because subjected to diffusion, external fields and collisions. They obey to a general equation, which is the Boltzmann equation.

Let us consider a distribution of particles $g(\mathbf{r},\mathbf{k},t)$. Its general equation is [1]:

$$\frac{\partial g}{\partial t}+\frac{\mathrm{d}\mathbf{r}}{\mathrm{d}t}\cdot\frac{\partial g}{\partial \mathbf{r}}+\frac{\mathrm{d}\mathbf{k}}{\mathrm{d}t}\cdot\frac{\partial g}{\partial \mathbf{k}}=\left(\frac{\partial g}{\partial t}\right)_{\text{collis}}. \tag{2}$$

The second term on the left is coming from the migration of particles and the third term is produced by the drift of particles due to an external action, for instance a generalized force $\mathbf{F}$. Equation (2) becomes the Boltzmann equation:

$$\frac{\partial g}{\partial t}+\mathbf{v}\cdot\frac{\partial \mathrm{g}}{\partial \mathbf{r}}+\mathbf{F}\cdot\frac{1}{\hbar}\frac{\partial g}{\partial \mathbf{k}}=\left(\frac{\partial g}{\partial t}\right)_{\text{collis}}. \tag{3}$$

When the collision terms are written explicitly, the Boltzmann equation turns out in an integro-differential form. As previously told, this equation is often solved in the relaxation time approximation for an easy comparison to experimental data. Before discussing in detail this approximation, let us describe the Boltzmann equation for phonons.

Phonons are quasiparticles introduced in the harmonic approximation of lattice vibrations by the quantization of vibrational modes. Let us remember that quasiparticles occur when a microscopic system, such as a solid, is modelled by an assembly of different weakly interacting particles in a free space corresponding to the volume occupied by the system. Therefore, the assembly of phonons is a gas where quasiparticles are interacting, producing the thermal transport in the lattice. The cubic terms of the corresponding Hamiltonian function are giving the three-phonons processes, which are distinguished in *normal* and *umklapp* processes. The umklapp processes can transfer momentum to the lattice as a whole, degrading the thermal current.

To solve the Boltzmann equation of phonons, let us suppose a distribution $n_{\mathbf{q}p}(\mathbf{r},t)$, for phonon state (**q**, *p*) about position **r** and time *t*, where **q** is the wave-number and *p* the polarization. Let us suppose a gradient ∇T of temperature $T = T(\mathbf{r})$ giving origin to a diffusion process. In this manner, we have a scalar term of the form:

$$-\mathbf{v}_p(\mathbf{q})\cdot\nabla T\frac{\partial n_{\mathbf{q}p}}{\partial T}.$$

In it, $\mathbf{v}_p(\mathbf{q})$ is the group velocity of phonon ($\mathbf{q}$, p). The distribution $n_{\mathbf{q}\,p}$ depends on position through the temperature $T = T(\mathbf{r})$. Moreover, scattering processes are changing the distribution.

If we have a stationary condition, the total variation must be equal to zero:

$$-\mathbf{v}_p(\mathbf{q})\cdot\nabla T\frac{\partial n_{\mathbf{q}p}}{\partial T}+\left.\frac{\partial n_{\mathbf{q}p}}{\partial t}\right|_{\text{scatt}}=0. \tag{4}$$

Eq.4 is the general form of Boltzmann equation for phonons subjected to a thermal gradient [1-3]. It becomes an integro-differential equation, when the scattering term representing the collisions of quasiparticles is explicitly given.

In the case of a small thermal gradient, the equation is solved linearizing it, by considering just small deviations from equilibrium. The deviation is given by $n_{\mathbf{q}p} - n^o_{\mathbf{q}p}$, where $n^o_{\mathbf{q}p}$ is the equilibrium distribution. To illustrate the approach, let us consider the case of elastic scattering of phonons, where the phonon process is given by $(\mathbf{q}, p)\rightarrow(\mathbf{q}', p')$, with conservation of energy. The probability of a transition from $(\mathbf{q}, p)$ to $(\mathbf{q}', p')$, in the time unit, is [1]:

$$P^{\mathbf{q}'p'}_{\mathbf{q}p}=n_{\mathbf{q}p}(n_{\mathbf{q}'p'}+1)Z^{\mathbf{q}'p'}_{\mathbf{q}p}. \tag{5}$$

In (5), $Z^{\mathbf{q}'p'}_{\mathbf{q}p}$ is the intrinsic probability, which does not depend on the occupation of phonon states $(\mathbf{q}, p)$ and $(\mathbf{q}', p')$. The transition probability from $(\mathbf{q}', p')$ to $(\mathbf{q}, p)$ is [1]:

$$\begin{aligned}P^{\mathbf{q}p}_{\mathbf{q}'p'}&=n_{\mathbf{q}'p'}(n_{\mathbf{q}p}+1)Z^{\mathbf{q}p}_{\mathbf{q}'p'}\\ Z^{\mathbf{q}p}_{\mathbf{q}'p'}&=Z^{\mathbf{q}'p'}_{\mathbf{q}p}\end{aligned} \tag{6}$$

In this manner, we can write the scattering term as [1]:

$$\left.\frac{\partial n_{\mathbf{q}p}}{\partial t}\right|_{\text{scatt}}=\sum_{\mathbf{q}'p'}\left(P^{\mathbf{q}p}_{\mathbf{q}'p'}-P^{\mathbf{q}'p'}_{\mathbf{q}p}\right)=\sum_{\mathbf{q}'p'}\left[n_{\mathbf{q}'p'}(n_{\mathbf{q}p}+1)-n_{\mathbf{q}p}(n_{\mathbf{q}'p'}+1)\right]Z^{\mathbf{q}'p'}_{\mathbf{q}p}. \tag{7}$$

And, linearizing it [1]:

$$\left.\frac{\partial n_{\mathbf{q}p}}{\partial t}\right|_{\text{scatt}}=\sum_{\mathbf{q}'p'}\left[(n_{\mathbf{q}'p'}-n^o_{\mathbf{q}'p'})-(n_{\mathbf{q}p}-n^o_{\mathbf{q}p})\right]Z^{\mathbf{q}'p'}_{\mathbf{q}p}. \tag{8}$$

Let us remember that we have, for the equilibrium distribution, $n^o_{\mathbf{q}p} = n^o_{\mathbf{q}'p'}$, because $n^o_{\mathbf{q}p}$ depends on energy only. For the conservation of energy, in the elastic process, $\hbar\,\omega_{\mathbf{q}p} = \hbar\,\omega_{\mathbf{q}'p'}$.

The linearized Boltzmann equation becomes:

$$-\mathbf{v}_p(\mathbf{q})\cdot\nabla T\,\frac{\partial n^o_{\mathbf{q}p}}{\partial T} = \sum_{\mathbf{q}'p'}\left[(n_{\mathbf{q}p} - n^o_{\mathbf{q}p}) - (n_{\mathbf{q}'p'} - n^o_{\mathbf{q}'p'})\right] Z^{\mathbf{q}'p'}_{\mathbf{q}p} \quad . \tag{9}$$

In the equation, $(\partial n_{\mathbf{q}\,p} / \partial T)$ is given only by the contribution of the equilibrium distribution $n^o_{\mathbf{q}p}$. To have the Boltzmann linearized equation in the general case, let us define $\Psi_{\mathbf{q}\,p}$ as:

$$n_{\mathbf{q}p} = n^o_{\mathbf{q}p} - \Psi_{\mathbf{q}p}\,\frac{\partial n^o_{\mathbf{q}p}}{\partial(\hbar\omega_{\mathbf{q}p})}\,. \tag{10}$$

Let us remember that ($x = \hbar\omega_{\mathbf{q}p}/k_BT$; k_B is the Boltzmann constant):

$$\frac{1}{k_BT}\frac{\partial}{\partial x}\left\{\frac{1}{e^x - 1}\right\} = \frac{1}{k_BT}\,n_{\mathbf{q}p}\left(n_{\mathbf{q}p} + 1\right).$$

Then, in the case of elastic scattering, the linearized equation is [7]:

$$-k_B\,T\,\mathbf{v}_p(\mathbf{q})\cdot\nabla T\,\frac{\partial n^o_{\mathbf{q}p}}{\partial T} = \sum_{\mathbf{q}'p'}\left[\Psi_{\mathbf{q}p}n^o_{\mathbf{q}p}(n^o_{\mathbf{q}p}+1) - \Psi_{\mathbf{q}'p'}n^o_{\mathbf{q}'p'}(n^o_{\mathbf{q}'p'}+1)\right] Z^{\mathbf{q}'p'}_{\mathbf{q}p} \tag{11}$$

$$k_B\,T\,\mathbf{v}_p(\mathbf{q})\cdot\nabla T\,\frac{\partial n^o_{\mathbf{q}p}}{\partial T} = \sum_{\mathbf{q}'p'}\left[\Psi_{\mathbf{q}'p'} - \Psi_{\mathbf{q}p}\right] Q^{\mathbf{q}'p'}_{\mathbf{q}p}\,. \tag{12}$$

$$Q^{\mathbf{q}'p'}_{\mathbf{q}p} = n^o_{\mathbf{q}p}(n^o_{\mathbf{q}p}+1)Z^{\mathbf{q}'p'}_{\mathbf{q}p}$$

In the case of three-phonon scattering, the linearized equation is [7]:

$$\begin{aligned} k_B\,T\,\mathbf{v}_p(\mathbf{q})\cdot\nabla T\,\frac{\partial n^o_{\mathbf{q}p}}{\partial T} = {} & \sum_{\mathbf{q}'p'}\sum_{\mathbf{q}''p''} Q^{\mathbf{q}''p''}_{\mathbf{q}p,\mathbf{q}'p'}\left[\Psi_{\mathbf{q}''p''} - \Psi_{\mathbf{q}'p'} - \Psi_{\mathbf{q}p}\right] + \\ & + \frac{1}{2}\sum_{\mathbf{q}'p'}\sum_{\mathbf{q}''p''} Q^{\mathbf{q}'p',\mathbf{q}''p''}_{\mathbf{q}p}\left[\Psi_{\mathbf{q}''p''} + \Psi_{\mathbf{q}'p'} - \Psi_{\mathbf{q}p}\right]. \end{aligned} \tag{13}$$

Summations on $\mathbf{q}'$ and $\mathbf{q}''$ concern phonons in the Brillouin Zone of the lattice. However, it is better to change the summation into an integration as:

$$\sum_{\mathbf{q}'} \rightarrow \frac{\Omega}{(2\pi)^3} \int \mathrm{d}^3\mathbf{q}' .$$

$\Omega = NV$ is the volume of the crystal, N the number of primitive cells of it, having volume V. Once function $\Psi_{\mathbf{q}p}$ is evaluated, with the iterative method [6,7] for instance, the density of the thermal current **U** can be determined. This density current is defined as:

$$\mathbf{U} = \frac{1}{\Omega} \sum_{\mathbf{q}p} \hbar\omega_{\mathbf{q}p} \mathbf{v}_{\mathbf{q}p} n_{\mathbf{q}p} = -\frac{1}{\Omega} \sum_{\mathbf{q}p} \hbar\omega_{\mathbf{q}p} \mathbf{v}_{\mathbf{q}p} \frac{\partial n^o_{\mathbf{q}p}}{\partial(\hbar\omega_{\mathbf{q}p})} \Psi_{\mathbf{q}p} . \quad (14)$$

In a Cartesian frame having unit vectors $\mathbf{u}_i$, current **U** is:

$$U_j = -\sum_i \kappa_{ji} \frac{\partial T}{\partial x_i} . \quad (15)$$

Tensor κ_{ij} is the thermal conductivity tensor, that, in a isotropic crystal is having non-null terms $\kappa_{xx} = \kappa_{yy} = \kappa_{zz} = \kappa$.

Phonon collisions. Phonons are interacting among them through *normal* and *umklapp* process. Normal processes do not produce thermal resistance, but are mixing the phonon states. The umklapp processes are producing resistivity and, for this reason, are important at high temperatures. For these processes, we have the conservation rules of momentum $\mathbf{q} + \mathbf{q}' = \mathbf{q}'' + \mathbf{g}$ and energy $\hbar\omega + \hbar\omega' = \hbar\omega''$. Note that, in the conservation of momentum we find **g**, which is a vector of the reciprocal lattice. For this reason, **q**" must be large enough to fulfil the conservation of energy, with an energy equal to the sum of the energies of phonons **q** and **q**', whereas the momentum is supplied by lattice. However, to have a population of high-energy phonons we must be at high temperatures.

When temperature is low, the mean free path of phonons corresponds to the size of the crystal. Let us suppose a cylindrical sample having diameter D; the mean free path is $\Lambda = D$ and then the thermal conductivity κ has the following proportionality:

$$\kappa \propto T^3 D . \quad (16)$$

It is caused by the behavior of the specific heat, which is proportional to the cube of temperature. However, normal and umklapp processes become relevant at high temperature, and then we need a different proportionality to cover all the range of temperature.

This proportionality is given by:

$$\kappa \propto T^3 e^{(-\beta\Theta/k_B T)}. \tag{17}$$

Therefore, (17) tells us that, in the range of low temperatures, the thermal conductivity increases with temperature, because the number of phonons is increasing with it. After reaching a maximum value, the conductivity starts decreasing because the number of scattering processes is increasing with temperature.

Besides the effect of the size of the sample and of phonon-phonon interaction, other mechanisms are scattering phonons. For instance, in a perfect lattice made of atoms of the same element, we can have atoms with different isotopic masses. Mass differences are small but they are sources of phonon scattering. Using a simple elastic theory, it is possible to find a Rayleigh scattering formula for the cross section σ of the diffusion from a point-like mass δM in a medium having density ρ, for waves with wave-number q [1]:

$$\sigma(q) = \frac{q^4}{4\pi\rho^2}(\delta M)^2. \tag{18}$$

The cross section is linked to the mean free path as $a^3 = \sigma\Lambda$, where a is the lattice constant. If each atom can differ of the same quantity, we have:

$$\Lambda(q) = \frac{4\pi}{a^3 q^4}\frac{M^2}{(\delta M)^2}. \tag{19}$$

$\Lambda(q)$ is strongly depending on q. The thermal conductivity κ can be evaluated as [1]:

$$\kappa = \frac{1}{3}\int C(q)v(q)\Lambda(q)\,d\mathbf{q}. \tag{20}$$

The integration runs on all the values of the wave-number.

Integral (20) is divergent when q goes to zero. This happens because specific heat and velocity are constant when q goes to zero, then we have:

$$\kappa \propto \int \frac{q^2 dq}{q^4} \propto \int \frac{dq}{q^2}. \tag{21}$$

However, phonon-phonon normal processes exist at low temperatures. These processes are not resistive, but they are mixing the phonon states. In this manner, the long-wavelength modes, which are modes scarcely diffused by isotopic defects, are transformed by the normal processes in modes having shorter wavelengths and then easily diffused.

Let us consider a specific wavenumber, given by:

$$\bar{q} \approx \frac{T}{\Theta} q_D . \tag{22}$$

In (22), we find the Debye wave-number q_D and the Debye temperature Θ. We have that [11]:

$$\Lambda \approx \Lambda(\bar{q}) \propto T^{-4}. \tag{23}$$

Then, the thermal conductivity κ influenced by the isotopic scattering has the following decreasing behavior with temperature:

$$\kappa \propto \left(\frac{M}{\delta M} \right)^2 \frac{1}{T} . \tag{24}$$

Thermal current and relaxation times. Let us consider again the thermal current density, given by the microscopic relation [15]:

$$\mathbf{U} = \frac{1}{\Omega} \sum_{\mathbf{q}p} n_{\mathbf{q}p} \hbar \omega_{\mathbf{q}p} \mathbf{v}_{\mathbf{q}p} . \tag{25}$$

Since the group velocity is given as

$$\mathbf{v}_{\mathbf{q}p} = \frac{\partial \omega_{\mathbf{q}p}}{\partial \mathbf{q}} , \tag{26}$$

we have that, for acoustic phonons, (26) is simply $\mathbf{v}_{\mathbf{q}p} = c_p \hat{\mathbf{q}}$, where c_p is the speed of the sound for the given polarization of the wave and $\hat{\mathbf{q}}$ is the unit vector of $\mathbf{q}$. In the general case, to evaluate the thermal conductivity we need the dispersion of angular frequency $\omega_{\mathbf{q}p}$, in reference to the wave-number. The main difficulty in evaluating (25) is the determination of the phonon distribution $n_{\mathbf{q}p}$. Let us try to use relaxation times for this task.

The relaxation time approximation consists in writing the derivative of the distribution with respect to time as [1]:

$$\frac{\partial n_{\mathbf{q}p}}{\partial t} = \frac{n^o_{\mathbf{q}p} - n_{\mathbf{q}p}}{\tau(\mathbf{q}, p)} , \tag{27}$$

$n^o_{\mathbf{q}p}$ is the equilibrium distribution. In (27) we see the relaxation time for the mode ($\mathbf{q}$, p). If there is a thermal gradient, from the Boltzmann equation:

$$\frac{\partial n_{\mathbf{q}p}}{\partial t} = \mathbf{v}_{\mathbf{q}p} \cdot \nabla T \left(\frac{\partial n_{\mathbf{q}p}}{\partial T} \right). \tag{28}$$

In a further approximation:

$$\left(\frac{\partial n_{\mathbf{q}p}}{\partial T} \right) = \left(\frac{\partial n^{o}_{\mathbf{q}p}}{\partial T} \right). \tag{29}$$

In (29), the variation of the distribution with respect to the temperature is evaluated through the equilibrium distribution. This is possible if we are considering a small gradient of temperature.

From (27) and (28), Joseph Callaway defined the difference between the distribution existing when there is a temperature gradient and that of equilibrium as [16-18]:

$$n_{\mathbf{q}p} - n^{o}_{\mathbf{q}p} = -\tau(\mathbf{q}, p)\ \mathbf{v}_{\mathbf{q}p} \cdot \nabla T\ \frac{\hbar\omega_{\mathbf{q}p}}{k_B T^2} \frac{e^x}{(e^x - 1)^2}. \tag{30}$$

In (30), we used again the dimensionless variable $x = \hbar\omega_{\mathbf{q}p} / k_B T$. The thermal current is given by:

$$\mathbf{U} = -\frac{1}{\Omega} \sum_{\mathbf{q}p} \tau(\mathbf{q}, p) \mathbf{v}_{\mathbf{q}p} \cdot \nabla T\ \frac{(\hbar\omega_{\mathbf{q}p})^2}{k_B T^2} \frac{e^x}{(e^x - 1)^2} \mathbf{v}_{\mathbf{q}p}. \tag{31}$$

In the case of anisotropic solids, we have a tensor for the thermal conductivity:

$$\kappa_{\alpha\beta} = \frac{1}{\Omega} \sum_{\mathbf{q}p} \tau(\mathbf{q}, p) \frac{(\hbar\omega_{\mathbf{q}p})^2}{k_B T^2} \frac{e^x}{(e^x - 1)^2} (\mathbf{v}_{\mathbf{q}p})_\alpha (\mathbf{v}_{\mathbf{q}p})_\beta. \tag{32}$$

α and β are corresponding to spatial components x,y,z. If we use the specific heat:

$$C_{ph}(\omega) = \frac{d}{dT} \left(\hbar\omega_{\mathbf{q}p} n^{o}_{\mathbf{q}p} \right) = \frac{(\hbar\omega_{\mathbf{q}p})^2}{k_B T^2} \frac{e^x}{(e^x - 1)^2}. \tag{33}$$

We have:

$$\kappa = \frac{1}{\Omega} \sum_{\mathbf{q}p} \tau(\mathbf{q}, p) C_{ph}(\omega) \mathbf{v}^2_{\mathbf{q}p} \cos^2\theta. \tag{34}$$

In the isotropic case, θ is the angle between the group velocity and the thermal gradient. Instead of the summation on the phonon states, we use an integration [15]:

$$\frac{1}{\Omega}\sum_{\mathbf{q}p} \rightarrow \frac{1}{(2\pi)^2}\sum_p \int d\mathbf{q}\,.$$

Ω is the volume of crystal. Then:

$$\kappa = \frac{1}{(2\pi)^2}\sum_p \int d\mathbf{q}\,\tau(\mathbf{q}, p)\, C_{ph}(\omega)\, v_{\mathbf{q}p}^2 \cos^2\theta\,. \tag{35}$$

Let us assume a general relaxation time $\tau(q)$ as a function $\tau(q) = Aq^{-n}$, then the thermal conductivity that we obtain is:

$$\kappa \propto T^{3-n}\int_0^{\Theta/T} \frac{x^{4-n}e^x}{(e^x-1)^2}\,dx\,. \tag{36}$$

In the next section, we will discuss in detail how Callaway used the relaxation times, to evaluate the thermal conductivity in dielectric solids.

Callaway theory. In 1959, Joseph Callaway proposed his model of thermal conductivity based on the relaxation time approximation, for investigating, in particular, the role of isotopic defects. This model is still used today to fit the experimental data of thermal conductivity; in it, also the phonon-phonon normal and umklapp processes are considered. Here, our discussion of Callaway model is based on his papers published in the Physical Review [16-18]. The formula for thermal conductivity that Callaway obtained is the following:

$$\kappa = \frac{\mathrm{c}^2}{2\pi^2}\int \tau_c\left(1+\frac{\beta}{\tau_N}\right) C_{ph}\, q^2 dq\,, \tag{37}$$

τ_c is a combination of relaxation times coming from the different scattering processes of phonons: boundary scattering, isotope effects, normal and umklapp processes for instance. C_{ph} is specific heat. τ_N is the relaxation time approximation coming from normal processes. β is given by the following formula:

$$\beta = \frac{\int_0^{\Theta/T} \frac{\tau_c}{\tau_N}\frac{e^x}{\left(e^x-1\right)^2}x^4 dx}{\int_0^{\Theta/T} \frac{1}{\tau_N}\left(1-\frac{\tau_c}{\tau_N}\right)\frac{e^x}{\left(e^x-1\right)^2}x^4 dx}\,. \tag{38}$$

Θ is the Debye temperature and $x = \hbar\omega_{\mathbf{q}p}/k_B T$. Let us consider a relaxation time given by:

$$\tau_u^{-1} = A\omega^4 + B_1 T^3 \omega^2 + c/L\,. \tag{39}$$

Term $A\omega^4$ represents a phonon scattering from point-like impurities and isotope defects. Term $B_1 T^3 \omega^2$ concerns the *umklapp* processes (B_1 contains the exponential factor in (17), which depend on temperature); c/L is the scattering from the boundary of the sample (c is the speed of the sound and L the size of the sample). In the case of a pure sample, A=0.

Let us assume for normal scattering:

$$\tau_N^{-1} = B_2\, T^3 \omega^2\,. \tag{40}$$

B_2 does not depend on temperature. Combining (39) and (40), we have:

$$\tau_c^{-1} = A\omega^4 + (B_1 + B_2) T^3 \omega^2 + \frac{c}{L}\,. \tag{41}$$

Callaway gives the thermal conductivity as:

$$\kappa = \frac{k_B}{2\pi^2 c}\left(I_1 + \beta I_2\right). \tag{42}$$

$$I_1 = \int_0^{k_B\Theta/\hbar} \tau_c \frac{\hbar^2\omega^2}{k_B^2 T^2} \frac{e^{\hbar\omega/k_B T}}{\left(e^{\hbar\omega/k_B T} - 1\right)^2} \omega^2 d\omega\,. \tag{43}$$

$$I_2 = \int_0^{k_B\Theta/\hbar} \frac{\tau_c}{\tau_N} \frac{\hbar^2\omega^2}{k_B^2 T^2} \frac{e^{\hbar\omega/k_B T}}{\left(e^{\hbar\omega/k_B T} - 1\right)^2} \omega^2 d\omega\,. \tag{44}$$

Let us use dimensionless variable $x = \hbar c q/k_B T$. We have:

$$I_1 = \left(\frac{k_B T}{\hbar}\right)^3 \int_0^{\Theta/T} \frac{x^4}{\left(Dx^4 + Ex^2 + \frac{c}{L}\right)} \frac{e^x}{\left(e^x - 1\right)^2} dx\,. \tag{45}$$

In (45), we have:

$$D = A\left(\frac{k_B T}{\hbar}\right)^4 ; \; E = (B_1 + B_2)T^3\left(\frac{k_B T}{\hbar}\right)^2 .$$

At low temperatures, it is the boundary scattering which is dominating with its relaxation time c/L; in this manner, approximating (45) with an integral from 0 to infinite, Callaway obtained:

$$I_1 = \frac{4\pi^2}{15}\frac{L}{c}\left(\frac{k_B T}{\hbar}\right)^3\left[1 - \frac{20\pi^2}{7}\frac{EL}{c} - 16\pi^4\frac{DL}{c}\right]. \tag{46}$$

Neglecting βI_2, the thermal conductivity is approximated as (Equation 23 of Ref.18):

$$\kappa = \frac{2k_B\pi^2 L}{15c^2}\left(\frac{k_B T}{\hbar}\right)^3\left[1 - 16A\left(\frac{\pi k_B T}{\hbar}\right)^4\frac{L}{c} - \frac{20}{7}(B_1 + B_2)T^3\left(\frac{\pi k_B T}{\hbar}\right)^2\frac{L}{c}\right]. \tag{47}$$

And also, in the case that *D=0*, we can have (Equation 26 of Ref.18):

$$I_1 = \left(\frac{k_B T}{\hbar}\right)^3 \frac{1}{E}\int_0^{\Theta/T} \frac{x^4}{x^2 + c/LE}\frac{e^x}{\left(e^x - 1\right)^2}dx . \tag{48}$$

From this integral, Callaway deduced the following formula [18]:

$$\begin{aligned} I_1 &= \left(\frac{k_B T}{\hbar}\right)^3 \frac{1}{E}\left[\frac{1}{3}\pi^2 - e^{-\Theta/T}\left(\frac{\Theta^2}{T^2} + \frac{2\Theta}{T} + 2\right) - \frac{\pi}{2}\left(\frac{c}{LE}\right)^{\frac{1}{2}}\right] = \\ &= \frac{k_B\pi^2}{3\hbar(B_1 + B_2)T^2}\left\{1 - \frac{3e^{-\Theta/T}}{\pi^2}\left(\frac{\Theta^2}{T^2} + \frac{2\Theta}{T} + 2\right) - \frac{3\hbar}{2\pi k_B T^{\frac{5}{2}}}\left[\frac{c}{L(B_1 + B_2)}\right]^{\frac{1}{2}}\right\}. \end{aligned} \tag{49}$$

As a consequence, the thermal conductivity in isotopically pure materials has a behaviour with temperature as T^{-2}, at low temperatures. The Callaway's theory was applied in [18], to the analysis of experimental data of thermal conductivity in Germanium, in the case of normal Ge and in the case of single isotope Ge [19], showing a remarkable agreement between theory and experiments. In fact, Callaway's paper was among the first works to point out the importance of the isotope scattering in reducing the thermal conductivity.

After this discussion on the theory concerning the Boltzmann equation for phonons and its solution in the relaxation time approximation, in a next paper, we will address how the thermal conductivity evaluated in this framework is in agreement with experimental data.

References

[1] Ziman, J.M. (1962). Electrons and phonons: The theory of transport phenomena in solids. Clarendon Press. Reprint Edition in 2001. ISBN-10: 0198507798, ISBN-13: 978-0198507796

[2] Gurevich, V.L. (1986). Transport in phonon systems. North-Holland. ISBN-10: 044487013X, ISBN-13: 978-0444870131

[3] Srivastava, G.P. (1990). The physics of phonons. Taylor and Francis. ISBN ISBN-10: 0852741537, ISBN-13: 978-0852741535

[4] Omini, M., & Sparavigna, A. (1995). An iterative approach to the phonon Boltzmann equation in the theory of thermal conductivity. Physica B, 212(2), 101-112. DOI: 10.1016/0921-4526(95)00016-3

[5] Omini, M., & Sparavigna, A. (1997). Effect of phonon scattering by isotope impurities on the thermal conductivity of dielectric solids. Physica B, 233(2-3), 230-240. DOI: 10.1016/s0921-4526(97)00296-2

[6] Omini, M., & Sparavigna, A. (1996). Beyond the isotropic-model approximation in the theory of thermal conductivity. Physical Review B, 53(14), 9064-9073. DOI: 10.1103/physrevb.53.9064

[7] Omini, M., & Sparavigna, A. (1997). Heat transport in dielectric solids with diamond structure. Nuovo Cimento D, 19(10), 1537-1564.

[8] Sparavigna, A. (1997). Thermal conductivity of solid neon: an iterative analysis. Physical Review B, 56(13), 7775-7778. DOI: 10.1103/physrevb.56.7775

[9] Sparavigna, A.C. (2015). Thermal conductivity of zincblende crystals. Mechanics, Materials Science & Engineering Journal, October 2015, 1-8. DOI: 10.13140/RG.2.1.1758.0565

[10] Broido, D.A., Ward, A., & Mingo, N. (2005). Lattice thermal conductivity of silicon from empirical interatomic potentials. Physical Review B, 72(1), 014308. DOI: 10.1103/physrevb.72.014308

[11] Kaburaki, H., Li, J., Yip, S., & Kimizuka, H. (2007). Dynamical thermal conductivity of argon crystal. Journal of Applied Physics, 102(4), 043514. DOI: 10.1063/1.2772547

[12] Turney, J.E., Landry, E.S., McGaughey, A.J.H., & Amon, C.H. (2009). Predicting phonon properties and thermal conductivity from anharmonic lattice dynamics calculations and molecular dynamics simulations. Physical Review B, 79(6), 064301. DOI: 10.1103/physrevb.79.064301

[13] McGaughey, A.J., & Kaviany, M. (2004). Quantitative validation of the Boltzmann transport equation phonon thermal conductivity model under the single-mode relaxation time approximation. Physical Review B, 69(9), 094303. DOI: 10.1103/physrevb.69.094303

[14] Li, W., Carrete, J., Katcho, N.A., & Mingo, N. (2014). ShengBTE: A solver of the Boltzmann transport equation for phonons. Computer Physics Communications, 185(6), 1747-1758. DOI: 10.1016/j.cpc.2014.02.015

[15] Ashcroft, N.W., & Mermin, N.D. (1976). Solid state physics. Saunders College Publishing. ISBN-10: 0030839939, ISBN-13: 978-0030839931

[16] Callaway, J. (1961). Low-temperature lattice thermal conductivity. Physical Review, 122(3), 787-790. DOI: 10.1103/physrev.122.787

[17] Callaway, J., & von Baeyer, H.C. (1960). Effect of point imperfections on lattice thermal conductivity. Physical Review, 120(4), 1149-1154. DOI: 10.1103/physrev.120.1149

[18] Callaway, J. (1959). Model for lattice thermal conductivity at low temperatures. Physical Review, 113(4), 1046-1051. DOI: 10.1103/physrev.113.1046

[19] Geballe, T.H., & Hull, G.W. (1958). Isotopic and other types of thermal resistance in Germanium. Physical Review, 110, 773-775. DOI: 10.1103/physrev.110.773

Elements of Calculus Quaternionic Matrices And Some Applications In Vector Algebra And Kinematics

Pivnyak G.G.[1], Kravets V.V. [2, a], Bas K. M. [2], Kravets T.V. [3], Tokar L.A.[4]

1 – Rector of National Mining University, Academician of National Academy of Sciences of Ukraine, professor, Ukraine

2 – Department of Automobiles and Automobile Sector, National Mining University, Dnepropetrovsk, Ukraine

3 – Department of Theoretical Mechanics, National University of Railway Transport Named After Academician V. Lazaryan, Dnepropetrovsk, Ukraine

4 – Foreign Languages Department, National Mining University, Dnepropetrovsk, Ukraine

a – prof.w.kravets@gmail.com

DOI **10.13140/RG.2.1.1165.0329**

Keywords: quaternionic matrices, monomial matrices, quaternion group, four-dimensional orthonormal basis, complex vector and scalar products, first curvature, second curvature, spiral-screw trajectory.

ABSTRACT. Quaternionic matrices are proposed to develop mathematical models and perform computational experiments. New formulae for complex vector and scalar products matrix notation, formulae of first curvature, second curvature and orientation of true trihedron tracing are demonstrated in this paper. Application of quaternionic matrices for a problem of airspace transport system trajectory selection is shown.

Introduction. As [2, 5] explain, mechanics belongs to engineering sciences according to a character of investigated physical phenomena, and to mathematical ones according to analytical approaches applied. Vector calculation is a dominating mathematical tool in mechanics of rigid bodies. Methods and approaches of computational mechanics are used to solve a wide range of engineering and technical problems, in particular those concerning space-flight including navigation, orientation, stabilization, stability, controllability [3, 11] as well as in dynamics of launcher, aircraft, ship, ground transport etc. [7, 17-21]. Computer technology application involves specific reference system introduction and the necessity to reduce vector notation of solution algorithm to coordinate, matrix form [14, 15]. Matrix calculations in computational experiment provide a number of known advantages. The use of specific mathematical tool in the form of quaternionic matrices calculation is quite sufficient to solve a wide range of problems concerning dynamic design of space, rocket, and aviation equipment, ground transport, robot technology, gyroscopy, vibration protection etc. in analytical dynamics. R. Bellman [1], A.I. Maltsev [10] described some types of quaternionic matrices. Quaternionic matrices were used to control orientation [4, 9], in the theory of rigid body finite rotation [13], in the theory of inertial navigation [11], and in kinematics and dynamics of a rigid body [8, 16-18].

Hence, mathematical tool of quaternionic matrices can be applied not only in analytical dynamics in terms of mathematical models development complementing and replacing vector calculation; it also turns to be well-adapted to modern computer technologies to carry out computational experiments concerning dynamics of mechanical systems in spatial motion. Moreover, mathematical models and their adequate algorithms gain group symmetry, invariant form, matrix compactability, and versatility; that helps accelerate programming, simplify verification of mathematical model and computational process improving the efficiency of intellectual work [2]. The paper makes systematic substantiation of basic matrices selection being initial and fundamental computation element for quaternionic matrices.

1. Problem definition. Develop a group of monomial (1, 0, -1) quadric matrices on a set of elements of four-dimensional orthonormal basis and opposite elements. Find out non-Abelian subgroups isomorphic to quaternion group forming a basis for quaternionic matrices. Place isomorphic matrices to quaternion and conjugate quaternion.

2. A group of monomial (1, 0, -1)-matrices. A system of four normalized and mutually orthogonal vectors is considered:

$$\|1 \quad 0 \quad 0 \quad 0\|, \quad \|0 \quad 1 \quad 0 \quad 0\|, \quad \|0 \quad 0 \quad 1 \quad 0\|, \quad \|0 \quad 0 \quad 0 \quad 1\|,$$

to which finite set of elements $e_1 \quad e_2 \quad e_3 \quad e_4$ (or 1, 2, 3, 4) and opposite elements $e_1^* \quad e_2^* \quad e_3^* \quad e_4^*$ (or 1^*, 2^*, 3^*, 4^*) are correlated. Opposite vectors of orthonormal four-dimensional basis match opposite elements of the set:

$$\|-1 \quad 0 \quad 0 \quad 0\|, \quad \|0 \quad -1 \quad 0 \quad 0\|, \quad \|0 \quad 0 \quad -1 \quad 0\|, \quad \|0 \quad 0 \quad 0 \quad -1\|.$$

Note that specific relativity theory, theory of finite rotation, and projective geometry use four-dimensional space.

Set of biquadrate even substitution shown as the total of two transpositions and identity permutations is formed with the help of introduced set of elements [6]. Expansion of the required substitution is:

$$A_0 = \begin{pmatrix} 1 & 2 & 3 & 4 \\ 1 & 2 & 3 & 4 \end{pmatrix}, A_1 = \begin{pmatrix} 1 & 2 & 3 & 4 \\ 2 & 1 & 4 & 3 \end{pmatrix}, A_2 = \begin{pmatrix} 1 & 2 & 3 & 4 \\ 3 & 4 & 1 & 2 \end{pmatrix}, A_3 = \begin{pmatrix} 1 & 2 & 3 & 4 \\ 4 & 3 & 2 & 1 \end{pmatrix};$$

$$B_0 = \begin{pmatrix} 1 & 2 & 3 & 4 \\ 1 & 2 & 3 & 4^* \end{pmatrix}, B_1 = \begin{pmatrix} 1 & 2 & 3 & 4 \\ 2 & 1 & 4 & 3^* \end{pmatrix}, B_2 = \begin{pmatrix} 1 & 2 & 3 & 4 \\ 3 & 4 & 1 & 2^* \end{pmatrix}, B_3 = \begin{pmatrix} 1 & 2 & 3 & 4 \\ 4 & 3 & 2 & 1^* \end{pmatrix};$$

$$C_0 = \begin{pmatrix} 1 & 2 & 3 & 4 \\ 1 & 2 & 3^* & 4 \end{pmatrix}, C_1 = \begin{pmatrix} 1 & 2 & 3 & 4 \\ 2 & 1 & 4^* & 3 \end{pmatrix}, C_2 = \begin{pmatrix} 1 & 2 & 3 & 4 \\ 3 & 4 & 1^* & 2 \end{pmatrix}, C_3 = \begin{pmatrix} 1 & 2 & 3 & 4 \\ 4 & 3 & 2^* & 1 \end{pmatrix};$$

$$D_0 = \begin{pmatrix} 1 & 2 & 3 & 4 \\ 1 & 2^* & 3 & 4 \end{pmatrix}, D_1 = \begin{pmatrix} 1 & 2 & 3 & 4 \\ 2 & 1^* & 4 & 3 \end{pmatrix}, D_2 = \begin{pmatrix} 1 & 2 & 3 & 4 \\ 3 & 4^* & 1 & 2 \end{pmatrix}, D_3 = \begin{pmatrix} 1 & 2 & 3 & 4 \\ 4 & 3^* & 2 & 1 \end{pmatrix};$$

$$F_0 = \begin{pmatrix} 1 & 2 & 3 & 4 \\ 1^* & 2 & 3 & 4 \end{pmatrix}, F_1 = \begin{pmatrix} 1 & 2 & 3 & 4 \\ 2^* & 1 & 4 & 3 \end{pmatrix}, F_2 = \begin{pmatrix} 1 & 2 & 3 & 4 \\ 3^* & 4 & 1 & 2 \end{pmatrix}, F_3 = \begin{pmatrix} 1 & 2 & 3 & 4 \\ 4^* & 3 & 2 & 1 \end{pmatrix};$$

$$R_0 = \begin{pmatrix} 1 & 2 & 3 & 4 \\ 1 & 2 & 3^* & 4^* \end{pmatrix}, R_1 = \begin{pmatrix} 1 & 2 & 3 & 4 \\ 2 & 1 & 4^* & 3^* \end{pmatrix}, R_2 = \begin{pmatrix} 1 & 2 & 3 & 4 \\ 3 & 4 & 1^* & 2^* \end{pmatrix}, R_3 = \begin{pmatrix} 1 & 2 & 3 & 4 \\ 4 & 3 & 2^* & 1^* \end{pmatrix}; S_0 = \begin{pmatrix} 1 & 2 & 3 & 4 \\ 1 & 2^* & 3 & 4^* \end{pmatrix},$$

$$S_1 = \begin{pmatrix} 1 & 2 & 3 & 4 \\ 2 & 1^* & 4 & 3^* \end{pmatrix}, S_2 = \begin{pmatrix} 1 & 2 & 3 & 4 \\ 3 & 4^* & 1 & 2^* \end{pmatrix}, S_3 = \begin{pmatrix} 1 & 2 & 3 & 4 \\ 4 & 3^* & 2 & 1^* \end{pmatrix}; T_0 = \begin{pmatrix} 1 & 2 & 3 & 4 \\ 1^* & 2 & 3 & 4^* \end{pmatrix}, T_1 = \begin{pmatrix} 1 & 2 & 3 & 4 \\ 2^* & 1 & 4 & 3^* \end{pmatrix},$$

$$T_2 = \begin{pmatrix} 1 & 2 & 3 & 4 \\ 3^* & 4 & 1 & 2^* \end{pmatrix}, T_3 = \begin{pmatrix} 1 & 2 & 3 & 4 \\ 4^* & 3 & 2 & 1^* \end{pmatrix};$$

as well as opposite substitutions:

$$\begin{array}{cccc} \overline{A_0}, & \overline{A_1}, & \overline{A_2}, & \overline{A_3}; \\ \overline{B_0}, & \overline{B_1}, & \overline{B_2}, & \overline{B_3}; \\ \dots & \dots & \dots & \dots \\ \overline{T_0} & \overline{T_1} & \overline{T_2} & \overline{T_3}. \end{array}$$

Each of them is quadratic monomial (1, 0, -1)-matrix.

Considered biquadratic substitutions and their corresponding (1, 0, -1) –monomial matrices form multiplicative group of 64-power and subgroups of 32-, 16-, 8-, 4-, and 2-powers represented by Cayley tables.

Non-Abelian subgroups, isomorphic to a group of quaternions. Two subgroups of 4-power, seven subgroups of 8-power, twenty-four subgroups of 16-power, and one subgroup of 32-power are separated using the analysis of multiplication table of 64-power group. Initial group order is multiple by the order of any of composed subgroups to match Lagrange theorem [6]. Two-power subgroups are not considered due to their triviality. Four-power subgroups are Abelian. Note that five subgroups of 8-power are Abelian ones and two of them are non-Abelian (marked in Table 1).

Table 1. Subgroups of 8-power monomial matrices

No.	Subgroup element
1	$A_0\ A_1\ A_2\ A_3\ \bar{A}_0\ \bar{A}_1\ \bar{A}_2\ \bar{A}_3$
2*	$A_0\ R_2\ S_3\ T_1\ \bar{A}_0\ \bar{R}_2\ \bar{S}_3\ \bar{T}_1$
3*	$A_0\ S_1\ T_2\ R_3\ \bar{A}_0\ \bar{S}_1\ \bar{T}_2\ \bar{R}_3$
4	$A_0\ T_1\ S_2\ R_3\ \bar{A}_0\ \bar{T}_1\ \bar{S}_2\ \bar{R}_3$
5	$A_0\ S_1\ R_2\ T_3\ \bar{A}_0\ \bar{S}_1\ \bar{R}_2\ \bar{T}_3$
6	$A_0\ R_1\ T_2\ S_3\ \bar{A}_0\ \bar{R}_1\ \bar{T}_2\ \bar{S}_3$
7	$A_0\ R_0\ S_0\ T_0\ \bar{A}_0\ \bar{R}_0\ \bar{S}_0\ \bar{T}_0$

Show that the obtained non-Abelian subgroups are isomorphic to quaternion group. Cayley tables of two non-Abelian subgroups are (Table 2).

It is known that quaternion is determined as a hypercomplex number:

$1a_0 + ia_1 + ja_2 + ka_3$, where $1a_0$ is scalar, $ia_1 + ja_2 + ka_3$ is vector part of quaternion, a_0, a_1, a_2, a_3 are real numbers, and $1, i, j, k$ are elements of basis where 1 is a real unit, i, j, k are explained as certain quaternions (hypercomplex units) or as basic vectors of three-dimensional space [3, 11]. Specific multiplication rules are adopted for elements of quaternion space basis:

$$i^2 = j^2 = k^2 = -1; ij = -ji = k; jk = -kj = i\ ;\ ki = -ik = j.$$

Set covering eight elements $1, i, j, k, -1, -i, -j, -k$ (where minus is a distinctive mark) makes a group of quaternions with the known multiplication table (Table 3) [6].

Table 2. Multiplication tables for non-Abelian subgroups

$**$	A_0	T_1	R_2	S_3	$\bar{A}_0$	$\bar{T}_1$	$\bar{R}_2$	$\bar{S}_3$
A_0	A_0	T_1	R_2	S_3	$\bar{A}_0$	$\bar{T}_1$	$\bar{R}_2$	$\bar{S}_3$
T_1	T_1	$\bar{A}_0$	$\bar{S}_3$	R_2	$\bar{T}_1$	A_0	S_3	$\bar{R}_2$
R_2	R_2	S_3	$\bar{A}_0$	$\bar{T}_1$	$\bar{R}_2$	$\bar{S}_3$	A_0	T_1
S_3	S_3	$\bar{R}_2$	T_1	$\bar{A}_0$	$\bar{S}_3$	R_2	$\bar{T}_1$	A_0
$\bar{A}_0$	$\bar{A}_0$	$\bar{T}_1$	$\bar{R}_2$	$\bar{S}_3$	A_0	T_1	R_2	S_3
$\bar{T}_1$	$\bar{T}_1$	A_0	S_3	$\bar{R}_2$	T_1	$\bar{A}_0$	$\bar{S}_3$	R_2
$\bar{R}_2$	$\bar{R}_2$	$\bar{S}_3$	A_0	T_1	R_2	S_3	$\bar{A}_0$	$\bar{T}_1$
$\bar{S}_3$	$\bar{S}_3$	R_2	$\bar{T}_1$	A_0	S_3	$\bar{R}_2$	T_1	$\bar{A}_0$
$*$	A_0	S_1	T_2	R_3	$\bar{A}_0$	$\bar{S}_1$	$\bar{T}_2$	$\bar{R}_3$
A_0	A_0	S_1	T_2	R_3	$\bar{A}_0$	$\bar{S}_1$	$\bar{T}_2$	$\bar{R}_3$
S_1	S_1	$\bar{A}_0$	R_3	$\bar{T}_2$	$\bar{S}_1$	A_0	$\bar{R}_3$	T_2
T_2	T_2	$\bar{R}_3$	$\bar{A}_0$	S_1	T_2	$\bar{R}_3$	$\bar{A}_0$	S_1
R_3	R_3	T_2	$\bar{S}_1$	$\bar{A}_0$	$\bar{R}_3$	$\bar{T}_2$	S_1	A_0
$\bar{A}_0$	$\bar{A}_0$	$\bar{S}_1$	$\bar{T}_2$	$\bar{R}_3$	A_0	S_1	T_2	R_3
$\bar{S}_1$	$\bar{S}_1$	A_0	$\bar{R}_3$	T_2	S_1	$\bar{A}_0$	R_3	$\bar{T}_2$
$\bar{T}_2$	$\bar{T}_2$	R_3	A_0	$\bar{S}_1$	$\bar{T}_2$	R_3	A_0	$\bar{S}_1$
$\bar{R}_3$	$\bar{R}_3$	$\bar{T}_2$	S_1	A_0	R_3	T_2	$\bar{S}_1$	$\bar{A}_0$

Table 3. Multiplication table for quaternion group

$*$	1	i	j	k	-1	$-i$	$-j$	$-k$
1	1	i	j	k	-1	$-i$	$-j$	$-k$
i	i	-1	k	$-j$	$-i$	1	$-k$	j
j	j	$-k$	-1	i	$-j$	k	1	$-i$
k	k	j	$-i$	-1	$-k$	$-j$	i	1
-1	-1	$-i$	$-j$	$-k$	1	i	j	k
$-i$	$-i$	1	$-k$	j	i	-1	k	$-j$
$-j$	$-j$	k	1	$-i$	j	$-k$	-1	i
$-k$	$-k$	$-j$	i	1	k	j	$-i$	-1

Comparison of multiplication tables for quaternion groups and determined non-Abelian subgroups of 8-power makes it possible to define their isomorphism.

4. Quaternion matrices. Process of comparing elements of quaternion space basis with monomial (1, 0, -1)-matrices of considered non-Abelian subgroups is not unique. Table 4 represents the list of definite alternatives to compare the two non-Abelian subgroups.

Table 4. Alternatives of comparing monomial matrices with elements of quaternion basis

Element of basis	Subgroup elements						
	A_0	A_0	A_0	$\cdots$	A_0	$\cdots$	A_0
1	S_1	T_2	R_3	$\cdots$	$\overline{S_1}$	$\cdots$	$\overline{R_3}$
i	T_2	R_3	S_1	$\cdots$	T_2	$\cdots$	$\overline{T_2}$
j	R_3	S_1	T_2	$\cdots$	$\overline{R_3}$	$\cdots$	$\overline{S_1}$
k	1	2	3	$\cdots$	16^*	$\cdots$	24
$No.$							
	A_0	A_0	A_0	$\cdots$	A_0	$\cdots$	A_0
1	T_1	S_3	R_2	$\cdots$	$\overline{T_1}$	$\cdots$	$\overline{S_3}$
i	S_2	R_3	T_1	$\cdots$	R_2	$\cdots$	$\overline{T_1}$
j	R_2	T_1	S_3	$\cdots$	S_3	$\cdots$	$\overline{R_2}$
k	1	2	3	$\cdots$	10^*	$\cdots$	24
$No.$							

Among other things the variety of alternatives is applied as follows: alternative No.16 - for the first non-Abelian group; alternative No.10 for the second non-Abelian subgroup i.e.

$$1 \leftrightarrow A_0, \quad i \leftrightarrow \bar{S}_1, \quad j \leftrightarrow T_2, \quad k \leftrightarrow \bar{R}_3,$$

$$1 \leftrightarrow A_0, \quad i \leftrightarrow \bar{T}_1, \quad j \leftrightarrow R_2, \quad k \leftrightarrow S_3.$$

These comparison alternatives meet the criterion of ordering, symmetry reflected in a possibility to apply operation of transposition. In this case it is expedient to use the definition of basis according to Table 5.

This definition reflects possibility of basic matrix transformation using transposition operations being introduced: complete (permutation of each row and column), external (permutation of the first row and column), and internal (permutation of kernel elements, i.e. excluding the first row and column).

Table 5. Basic matrices, isomorphic to quaternion elements

Quaternion elements	Basic matrices	Definitions
l	$A_0 = \begin{Vmatrix} 1 & 0 & 0 & 0 \\ 0 & 1 & 0 & 0 \\ 0 & 0 & 1 & 0 \\ 0 & 0 & 0 & 1 \end{Vmatrix}$	$A_0 = E_0$
i	$\bar{T}_1 = \begin{Vmatrix} 0 & 1 & 0 & 0 \\ -1 & 0 & 0 & 0 \\ 0 & 0 & 0 & -1 \\ 0 & 0 & 1 & 0 \end{Vmatrix}$ $\bar{S}_1 = \begin{Vmatrix} 0 & -1 & 0 & 0 \\ 1 & 0 & 0 & 0 \\ 0 & 0 & 0 & -1 \\ 0 & 0 & 1 & 0 \end{Vmatrix}$	$\bar{T}_1 = E_1,\ \bar{S}_1 = {}^tE_1$
j	$R_2 = \begin{Vmatrix} 0 & 0 & 1 & 0 \\ 0 & 0 & 0 & 1 \\ -1 & 0 & 0 & 0 \\ 0 & -1 & 0 & 0 \end{Vmatrix}$ $T_2 = \begin{Vmatrix} 0 & 0 & -1 & 0 \\ 0 & 0 & 0 & 1 \\ 1 & 0 & 0 & 0 \\ 0 & -1 & 0 & 0 \end{Vmatrix}$	$R_2 = E_2,\ T_2 = {}^tE_2$
k	$S_3 = \begin{Vmatrix} 0 & 0 & 0 & 1 \\ 0 & 0 & -1 & 0 \\ 0 & 1 & 0 & 0 \\ -1 & 0 & 0 & 0 \end{Vmatrix}$ $\bar{R}_3 = \begin{Vmatrix} 0 & 0 & 0 & -1 \\ 0 & 0 & -1 & 0 \\ 0 & 1 & 0 & 0 \\ 1 & 0 & 0 & 0 \end{Vmatrix}$	$S_3 = E_3,\ \bar{R}_3 = {}^tE_3$
-1	$\bar{A}_0 = \begin{Vmatrix} -1 & 0 & 0 & 0 \\ 0 & -1 & 0 & 0 \\ 0 & 0 & -1 & 0 \\ 0 & 0 & 0 & -1 \end{Vmatrix}$	$\bar{A}_0 = I$
-i	$T_1 = \begin{Vmatrix} 0 & -1 & 0 & 0 \\ 1 & 0 & 0 & 0 \\ 0 & 0 & 0 & 1 \\ 0 & 0 & -1 & 0 \end{Vmatrix}$ $S_1 = \begin{Vmatrix} 0 & 1 & 0 & 0 \\ -1 & 0 & 0 & 0 \\ 0 & 0 & 0 & 1 \\ 0 & 0 & -1 & 0 \end{Vmatrix}$	$T_1 = {}^tE_1^t,\ S_1 = E_1^t$
-j	$\bar{R}_2 = \begin{Vmatrix} 0 & 0 & -1 & 0 \\ 0 & 0 & 0 & -1 \\ 1 & 0 & 0 & 0 \\ 0 & 1 & 0 & 0 \end{Vmatrix}$ $\bar{T}_2 = \begin{Vmatrix} 0 & 0 & 1 & 0 \\ 0 & 0 & 0 & -1 \\ -1 & 0 & 0 & 0 \\ 0 & 1 & 0 & 0 \end{Vmatrix}$	$\bar{R}_2 = {}^tE_2^t,\ \bar{T}_2 = E_2^t$
-k	$\bar{S}_3 = \begin{Vmatrix} 0 & 0 & 0 & -1 \\ 0 & 0 & 1 & 0 \\ 0 & -1 & 0 & 0 \\ 1 & 0 & 0 & 0 \end{Vmatrix}$ $R_3 = \begin{Vmatrix} 0 & 0 & 0 & 1 \\ 0 & 0 & 1 & 0 \\ 0 & -1 & 0 & 0 \\ -1 & 0 & 0 & 0 \end{Vmatrix}$	$\bar{S}_3 = {}^tE_3^t,\ R_3 = E_3^t$

Each quaternion and conjugate quaternion is correlated to two matrices of the ordered structure:

$$\begin{Vmatrix} A \\ {}^tA^t \\ {}^tA \\ A^t \end{Vmatrix} = \begin{Vmatrix} E_0 & E_1 & E_2 & E_3 \\ E_0 & {}^tE_1^t & {}^tE_2^t & {}^tE_3^t \\ E_0 & {}^tE_1 & {}^tE_2 & {}^tE_3 \\ E_0 & E_1^t & E_2^t & E_3^t \end{Vmatrix} \begin{Vmatrix} a_0 \\ a_1 \\ a_2 \\ a_3 \end{Vmatrix}$$

Respectively, expansion is as follows:

$$A=\begin{Vmatrix} a_0 & a_1 & a_2 & a_3 \\ -a_1 & a_0 & -a_3 & a_2 \\ -a_2 & a_3 & a_0 & -a_1 \\ -a_3 & -a_2 & a_1 & a_0 \end{Vmatrix}; \quad {}^{t}A=\begin{Vmatrix} a_0 & -a_1 & -a_2 & -a_3 \\ a_1 & a_0 & -a_3 & a_2 \\ a_2 & a_3 & a_0 & -a_1 \\ a_3 & -a_2 & a_1 & a_0 \end{Vmatrix};$$

$${}^{t}A^{t}=\begin{Vmatrix} a_0 & -a_1 & -a_2 & -a_3 \\ a_1 & a_0 & a_3 & -a_2 \\ a_2 & -a_3 & a_0 & a_1 \\ a_3 & a_2 & -a_1 & a_0 \end{Vmatrix}; \quad A^{t}=\begin{Vmatrix} a_0 & a_1 & a_2 & a_3 \\ -a_1 & a_0 & a_3 & -a_2 \\ -a_2 & -a_3 & a_0 & a_1 \\ -a_3 & a_2 & -a_1 & a_0 \end{Vmatrix}.$$

5. Transposition. Composed matrices are of necessary ordering as they are transformed into each other by proposed operation of complete, external, and internal transposition. Matrix ${}^{t}A$ is formed from matrix A as a result of the first row and first column permutation matrix ${}^{t}A^{t}$ is transposed relative to matrix A and matrix A^{t} is transposed relative to ${}^{t}A$, i.e. following transposition rules are applied:

$$\begin{aligned} &{}^{t}\left(A\right)^{t}={}^{t}A^{t}, && {}^{t}\left(A\right)={}^{t}A, && \left(A\right)^{t}=A^{t}, \\ &{}^{t}\left({}^{t}A^{t}\right)^{t}=A, && {}^{t}\left({}^{t}A^{t}\right)=A^{t}, && \left({}^{t}A^{t}\right)^{t}={}^{t}A, \\ &{}^{t}\left({}^{t}A\right)^{t}=A^{t}, && {}^{t}\left({}^{t}A\right)=A, && \left({}^{t}A\right)^{t}={}^{t}A^{t}, \\ &{}^{t}\left(A^{t}\right)^{t}={}^{t}A, && {}^{t}\left(A^{t}\right)={}^{t}A^{t}, && \left(A^{t}\right)^{t}=A. \end{aligned}$$

6. Approbation of quaternion matrices. In equivalent formulation the quaternion matrices represent basic operations of vector algebra in a particular case when scalar part of quaternion is equal to zero. It is quite understood that following correlations of scalar and vector product of several vectors and multiplicative compositions of quaternion matrices are true [9]:

– for two vectors $\bar{a}$, $\bar{b}$

$$\left\|\frac{\bar{a}\cdot\bar{b}}{0}\right\|\leftrightarrow\frac{1}{2}\left(A_0+A_0^{t}\right)\cdot b_0, \qquad \left\|\frac{0}{\bar{a}\times\bar{b}}\right\|\leftrightarrow\frac{1}{2}\left(A_0-A_0^{t}\right)\cdot b_0;$$

– for three vectors $\bar{a}$, $\bar{b}$, $\bar{c}$

$$\left\|\frac{\bar{a}\cdot\left(\bar{b}\times\bar{c}\right)}{0}\right\|\leftrightarrow\frac{1}{4}\left(A_0+A_0^{t}\right)\left(B_0-B_0^{t}\right)\cdot c_0, \left\|\frac{0}{\bar{a}\times\left(\bar{b}\times\bar{c}\right)}\right\|\leftrightarrow\frac{1}{4}\left(A_0-A_0^{t}\right)\left(B_0-B_0^{t}\right)\cdot c_0;$$

– for four vectors $\bar{a}$, $\bar{b}$, $\bar{c}$, $\bar{d}$

$$\left\| \begin{matrix} \bar{a}\cdot\left[\bar{b}\times\left(\bar{c}\times\bar{d}\right)\right] \\ 0 \end{matrix} \right\| \leftrightarrow \frac{1}{8}\left(A_0+A_0^t\right)\left(B_0-B_0^t\right)\left(C_0-C_0^t\right)\cdot d_0,$$

$$\left\| \begin{matrix} 0 \\ \bar{a}\times\left[\bar{b}\times\left(\bar{c}\times\bar{d}\right)\right] \end{matrix} \right\| \leftrightarrow \frac{1}{8}\left(A_0-A_0^t\right)\left(B_0-B_0^t\right)\left(C_0-C_0^t\right)\cdot d_0,$$

$$\left\| \begin{matrix} 0 \\ \left(\bar{a}\times\bar{b}\right)\times\left(\bar{c}\times\bar{d}\right) \end{matrix} \right\| \leftrightarrow \frac{1}{8}\left[\left(A_0+A_0^t\right)\left(B_0+B_0^t\right)-\left(B_0+B_0^t\right)\left(A_0+A_0^t\right)\right]\left(C_0-C_0^t\right)\cdot d_0,$$

and other correlations.

7. Kinematics. To illustrate abovementioned correlations application kinematic problem on selecting motion trajectory for reusable airspace transport system is considered [12]. Development of completely reusable airspace transport system in Ukraine involves solution of a number of specific problems; territorial limitations are one of them. Traditional flight trajectory for rocket-and-space systems in the form of sloping lines in a shooting plane turns to be unacceptable due to impossibility to ensure safety exclusion area. Use of airspace system in which AH-225 launch plane is the first stage and aircraft-spacecraft with supersonic combustion ramjet is the second stage helps implementing innovative payload ascent trajectory in the form of spiral line (Fig. 1).

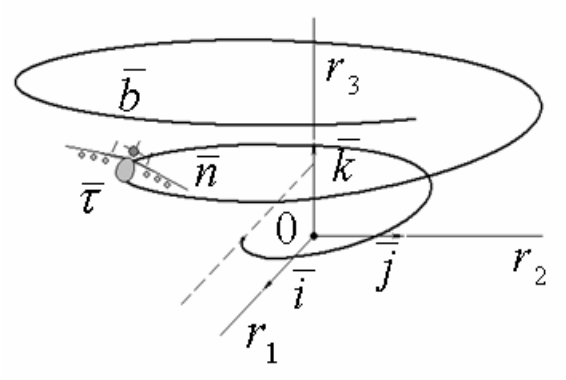


Fig. 1. Ascent trajectory in the form of spiral line

Assume that spatial trajectory is given in a fixed coordinate system of ground complex (air facilities) by a hodograph

$$\bar{r}=\bar{i}\left(\rho_0+\rho_1 t+\rho_2 t^2+\rho_3 t^3\right)\cos\omega t+\bar{j}\left(\rho_0+\rho_1 t+\rho_2 t^2+\rho_3 t^3\right)\sin\omega t+\bar{k}\left(h_0+h_1 t+h_2 t^2+h_3 t^3\right),$$

where $\omega,\rho_i,h_i\,(i=0,1,2,3)$ are variable trajectory parameters determined on given boundary conditions and apparent dependence: $\omega t_k=2\pi n$ where n is the number of spirals and t_k is staging time.

Following kinematic trajectory parameters are applied as initial data: $H(0)$, $L(0)$, $H(t_k), L(t_k)$ are altitude and distance from air facilities in horizontal plane up to the point of first stage entry into spiral trajectory $(t=0)$ and in a staging point $(t=t_k); v(0), w(0), v(t_k), w(t_k)$ are horizontal and vertical components of launch plane velocity in a point of spiral trajectory $(t=0)$ and a moment

of aircraft-spacecraft separation $(t = t_k)$. The specified initial data are used to develop two independent systems of algebraic equations relative to variable parameters of the required trajectory – both linear and non-linear. These systems admit following analytical solution

$$h_0 = H(0), \quad h_1 = w(0),$$

$$h_2 = 3\frac{H(t_k)-H(0)}{t_k^2} - \frac{w(t_k)+2w(0)}{t_k},\ h_3 = \frac{w(t_k)+w(0)}{t_k^2} - 2\frac{H(t_k)-H(0)}{t_k^3},$$

$$\rho_0 = L(0), \qquad \rho_1 = \sqrt{v^2(0)-\omega^2 L^2(0)},$$

$$\rho_2 = 3\frac{L(t_k)-L(0)}{t_k^2} - 2\frac{\sqrt{v^2(0)-\omega^2 L^2(0)}}{t_k} - \frac{\sqrt{v^2(t_k)-\omega^2 L^2(t_k)}}{t_k},$$

$$\rho_3 = \frac{\sqrt{v^2(t_k)-\omega^2 L^2(t_k)}}{t_k^2} + \frac{\sqrt{v^2(0)-\omega^2 L^2(0)}}{t_k^2} - 2\frac{L(t_k)-L(0)}{t_k^3},$$

at evident $v^2(t) \geq \omega^2 L^2(t)$ condition.

Following basic kinematic parameters are found out analytically for the obtained spiral trajectory: single vectors of tangential $\bar{\tau}$, principal normal $\bar{n}$, binormal $\bar{b}$ as well as first curvature K, second curvature χ, matrix of матрица direction cosines connecting axes of moving trihedron and fixed axes of ground complex, i.e.

$$\bar{\tau} = \frac{\dot{\bar{r}}}{V}, \qquad \bar{n} = -\frac{\dot{\bar{r}} \times (\dot{\bar{r}} \times \ddot{\bar{r}})}{V^4 K}, \quad \bar{b} = -\frac{\dot{\bar{r}} \times [\dot{\bar{r}} \times (\dot{\bar{r}} \times \ddot{\bar{r}})]}{V^5 K},$$

$$K = \frac{|\dot{\bar{r}} \times \ddot{\bar{r}}|}{V^3}, \qquad \chi = -\frac{\dot{\bar{r}} \cdot (\ddot{\bar{r}} \times \dddot{\bar{r}})}{\frac{1}{V^2}\begin{vmatrix} \dot{\bar{r}} & \ddot{\bar{r}} \\ \dot{\bar{r}} \cdot \dot{\bar{r}} & \dot{\bar{r}} \cdot \ddot{\bar{r}} \end{vmatrix} \cdot \begin{vmatrix} \dot{\bar{r}} & \ddot{\bar{r}} \\ \dot{\bar{r}} \cdot \dot{\bar{r}} & \dot{\bar{r}} \cdot \ddot{\bar{r}} \end{vmatrix}},$$

$$V^2 = \dot{\bar{r}} \cdot \dot{\bar{r}}.$$

It is convenient to calculate complex vector products used in the given formulas with the help of proposed matrix algorithms adapted for computer implementation:

$$\dot{\bar{r}} \times \ddot{\bar{r}} \leftrightarrow \frac{1}{2}(\dot{R} - \dot{R}^t)\ddot{r},$$

$$\dot{\bar{r}} \cdot \dot{\bar{r}} \leftrightarrow \frac{1}{2}(\dot{R} + \dot{R}^t)\dot{r}, \qquad \dot{\bar{r}} \times (\dot{\bar{r}} \times \ddot{\bar{r}}) \leftrightarrow \frac{1}{4}(\dot{R} - \dot{R}^t)^2 \ddot{r},$$

$$\dot{\bar{r}} \cdot (\ddot{\bar{r}} \times \dddot{\bar{r}}) \leftrightarrow \frac{1}{4}(\dot{R} + \dot{R}^t)(\ddot{R} - \ddot{R}^t)\dddot{r}, \quad \dot{\bar{r}} \times [\dot{\bar{r}} \times (\dot{\bar{r}} \times \ddot{\bar{r}})] \leftrightarrow \frac{1}{8}(\dot{R} - \dot{R}^t)^3 \ddot{r}.$$

Note also that

$$\begin{vmatrix} \dot{\bar{r}} & \ddot{\bar{r}} \\ \dot{\bar{r}}\cdot\dot{\bar{r}} & \dot{\bar{r}}\cdot\ddot{\bar{r}} \end{vmatrix}\cdot\begin{vmatrix} \dot{\bar{r}} & \ddot{\bar{r}} \\ \dot{\bar{r}}\cdot\dot{\bar{r}} & \dot{\bar{r}}\cdot\ddot{\bar{r}} \end{vmatrix}\leftrightarrow\frac{1}{16}\dddot{r}^t\left(\dot{R}-\dot{R}^t\right)^4\ddot{r}.$$

Where $\dot{R}$, $\dot{R}^t$, $\ddot{R}$, $\ddot{R}^t$ are quaternion matrices with zero scalar part.

Thus, we obtain following formulas in quaternion matrices:

$$\bar{\tau}\leftrightarrow\frac{1}{V}\dot{r},\ \bar{n}\leftrightarrow-\frac{1}{4V^4K}\left(\dot{R}-\dot{R}^t\right)^2\ddot{r},\ \bar{b}\leftrightarrow-\frac{1}{8V^5K}\left(\dot{R}-\dot{R}^t\right)^3\ddot{r},$$

$$\chi=-\frac{4V^2\left(\dot{R}+\dot{R}^t\right)\left(\ddot{R}-\ddot{R}^t\right)\dddot{r}}{\ddot{r}^t\left(\dot{R}-\dot{R}^t\right)^4\ddot{r}},\qquad K^2=\frac{\ddot{r}^t\left(\dot{R}-\dot{R}^t\right)^2\ddot{r}}{4V^6},\ V^2=-\frac{1}{4}\dot{r}^t\left(\dot{R}+\dot{R}^t\right)^2\dot{r}.$$

Dependence of moving trihedron orts and basic reference system in quaternion matrices is:

$$\left\|0\ \bar{\tau}\ \bar{n}\ \bar{b}\right\|=\frac{1}{4V^4K}\left\|0\ \bar{i}\ \bar{j}\ \bar{k}\right\|\left\|0\left|4V^3K\dot{r}\right|-\left(\dot{R}-\dot{R}^t\right)^2\ddot{r}\right|-\frac{1}{2V}\left(\dot{R}-\dot{R}^t\right)^3\ddot{r}\right\|.$$

Matrix of direction cosines can be found directly from it.

Summary. It is proposed to apply mathematical tool of quaternion matrices for analytical and computational mechanics; it is sufficient both for mathematical model development and for computational experiments. Algorithms in quaternion matrices are adapted for computer technology. Calculation of quaternion matrices is isomorphic to algebra of quaternions and vector algebra in three-dimensional space [3, 11].

Basis for introduced set of four quaternion matrices on a set of elements of four-dimensional orthonormal space and opposite element in the form of monomial (1, 0, -1)-matrices making two non-Abelian subgroups of 8-power is determined. Isomorphism of elements of quaternion space basis and developed sets of basic matrices are shown. Symmetry of quaternion matrices is reflected in three transposition operations and expedient marks. The results are the basic computational elements for quaternion matrices. Complex vector and scalar products used in mechanics are represented in the equivalent formulation by the considered quaternion matrices. Problem of determining basic kinematic parameters of spiral trajectory of reusable airspace transport system is solved analytically. Calculation algorithms are represented in the form of quaternion matrices providing convenient computer implementation.

References

[1] Bellman, R. Introduction into matrix theory. – M.: Nauka, 1976. – 352 pp.

[2] Blekhman,I.I. Mechanics and applied mathematics: Logics and peculiarities of mathemcatics application. / I.I. Blekhman, A.D. Myshkis, Y.G. Panovko. – M.: Nauka. Glavnaia red. phis.-mat. lit., 1983. – 328 pp.

[3] Branets, V.N., Shmyglevskiy, I.P. Mechanics of space flight: Application of quaternions in problems of rigid body orientation. – M.: Nauka, 1973. – 320 pp.

[4] Ikes, B.P. New method to perform numerical calculations connected with operation of orientation system control based on quaternion application // Raketnaia Tekhnika I kosmonavtika. – 1970. – 8, No.1. – pp.13−19.

[5] S.P. Timoshenko Institute of Mechanics of NAN of Ukraine (1918-2008). – 90th anniversary of the Institute (History. Structure. Information aspects) / Under general editorship of A.N. Guz. Compilors: I.S. Chernyshenko, Y.Y. Rushytskiy. – K.: Litera LTD, 2008. – 320 pp.

[6] Kargapolov, M.I., Merzliakov, Y.I. Foundations of group theory. – M.: Nauka, 1982. – 288 pp.

[7] Koshliakov V.N. Problems of rigid body dynamics and applied theory of gyroscopes. Analytical methods. – M.: Nauka, 1985. – 288 pp.

[8] Kravets, T.V. On the use of quaternion matrices to describe rotating motion of rigid body in space. // Tekhnicheskaia mekhanika. – 2001. – No.1. – pp.148-157.

[9] Kravets, V.V., Kravets, T.V., Kharchenko, A.V. Representation of multiplicative compositions of four vectors by quaternion matrices. // Vostochno-Evropeiskiy zhurnal peredovykh tekhnologiy. – 2010. −5/4(47) – pp.15-29.

[10] Maltsev, A.I. Foundations of linear algebra. – M.: Nauka, 1970. – 400 pp.

[11] Onishchenko, S.M. Hypercomplex numbers in a theory of inertial navigation. Autonomous systems. − Kyiv: Naukova dumka, 1983. − 208 pp.

[12] Panov, A.P., Gusynin, V.P., Serdiuk, I.I., Karpov, A.S. Identifying of kinematic parameters of airspace system stage motion. // Tekhnicheskaia mekhanika. – 1999 – No.1. – pp.76-83.

[13] Plotnikov, P.K., Chelnokov, Y.N. Quaternion matrices in a theory of rigid body finite rotation // Collection of scientific papers in theoretical mechanics. − M.: Vysshaia shkola , 1981.− Issue 11.− pp. 122 − 128.

[14] Strazhegva, I.V., Melkumov, V.S. Vector and matrix method in flight mechanics. − M.: Mashinostroienie, 1973. − 260 pp.

[15] Frezer, R., Dunkan, V., Kollar, A. Matrix theory and its application for differential equations in Dynamics. – M.:Publishing house “Inostrannaia literatura”, 1950. – 445 pp.

[16] Chelnokov, Y.N. Quaternion and biquaternion models and rigid body mechanics method and their application. Geometry and kinematics of motion . – M.: FIZMATLIT, 2006. – 512 pp.

[17] Kravets, V.V., Kravets, T.V. On the Nonlinear Dynamics of Elastically Interacting Asymmetric Rigid Bodies // Int. Appl. Mech. – 2006. – 42, №1. – p.110 − 114.

[18] Kravets, V.V., Kravets, T.V., Kharchenko, A.V. Using Quaternion Matrices to Describe the Kinematics and Nonlinear Dynamics of an Asymmetric Rigid Body // Int.Appl.Mech. – 2009. – 45, № 2 – p. 223− 231.

[19] Larin, V.B. On the Control Problem for a Compound Wheeled Vehicle// Int.Appl.Mech. – 2007. – 43, № 11 – p. 1269− 1275.

[20] Lobas, L.G., Verbitsky, V.G. Quantitative and Analytical Methods in Dynamics of Wheel Machines. – Kyiv: Naukova Dumka, 1990. – 232 p.

[21] Martynyuk, A.A. Qualitative Methods in Nonlinear Dynamics: Novel Approaches to Liapunov’s Matrix Functions. – New York – Basel: Marsel Dekker, 2002. – 301 p.

The Boltzmann Equation Of Phonon Thermal Transport Solved In the Relaxation Time Approximation – II – Data Analysis

Amelia Carolina Sparavigna[1]

1 – Department of Applied Science and Technology, Politecnico di Torino, Torino, Italy

DOI **10.13140/RG.2.1.2026.4724**

Keywords: Thermal Conductivity, Phonons, Boltzmann Equation.

ABSTRACT. As discussed in a previous paper [1], the thermal transport in dielectric solids can be obtained by using the Boltzmann equation of an assembly of phonons subjected to a thermal gradient. Solving this equation in the framework of the relaxation time approximation, from the phonon distribution that we obtain, the thermal conductivity of the solid can be easily given. Here we use such an approach to analyse the data of the thermal conductivities of some dielectric materials.

Introduction. In a dielectric solid subjected to a thermal gradient, the thermal transport is supported by the vibrations of crystal lattice, because other carriers such as electrons freely moving in the solid are absent. Therefore, responsible of the thermal conductivity are the phonons which are coming from the quantization of lattice vibrational modes. In this manner, phonons arise as the quasiparticles occurring because the solid is modelled as an assembly of weakly interacting particles, existing in a free volume coincident to that of the considered solid. In this volume, phonons are giving the thermal transport. The resistive processes producing a finite thermal conductivity are coming from scattering mechanisms due to point- and extended defects of the crystal lattice, from the scattering at the boundaries of the crystal and from the cubic terms of lattice Hamiltonian function, which are giving phonon-phonon scattering processes. They can differ in normal and umklapp processes [1]; in umklapp processes, momentum is transferred to the lattice as a whole, degrading the thermal current.

The thermal transport of phonons in a semiclassical approach can be determined by means of the Boltzmann equation, an equation of statistical mechanics, which is describing system not in the thermodynamics equilibrium [2-4]. For phonons, this happens when an assembly of them is subjected to a thermal gradient. The solution of the Boltzmann equation had been given by means of several approaches; among them, we have proposed a solution based on an iterative method [5-9]. A quite simple solution is that given in [1], where we have discussed the relaxation time approximation. In [1], we have also reported the Callaway's approach to the description of the scattering processes in this approximation [10-12]. In particular, Callaway investigated the role of isotopic defects as source of scattering processes that can strongly reduce the thermal conductivity of solids. Here, we consider the relaxation times to determine the thermal conductivity of some dielectric solids. In particular, we will discuss the thermal conductivity of Germanium, Silicon and Diamond.

The thermal conductivity. In a lattice, phonons move changing position and momentum and are subjected to collisions. They obey to a general equation, which is the Boltzmann equation of the distribution $n_{\mathbf{q}p}(\mathbf{r},t)$, for a phonon state with wave-number **q** and polarization *p*, about position **r** and time *t*. Let us suppose a gradient ∇T of temperature $T = T(\mathbf{r})$; the gradient is giving origin to a diffusion process of phonons.

Besides diffusion, phonons are also subjected to scattering mechanisms. Then, in the case of stationary condition, an equation is originated for the phonon distribution:

$$-\mathbf{v}_p(\mathbf{q})\cdot\nabla T\,\frac{\partial n_{\mathbf{q}p}}{\partial T}+\left.\frac{\partial n_{\mathbf{q}p}}{\partial t}\right|_{\text{scatt}}=0\,. \tag{1}$$

Eq.1 is the general form of Boltzmann equation for phonons subjected to a thermal gradient [2-4]. $\mathbf{v}_p(\mathbf{q})$ is the group velocity of the given phonon mode:

$$\mathbf{v}_{\mathbf{q}p}=\frac{\partial\omega_{\mathbf{q}p}}{\partial\mathbf{q}}\,.$$

For acoustic phonons, this velocity is simply $\mathbf{v}_{\mathbf{q}p}=c_p\,\hat{\mathbf{q}}$, where c_p is the speed of the sound for the given polarization of the wave, and $\hat{\mathbf{q}}$ is the unit vector of $\mathbf{q}$.

Eq.1 becomes an integro-differential equation when the scattering term representing the collisions of quasiparticles is explicitly given. In the first part of our discussion [1], we have detailed the scattering terms and discussed them. Here, we just remember that phonons are scattered by others phonons in the three-phonon processes (normal and umklapp), by point- and extended defects of the lattice and by the boundaries of the crystal.

In the case of a small thermal gradient, the equation is solved linearizing it, by considering just small deviations from equilibrium. The deviation is given by $n_{\mathbf{q}p}-n^o_{\mathbf{q}p}$, where $n^o_{\mathbf{q}p}$ is the equilibrium distribution. To have the Boltzmann linearized equation in the general case, let us define $\Psi_{\mathbf{q}p}$ as:

$$n_{\mathbf{q}p}=n^o_{\mathbf{q}p}-\Psi_{\mathbf{q}p}\,\frac{\partial n^o_{\mathbf{q}p}}{\partial(\hbar\omega_{\mathbf{q}p})}\,. \tag{2}$$

In (2) we have the energy of a phonon, which is $\hbar\omega_{\mathbf{q}p}$. Once function $\Psi_{\mathbf{q}p}$ is evaluated, with the iterative method [4-9] for instance, the density of the thermal current **U** can be determined.

The density current is defined as:

$$\mathbf{U}=\frac{1}{\Omega}\sum_{\mathbf{q}p}\hbar\omega_{\mathbf{q}p}\mathbf{v}_{\mathbf{q}p}n_{\mathbf{q}p}=-\frac{1}{\Omega}\sum_{\mathbf{q}p}\hbar\omega_{\mathbf{q}p}\mathbf{v}_{\mathbf{q}p}\,\frac{\partial n^o_{\mathbf{q}p}}{\partial(\hbar\omega_{\mathbf{q}p})}\Psi_{\mathbf{q}p}\,. \tag{3}$$

$\Omega = NV$ is the volume of the crystal, N the number of primitive cells of it, having volume V. In a Cartesian frame having unit vectors $\mathbf{u}_i$, current **U** is:

$$U_j=-\sum_i\kappa_{ji}\frac{\partial T}{\partial x_i}\,. \tag{4}$$

Tensor κ_{ij} is the thermal conductivity tensor, that in an isotropic crystal, is having non-null terms $\kappa_{xx} = \kappa_{yy} = \kappa_{zz} = \kappa$.

The main difficulty in evaluating (3) is the determination of the phonon distribution $n_{\mathbf{q}p}$. Let us try to use relaxation times for this task. The relaxation time approximation consists in writing the derivative of the distribution with respect to time as [2]:

$$\frac{\partial n_{\mathbf{q}p}}{\partial t} = \frac{n^o_{\mathbf{q}p} - n_{\mathbf{q}p}}{\tau(\mathbf{q}, p)}. \tag{5}$$

$n^o_{\mathbf{q}p}$ is the equilibrium distribution. In (5) we see the relaxation time for the mode (**q**, *p*). Joseph Callaway defined the difference between the distribution existing when there is a temperature gradient and that of equilibrium, which is the Bose-Einstein distribution, as [10-12]:

$$n_{\mathbf{q}p} - n^o_{\mathbf{q}p} = -\tau(\mathbf{q}, p)\ \mathbf{v}_{\mathbf{q}p} \cdot \nabla T\ \frac{\hbar\omega_{\mathbf{q}p}}{k_B T^2} \frac{e^x}{(e^x - 1)^2}. \tag{6}$$

In (6), we used the dimensionless variable $x = \hbar\omega_{\mathbf{q}p} / k_B T$. The thermal current is given by:

$$\mathbf{U} = -\frac{1}{\Omega} \sum_{\mathbf{q}p} \tau(\mathbf{q}, p)\, \mathbf{v}_{\mathbf{q}p} \cdot \nabla T\ \frac{(\hbar\omega_{\mathbf{q}p})^2}{k_B T^2} \frac{e^x}{(e^x - 1)^2} \mathbf{v}_{\mathbf{q}p}. \tag{7}$$

In the case of anisotropic solids, we have a tensor for the thermal conductivity:

$$\begin{aligned} \kappa_{\alpha\beta} &= \frac{1}{\Omega} \sum_{\boldsymbol{q}p} \tau(\boldsymbol{q}, p) \frac{(\hbar\omega_{\boldsymbol{q}p})^2}{k_B T^2} \frac{e^x}{(e^x - 1)^2} (\mathbf{v}_{\boldsymbol{q}p})_\alpha (\mathbf{v}_{\boldsymbol{q}p})_\beta \\ &= \frac{1}{\Omega} \sum_{\boldsymbol{q}p} \tau(\boldsymbol{q}, p)\ C_{ph}(\omega)\, (\mathbf{v}_{\boldsymbol{q}p})_\alpha (\mathbf{v}_{\boldsymbol{q}p})_\beta. \end{aligned} \tag{8}$$

α and β are corresponding to spatial components x, y, z. We have also used the specific heat $C_{ph}(\omega)$.

Therefore, we have, in the isotropic case:

$$\kappa = \frac{1}{\Omega} \sum_{\mathbf{q}p} \tau(\mathbf{q}, p) C_{ph}(\omega)\, \mathbf{v}^2_{\mathbf{q}p} \cos^2\theta. \tag{9}$$

In (9), θ is the angle between the group velocity and the thermal gradient. Instead of the summation on the phonon states, we can use an integration:

$$\frac{1}{\Omega}\sum_{\mathbf{q}p} \rightarrow \frac{1}{(2\pi)^2}\sum_{p}\int d\mathbf{q}\,,$$

Ω is the volume of crystal. Then:

$$\kappa = \frac{1}{(2\pi)^2}\sum_{p}\int d\mathbf{q}\;\tau(\mathbf{q},p)\;C_{ph}(\omega)\,v_{\mathbf{q}p}^2\cos^2\theta\,. \tag{10}$$

Callaway's relaxation times and thermal conductivity. First of all, let us note that in [10-12], Callaway used a Debye-like phonon spectrum and a Debye description of the density-of-states. Therefore, the thermal conductivity he derived is suitable for the low temperature region where the model is valid. Moreover, an averaged phonon velocity v_s for longitudinal and transverse branches is used. In [10-12], Callaway proposed the following relaxation times for collisions:

$$\tau_d^{-1} = A\omega^4\;;\;\tau_b^{-1} = \frac{v_s}{L}\;;\;\tau_N^{-1} = B_2T^3\omega^2\;;\;\tau_U^{-1} = B_1T^3\omega^2 = b_1T^3\omega^2\,\exp(-\Theta/aT)\,,$$

$A\omega^4$ is the scattering from impurity such as point-like defects and isotope defects. The isotope scattering takes the form proposed by Klemens [13]. The boundary scattering v_s/L contains the average speed of sound and L the characteristic length of the crystal. Callaway model assumes that the scattering at the surface boundary is purely diffusive. The three-phonon normal process is that derived by Herring [14] for longitudinal phonon scattering under momentum conservation conditions at low temperatures. The relaxation time for an umklapp process was suggested by Peierls [15]. Since, in the relaxation time approximation, an addition of the transition probabilities leads to an addition of the reciprocal relaxation times, the total relaxation time for the abovementioned scattering mechanisms is given by:

$$\tau_c^{-1} = \tau_d^{-1} + \tau_N^{-1} + \tau_U^{-1} + \tau_b^{-1} = A\omega^4 + \left(B_1 + B_2\right)T^3\omega^2 + \frac{v_s}{L}\,.$$

Let us note that the relaxation time for umklapp processes is $\tau_U \propto e^{\Theta/aT}$ [15]. As a consequence, the contribution of such umklapp processes to the thermal resistivity is decreasing when temperature decreases. From Eqs. (16), (19)-(21) of [12], Callaway deduced the following expression for the thermal conductivity:

$$\kappa = \frac{k_B}{2\pi^2 v_s}\left(\frac{k_B T}{\hbar}\right)^3 \left\{ \int_0^{\Theta/T} \frac{\tau_c x^4 e^x}{\left(e^x-1\right)^2} dx + \frac{\left[\int_0^{\Theta/T} \frac{\tau_c}{\tau_N} \frac{x^4 e^x}{\left(e^x-1\right)^2} dx\right]^2}{\int_0^{\Theta/T} \frac{1}{\tau_N}\left(1-\frac{\tau_c}{\tau_N}\right) \frac{x^4 e^x}{\left(e^x-1\right)^2} dx} \right\} \tag{11}$$

In this equation we have k_B Boltzmann constant, v_s speed of the sound, Θ Debye temperature, and x dimensionless variable $x = \hbar\omega / k_B T$. We have the two relaxation times, τ_N and τ_c, as given above.

Thermal conductivity of Germanium. Under standard conditions, Germanium is a material having the same lattice of diamond. Germanium can be produced, for its use in semiconductors, with a very high purity. Since it is an element having five naturally occurring isotopes, of which ^{74}Ge is the most common isotope, in the measurements of thermal conductivity in natural samples and in isotopically enriched samples, we can see the effect of isotope defects. As told in [12], Glen Slack was the researcher that first emphasized the role of isotope effects [16]. Therefore, let us see if expression (11) can give us a good agreement with experimental data of Germanium.

Let us use for Germanium, the following parameters: $v_s = 3.5\times10^5\, cm/s$, $L = 0.18\, cm$, $\Theta = 375\, K$, $a = 1.$, $A = 2.57\times10^{-44}\, s^3$, $B_2 = 3.\times10^{-23}\, s/K^3$ and $b_1 = 3.\times10^{-23}\, s/K^3$. The result of calculation is given in the Figure 1, where some experimental data of Geballe and Hull [17] are also given for comparison. The upper curve represents the isotopically enriched sample, that is a sample were the isotope relaxation time is not considered; the lower curve is giving the thermal conductivity of a natural sample.

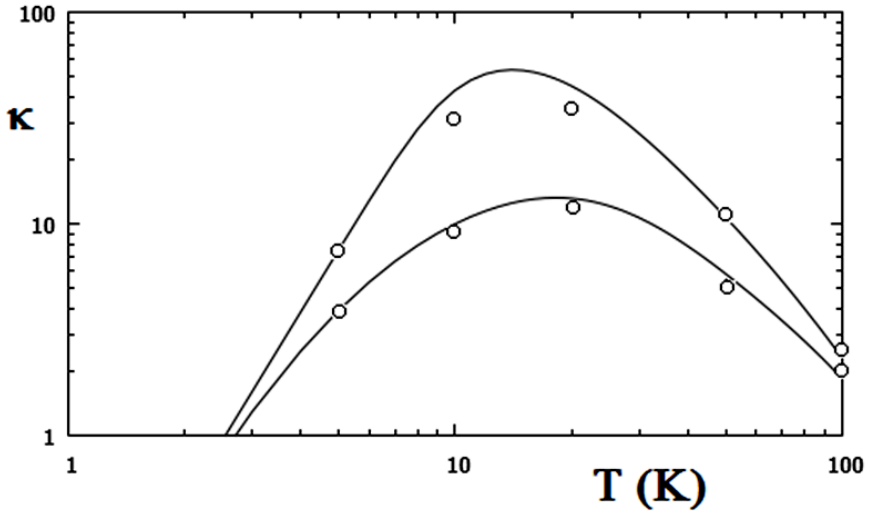


Fig. 1. Thermal conductivity ($W{\cdot}cm^{-1}{\cdot}K^{-1}$) of enriched and natural Germanium. The pure sample has the larger thermal conductivity. The dots are representing some of the experimental data of Geballe and Hull [17].

In the Figure 1, the peak of the thermal conductivity in enriched Ge is not perfectly adapted to experimental data; however, this happens also if we use a more precise microscopic model [18]. Probably, this is due to the scattering mechanism from boundaries, which is not properly modelled by the relaxation time.

In the Figure 2, it is shown the role of the isotope scattering in reducing the thermal conductivity, for different values of parameter *A*. The other parameters are the same as in the Figure 1. In the Figure 3, it is shown the role of the characteristic length *L* of the material in changing the thermal conductivity. Note that at high temperatures, length *L* is irrelevant. In the Figure 3, the isotopic scattering is neglected (*A*=0). The other parameters are the same as in the Figure 1.

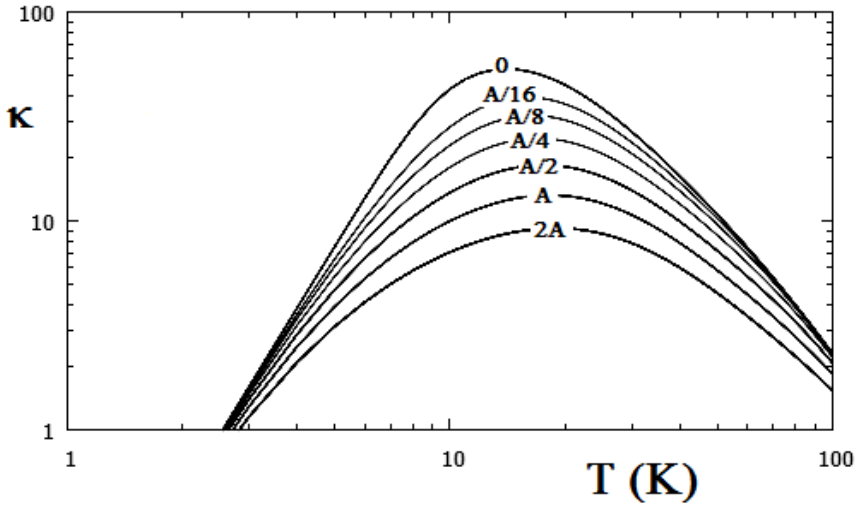


Fig. 2. Role of the isotope scattering in reducing the thermal conductivity ($W \cdot cm^{-1} \cdot K^{-1}$). The curves are giving the thermal conductivity for several values of A. The other parameters are the same as in the Fig.1.

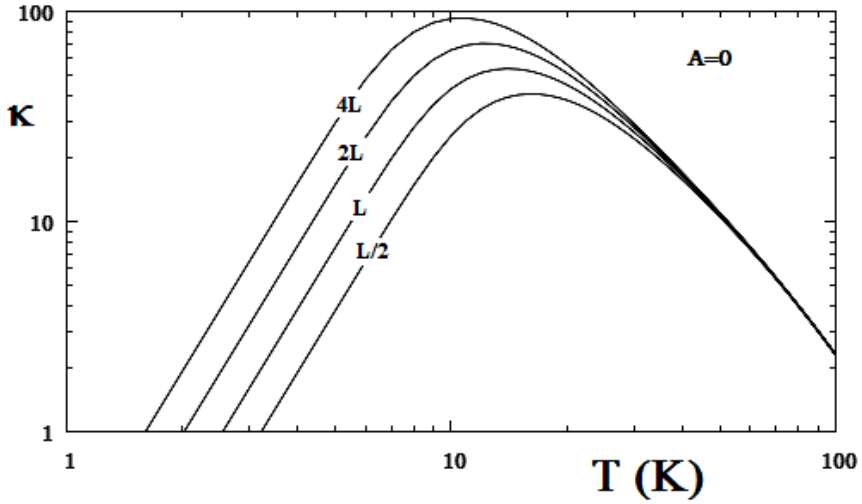


Fig. 3. Role of the characteristic length L of the material in changing the thermal conductivity ($W \cdot cm^{-1} \cdot K^{-1}$). Note that at high temperatures, length L is irrelevant. The isotopic scattering is neglected (A=0). The other parameters are the same as in Figure 1.

A short note on the values of parameters used for calculating the reciprocal of relaxation times could be interesting. Let us consider a temperature near the value of the peak of thermal conductivity. For instance, we can assume $T = 20\,K$. Parameters A and B_2 are that appearing in the reciprocal relaxation times $\tau_d^{-1} = A\omega^4$ and $\tau_N^{-1} = B_2 T^3 \omega^2$. We can estimate the phonon frequency that we have in reciprocal of relaxation times as $\omega = k_B T/\hbar$. Therefore, considering $A = 2.57\times10^{-44} s^3$ and $B_2 = 3.\times10^{-23} s/K^3$:

$$\tau_d^{-1} = A\omega^4 = A\left(\frac{k_B T}{\hbar}\right)^4 = 1.2\times10^6 s^{-1},$$

$$\tau_N^{-1} = B_2 T^3 \omega^2 = B_2 T^3 \left(\frac{k_B T}{\hbar}\right)^2 = 1.6\times10^6 s^{-1}.$$

Around the temperature of the peak, these reciprocals of relaxation times are about $10^6 s^{-1}$. The reciprocal of relaxation time of the boundary scattering is $\tau_B^{-1} = v_s / L = 2\times10^6 s^{-1}$. It has a value, which is not depending on temperature; for this reason, at temperatures above that of the peak, the boundary scattering becomes less relevant and negligible, as depicted in the Figure 3. In fact, if we consider a higher temperature, for instance $T = 100K$, and estimate the reciprocal relaxation times as did previously, we obtain:

$$\tau_d^{-1} = A\omega^4 = A\left(\frac{k_B T}{\hbar}\right)^4 = 7.5\times10^8 s^{-1},$$

$$\tau_N^{-1} = B_2 T^3 \omega^2 = B_2 T^3 \left(\frac{k_B T}{\hbar}\right)^2 = 5.1\times10^9 s^{-1}.$$

These reciprocals are quite larger than the term coming from the boundary scattering. Let us also note that the effect of three-phonon scattering is larger than that of the scattering from isotope defects. This is in agreement with an increasing role of phonon-phonon scattering at higher temperatures.

Silicon thermal conductivity. Silicon is a solid at room temperature, with relatively high melting point of 1414 °C. It has a relatively high thermal conductivity. In its crystalline form, its lattice is, like that of Germanium, a diamond cubic crystal structure. Silicon is a semiconductor where the number of free charge carriers increases with temperature.

Let us use for Silicon the following parameters: $v_s = 6.7\times10^5 cm/s$, $L = 1.cm$, $\Theta = 645K$, $a = 1.$, $A = 1.2\times10^{-44} s^3$, $B_2 = 2.\times10^{-24} s/K^3$ and $b_1 = 2.\times10^{-24} s/K^3$. The result of calculation from Eq.11 is given in the Figure 4. The upper curve represents the isotopically pure sample, the lower curve the thermal conductivity of the natural sample.

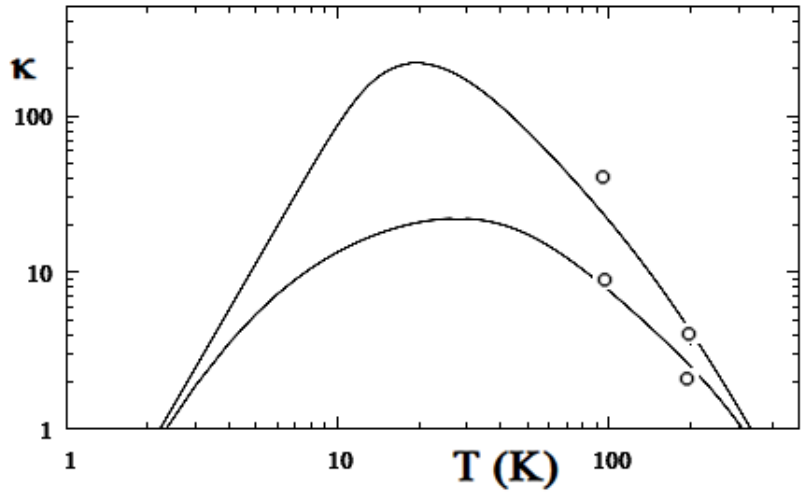


Fig. 4. Thermal conductivity ($W{\cdot}cm^{-1}{\cdot}K^{-1}$) of isotopically pure and natural Silicon. The pure sample has the larger thermal conductivity. The dots are representing some of the experimental data of Capinski, Maris and Tamura [19].

Diamond. It is a metastable allotrope of carbon, where atoms are arranged in a face-centered cubic crystal structure, which is the diamond lattice. In it, each carbon atom is surrounded by four neighboring carbon atoms, which are forming a tetrahedral shaped unit. Diamond is a material having exceptional physical characteristics. Most notable are its extreme hardness and thermal conductivity (900–2320 $W{\cdot}m^{-1}{\cdot}K^{-1}$) [20]. Above 1973 K, and in vacuum or oxygen-free atmosphere, diamond converts to graphite, whereas, in air, transformation starts at ~700 °C [21].

To apply (11), let us use for diamond the following parameters: $v_s = 18.\times 10^5\, cm/s$, $L = 0.7\, cm$, $\Theta = 2230\, K$, $a = 5.$, $A = 0.05\times 10^{-45}\, s^3$, $B_2 = 3.\times 10^{-26}\, s/K^3$ and $b_1 = 12.\times 10^{-26}\, s/K^3$. The thermal conductivity is given in the Figure 5.

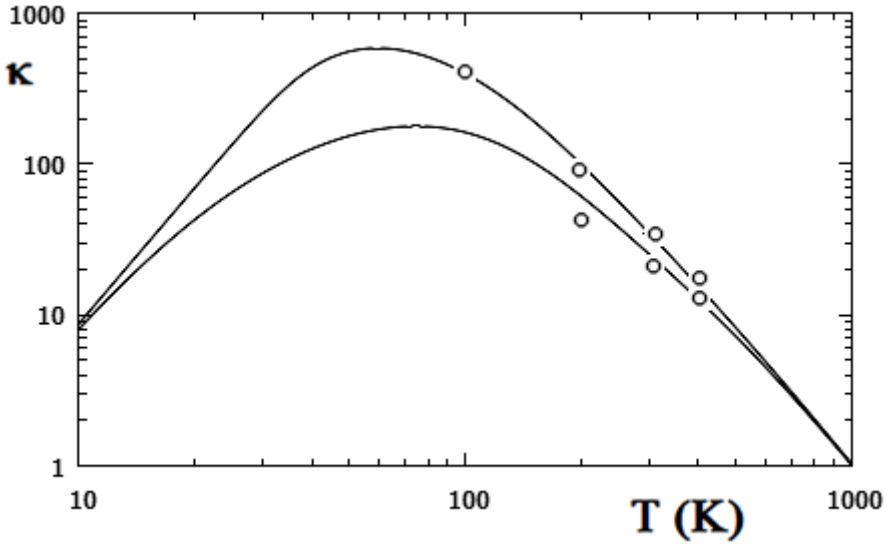


Fig. 5. Thermal conductivity ($W{\cdot}cm^{-1}{\cdot}K^{-1}$) of isotopically enriched and natural Diamond. The enriched sample has the larger thermal conductivity. Dots are representing some of the experimental data from Ref.20.

Another approach based on relaxation times. The Callaway model is not considering any distinction between longitudinal and transverse phonon. M.G. Holland in [22], proposed an analysis of lattice thermal conductivity, where longitudinal and transverse phonons have their specific relaxation times. In Holland's model, the relaxation time of the isotope scattering is the same of Callaway's model. In the boundary scattering, Holland introduced a factor to simulate a non-fully diffusive event. However, the main change in his model was in the relaxation times for normal and umklapp phonon-phonon scattering mechanisms, which were arranged to capture the high-temperature behavior of thermal conductivity. The Holland's relaxation time expressions are different for normal and umklapp processes, and are also involving distinct parameters for longitudinal and transverse acoustic phonons. In this manner, the Holland's model can describe the thermal conductivity at higher temperatures, better than the Callaway's model. Of course, in a relaxation time approximation, besides changing the expression of relaxation times it is also possible to add the contribution of other scattering mechanisms, such as the four-phonon scatterings (an expression for them was given by Klemens [23]), to improve the fitting of theoretical model to experimental data.

Let us conclude remembering that, as discussed in [1], several other approaches to the analysis of thermal conductivity in dielectric solids are possible, from variational techniques to first-principle calculations [4, 24-28].

References

[1] Sparavigna, A.C. (2016). The Boltzmann equation of phonon thermal transport solved in the relaxation time approximation – I – Theory. Mechanics, Materials Science & Engineering Journal, March 2016, 1-13. DOI 10.13140/RG.2.1.1001.1923

[2] Ziman, J.M. (1962). Electrons and phonons: The theory of transport phenomena in solids. Clarendon Press. Reprint Edition in 2001. ISBN-10: 0198507798, ISBN-13: 978-0198507796

[3] Gurevich, V.L. (1986). Transport in phonon systems. North-Holland. ISBN-10: 044487013X, ISBN-13: 978-0444870131

[4] Srivastava, G.P. (1990). The physics of phonons. Taylor and Francis. ISBN-10: 0852741537, ISBN-13: 978-0852741535

[5] Omini, M., & Sparavigna, A. (1995). An iterative approach to the phonon Boltzmann equation in the theory of thermal conductivity. Physica B, 212(2), 101-112. DOI: 10.1016/0921-4526(95)00016-3

[6] Omini, M., & Sparavigna, A. (1997). Effect of phonon scattering by isotope impurities on the thermal conductivity of dielectric solids. Physica B, 233(2-3), 230-240. DOI: 10.1016/s0921-4526(97)00296-2

[7] Omini, M., & Sparavigna, A. (1996). Beyond the isotropic-model approximation in the theory of thermal conductivity. Physical Review B, 53(14), 9064-9073. DOI: 10.1103/physrevb.53.9064

[8] Omini, M., & Sparavigna, A. (1997). Heat transport in dielectric solids with diamond structure. Nuovo Cimento D, 19(10), 1537-1564.

[9] Sparavigna, A.C. (2015). Thermal conductivity of zincblende crystals. Mechanics, Materials Science & Engineering Journal, October 2015, 1-8. DOI: 10.13140/RG.2.1.1758.0565

[10] Callaway, J. (1961). Low-temperature lattice thermal conductivity. Physical Review, 122(3), 787-790. DOI: 10.1103/physrev.122.787.

[11] Callaway, J., & von Baeyer, H.C. (1960). Effect of point imperfections on lattice thermal conductivity. Physical Review, 120(4), 1149-1154. DOI: 10.1103/physrev.120.1149

[12] Callaway, J. (1959). Model for lattice thermal conductivity at low temperatures. Physical Review, 113(4), 1046-1051. DOI: 10.1103/physrev.113.1046

[13] Klemens, P.G. (1951). The thermal conductivity of dielectric solids at low temperatures. Proceedings of the Royal Society A: Mathematical, Physical and Engineering Sciences, 208(1092), 108-133. DOI: 10.1098/rspa.1951.0147

[14] Herring, C. (1954). Role of low-energy phonons in thermal conduction. Physical Review, 95(4), 954-965. DOI: 10.1103/physrev.95.954

[15] Peierls, R.E. (1955). Quantum Theory of Solids. Oxford University Press, New York. ISBN-13: 9780198507819, DOI: 10.1093/acprof:oso/9780198507819.001.0001

[16] Slack, G.A. (1957). Effect of isotopes on low-temperature thermal conductivity. Physical Review, 105, 829.831. DOI: 10.1103/PhysRev.105.829

[17] Geballe, T.H., & Hull, G.W. (1958). Isotopic and other types of thermal resistance in Germanium. Physical Review, 110, 773-775. DOI: 10.1103/physrev.110.773

[18] Sparavigna, A. (2002). Influence of isotope scattering on the thermal conductivity of diamond. Physical Review B, 65, 064305. DOI: 10.1103/PhysRevB.65.064305

[19] Capinski, W.S., Maris, H.J., & Tamura, S. (1999). Analysis of the effect of isotope scattering on the thermal conductivity of crystalline silicon. Physical Review B, 59(15), 10105-10110. DOI: 10.1103/physrevb.59.10105

[20] Wei, L., Kuo, P.K., Thomas, R.L., Anthony, T., & Banholzer, W. (1993). Thermal conductivity of isotopically modified single crystal diamond. Physical Review Letters, 70(24), 3764-3767. DOI: 10.1103/PhysRevLett.70.3764

[21] John, P., Polwart, N., Troupe, C.E., & Wilson, J.I.B. (2002). The oxidation of (100) textured diamond. Diamond and Related Materials, 11 (3–6), 861-866. DOI: 10.1016/S0925-9635(01)00673-2

[22] Holland, M.G. (1963). Analysis of lattice thermal conductivity. Physical Review, 132(6), 2461-2471. DOI: 10.1103/physrev.132.2461

[23] Klemens, P. (1976). Thermal Conductivity, Springer. DOI: 10.1007/978-1-4899-3751-3

[24] Broido, D.A., Ward, A., & Mingo, N. (2005). Lattice thermal conductivity of silicon from empirical interatomic potentials. Physical Review B, 72(1), 014308. DOI: 10.1103/physrevb.72.014308

[25] Kaburaki, H., Li, J., Yip, S., & Kimizuka, H. (2007). Dynamical thermal conductivity of argon crystal. Journal of Applied Physics, 102(4), 043514. DOI: 10.1063/1.2772547

[26] Turney, J.E., Landry, E.S., McGaughey, A.J.H., & Amon, C.H. (2009). Predicting phonon properties and thermal conductivity from anharmonic lattice dynamics calculations and molecular dynamics simulations. Physical Review B, 79(6), 064301. DOI: 10.1103/physrevb.79.064301

[27] McGaughey, A.J., & Kaviany, M. (2004). Quantitative validation of the Boltzmann transport equation phonon thermal conductivity model under the single-mode relaxation time approximation. Physical Review B, 69(9), 094303. DOI: 10.1103/physrevb.69.094303

[28] Li, W., Carrete, J., Katcho, N.A., & Mingo, N. (2014). ShengBTE: A solver of the Boltzmann transport equation for phonons. Computer Physics Communications, 185(6), 1747-1758. DOI: 10.1016/j.cpc.2014.02.015

Automation of Analysis And Structural-Parametric Synthesis of Planetary Gearboxes With Two Degrees Of Freedom

D. Volontsevich[1, a], S. Pasechnyi[2]

1 – Doctor of technical sciences, professor, Transport Machine Building Faculty, National Technical University "Kharkov Polytechnic Institute", Kharkov, Ukraine

2 – Graduate student, Transport Machine Building Faculty, National Technical University "Kharkov Polytechnic Institute", Kharkov, Ukraine

a – vdo_khpi@ukr.net



DOI **10.13140/RG.2.1.1335.9763**

Keywords: planetary gearboxes, analysis and structural-parametric synthesis, quantitative criteria of quality.

ABSTRACT. The planetary gears in transmissions of non-rail ground transport vehicles are widely used. Mostly, all modern automatic transmissions are based on the planetary mechanisms. The design of the optimal schematic diagram and the calculations of the parameters is extremely complicated. Moreover, this process is automated particularly. The design of kinematic schemes, which based on the selected linkages is the most complicated process for automatization. The algorithm and software for analysis and structural-parametric synthesis of planetary gearboxes with two degrees of freedoms is considered. The suggested approach can be applied to elementary planetary gears and systems with two or more satellites and double-wheel gears. The software is implemented only for planetary gearboxes with two degrees of freedom. The software for the planetary gearboxes with three degrees of freedom is implemented at the nearest time. The quantitative criteria of quality for estimation of planetary gearboxes quality are developed. These criteria allow to numerically evaluating the following characteristics of planetary gearboxes as the presence and magnitude of the circulating power, the relative magnitude of the torque on brakes and clutches, the relative speed of rotation of the central units, satellites and open-loop brakes and clutches and much more. The generated kinematics schemes are compared according to selected multiple criteria or integrated criteria with weights coefficients.

Introduction. Planetary transmissions are used in the power transmission of self-propelled vehicles from the first decades of the twentieth century.

At the beginning the use of planetary gearboxes has been extremely rare. This is due to the absence at that time a well-developed theory of planetary gears and a relatively low technological level of mechanical engineering.

Later the use of planetary gearboxes is continuously increased, and by the turn of XX-XXI centuries, has become almost an absolute status.

Now planetary gears are used as part of the power transmission of the majority of samples of cars and trucks, buses, industrial and agricultural tractors, construction and road vehicles, armored vehicles and other types of self-propelled vehicles of the land for various purposes.

Planetary gears an extremely widely used not only planetary gears in transmissions, but also in other transmission units – the mechanisms of rotation of tracked vehicles, in gears for the separate or the summation of power, in transmissions power take, in a distributing boxes, in the board and wheel gear units, etc.

There is every reason to believe that in the foreseeable future, the level of use of planetary gearboxes, subject to their further improvement will only increase [1].

After the traction calculation and determining of gear ratios in the gearbox there is a problem before the designer of choice the most rational scheme of its design, that implements prescribed ratios. The choice

of the kinematic scheme of planetary gearboxes is the most difficult and important task for the designer as for given ratios can build a large variety of different schemes. These schemes will differ in complexity, efficiency size, and a number of other factors affecting the level of technical design [2].

This work is dedicated to the automation of the design process of planetary gearboxes for substantial savings of time and labor.

Analysis of recent achievements and publications. Now the designers use a method of synthesis of the planetary gearboxes, which was developed by M. Kreines. His followers [1-9] have repeatedly modified this method. For a planetary transmission with two degrees of freedom, this method is well developed and is easily automated, but it contains one point, requiring direct human intervention. This stage of testing the possibility of building a kinematic scheme of a given block diagram. The problem is that not every block diagram can be implemented as a kinematic scheme because not possible to carry out communication between the elements of planetary mechanisms and controls.

Of course, similar problems leading developers of planetary gearboxes have been resolved, but the available literature there is not comprehensive information on this issue, especially since there is no available software products that allow us to solve these problems.

The aim and problem statement. The purpose of this paper is to construct an algorithm and software for the automated synthesis of planetary gearboxes with two degrees of freedom on the set gear ratio.

To achieve this goal it is necessary:

– to carry out the generation of all possible combinations of connections between elements of the planetary transmission, that could constitute scheme;

– to determine the number and position of the controls - clutches and brakes;

– to calculate the internal gear ratio of each planetary mechanism, as well as basic kinematic and power characteristics of planetary gearboxes;

– to carry out culling of schemes at the limitations associated with the value and sign of the internal gear ratios;

– to check out the possibility of constructing kinematic schemes remaining after culling;

– to calculate numerical quality criteria;

– to sort resulting schemes in selected quality criteria.

The algorithm generating all possible combinations of connections between elements of the planetary gearboxes to create the block diagram of transmission. The initial data for the solution of the problem are the values of gear ratios for the proposed planetary transmission, which are not equal to 1. In the realized software product of their number cannot exceed four. Later, when the software product can operate with a planetary transmission with three degrees of freedom, as input data must be entered the degrees of freedom of the transmission.

We used the original algorithm for constructing all possible combinations of connections for planetary gearboxes. Those schemes that do not meet the criteria for synthesis rejected.

An algorithm for constructing all possible links combinations:

1. Determination using table 1 minimum number of planetary gears and the necessary controls.

2. Determination of the minimum number of permanent links between the elements of planetary gears at a given number of degrees of freedom is performed by using the formula:

$$N = 2n_{EPM} - W, \tag{1}$$

where N – number of permanent links between the elements of planetary gears;

n_{EPM} – the number of elementary planetary mechanisms;

W – number of degrees of freedom.

3. Enumerating all the possible options for connections between the elements of planetary gears:
– input link in turn is connected to all elements
– output link in turn is connected to all the remaining elements;
– for the selected input and output checks all combinations of permanent links.

4. For each of the resulting combinations of links determined by elements, which can be connected to the brakes;

5. Rejection of options is carried out according to the following criteria:
– not allowed a direct connection between input and output;
– braking is not permitted input and output shafts;
– not allowed constant communication between elements of the same planetary mechanism;
– not allowed connection of element which is connected to the drive shaft, with elements belonging to the previous planetary rows;
– not allowed connection of element which is connected to the driven shaft, with elements belonging to the previous planetary rows.

Table 1. The minimum number of structural elements of the planetary gearboxes [1]

number of degrees of freedom W	The main elements of the planetary gearboxes	Number of elements in the planetary gearboxes with the number of gears forward and reverse (without direct transfer)											
		1	2		3	4	5	6	7	8	9	10	11
2	locking clutch – n_{LC}	1	1		1	1	1	1	1	1	1	1	1
	stopping brake – n_{SB}	1	2		3	4	5	6	7	8	9	10	11
	elementary planetary mechanisms – n_{EPM}	1	2		3	4	5	6	7	8	9	10	11
3	locking clutch – n_{LC}	–	2	2	2	2	2	2	2	2	2	2	2
	stopping brake – n_{SB}	–	2	1	2	2	2	3	3	3	3	4	4
	elementary planetary mechanisms – n_{EPM}	–	1	2	3	3	3	4	4	4	4	5	5

The algorithm for determining the internal gear ratios of the planetary sets according predetermined gear ratios of planetary gearboxes and a full analysis of the scheme.

In any planetary transmission the speed of all central elements are interconnected via the internal gear ratios. For each planetary mechanism can be written Willis's equation:

$$\omega_a - k\omega_b + \omega_h(k-1) = 0\,, \tag{2}$$

where k – internal gear ratio of planetary mechanism, which for simple planetary mechanisms is defined as the ratio of the number of teeth on the crown gear and the sun gear.

Determination of internal gear ratios of the planetary mechanisms according to known gear ratios of planetary transmission is associated with the solution of the system of variable structure. It was therefore decided to find internal ratios for all planetary mechanisms by searching in the specified range with the selected step and provide the necessary precision. If the solution in a specified range with satisfying accuracy, has not been found, then this scheme is eliminated because of the impossibility to implement the specified gear ratios.

Further, in accordance with the found internal gear ratio determines the lowest possible number of teeth on all gears under the terms of alignment, assembly and neighborhood. After that, we spend a full kinematic and power analysis of scheme according to known methods of synthesis of planetary gears [1-6].

It includes:

– Determining the relative rotational speed of central links of the planetary transmission and satellites in all gears, provided that the rotational speed of the drive shaft $\omega_{IN} = 1$;

– Determination of the relative torques on all central links of the planetary transmission and elements of controls without losses in engagement with the proviso that $M_{IN} = 1$;

– Determination of the relative torques on all central links of the planetary transmission and elements of controls, taking into account losses in engagement with the proviso that $M_{IN} = 1$;

– determine quantitative of quality criteria [11];

– determining the integral quality assessment of the scheme [11].

The algorithm for determining the quantitative criteria of quality planetary gearboxes.

To automate parametric synthesis of planetary gearboxes is not enough to generate all possible schemes, also need to quantify qualitative criteria, and only choose the best scheme. Defining quality criteria is performed based on data obtained from kinematic and force calculations.

The proposed system of criteria for quality schemes of planetary gearboxes is not meant to completely objective and comprehensive assessment of the actual transmission as a technical product. This system allows you to perform a comparative assessment of different planetary gearboxes on the schematic level, assess the degree of perfection of the kinematic scheme. These simple and rather obvious criteria, however, possible to obtain a quantitative estimate of the most important indicators of the analyzed kinematic scheme in a form suitable for comparison of the several variants of planetary gearboxes under selecting the best out of the scheme under consideration.

To determine the quantitative criteria of quality of planetary gearboxes were taken as the basis of criteria given in [1]:

1) The criterion of the power transmitted by the elements of the planetary transmission on the forward gears.

This criterion estimates the amount of power transmitted by the element of the planetary transmission as a fraction of the input power. The value of this criterion is determined by the expression:

$$K_1 = \frac{N_{FG\max}}{N_{IN}}\,, \tag{3}$$

where $N_{FG\max}$ – maximum power transmitted most stressful element the planetary gear to the forward gears;

N_{IN} – the power supplied to the planetary transmission.

2) The criterion of the power transmitted by the elements of the planetary transmission on the reverse gears.

This criterion has the same meaning and is determined as well as the previous one, only for reverse gears:

$$K_2 = \frac{N_{RG\max}}{N_{IN}}. \quad (4)$$

3) The criterion of the loading of the locking clutch.

This criterion reflects the value of the maximum torque transmitted by included locking clutch, and allows roughly estimating the axial and radial dimensions of the clutch. The value of this criterion is determined by the expression:

$$K_3 = \frac{M_{LC\max}}{M_{IN}}, \quad (5)$$

where $M_{LC\max}$ – maximum torque transmitted included locking clutch;

M_{IN} – torque supplied to input of the planetary transmission.

According to the analysis of many real schemes of planetary gearboxes can be considered optimal criterion values in the range 0.6 ... 0.8.

4) The criterion of the loading of the stopping brake.

This criterion reflects the value of the maximum torque transmitted by included stopping brake. The value of this criterion is determined by the expression:

$$K_4 = \frac{M_{SB\max}}{|i_{PGB}|}, \quad (6)$$

where $M_{SB\max}$ – maximum torque transmitted included stopping brake;

$|i_{PGB}|$ – the absolute value of the transmission ratio of the planetary transmission on the transfer for which the specified torque $M_{SB\max}$.

It should be noted, that this criterion makes it impossible to estimate the size of the required brake that are included at different levels of transmission.

5) The criterion that determines the speed of rotation of the bearings placed in satellites.

This criterion reflects the value of the maximum speed of the "high-speed" satellite of the planetary transmission. It determines the reliability and durability of bearings satellites. The value of this criterion is determined by the expression:

$$K_5 = \frac{\left|\omega_{sat\max}\right|}{\left|\omega_{\max}\right|}, \tag{7}$$

where $\omega_{sat\max}$ – maximum relative angular velocity of the satellite in the planetary set which is loaded with non-zero torque;

$\omega_{\max}$ – the angular velocity of the high-speed main link in the planetary mechanism, which was defined the maximum relative angular velocity of the satellite and on the same transmission.

Criterion K_5 values for various planetary mechanisms may be larger or smaller than unity. The lower the value of this criterion, the higher, ceteris paribus, the reliability and durability of the planetary transmission.

6) The criterion of the relative speed of rotation of the locking clutches and disc brakes, which were switched off.

This criterion reflects the value of the maximum relative angular velocity of the master and slave disks of the "high-speed" clutch or disc brake, which were switched off. It allows you to assess the level of power loss, the amount of heating and deterioration of working drives in friction control elements, which were switched off. The value of this criterion is determined by the expression:

$$K_6 = \frac{\left|\omega_{LC(SB)\max}\right|}{\left|\omega_{IN}\right|}, \tag{8}$$

where $\omega_{LC(SB)\max}$ – the maximum relative angular velocity in the "high-speed" clutch or disc brake, which were switched off;

ω_{IN} – the angular velocity of the driving link of the planetary transmission.

7) The criterion a weighted average level of efficiency.

This criterion reflects the level of power loss in planetary transmission considering on the relative time of work on each gear. The value of this criterion is determined by the expression:

$$K_7 = \frac{1}{\sum t_i \eta_i}, \tag{9}$$

where $\sum t_i \eta_i$ – the sum of products of relative work time of the planetary gear on the *i*-th transmission and the calculated efficiency of the planetary transmission on this transmission.

8) Criterion average usage elementary planetary rows in the structure of planetary transmission.

This criterion reflects the average number of elementary planetary rows, which were considered in the analysis planetary transmission, involved in the power transmission. The value of this criterion is determined by the expression:

$$K_8 = \frac{n_G n_{EPM}}{\sum n_{LEPM}}, \tag{10}$$

where n_G – number of gears in the planetary transmission, with the exception of direct drive;

n_{EPM} – the number of elementary planetary mechanisms are considered when analyzing planetary transmission;

$\sum n_{LEPM}$ – the total number of loaded elementary planetary mechanisms on all gears in the planetary transmission, with the exception of direct drive.

The criterion K_8 assessed the degree of participation of elementary planetary mechanisms in the formation of all gears in the planetary transmission. Also, the criterion is estimated number of elementary planetary mechanisms operating at idle rotation without doing useful work in this valid and reducing the efficiency of the planetary transmission.

9) The criterion of the complexity of the device planetary transmission.

This criterion shows how much more in the planetary transmission is used control elements and the elementary planetary mechanisms than is necessary in the minimum configuration. The value of this criterion is determined by the expression:

$$K_9 = \frac{\left(n_{LC} + n_{SB} + n_{FW} + n_{EPM}\right)}{\left(n_{LC} + n_{SB} + n_{EPM}\right)_{\min}}, \tag{11}$$

where $\left(n_{LC} + n_{SB} + n_{FW} + n_{EPM}\right)$ – the number of locking clutch – n_{LC}, stopping brake – n_{SB}, freewheel – n_{FW} and elementary planetary mechanisms – n_{EPM}, that were included in the planetary transmission which are considered; $\left(n_{LC} + n_{SB} + n_{EPM}\right)_{\min}$ – number of locking clutches, brakes, and elementary planetary mechanisms, the minimum required for the synthesis of a simple planetary transmission, which is similar to the analyzed according to the number of degrees of freedom and number of gears.

10) The criterion of complexity of control system planetary transmission.

This criterion assesses the number of "on" and "off" the friction elements with an external control for consistent implementation all gears in the planetary transmission. If the scheme of planetary transmission provides controls with internal automaticity (freewheel), their switching “on” and “off” are not taken into account. This is done because they do not require external control and simplify the control system of the planetary transmission. The value of this criterion is determined by the expression:

$$K_{10} = \frac{\left(n_{LC,SB"ON"} + n_{LC,SB"OFF"}\right)}{n_G}, \tag{12}$$

where $n_{LC,SB"ON"}$ – number of locking clutches – n_{LC} and brakes – n_{SB}, are switched "on" for each of the next gear in the planetary transmission; $n_{LC,SB"OFF"}$ – number of locking clutches – n_{LC} and brakes – n_{SB}, are switched "off" for each of the next gear in the planetary transmission;

n_G – number of gears in the planetary transmission.

When analyzing the quality criteria, some of which have been improved and new proposed allowing to more fully evaluate the degree of quality of scheme planetary transmission. Thus, the criterion of the loading of the stopping brake of planetary transmission proposed to define:

$$K_4 = \frac{M_{SB\max}}{M_{IN}}, \tag{13}$$

where $M_{SB\max}$ – maximum torque transmitted included stopping brake;

M_{IN} – torque supplied to input of the planetary transmission.

The criterion that determines the speed of rotation of the bearings placed in satellites proposed to define in two modes:

$$K_{5(1)} = \frac{\left|\omega_{sat\max(1)}\right|}{\left|\omega_{IN}\right|}, \tag{14}$$

where $\omega_{sat\max(1)}$ – the maximum angular velocity of the satellite in any planetary mechanism, that loaded torque;

ω_{IN} – the angular velocity of the driving link of the planetary transmission.

$$K_{5(2)} = \frac{\left|\omega_{sat\max(2)}\right|}{\left|\omega_{IN}\right|}, \tag{15}$$

where $\omega_{sat\max(2)}$ – the maximum angular velocity of the satellite in any planetary mechanism, that not loaded torque.

We have proposed a criterion of the loading of the brakes planetary transmission, which are involved in the braking of the machine:

$$K_{11} = \frac{M_{SB\max}}{M_{OUT}}, \tag{16}$$

where $M_{SB\max}$ – the value of the maximum torque at the brake which is loaded in the braking mode of the machine;

M_{OUT} – necessary for braking machines maximum braking torque is given to the output shaft of the planetary transmission.

We have also proposed a criterion for number axial layers (axial dimension). This criterion is the ratio between the total number of vertical lines and planes engaging gears on kinematic scheme at the level of the axes of the satellites and the number of elementary planetary mechanisms composing planetary transmission.

We have also proposed a criterion for number radial layers (radial dimension). This criterion is the ratio between the total number of horizontal lines in the saturated vertical section on kinematic scheme and the number of central links in one elementary planetary mechanism.

The proposed set of quantitative performance criteria allows to find the best kinematic scheme of planetary transmission in series under consideration. Here are various approaches to this issue.

If we assume that all of the proposed criteria are equally important, the overall integrated assessment of the scheme quality obtained by summing the values of these criteria.

If we assume that the quality criteria have not equal importance, we should use weighting coefficients. In the process of selecting weighting coefficients should respect the equality of their sum to one. If necessary, the weighting coefficients for certain criteria may be set to zero.

With this approach, the comparison of schemes for planetary gearboxes should be made for a sum of products of values of the criteria on their weighting coefficients.

An algorithm for constructing the kinematic scheme from the structural scheme.

After the creation of the structural scheme you need to make commutation of elements of the gearbox. This is due to the need to test the feasibility of the kinematic scheme.

The problem of modeling route (trace) is one of the most difficult tasks in the general problem of design automation. This is due to several factors, in particular the variety of ways of design and technological implementation of different routes, for each of which apply specific optimization criteria and constraints. From a mathematical point of view the trace - the most complicated task of choosing the optimal solution from a large number of options.

To perform commutation was developed the original algorithm. To find the shortest path between the elements was used wave algorithm Lee, which can be called one the most universal routing algorithms. Wave algorithm allows you to create a path between the two key points in any maze, where it can be formed. The only drawback of the algorithm is that it needs a large amount of memory.

The essence of the algorithm Lee can be summarized as follows:

Cells of start and finish are marked on the two-dimensional plaid card (matrix) consisting of a "passable" and "impassable" cells. The goal of the algorithm is the shortest route between the start cell and the finish cell, if possible. For this the wave propagates from the start in all directions. Each cell is traversed by the wave will be marked as "traversed". A wave cannot pass through the cells that where marked as "passed" or "impassable". The wave moves until it reaches the finish point, or until there are no more cells that wave is not passed. The path from start to finish is impossible to build if the wave has passed all of the available cells but is not reached the finish cell. The path is laid and stored in the array (passed by the coordinates of cells on the plane) after the wave has reached the finish cell.

For the tasks assigned originated the need for substantial improvements of the algorithm. For example, added the ability to find the shortest path between not only two points, and also between the polylines (point – element, polyline – link). The route will be laid between a pair of points belonging to the polylines, so that the path length is a minimum. To avoid unnecessary bends route have been introduced the priorities in the direction of movement. Priorities motion are chosen so that

the route has as less as possible bends. If you change the initial priority of movement you can get a variety of routes, but their length will be the same.

For the construction of the kinematic scheme searches a sequence of connections, that to allow all connections.

The most difficult for commutation are schemes, in which the components are connected to the driving and driven shafts, owned by one planetary gear that located between the other planetary gears, and schemes, in which communications is not carried out along the shortest path. (Fig. 1).

In the event that none of the connection cannot be made by the shortest route, we must allow to carry out the first connection is not on the shortest route. (Fig. 1).

For maximum efficiency of the algorithm all elements, which are simultaneously connected to the drive shaft (for example INPUT-11-32, fig. 1), are united in chains and each of them is taken as the input element (11 and 32).

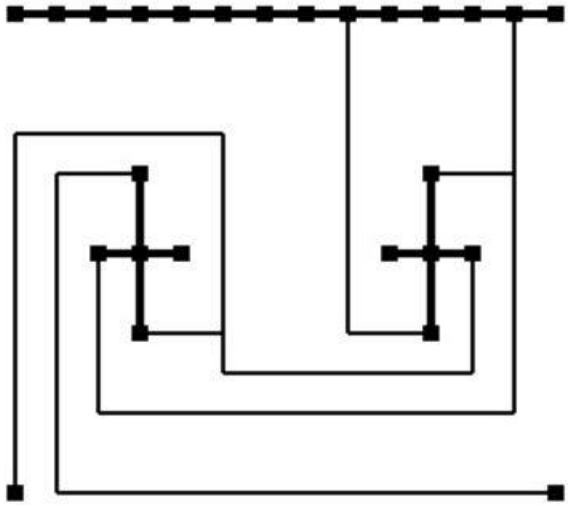


Fig. 1. Example of complicated scheme for commutation

Planetary mechanism is submitted on the kinematic scheme in the form of cross, as shown in Fig. 1, for | *k* | = [1.5 ... 8], or in the form of the letter "П" for | *k* | = [1 ... 1.5[, as shown in Fig. 2, depending on the internal gear ratio.

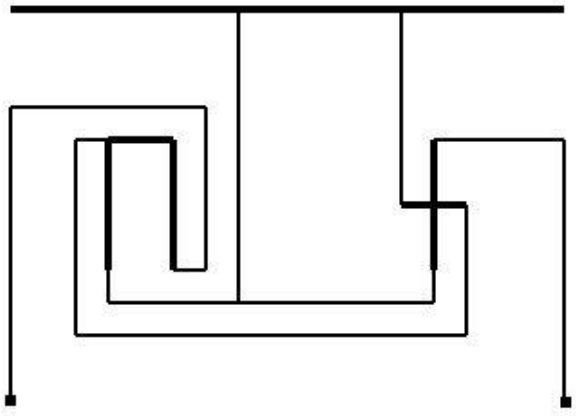


Fig. 2. Kinematic scheme with rows of different structures

Planetary rows presented in the form of a cross are elementary planetary rows or planetary rows with twin satellites (for | *k* |> 4.5). Planetary rows presented in the form of the letter "P" - planetary rows with two solar or two epicyclical gears. Planetary rows, presented in the form of the letter "П" at the time of commutation can roll over and turn around, to enhance the quality built kinematic schemes. Above and below the planetary rows left three lanes of communications, six between the gear sets, and three on each end.

To determine the order of connections you need to find a chain that contains the input element and to hold the first connection based on imposed limitations. Then all other communications are conducted in the order in which they appear in the code. If any link fails to hold, it is adjustable to a position above or to the position of number two (after the base connection with the restriction). This continues for as long as it will be carried out all connections, or two connections begin to change places with each other. In the second case, the first connection performed with other restriction and the algorithm is repeated. This continues until it is able to hold all connections, or options constraints is not end. If the connection fails, it is believed that the kinematic scheme cannot be implemented.

Description of the program and its interface.

The program's interface is shown in Fig. 3.

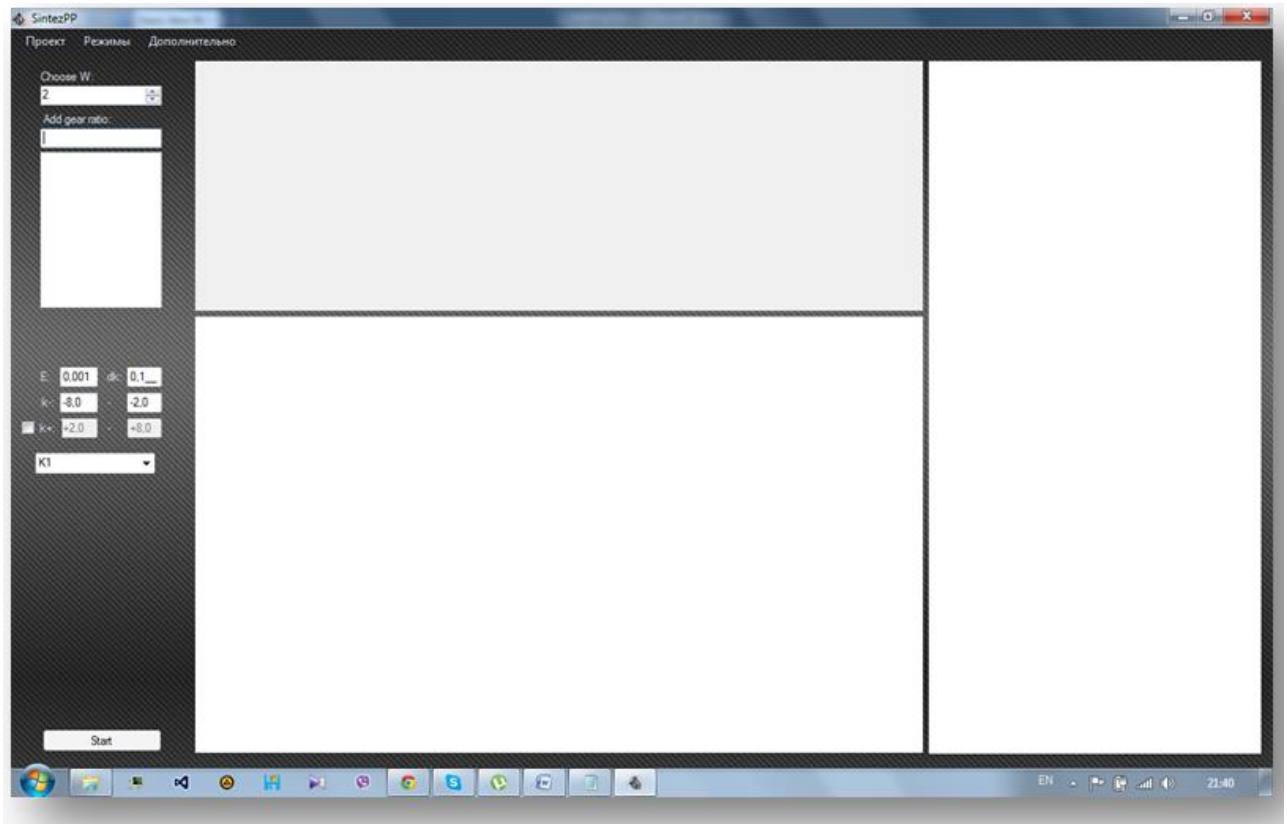


Fig. 3. Interface of program

After starting the program opens the main form. On the form, you need to choose the number of degrees of freedom of the control panel. Then you need to add the gear ratios.

If the user desires to independently specify which elements are connected to the input and output shafts, it should select "Generate with In and Out" in the program menu. If necessary, you can change the search options internal gear ratios. Then press the "Next" button and wait until you see the results of calculations (Fig. 4).

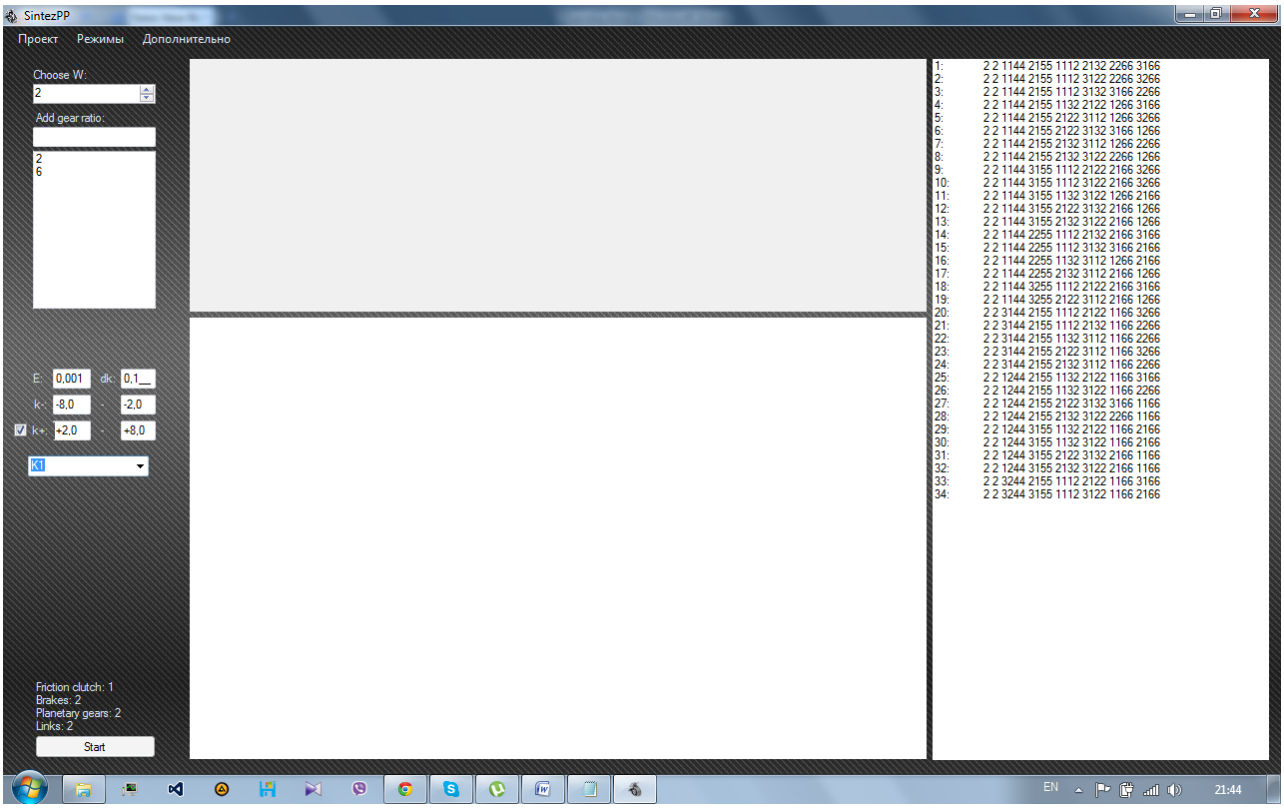


Fig. 4. Codes generated schemes

To view a particular scheme you must click on her arm. After this the screen will show it's block diagram and in the field underneath – the results of the kinematic analysis (Fig. 5). To select the best scheme, the program provides the ability to sort schemes by criteria of quality.

The results of the program can be saved to a file. To do this, you must perform a "Project -> Save" and choose a directory to save. To open the saved calculations, you must perform a "Project -> Load". It is also possible to save the results of calculations in Excel-file, it is necessary to execute "Project -> Save as XLS».

You also have the possibility of calculating the particular scheme. To use this module of the program, the operator must make himself a block diagram.

To start the mode of calculation of a particular scheme, you must select the manual mode in the menu and enter gear ratios. In the graphics area will appear icons of planetary ranks without connections. Then user must select in the graphical field the pairs of elements that it wants to attach with each other (Fig. 6). When the user has set all the necessary connections, except for the brakes, the program offers to determine the elements that are connected to the brakes automatically. This is possible because in a planetary transmission with two degrees of freedom the position of the brake is uniquely determined. Pairs of connections are written to the vector, which has the following structure:

X – the amount of basic planetary mechanisms;

X – the amount of brakes;

XX44 – element, which connected to the driving shaft;

XX55 – element, which connected to the driven shaft;

XXXX – connections;

…

XX66 – element, which connected to the brakes; and others.

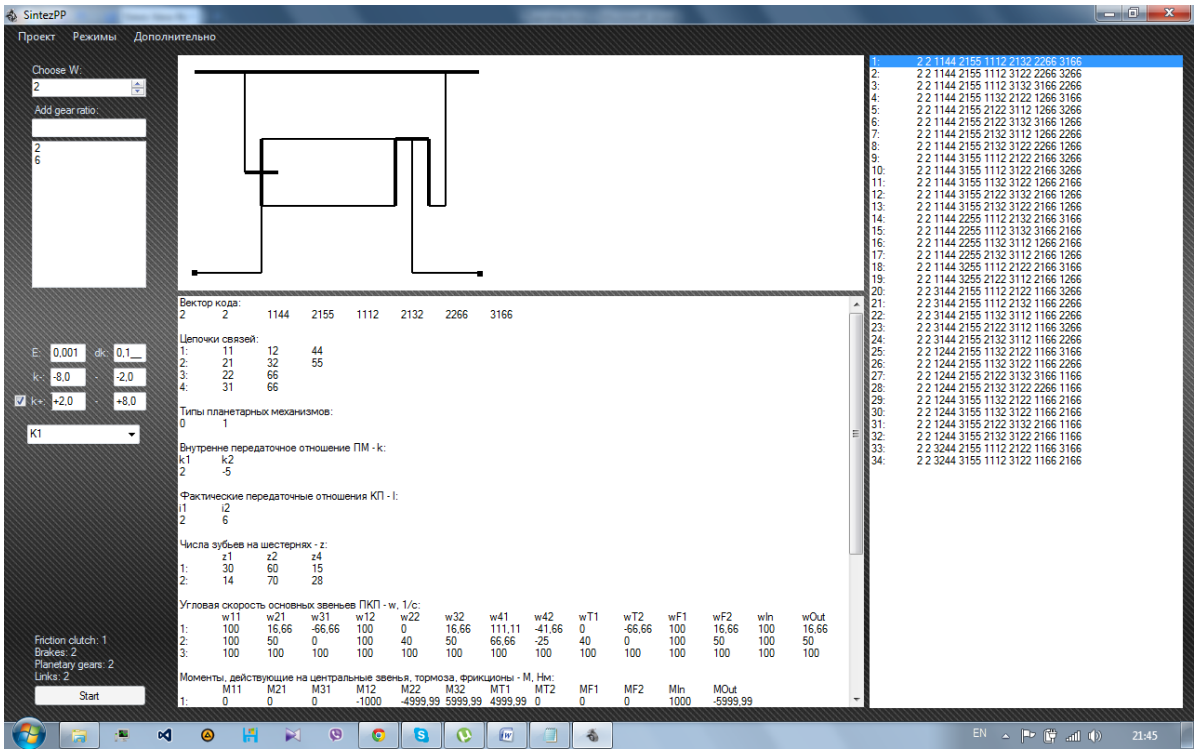


Fig. 5. View of calculation results for a particular scheme

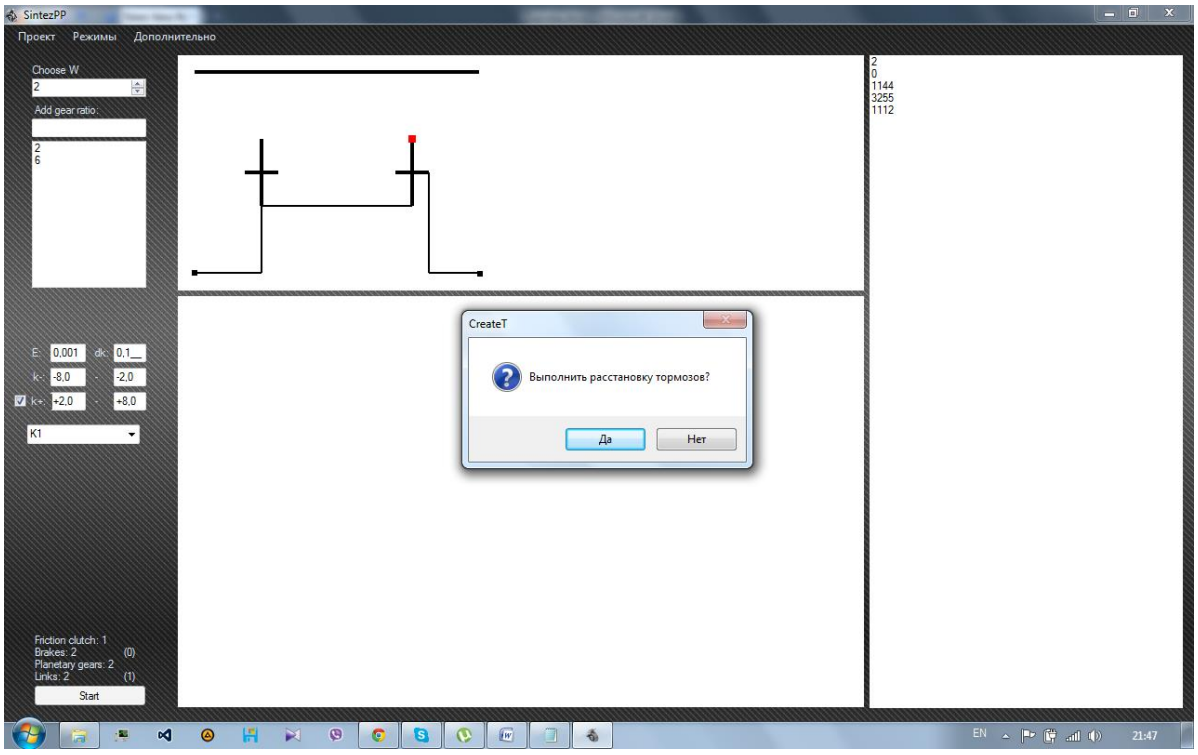


Fig. 6. Example of calculation of particular scheme

If at some stage, the calculations turned out that to implement the scheme cannot be given, the program displays an appropriate message.

Conclusion. As a result of this work proposes an algorithm and software that make possible according specify gear ratios [12] in automatic mode to obtain a kinematic scheme of a planetary transmission with two degrees of freedom, with an arbitrary structure of planetary mechanisms, which satisfies all design constraints, and has the best performance on selected quantitative quality criteria.

As a further research is planned to expand the capabilities of the algorithm and software on planetary transmission with three degrees of freedom.

References

[1] Filichkin N.V. Analiz planetarnyih korobok peredach transportnyih i tyagovyih mashin [Analysis of planetary gearboxes for wheeled and tracked machines: Textbook] / Filichkin N.V. Uchebnoe posobie. Kompyuternaya versiya, ispravlennaya i dopolnennaya. –Chelyabinsk: Izd. YuUrGU, 2008. – 178 P.

[2] Sharipov V.M. Planetarnyie korobki peredach kolesnyih i gusenichnyih mashin [Planetary transmission of wheeled and tracked vehicles] / Sharipov V.M., Krumboldt L.N., Marinkin A.P. Pod obsch. red. V.M. Sharipova. –M.: MGTU «MAMI», 2000. – 142 P.

[3] Krasnenkov V.I., Vashets A.D. Proektirovanie planetarnyih mehanizmov transportnyih mashin [Design of planetary mechanisms for vehicles.]. –M.: Mashinostroenie, 1986. –272 P.

[4] Kudryavtsev V.N. Planetarnyie peredachi: Spravochnik [Planetary Transmission: Handbook] / Kudryavtsev V.N., Kirdyashev Yu.N. –L.: Mashinostroenie, 1977. – 536 P.

[5] Shelomov V.B. Strukturnyiy sintez kinematicheskih shem planetarnyih korobok [Structural synthesis of kinematic schemes of planetary gearboxes] / V.B. Shelomov // SPb STU. –2010. –№1. T8. –P. 52-61.

[6] Melnikov O.A. Sintez kinematicheskih shem planetarnyih korobok peredach so sdvoennyimi satellitami dlya perspektivnyih gusenichnyih mashin: dis… kand. tehn. nauk [Synthesis of kinematic schemes of planetary transmission with twin satellites for perspective tracked vehicles: thesis of a Cand.Tech.Sci]: 05.05.03 / Melnikov Oleg Aleksandrovich. –Volgograd, 2004. – 192 P.

[7] Kuris E.V. Osnovyi novyih metodov kinematicheskogo rascheta korobok peredach: dis… kand. tehn. nauk [Fundamentals of new methods for calculating the kinematic transmissions: thesis of a Cand.Tech.Sci]: 05.03.01 / Kuris Eduard Valerevich. –Rostov-na-Donu, 2009. – 203 P.

[8] Salamandra K.B. Sintez shem mnogoskorostnyih kombinirovannyih korobok peredach s nepodvizhnyimi i podvizhnyimi osyami zubchatyih koles: dis… kand. tehn. nauk [Synthesis schemes multispeed transmissions combined with fixed and moving axes gears: thesis of a Cand.Tech.Sci]: 05.02.18 / Salamandra Konstantin Borisovich. –Moskva, 2009. – 172 P.

[9] Sadyikova A.Ya. Strukturnyiy sintez planetarnyih zubchatyih korobok peredach s odnoventsovyimi satellitami: dis… kand. tehn. nauk [Structural synthesis of planetary gearboxes with satellites having one ring gear: thesis of a Cand.Tech.Sci]: 05.02.18 / Sadyikova Anna Yakovlevna. –Ufa, 2006. – 167 P.

[10] Kozadaev A.S. Realizatsiya volnovogo algoritma dlya opredeleniya kratchayshego marshruta na ploskosti pri modelirovanii trass s prepyatstviyami [Implementation of the wave algorithm for determine the shortest route on the plane for the simulation the runs with obstacles] / A.S. Kozadaev, E.V. Dubovitskiy // Vestnik TGU, –T.15, –Vyip. 6, 2010.

[11] Volontsevich D.O. K voprosu o kolichestvennyih kriteriyah kachestva kinematicheskih shem planetarnyih korobok peredach [On the question of quantitative quality criteria kinematic schemes of planetary gearboxes] / D.O. Volontsevich, E.O. Veretennikov, S.S. Pasichniy // Visnik NTU "HPI", Zbirnik naukovih prats. Seriya: Transportne mashinobuduvannya. – Harkiv: NTU «HPI», –2013. – №31 (1004). – P. 105-110.

[12] Volontsevich D.O. K voprosu razbivki peredatochnyih otnosheniy bortovyih planetarnyih korobok peredach gusenichnyih mashin [On the question of determining the gear ratios of the planetary side transmissions tracked vehicles] / D.O. Volontsevich, E.A. Veretennikov // Vostochno-Evropeyskiy zhurnal peredovyih tehnologiy. –2011. –№2/7 (50). –P. 25-27.

Intellectual Drive With Electric Engines On a Stock Car

Bazhynov O.V.[1], Veselaya M.A.[1]

1 – Kharkiv National Automobile and Highway University, Kharkov, Ukraine

DOI **10.13140/RG.2.1.3296.9369**

Keywords: electric drive, ac electronic motor, current, voltage, inverter, current controller.

ABSTRACT. The concept of installing smart electric drive, battery unit and control system of a stock car is presented. This work is devoted to AEM control law consisting of auto power plant, providing minimum current consumption for a given traction and speed mode. The practicability of AEM static model usage in the process of synthesis of optimal control of auto power plant with traction electric drives and also choice and substantiation of its basic parameters and characteristics is demonstrated.

Introduction. The complex problem of the scientific substantiation of the basic parameters and characteristics is appeared during designing the new auto power plants. To solve this problem techniques based on the conducting numerical experiments with appropriate mathematical models are used. However, comparative analysis of different design solutions is not possible without algorithms control power plant optimization as whole and individual aggregates that are the parts of it. This work is dedicated to the investigation of AEM control law consisting of auto power plant, providing minimum current consumption for given traction and speed mode.

Reference analysis. Sufficiently large number of domestic and foreign researchers' works dedicated to identifying mathematical models of traction electric drive different vehicles and synthesis of optimal control auto power plants are appeared in recent years. This shows the urgency of the problem.

In particular approaches to modeling the power plant of hybrid vehicles, including the AEM as an auxiliary electric drive, and relevant control systems are shown in the articles [1-4].

The problems of AEM mathematical modeling and optimization of the stator current vector are analyzed in the articles [4-8].

The traction electric motor model. However, the task of comparative analysis of different design solutions of auto power plants on the basis of computing experiment raises a number of features in the synthesis models both the object of control and controlling actions. The questions of technical implementation control laws are insignificant. At the same time optimal control vector current on all traction and speed modes under the given constraints and quality criteria of particular importance achieve special value. Herewith the level of complexity of the models ought to provide the ability of the power plant examination in a standard driving cycle of the vehicle.

Let us conduct the investigation of different approaches to the modeling of traction electric vehicle based on the optimal control of AEM vector stator current estimate of the magnitude and modeling errors caused by neglecting AEM dynamic properties under control stepped actions.

The object of article. To achieve this goal it is necessary to develop the block diagrams of dynamic and static models of electric traction and transmission model car. Comparative analysis of models can be made on time dependences of the main variables obtained for stepped control actions and optimal management of the stator current vector, taking into account the restrictions permissible mode of AEM field.

Let us consider the coordinate system (d,q) connected to the rotor AEM and fixed relatively to it. We assume that the axis *d* is aligned with the axis of the magnetic flux of the rotor. In this coordinate system equations for electromagnetic processes in AEM scalar form can be written as

$$\begin{cases} u_d = R_1 \cdot i_d + L_{1d} \cdot \dfrac{d\, i_d}{dt} - p_p \cdot \omega \cdot L_{1q} \cdot i_q \\ u_q = R_1 \cdot i_q + L_{1q} \cdot \dfrac{d\, i_q}{dt} + p_p \cdot \omega \cdot L_{1d} \cdot i_d + p_p \cdot \omega \cdot \psi_{mag} \\ M_{VD} = \dfrac{3}{2} \cdot p_p \cdot \left(\psi_{mag} + i_d \cdot \left(L_{1d} - L_{1q}\right)\right) \cdot i_q \end{cases} \quad (1)$$

where u_d, u_q, i_d, i_q are projections of vectors of voltage and current of the stator to the axis coordinate system which rotates, L_{1d} i L_{1q} – full inductance of stator windings in longitudinal and transverse axes, R_1 – resistance phase windings, ψ_{mag} – vector flux stator on the magnetic flux of the rotor, p_p – the number of pole pairs, ω – angular velocity of the rotor, M_{VD} – AEM electromagnetic moment.

Based on equations reduced electromagnetic control point AEM can be carried out by adjusting the longitudinal and transverse components of the stator current area subject to the limitations of acceptable modes.

The component of the stator current AEM i_d^* and i_q^* required for a given traction and speed limits are determined by the selected test quality control. If the criterion of quality acts minimum total current consumption AEM in static mode, the optimal relationship $\left[i_d^*, i_d^*\right] = f\left(\beta_M, \omega\right)$ can be obtained from the criterion:

$$\begin{cases} i_d^* = \arg \min\limits_{i_d \in [-I_{\max}, 0]} \left(I_m\left(i_d, M_{VD\,zd}\right)\right) \\ i_q^* = \sqrt{\left(\min\limits_{i_d \in [-I_{\max}, 0]} \left(I_m\left(i_d, M_{VD\,zd}\right)\right)\right)^2 - i_d^2} \end{cases} M_{VD\,zd} = \text{const}, \quad (2)$$

where $I_m = \sqrt{i_d^2 + \left(\dfrac{2 \cdot M_{VD\,zd}}{3 \cdot p_p}\right)^2 \cdot \dfrac{1}{\left(\psi_{mag} + i_d \cdot \left(L_{1d} - L_{1q}\right)\right)^2}}$ is module vector stator current (AEM total current consumption);

$M_{VD\,zd}$ – electromagnetic moment that is set needed to maintain the desired auto traction speed mode,

$\beta_M \in [-1,1]$ – electromagnetic control signal point AEM; $\beta_M = M_{VD\,zd} / M_{VD\max}$;

$M_{VD\max}$ – maximum torque of AEM.

Obviously the best according to selected criteria ratio of longitudinal and transverse components of the current can be achieved only in those areas of the region acceptable modes of AEM, where there is no mode of field weakening.

As a regulator traction electric current in [4] the controller looks like,

$$\begin{cases} u_d^* = k_{pd} \cdot \left(i_d^* - i_d\right) + k_{id} \cdot \int_0^t \left(i_d^* - i_d\right) dt - \omega \cdot p_p \cdot \hat{L}_{1q} \cdot i_q - R_{ad} \cdot i_d \\ u_q^* = k_{pq} \cdot \left(i_q^* - i_q\right) + k_{iq} \cdot \int_0^t \left(i_q^* - i_q\right) dt + \omega \cdot p_p \cdot \hat{L}_{1d} \cdot i_d - R_{aq} \cdot i_q \end{cases} \quad (3)$$

where $k_{pd} = a_c \cdot \hat{L}_{1d}$; $k_{pq} = a_c \cdot \hat{L}_{1q}$; $k_{id} = a_c \cdot \left(\hat{R}_1 + R_{ad}\right)$; $k_{iq} = a_c \cdot \left(\hat{R}_1 + R_{aq}\right)$; $R_{ad} = a_c \cdot \hat{L}_{1d} - \hat{R}_1$; $R_{aq} = a_c \cdot \hat{L}_{1q} - \hat{R}_1$; $\hat{L}_{1d}$, $\hat{L}_{1q}$, $\hat{R}_1$ are assessment values of L_{1d}, L_{1q} and R_1 therefore;

a_c – is parameter that determines the required bandwidth closed-loop control system. Usually it is $a_c \square R_1 / L_{1q}$.

The first two components of expressions for the longitudinal and transverse channels are standard PI –control. The third component of data expressions are intended to compensate for the current dynamics of connectivity between the longitudinal and transverse channels of AEM model. The last fourth components provide active damping.

Converting received on the output current regulator voltage task signal with coordinate system (d,q) that rotates in fixed (x,y) can be carried out according to the expression [5]:

$$\begin{cases} u_x^* = u_d^* \cdot \cos Q_c - u_q^* \cdot \sin Q_c \\ u_y^* = u_d^* \cdot \sin Q_c + u_q^* \cdot \cos Q_c \end{cases}, \quad (4)$$

where Q_C is the AEM angle rotor.

Inverse transformation of coordinates to components of the stator current entering the input of the regulator is performed according to terms:

$$\begin{cases} i_d = i_x \cdot \cos Q_c + i_y \cdot \sin Q_c \\ i_q = -i_x \cdot \sin Q_c + i_y \cdot \cos Q_c \end{cases} \quad (5)$$

The transformation phase 2/3 for signals of voltage setting is carried according to expression [6, p.21]:

$$\begin{cases} u_A^* = u_x^* \\ u_B^* = -\frac{1}{2}\cdot u_x^* + \frac{\sqrt{3}}{2}\cdot u_y^* \\ u_C^* = -\frac{1}{2}\cdot u_x^* - \frac{\sqrt{3}}{2}\cdot u_y^* \end{cases} \quad (6)$$

The value of phase currents obtained based on sensor signals DT_A and DT_C power can be reduced to a fixed coordinate system (x, y) using expressions:

$$\begin{cases} i_x = i_A \\ i_y = \frac{i_B - i_C}{\sqrt{3}} \cdot \end{cases} \quad (7)$$

The inertia of the three –phase inverter with LIM can be characterized by the amount of clean delay period of pulse –width modulation T_{PWM}.

To simplify the task let us consider the inverter as a linear amplifier with amplification constant $k_u = 1$ and time constant $T_u = T_{\text{PWM}}$ [6, s.123],

$$\begin{bmatrix} u_A \\ u_B \\ u_C \end{bmatrix} = \frac{k_u}{\text{p}\cdot T_u + 1} \cdot \begin{bmatrix} u_A^* \\ u_B^* \\ u_C^* \end{bmatrix} \quad (8)$$

where p is differentiation operator.

Using coordinate transformations, you can receive description of the three –phase LIM inverter with first fixed (x, y), and then connected to the rotor coordinate system that rotates: (d, q):

$$\begin{cases} (\text{p}\cdot T_u + 1)\cdot u_A = k_u \cdot u_A^* \\ (\text{p}\cdot T_u + 1)\cdot \frac{u_B - u_C}{\sqrt{3}} = k_u \cdot \frac{u_B^* - u_C^*}{\sqrt{3}} \end{cases}; \quad (9)$$

$$\begin{cases} T_u \cdot \frac{d\,u_x}{dt} + u_x = k_u \cdot u_x^* \\ T_u \cdot \frac{d\,u_y}{dt} + u_y = k_u \cdot u_y^* \end{cases}; \quad (10)$$

$$T_u \cdot \frac{d}{dt}\cdot (u_x + ju_y) + (u_x + ju_y) = k_u \cdot (u_x^* + ju_y^*); \quad (11)$$

$$T_u \cdot \frac{d}{dt} \cdot \left(\left(u_d + j u_q \right) \cdot e^{jQ_c} \right) + \left(u_d + j u_q \right) \cdot e^{jQ_c} = k_u \cdot \left(u_d^* + j u_q^* \right) \cdot e^{jQ_c}; \quad (12)$$

$$T_u \cdot \frac{d\, u_d}{dt} + j T_u \cdot u_d \cdot \omega_e + j T_u \cdot \frac{d\, u_q}{dt} - T_u \cdot u_q \cdot \omega_e + u_d + j u_q = k_u \cdot u_d^* + j k_u \cdot u_q^*; \quad (13)$$

$$\begin{cases} u_d = \dfrac{k_u}{T_u \cdot \mathrm{p}+1} \cdot u_d^* + \dfrac{T_u \cdot p_p \cdot \omega}{T_u \cdot \mathrm{p}+1} \cdot u_q \\ u_q = \dfrac{k_u}{T_u \cdot \mathrm{p}+1} \cdot u_q^* - \dfrac{T_u \cdot p_p \cdot \omega}{T_u \cdot \mathrm{p}+1} \cdot u_d \end{cases}. \quad (14)$$

The last expression (14), which is mathematical description of the LIM inverter in coordinate system which rotates (d,q), displays as existing mutual longitudinal and transverse control channels, which are enhanced by increasing the AEM rotor speed. These mutual influences can be seen as disturbance acting on the current circuits. For their minimization it is necessary to reduce the value of the LIM period.

Automobile transmission elements that load the electric drive are characterized quite large exact moment of inertia. Process time coefficients speed control rotor AEM consisting propulsion vehicle are significantly greater than time constants of AEM, current regulator and inverter with LIM. This allows ignoring the dynamic properties of the actual electric traction in the study of different traction speed modes of auto power plant.

One of the options simplified block diagram of the traction electric drive with AEM is shown in Fig. 1.

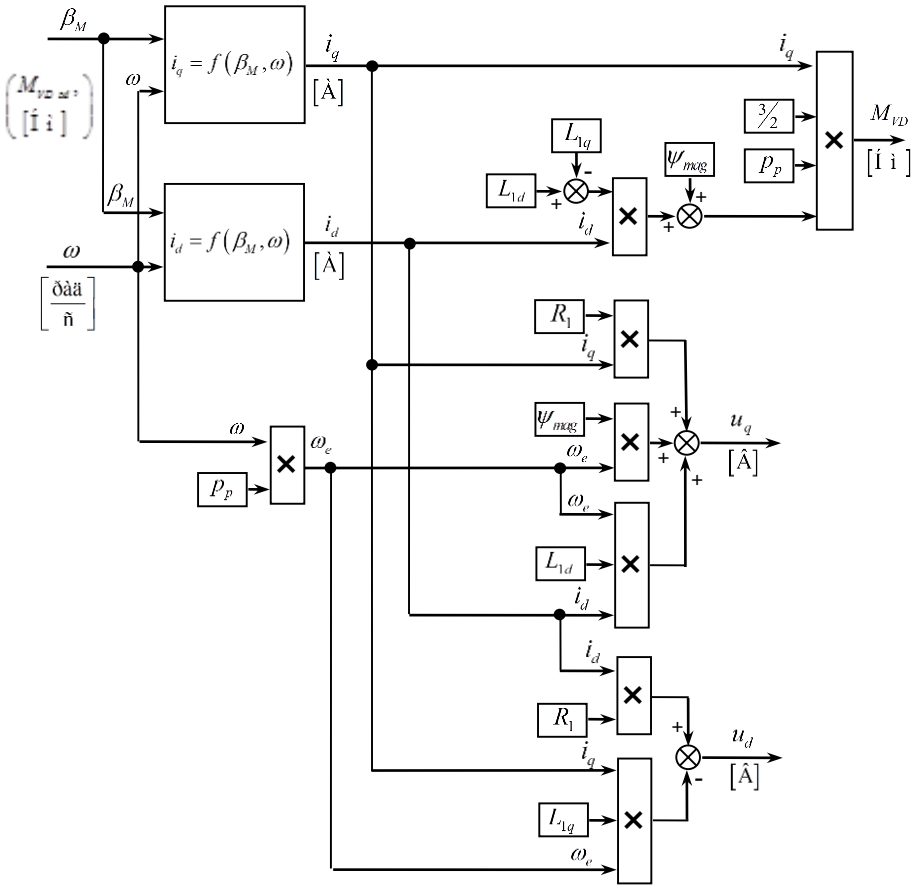
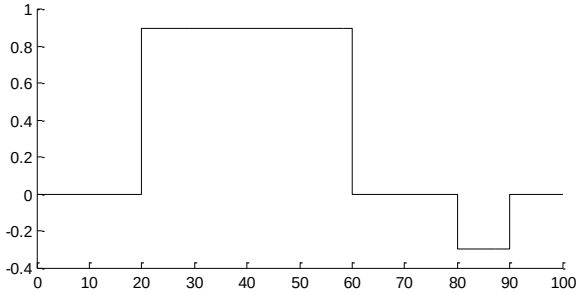


Fig. 1. The simplified block diagram of a static model traction electric drive with ac electronic motor

The shown model takes into account only the static properties of the optimal control of AEM longitudinal and transverse components of stator current.

The reaction of vehicle transmission model with traction electric drive based on AEM on stepped control effect in motion with constant gear ratio transmission without the road longitudinal slope ($\Theta = 0$) is shown on Fig. 2.



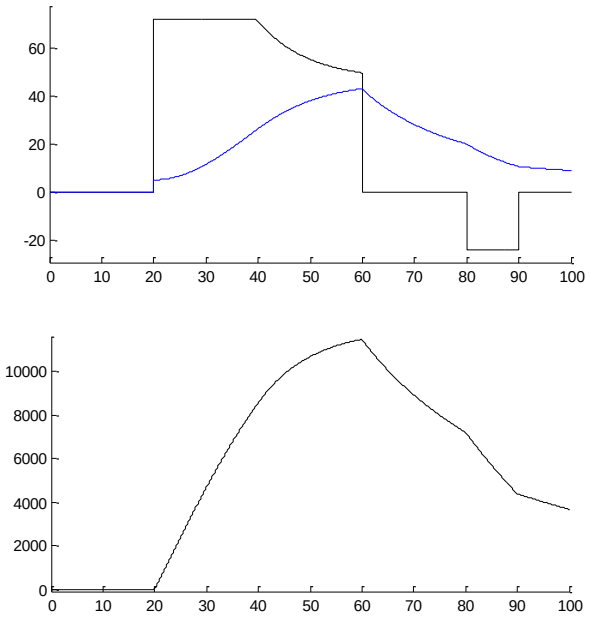


Fig. 2. Electric vehicle reaction on stepped control effect

In this case, the static electric traction model is used. AEM rotor speed is expressed in rotations per minute: $n = 30 \cdot \omega / \pi$. M_C is moment of resistance reduced to a AEM shaft.

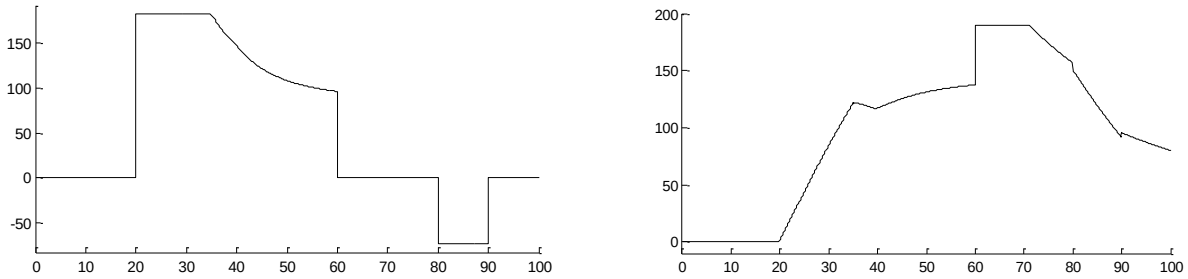
The redistribution in the areas of the region acceptable modes of AEM, where it is impossible to maintain the optimal ratio of longitudinal and transverse components of the currents is carried so that the total power consumption does not exceed $I_{\max}$, and electromagnetic torque is close to the given one.

Figure 3 illustrates the nature of the current change and AEM primary voltage at this traction and speed mode.

Power consumed by AEM can be defined as the sum of instantaneous power phase stator.

$$P_{ptr} = u_A \cdot i_A + u_B \cdot i_B + u_C \cdot i_C = \frac{3}{2}\left(u_d \cdot i_d + u_q \cdot i_q\right) \tag{15}$$

The change of power consumed from the power network AEM, while auto accelerates or of that which is given to the network as a result of the kinetic energy recovery braking is shown on Figure 4.



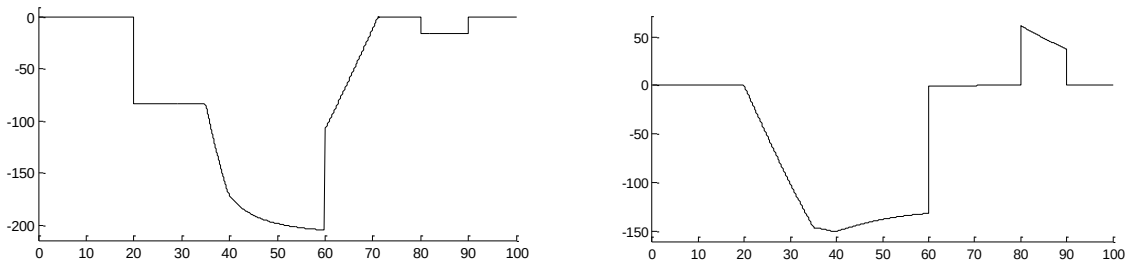


Fig. 3. Change of longitudinal and transverse components of current and voltage brushless electric vehicle traction under stepped control actions.

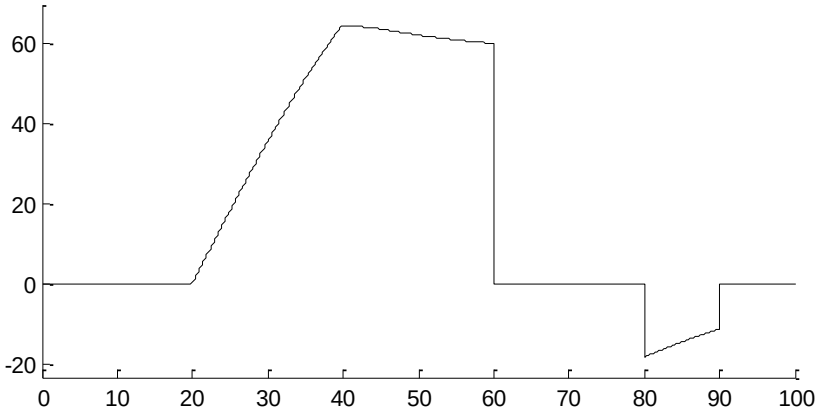


Fig. 4. Power consumed or given in traction electric onboard network of the auto.

The comparative analysis of auto transmission model with the electric traction powertrain when using static and dynamic models of AEM at the stepped control effects and optimal control of current vector shows that mean square error of current components of current and voltage, electromagnetic torque and rotor speed of AEM are: $\sigma_{Iq} = 0,90478$ A; $\sigma_{Id} = 0,57824$ A; $\sigma_{Uq} = 0,35869$ B; $\sigma_{Ud} = 0,56286$ B; $\sigma_{Mvd} = 0,37262$ Í ì ; $\sigma_n = 1,6344$ ì èí $^{-1}$ accordingly.

Summary. Thus, the extent of errors of basic variables of modeling caused by neglect of AEM dynamic properties, are quite small compared with the range of changes in the relevant variables. It confirms the use of AEM static model in the synthesis of optimal control of power plant electric auto traction and also the choice and grounding of its basic characteristics and parameters.

References

[1] Smirnov, P.P., Kalmikov, V.I. (2007), "*Obosnovanie ispolzovaniya ventilnih elektricheskih mashin v hibridnih silovih ustanovkah avtomobiley"* [Usage substantiation of ac electronic motors in auto hybrid power plant]. Automobile transport, № 21, pp. 31 –33.

[2] Smirnov, O.P. (2007), "*Sinergetichniy pidhid do stvorennya silovoi ustanovki avtomobilya"* [Synergetic approach to design auto power plant]. Vestnik KhNADU, № 37, pp. 131 –133.

[3] Smirnov, O.P., Smirnova A.O., (2007), "Shemnie resheniya i osobenosti postroenia avtomobiley s hibridnoy silovoy ustanovkoy" [Circuit solutions and design features of autos with hybrid power plant]. Transport, Environment – Sustainable Development: XIII International Scientific Conference, 10 –12 May 2007. Varna, Bulgaria, pp. 613 –619.

[4] Borodenko, Y.M., Serikov, O.P., Smirnov O.P., (2008), "Systema keruvanya hibridnoy silovoy ustanovkoy z pnevmodvigunom" [The control system of the hybrid power plant with pneumatic engine]. NEWS Automobile and Road Institute "DonNTU", №1(6), pp. 32 –38.

[5] Smirnov, O.P., (2008), "Perspektivi razvitiya system elektropitaniya transportnih sredstv" [Prospects for the development of power supply systems of vehicles]. Transport, Environment – Sustainable Development: XIV International Scientific Conference, 8 –10 May 2008. Varna, Bulgaria, pp. 295 –301.

[6] Smirnov, D.O., Saraev, A.V., (2008), "Shemni rishenya zastosuvanya ventilnih mashin u elektroprivodi" [Circuit solutions of ac electronic motor usage in electrical drive]. Vestnik KhNADU, № 41, pp. 45 –47.

[7] Smirnova, A.O., (2008), "Osobenosti postroeniya hybridnih sylovih ustanovok" [Designing features of hybrid power plants]. Transport, Environment – Sustainable Development: XIV International Scientific Conference, 8 –10 May 2008. Varna, Bulgaria, pp. 291 –295.

[8] Gnatov, A.V., Smirnov, O.P., (2008), "Vikoristannya komp'yuternih technologiy dlya pidgotovki elektromehanikov avtomobilnogo profilya" [Using the computer technology to train auto electro mechanics]. Economic and legal aspects of social priorities and trends in the development of education under conditions of integration Ukraine into the global educational system: Scientific Conference, 17 –18 April 2008. Kharkov, pp. 112 –115.

A Numerical-Analytical Approach to the Analysis of Non-Stationary Temperature Fields in Multiply-Connected Solids

Roman Kushnir[1] & Tetyana Solyar[1,a]

1 – Pidstryhach Institute for Applied Problems of Mechanics and Mathematics, National Academy of Sciences of Ukraine, 3-B Naukova St., 79060, Lviv, Ukraine

2 – tanya@iapmm.lviv.ua



DOI **10.13140/RG.2.1.1167.0165**

Keywords: integral Laplace transformation, non-stationary temperature fields, multiply connected solids, plate with heat emission.

ABSTRACT. A technique for the analysis of non-stationary temperature fields in multiply connected solids is presented. This technique rests upon the Laplace integral transformation along with the method of boundary-integral equations. The inversion for the Laplace transformation is performed by making use of the well-known general analytical-numerical Prudnikov's formula, which has been efficiently adopted for solving non-stationary heat-conduction problems to achieve the solution within the controllable accuracy. On this basis, the temperature fields in solids with openings and multiply-connected plates with heat emission are analyzed.

1. Introduction. It is well known that the non-stationary heat-conduction problems for multiply connected solids present a challenge for the dominant analytical modes of attack and, thus, they are readily attempted by means of the numerical procedures. One of the simplest, from the mathematical standpoint, methods for the solution of such problems is based upon the application of Laplace integral transformation. For the determination of Laplace image-function for the temperature, the method of boundary-integral equations can be efficiently used. Then, the inversion procedures, i.e. the construction of original function, cause certain mathematical complications.

There exist a great number of various methods for the numerical Laplace inversion, which, in general, is an ill-posed problem. Due to this reason, a great many of the new developed methods are devoted to the special classes of problems. For instance, the method of decomposition by the Eigen functions is presented in [13] for the analysis of transient phenomena in a porous medium. In [15], the efficiency analysis for the methods of numerical Laplace inversion is presented concerning the homogenization problems in linear viscoelastic materials. A numerical-analytical inversion formula based on the quadrature formulas is suggested in [11] for a class of functions which rapidly vanish for greater values of the time.

Among these methods, an inversion formula suggested by Prudnikov [3] presents a great deal of interest. This formula is based on the explicit relationship involving two series. One of these series has a form of the Fourier series with the coefficients presented by the Laplace transformations. The second one is the exponential series, which contains the values of the original-functions.

In this paper, the approximate inversion formulas for the Laplace transformation are obtained because of the foregoing explicit relationship in which, by making use of the developed technique, the Fourier series convergence is accelerated and the remainder term is accounted. A key feature of the inversion-formula is that it contains the exact values of the original-function at both initial and infinitely distant moments of time. Due to this reason, this formula cannot be regarded as the universal one as it can be used only if the mentioned parameters are given a priori. This makes this inversion-formula to be applicable for certain classes of problems. The employment of the a priori date on the original-function in this formula is a kind of regularization of the ill-posed, in general, problem on inversion

for the Laplace transformation. One of such classes is presented by the non-stationary problems of the heat-conduction theory.

2. Formulation of the Heat-Conduction Problem for Multiply-Connected Solids and its Laplace-Image Analogue.

In the Cartesian coordinate system (x, y, z), the problem on determination of the non-stationary temperature field T in a multiply-connected body *D*, bounded by the surface *S*, is governed [4] by the following heat-conduction equation:

$$\Delta T - \frac{1}{a}\frac{\partial T}{\partial \tau} = w,\ (x, y, z) \in D,\ \tau > 0 \tag{1}$$

along with the boundary,

$$MT = g,\ (x, y, z) \in S,\ \tau > 0 \tag{2}$$

and initial conditions

$$T\big|_{\tau=0} = T_0,\ (x, y, z) \in D. \tag{3}$$

Here Δ is the Laplace differential operator, $w = -W/\lambda$, λ is the heat conductivity, *a* denotes the coefficient of thermal diffusivity, *W* is the density of heating sources, τ stands for the time variable, $g = \alpha_s T_s$, α_s is the thermal emission, T_s is the temperature of medium which surrounds surface *S*, M denotes the differential operator describing the type of the heat-exchange boundary condition (in the case of convective heat exchange $MT = \lambda \partial T/\partial n + \alpha_S T$, where $\partial T/\partial n$ is the normal derivative with respect to surface *S*) .

To solve this problem, we employ the Laplace integral transformation method with further implication of a numerical inversion technique. Introducing $t = a\tau$ and applying the Laplace transformation with respect to the introduced variable *t* to Eqs. (1) – (3), we arrive at the following boundary-value problem:

$$(\Delta - s)\tilde{T} = \tilde{w} - T_0,\ (x, y, z) \in D, \tag{4}$$

$$M\tilde{T} = \tilde{g},\ (x, y, z) \in S. \tag{5}$$

Here $\tilde{T}$, $\tilde{w}$, and $\tilde{g}$ are the Laplace image-functions for *T*, *w*, and g, respectively, and s is the transformation parameter. Solution of the obtained problem can be reduced to the following Helmholtz equation

$$(\Delta - m^2)F = V,\ (x, y, z) \in D \tag{6}$$

under the boundary condition

$$MF = \Psi\ ,\ (x, y, z) \in S\ , \tag{7}$$

where V and Ψ are given functions and m^2 is a complex constant. Then $\tilde{T}(s) = F\big|_{m^2=s}$ at $V = w - T_0$ and $\Psi = \tilde{g}$.

Solution of Equation (6) can be found by means of the known technique based on the boundary-integral equations method [1, 2, 14].

3. Construction of the Inversion Formula.

Consider a problem on the determination of function $f(t)$ by its Laplace image-function $F(s) = \int_0^\infty f(t)\exp(-st)dt$. Assume $F(s)$ to be an analytical function for $\mathrm{Re}(s) > d$, where d is a known constant. Then the explicit formula [3]

$$f(t) = \frac{1}{l}\exp\left(c\frac{t}{l}\right)\sum_{n=-\infty}^{\infty} F(s_n)\exp\left(2\pi n i\frac{t}{l}\right) - R_1 \tag{8}$$

can be used for $0 < t < l$, where $s_n = (c + 2\pi n i)/l$, c is a constant allowing for the optimization of the solution convergence ($\mathrm{Re}(c) > 0$), l is a constant for which $f(t) \approx f(l)$ at $t > l$, and

$$R_1 = \sum_{n=1}^{\infty}\exp(-nc)\, f(t + nl)\,. \tag{9}$$

Note that function $f_*(t) = f(t) + R_1(t)$ can be determined by the formula

$$f_*(t) = \frac{1}{2\pi i}\int_{d-i\infty}^{d+i\infty}\chi F(s)\exp(st)ds\,, \tag{10}$$

where $\chi(s) = 1/(1 - \exp(ls - c))$.

This can be shown in the way that letting $F(s) \to 0$ as $|s| \to \infty$ and $\mathrm{Re}(s) > d$ and applying the Jordan's theorem along with the residue theorem [3] and expression $\chi = \sum_{n=0}^{\infty}\exp(-nc + nls)$, where $\mathrm{Re}(s) < \mathrm{Re}(c/l)$, we can obtain Eqs. (8) and (9).

Formula (10) is convenient for the evaluation of accuracy in the approximate formulae, which can be obtained from (8) and (9).

By neglecting R_1, formula (8) resembles the well known approximate inversion-formula, which is based on the representation of the original-function by the Fourier series [12].

The error of computation by formula (8) contains two principal values. One of them is the residual term R_1. For many practical cases, it can be made infinitesimally small by a proper choice for the parameter c in the coefficient $\exp(-c)$. For the case when function $f(t)$ are bounded at $t > l$, formula (9) yields the assessment $|R_1| < |f|_{\max}\left[\exp\left(\mathrm{Re}(c)\right)-1\right]^{-1}$, from which the parameter c can be computed for given accuracy. Here $|f|_{\max}$ denotes the maximum value of $f(t)$ for $t > l$. The second principal value is the error of the series computation, multiplied with $\exp(ct/l)$, which, in general, increases with increment of c. By this reason, the use of formula (8) for greater values of c calls for the computation of series with higher accuracy. On the other hand, the series in formula (8) is usually slowly the convergent one. In [15], for example, there were involved over 10000 terms in the mentioned series to achieve a proper accuracy of computation. Thus, the ill-posedness of the problem on construction of the Laplace inversion originates a new ill-posed problem, which lies in the computation of the slowly convergent series within the controllable accuracy. Thus, it is reasonable to employ formula (8) directly at $R_1 = 0$ only if there is no a priory data about the original-function. In what follows, we consider the cases of advancement in formula (8), which can be achieved by making use of certain a priori knowledge about function $f(t)$.

3.1. Approximate Computation of R_1.

Term R_1 in formula (9) can be evaluated approximately, when the asymptotic value $f_\infty(t)$ of function $f(t)$ at $t \to \infty$ is known. Introduce parameter l so that $f(t) \cong f_\infty(t)$ at $t > l$. Then $R_1 = A(t,l,c) + \varepsilon_1$, where $A(t,l,c) = \sum_{n=1}^{\infty} \exp(-nc)\, f_\infty(t+nl)$, $\varepsilon_1 = \sum_{n=1}^{\infty} \exp(-nc)\left[f(t+nl) - f_\infty(t+nl)\right]$. Value of ε_1 can be made infinitesimally small by control of parameter c and l (by letting the latter one to be sufficiently great). Then, term R_1 in (8) can be approximately substituted by A.

Note that the series for determination of function A can be summed up in a closed form for many practical cases. For instance, when $f_\infty = \mathrm{const}$, then $A = f_\infty/(\exp(c)-1)$. In this case the approximate inversion formula can be given as

$$f(t) \approx \frac{1}{l}\exp\left(c\frac{t}{l}\right)\sum_{n=-\infty}^{\infty} F(s_n)\exp\left(2\pi n i\frac{t}{l}\right) - \frac{f_\infty}{\exp c - 1}.$$

If $f_\infty = a + bt$ (a and b are constants), then

$$A \cong \left(f_\infty + \frac{bl\exp(c)}{\exp(c)-1}\right)\frac{1}{\exp(c)-1}.$$

3.2. Acceleration of the Series Convergence.

As a rule, the series in formula (8) are slowly convergent. If $f(0)$ and $f'(0)$ are known and

$\int_0^\infty f''(t)\exp(-st)dt$ exists, then the asymptotic representation $F(s_n) \to f(0)/s_n + f'(0)/s_n^2 + ...$ can be obtained at $n \to \infty$ from integration of expression $F(s) = \int_0^\infty f(t)\exp(-st)dt$ by parts. In this case, formula (8) can be represented by the following accelerated series [5 – 7]:

$$f(t) = \frac{1}{l}\exp\left(c\frac{t}{l}\right)\sum_{n=-\infty}^{\infty}\tilde{F}_n \exp\left(2\pi n i\frac{t}{l}\right) + \frac{1}{1-\exp(-c)}\left(f(0) + lf'(0)\left(\frac{t}{l} + \frac{1}{\exp(c)-1}\right)\right) - R_1, \quad (11)$$

where $\tilde{F}_n = F_n - \left(f(0)/s_n + f'(0)/s_n^2\right)$ and $\tilde{F}_n = O(n^{-3})$ as $n \to \infty$.

3.3. Selection of Parameters c and l.

The residual term R_1 of the inversion formula contains the value of the original-function at $t > l$. In the case when this value is known for greater arguments (the asymptotic value of the original-function) the residual term can be easily computed. Then the parameter l should be chosen in the way to make the original-function as close as possible to the asymptotic value. This can be achieved, for instance, by means of the computational experiments.

The error of the residual term can be reduced by a proper choice of the parameter *c* by means of the factor $\exp(-c)$. However, the inversion formula contains the Fourier series involving the factor $\exp(tc/l)$. Thus, when the value of c is sufficiently great, then the mentioned series should be computed with higher accuracy for the reason that the error of computation of the inversion formula is equal to the error of computation of the series multiplied with $\exp(c)$. From the numerical experiments, we established the reasonable range for *c* within $2 \div 4$.

To demonstrate the effect of parameter c, we consider a non-stationary heat-conduction problem for a thermally-insulated strip $-H < y < H$, which is heated by a heat flux of intensity q_0 over its end-faces. The strip was of zero temperature at the initial moment of time. The Laplace-image for the temperature has the form [4]

$$T = q\frac{\sinh(\sqrt{s}y)}{s\sqrt{s}\cosh(\sqrt{s}H)},$$

where $q = q_0/\lambda$. The original for the latter expression can be obtained exactly [4] in the form

$$\frac{T}{q} = y + 2H\sum_{n=0}^{\infty}\frac{(-1)^n}{\mu_n^2}\sin\mu_n\frac{y}{H}\exp\left(-\frac{\mu_n^2}{H^2}t\right),$$

where $\mu_n = \pi(n+0.5)$.

When using Equation (8) for computation of the original temperature for different values of *c*, the relative error of computations can be evaluated by comparing the results with the foregoing exact solution (see Table 1). It has been assumed that $l'=l/H^2=0.375$ (at $t \approx l$, the temperature reaches the

asymptotic regime); in the series we adopted 40 terms. The first column shows the dimensionless time variable $t' = t / H^2$; the second column presents the values of temperature computed by the exact formula. The third, fourth, fifth, and sixth columns show the relative errors ε (%) in computation of the inversion formula at $c = 1$, 2, 3, and 4, respectively. As we can see, the optimal choice for l (for $t > l$, the temperature approaches its asymptotic values) makes the error of inversion formula to be irrespective of the parameter c which varies within $1 \le c \le 4$.

Table 1. Relative errors in computation of the temperature in a strip for different values of parameter c

t'	T/q	ε, $c=1$	ε, $c=2$	ε, $c=3$	ε, $c=4$
0,0094	0,1092	4,15	2,22	1,53	1,31
0,0469	0,2441	1,13	0,54	0,34	0,29
0,0844	0,3237	0,59	0,29	0,21	0,20
0,1219	0,3782	0,36	0,19	0,16	0,18
0,1594	0,4159	0,23	0,14	0,14	0,18
0,1969	0,4419	0,16	0,11	0,12	0,18
0,2344	0,4598	0,10	0,07	0,09	0,16
0,2719	0,4723	0,06	0,029	0,02	0,03
0,3094	0,4808	-0,01	-0,07	-0,19	-0,46

It is worth noting that the foregoing inversion-formulae can be efficient only under known a priori information about the original-function. For the heat-conduction problems, such information (for instance, $f(0)$ and $f'(0)$) is feasible.

4. Solution of the Three-Dimensional Non-Stationary Heat-Conduction Problem in Terms of the Image-Function.

To solve the problem (4) and (5) in terms of image-functions, we employ the boundary-integral equations technique. The integral representation of a solution to the Helmholtz equation (6) can be given [10] as

$$F = \int_s (F'|_s G - F|_s G')ds - \int_D VGd\omega, \tag{12}$$

where $G = \exp(-mR)/(4\pi)$, $R^2 = (x-x_0)^2 + (y-y_0)^2 + (z-z_0)^2$, and G' is the normal derivative in the direction of outer normal-vector of surface S at (x_0, y_0, z_0). Putting the boundary condition (7) into formula (12) and letting $(x, y, z) \to S$, we can obtain the integral equation

$$\frac{1}{2} F\Big|_s = -\int_S F|_s (G' + \frac{\alpha_s}{\lambda} G)ds - \int_D VGdD + \int_S \frac{\Psi}{\lambda} Gds \tag{13}$$

for determination of F on S. Here we used the basic features of the double-layer potential [10].

Integral equation for the determination of temperature contains the integrals of the following kind:

$$I(x,y,z)=\int_{\Omega} fQd\Omega, \tag{14}$$

where $f=f(x_0,y_0,z_0)$ is either given or quested-for function (T or T'), $Q=Q(x,y,z,x_0,y_0,z_0)$ is a given function (G, the kernel of equation, or G'), and Ω is one of the limiting surfaces. Consider the case when the equation of surface Ω is given parametrically as

$$x=\varphi(\xi,\eta),\ y=\psi(\xi,\eta),\ z=\gamma(\xi,\eta),$$

where $(\xi,\eta)\in\Omega^*$ and Ω^* is a rectangular domain: $a\le\xi\le b$, $c\le\eta\le d$. Then (14) can be given as [1]:

$$I(x,y,z)=\int_{\Omega^*} f_*(\xi,\eta)Q_*(x,y,z,\xi,\eta)B(\xi,\eta)d\xi d\eta, \tag{15}$$

where $f_*(\xi,\eta)Q_*(x,y,z,\xi,\eta)=\left(fQ\right)\Big|_{\substack{x_0=\varphi(\xi,\eta),\\ y_0=\psi(\xi,\eta),\\ z_0=\gamma(\xi,\eta)}}$, $B=\sqrt{E_1E_2-E_3^2}$, $E_1=\left(\frac{\partial\varphi}{\partial\xi}\right)^2+\left(\frac{\partial\psi}{\partial\xi}\right)^2+\left(\frac{\partial\gamma}{\partial\xi}\right)^2$,

$E_2=\left(\frac{\partial\varphi}{\partial\eta}\right)^2+\left(\frac{\partial\psi}{\partial\eta}\right)^2+\left(\frac{\partial\gamma}{\partial\eta}\right)^2$, and $E_3=\frac{\partial\varphi}{\partial\xi}\frac{\partial\varphi}{\partial\eta}+\frac{\partial\psi}{\partial\xi}\frac{\partial\psi}{\partial\eta}+\frac{\partial\gamma}{\partial\xi}\frac{\partial\gamma}{\partial\eta}$.

Let us reticulate domain Ω* by grid points (ξ_k,η_j), where $\xi_k=a+kh$, $k=\overline{0,N}$, $h=(b-a)/N$, $\eta_j=b+jH$, $j=\overline{0,M}$, $H=(d-c)/M$, N+1 and M + 1 are the numbers of points by ξ and η, respectively. Let the values of function f_* be given in the grid points $f_*(\xi_k,\eta_j)=f_{kj}$. Then we can approximate this function for each of the elementary rectangle by Lagrange polynomials with four grid points at the corners of the rectangle. Note that the interpolation polynomials are linear by each variable. Then function $f_*(\xi,\eta)$ at a point of Ω* can be given by the following interpolation formula [1, 14]:

$$f_*(\xi,\eta)\approx\sum_{k=0}^{N}\sum_{j=0}^{M} f_{kj}S_h(\xi-\xi_k)S_H(\eta-\eta_j),\qquad S_\alpha(S)=\begin{cases}0, & |S|\ge\alpha,\\ 1-|S|/\alpha, & |S|<\alpha.\end{cases}$$

With the latter formula in mind, Eq. (15) can be given as

$$I(x,y,z)\approx\sum_{k=0}^{N}\sum_{j=0}^{M} f_{kj}\int_{-h}^{h}\int_{-H}^{H} Q_*(x,y,z,\ \xi+a+kh,\ \eta+c+jH)B(\xi+a+kh,\ \eta+c+jH)S_h(\xi)S_H(\eta)d\xi d\eta.$$

Here $B(\xi,\eta)=0$, when (ξ,η) falls beyond the rectangle $a<\xi<b$, $c<\eta<d$.

When solving the integral equation (13), the point (x, y, z) is to be taken as one of the grid points on the surface Ω^*: $x_{\nu\mu} = \varphi(\xi_\nu, \eta_\mu)$, $y_{\nu\mu} = \psi(\xi_\nu, \eta_\mu)$, $z_{\nu\mu} = \gamma(\xi_\nu, \eta_\mu)$. Thus, we obtain

$$I_{\nu\mu} = \sum_{n=0}^{N}\sum_{m=0}^{M} f_{nm} Q_{\nu\mu nm} \quad , \ \nu = \overline{0, N} \ , \ \mu = \overline{0, M} \ , \ n = \overline{0, N} \ , \ m = \overline{0, M} \ , \tag{16}$$

$$Q_{\nu\mu nm} = \int_{-h}^{h}\int_{-H}^{H} Q_*\left(x_{\nu\mu}, y_{\nu\mu}, z_{\nu\mu}, \ \xi + a + nh, \ \eta + c + mH\right)$$

$$\times B\left(\xi + a + nh, \ \eta + c + mH\right) S_h\left(\xi\right) S_H\left(\eta\right) d\xi d\eta \ . \tag{17}$$

where $I_{\nu\mu} = I(x_{\nu\mu}, y_{\nu\mu}, z_{\nu\mu})$.

By making use the representation (16) for integrals appearing in Eq. (12) and applying the boundary transition, we arrive at

$$\frac{1}{2} F_{\nu\mu} = \sum_{n=0}^{N}\sum_{m=0}^{M}\left(F'_{nm} G_{\nu\mu nm} - F_{nm} G'_{\nu\mu nm}\right) + V_{\nu\mu} \ , \ \nu = \overline{0, N} \ , \ \mu = \overline{0, M} \ , \tag{18}$$

where $V_{\nu\mu} = -\int_D VGdD$ at $x = x_{\nu\mu}$, $y = y_{\nu\mu}$, $z = z_{\nu\mu}$, and the coefficients $G_{\nu\mu nm}$ and $G'_{\nu\mu nm}$ (with exception for $G'_{\nu\mu nm}$ at $\nu = n, \ \mu = m$, for which the integral appears to be singular) can be computed by means of formula (17) where Q is substituted by G and G', respectively. The coefficient $G'_{\nu\mu nm}$ at $\nu = n, \ \mu = m$ can be computed by well-known methods presented in [1, 2].

The discrete analogue (18) for Eq. (12) contains unknown values F_{nm} and F'_{nm}. To determine them, we use the boundary condition (18), which yields $F'_{nm} = \alpha_{nm} F_{nm} + q_{nm}$ at $\alpha_{nm} = -\alpha_s(x_{nm}, y_{nm}, z_{nm}) / \lambda$, $q_{nm} = \Psi(x_{nm}, y_{nm}, z_{nm}) / \lambda$. On the basis of (18), we finally obtain the following system of equations:

$$\sum_{n=0}^{N}\sum_{m=0}^{M} F_{nm} A_{\nu\mu nm} = a_{\nu\mu}, \ \nu = \overline{O, N} \ , \ \mu = \overline{O, M} \ , \tag{19}$$

where $A_{\nu\mu nm} = \alpha_{nm} G_{\nu\mu nm} - G'_{\nu\mu nm} - \delta_{\nu,n}\delta_{\mu,m} / 2$ and $a_{\nu\mu} = -\sum_{n=0}^{N}\sum_{m=0}^{M} q_{nm} G_{\nu\mu nm} - V_{\nu\mu}$.

These relations allow for the construction of original for the temperature appearing in the inversion formula. Consider application of these relations to computation of three-dimensional non-stationary temperature fields.

4.1. Computation of Three-Dimensional Non-Stationary Temperature Fields in Solids Heated by Concentrated Heat Sources.

Having solved the heat-conduction problem in terms of the image-function, the temperature can be found by means of formula (11), which contains functions $T_0 = T_0(x, y, z, 0)$, $T'(x, y, z, 0)$, T_∞, and $\tilde{T}(x, y, z, s_n)$. The first of these functions can be determined from the initial condition. By making

use of Eqs. (1) – (3), we can find $T'(x,y,z,0)=\left(\Delta T-w\right)\big|_{\tau=0}=\Delta T_0-w\big|_{\tau=0}$. The asymptotic value for the temperature T_∞ can be determined from the following boundary-value problem:

$$\Delta T_\infty = w_\infty,\ (x,y,z)\in D,\ MT_\infty = g_\infty,\ (x,y,z)\in S$$

by making use of the proposed technique. Functions $\tilde{T}(x,y,z,s_n)$ can be found from (11) at $s=s_n$, $n=0,\pm1,\ldots$

To evaluate the accuracy of the proposed technique, we consider the following example. Consider the heat-conduction problem for an infinite body (the space) with an ellipsoidal opening. Let the body is heated constantly by a heat source of intensity λQ, which is located at (x_q,y_q,z_q). The temperature is expected to be vanishing at the points of infinity. The medium, which fills the opening, exchange the heat according to the Newtonian law. At the initial time moment, the temperatures of both the surrounding and body are zero. Let us represent the temperature of the body T in the form

$$T=T_1+T_*, \tag{20}$$

where T_* is the solution for the simply-connected space and T_1 is the shifting function. Function T_* can be given [4] as

$$T_*=\frac{Q}{4\pi R}\operatorname{erfc}\left(\frac{R}{\sqrt{4t}}\right), \tag{21}$$

where $R=\sqrt{(x-x_q)^2+(y-y_q)^2+(z-z_q)^2}$. Then T_1 can be determined from the homogeneous heat conduction equation under the following boundary and initial conditions

$$\lambda\frac{\partial T_1}{\partial n}+\alpha_s T_1=\phi,\quad T_1\big|_{t=0}=0,$$

where $\phi=-\left(\lambda\partial T_*/\partial n+\alpha_s T_*\right)$, $(x,y,z)\in S$. By making use of the Laplace transformation and having the formula

$$\tilde{T}_*=\frac{Q}{4\pi R}\exp(-kR),\ k=\sqrt{s},$$

in mind, we can obtain

$$\tilde{\phi} = \left(\lambda \left(\frac{k}{R} + \frac{1}{R^2} \right) \left((x - x_q) n_1 + (y - y_q) n_2 + (z - z_q) n_3 \right) - \frac{\alpha_s}{R} \right) \exp(-kR),$$

where n_1, n_2, n_3 – are the directional cosines. Thus, the shifting function T_1 can be found from the integral equation at $V=0$, $\psi = \tilde{\phi}$.

To evaluate the accuracy of approximate solution, we assume that T_* is to be the exact solution of the heat-conduction problem for points (x_q, y_q, z_q), which falls within the ellipsoidal opening. Moreover, this function meets the condition

$$\lambda \partial T_* / \partial n + \alpha_s T_* = -\phi \tag{22}$$

at $(x, y, z) \in S$. Assume function T_* to be unknown. By making use of the proposed algorithm, T_* can be determined within the domain D as a solution of the homogeneous non-stationary heat-conduction equation under condition (22) and the initial condition $T_*|_{t=0} = 0$.

The computations were implemented for the case of ellipsoidal opening with semiaxes $r_2/r_1 = 1$, $r_3/r_1 = 2$ at $x_q = 0$, $y_q = 0$, $z_q/r_1 = 1$, $r_1\alpha_s/\lambda = 0.1$.

Table 2 presents the values of T_a / T depending on $\theta = a\tau / r_1^2$, where T_a and T are the values of the temperature computed by means of the proposed algorithm and the exact formula, respectively. The values in columns 1 and 2 are presented for the points $A(0;0;r_3)$, $B(-0.95r_1; -0.1r_1; -0.6r_1)$ at c=4, $L = l / r_1^2 = 0.06$. The values in columns 3 and 4 are presented for the points $C(0;0;-r_3)$, $D(-0.99r_1; -0.1r_1; 0.2r_1)$ at c=4, $l / r_1^2 = 12$.

Table 2. The temperature in a body with opening, computed by means of the proposed algorithm (T_a) and the exact formula (T)

	1	2		3	4
θ	T_a / T	T_a / T	θ	T_a / T	T_a / T
0,6	0,9967	0,9416	0,012	0,8523	1,0043
1,2	0,9961	0,9825	0,024	0,9768	1,0023
1,8	0,9962	0,9895	0,036	1,0102	1,0016
2,4	0,9961	0,9923	0,048	0,9829	1,0009
3,0	0,9958	0,9945	0,06	0,9868	0,9998
3,6	0,9946	0,9957	0,072	0,9888	0,9974
4,2	0,9917	0,9967	0,084	0,9903	0,9903

As we can see from the Table 2, the proposed algorithm allows for the computation of the temperature within the wide range of the time with high accuracy with exception for the sufficiently small and great values of the time parameter θ. For both values of L, the temperature can be determined within $1 \div 2\%$ of accuracy. It is worth noting that at for the small values of time, the algorithm in the case $L = 6$ is more accurate than in the case $L = 12$. The same pattern holds for the other classes of problems. Thus, we can control the accuracy of computation by a proper choice of the parameter L

for the small or great values of the time-parameter. On the other hand, different choices for *L* present an additional tool for the improvement of the accuracy.

4.2 Determination of the Temperature Field in a Half-Space $z > 0$ with an Ellipsoidal Opening.

Consider the non-stationary heat-conduction problem for a half-space containing an ellopsoidal opening an is heated by a concentrated heating source Q at (x_q, y_q, z_q). The half-space and the mediums, which surround its limiting plane and the surface of opening, are being under the condition of Newtonian heat exchange.

For determination of the image for temperature, we used the integral representation for the solution to the Helmholtz equation under which the boundary condition on the plane surface is satisfied exactly. By making use of the proposed algorithm, we computed the temperature at $(0;0;H)$, when the semiaxes $r_1 = 0{,}1$, $r_2/r_1 = 1.5$, $r_3/r_1 = 2$ of the opening are directed along the coordinate axes OX, OY, OZ under the following parameters $\alpha_S = 0$, $x_q = y_q = 0$, $z_q/r_1 = 0.01$, $H/r_3 = 2$ and different values of $\chi = \alpha_\Omega / \lambda$ characterizing the emission of Ω.

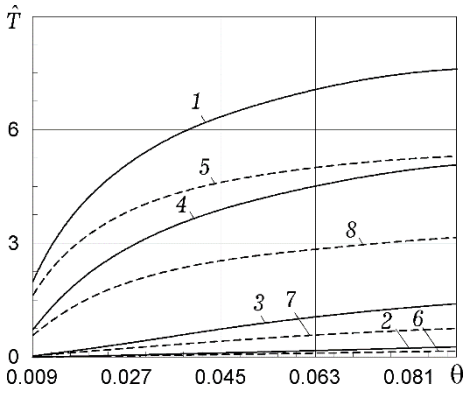


Fig. 1. Dependence of the temperature T on the time parameter θ at $\chi = 1$ (curves 1-4) and $\chi = 10$ (curves 5-8)

In Figure 1 the distributions of $T = aT/Q$ at $A(0;0;0,2r_1)$, $B(0;0;0,6r_1)$, $C(-0,1r_1;-1,5r_1;3,8r_1)$, and $D(-0,58r_1;0;2,4r_1)$ are shown versus the parameter $\theta = t$. As we can observe, the emission from the surface of opening affects the temperature in the half-space substantially. The temperature on this surface varies along the boundary and, at the points of infinity it is lesser by the order of ten than at the points located near to the limiting plane.

5. Solution of the Non-Stationary Heat-Conduction Problems for Plates with Thermal Emission.

Here we employ the proposed technique for determination of non-stationary temperature fields in multiply-connected plates with thermal emission. Consider a thin plate with mid-surface D, which is bounded by curves $L_0, L_1, \ldots, L_N$ with outer contour L_0 enveloping all the other contours. In the case of absence of L_0, we shall have the infinite plate. The plate is heated by the internal heating sources and the outer medium, which exchange the heat with the plate through the surfaces $z = \pm h$ and the cylindrical surfaces (the surfaces of openings) in accordance to the Newton's law (2). At the initial moment of time, its temperature is given by (3). For determination of the temperature field in the plate we employ the averaging technique to Eq. (1) to obtain [8] the equation

$$\Delta T - \chi^2 T = \frac{1}{a}\frac{\partial T}{\partial \tau} - W\ ,\ (x,y) \in D\ ,\ \tau > 0\ , \tag{23}$$

which is to be solved under the boundary and initial conditions (2) and (3).

Here $W = w/(2\lambda h) + \chi^2 t_c$, $\Delta = \partial^2/\partial x^2 + \partial^2/\partial y^2$, $\chi^2 = \alpha^+/(\lambda h)$, $L = L_0 + L_1 + \ldots + L_N$, t_c is the temperature of medium contacting with the limiting planes $z = \pm h$, $\alpha^+ = \alpha^-$ are the thermal emission coefficients of the limiting planes, T_c is the temperature of medium contacting with the cylindrical surface, w is the density of heat sources, which is averaged by the unit area, α is the thermal emission of the cylindrical surface.

By applying to Equations (23) and (2), with Eq. (3) in mind, the Laplace transformation with respect to $t = a\tau$, we arrive at the following boundary-value problem:

$$\Delta \tilde{T} - \chi_1^2 \tilde{T} = -T_0 - \tilde{W}\ ,\ (x,y) \in D\ ,$$
$$\lambda \frac{\partial \tilde{T}}{\partial n} + \alpha(\tilde{T} - \tilde{T}_c) = 0\ ,\ (x,y) \in L \tag{24}$$

for determination of $\tilde{T}(x,y)$. Here $\chi_1^2 = \chi^2 + s$, s is the transformation parameter. Here and in what follows, the tilde denotes the Laplace image-functions.

Assume the image of temperature $\tilde{T}(x,y,s)$ to be known and $T(x,y,t) \to T_\infty(x,y,t)$ as $t \to \infty$. Then the temperature $T(t)$ can be computed through formula (11) under additional information on the parameters involved. Within the framework of the formulated heat-conduction problems, the temperature at the initial moment of time is given by condition (3). The time-derivative of temperature at the initial moment of time can be determined form Eq. (23) as

$$\left.\frac{\partial T}{\partial t}\right|_{t=0} = (\Delta - \chi^2)T_0 + W(x,y,0)\,. \tag{25}$$

The asymptotic value of temperature $T_\infty(x,y,t)$ can be found in the following manner. Let the parameter l be great enough to fulfill the condition $T(x,y,t) \approx T_\infty(x,y,t)$ for $t > l$. By making use of the abovementioned technique, we can represent

$$R_1 \cong \sum_{n=1}^{\infty} \exp(-nc)\, T_\infty(t + nl)\,. \tag{26}$$

As we can see, the formulated problem is reduced to the solution of a sequence of nonhomogeneous Helmholtz equations

$$\Delta F - m^2 F = f\ ,\ (x,y) \in D\ , \tag{27}$$

under the boundary condition

$$\frac{\partial F}{\partial n}+\beta(F-q)=0, \tag{28}$$

where f, q, and β are given functions. Then $\tilde{T}_n=F\big|_{m^2=\chi^2+s_n}$, $f=-T_0-\tilde{W}$, $\beta=\alpha/\lambda$, $q=\tilde{T}_c$.

To solve the problem (27) and (28), we use the boundary-integral equations method. Let us represent the general solution of Eq. (27) as [10]

$$F(x,y)=\int_L (FG'-F'G)ds+\Phi_1, \tag{29}$$

where G is the fundamental solution of Eq. (27), $G'=\partial G/\partial n_0$ is the derivative along the outer normal to the contour L by the coordinates (x_0,y_0), $F'=\partial F/\partial n_0$, and $\Phi_1=\int_D f(x_0,y_0)G(x,y,x_0,y_0)dx_0dy_0$. In the general case, the fundamental solution can be presented as $G=-K_0(mr)/(2\pi)$, where $r=\sqrt{(x-x_0)^2+(y-y_0)^2}$ and $K_0(mr)$ is the Macdonald's function.

Consider the solution (29), when $(x,y)\to L$. By taking into account the features of the double-layer potential [10], the expression (29) yields

$$\frac{1}{2}F(x,y)=\int_L (FG'-F'G)ds+\Phi_1(x,y),\ (x,y)\in L. \tag{30}$$

Since the condition $F'=-\beta(F-q)$ takes place on the curve L, the relation (30) yields

$$\frac{1}{2}F(x,y)=\int_L (G'+\beta G)Fds+\Phi(x,y), \tag{31}$$

where $\Phi(x,y)=\Phi_1(x,y)-\int_L \beta qGds$.

As follows from Eq. (31), expression (29) allows for the direct determination of image for the temperature on the boundary of plate. By applying the inversion formula, the original for temperature on the boundary can be found directly without additional computations.

Consider the problem on numerical construction of solutions to the integral equations (30). For this purpose, we first construct the numerical solution to Eq. (30) by means of the mechanical-quadrature method under boundary condition (28). For the simplicity sake, we assume the contour L to be a single one. Equation (31) contains the integrals along the closed path with the integrands containing the Macdonald's functions or their derivatives:

$$C(x,y)=\int_L f(s)Q(r)ds\,,\ D(x,y)=\int_L f(s)\frac{\partial Q(r)}{\partial n_0}ds\,, \tag{32}$$

where $r=\sqrt{(x-\xi)^2+(y-\eta)^2}$ and $Q(r)=-K_0(mr)/2\pi$, $f(s)$ is a given function. By taking into account the form of Macdonald's functions at small arguments, the integrands can be given in the form of superposition of functions having the logarithmic singularities or the Cauchy's kernels. To construct the quadratures, we describe the boundary in the parametric form: $x=\varphi(\gamma)$, $y=\psi(\gamma)$, $0<\gamma\le 2\pi$ and introduce the grid points $x_n=\varphi(\gamma_n)$, $y_n=\psi(\gamma_n)$ and $\tilde{x}_n=\varphi(\tilde{\gamma}_n)$, $\tilde{y}_n=\psi(\tilde{\gamma}_n)$, where $\tilde{\gamma}_n=hn$, $\tilde{\gamma}_n=h(n-1/2)$, $n=1,\ldots,N.$ Then the following formulae [7]

$$C(\tilde{x}_\nu,\tilde{y}_\nu)=h\sum_{n=1}^{N}C_{\nu n}f_n+O(N^{-5})\,,\ D(\tilde{x}_\nu,\tilde{y}_\nu)=h\sum_{n=1}^{N}D_{\nu n}f_n+O(N^{-5}) \tag{33}$$

hold, where $C_{\nu n}=s_n'\left[Q(r_{\nu,n})+\alpha_{\nu,n}V(r_{\nu,n})\right]$, $V(r)=-\dfrac{I_0(mr)}{2\pi}$, $D_{\nu n}=s_n'\left[Q'(r_{\nu,n})+\alpha_{\nu,n}V'(r_{\nu,n})\right]\dfrac{\partial r}{\partial n_0}$ at $x=x_\nu$, $y=y_\nu$, $\xi=\xi_n,\eta=\eta_n$, $V'(r)=-mI_1(mr)/2\pi$, $Q'(r)=mK_1(mr)/2\pi$, $r_{\nu n}=\sqrt{(\tilde{x}_\nu-x_n)^2+(\tilde{y}_\nu-y_n)^2}$.

Now we can use the latter formulae to solve integral equation (30). By making use of the collocation method, we demand equation (30) to be satisfied at points $(\tilde{x}_\nu,\tilde{y}_\nu)$, $\nu=\overline{1,N}$ exactly. As a result, we arrive at the following system of equations:

$$\frac{1}{2}\tilde{F}_\nu=\int_L\left[FG'(\chi r_\nu)-F'G(\chi r_\nu)\right]ds+\Phi_\nu\,,$$

where $\tilde{F}_\nu=F(\tilde{x}_\nu,\tilde{y}_\nu)$, $r_\nu=\sqrt{(\tilde{x}_\nu-x_0)^2+(\tilde{y}_\nu-y_0)^2}$, and $\Phi_\nu=\Phi_1(\tilde{x}_\nu,\tilde{y}_\nu)$.

Having applied the quadrature formulas (33) to the latter equation and using the boundary condition $F_n'=-\beta_nF_n+\beta_nq_n$, we obtain the system of equations

$$\sum_{n=1}^{N}E_{\nu n}^{*}F_n=-b_\nu\,,\ \nu=\overline{1,N}\,, \tag{34}$$

where $E_{\nu n}^{*}=hE_{\nu n}$ for $n\ne\nu,\nu+1,\ \nu-1,\nu+2$; $E_{\nu n}^{*}=hE_{\nu n}-9/32$ for $n=\nu,\nu+1$; and $E_{\nu n}^{*}=hE_{\nu n}+1/32$ for $n=\nu-1,\nu+2.$ Here we also used the interpolation formula $\tilde{F}_\nu=9(F_\nu+F_{\nu+1})/16-(F_{\nu-1}+F_{\nu+2})/16+O(h^4)$ for values of $\tilde{F}_\nu$.

In the following section, we present an application of the proposed technique to analysis of temperature fields in multiply-connected solids with thermal emission.

5.1. Examples of the Numerical Determination of the Temperature Fields in Plates with Thermal Emission.

Here we present the numerical analysis for the plates of different shape subjected to the heating by a source of strength q (averaged by the thickness), which is situated at (x_q, y_q). The boundary is assumed be under the conditions of Newtonian heat exchange with the surrounding media of zero temperature. We also assumed that the initial temperature was zero. We implemented formula (11) under $c = 3$ and $l = 0.25\ m^2$, when holding up to 20 – 40 terms in the involved series and 40 – 80 grid points in the solution of integral equations. This allowed for the achievement of accuracy within 99%. The parameters $\alpha_* = H\alpha / \lambda$, $\chi_* = \chi^2 H^2$, and $Q = q / \lambda$ were introduced, where H is a characterizing linear parameter of the plate. The residual term in the inversion formula has been determined for the case of stationary heating (asymptotic value). We also put $\chi_*^2 = 1.2$ and $\alpha_* = 0.02$.

Consider a plate with a square opening, whose side semi-length is denoted by *A*. Let the heat source is located in the point $(1.5A,\ 0)$. The distribution of temperature $T_* = T / Q$ versus t is shown in Fig. 2 (on the right) for the points of plate, $\gamma = \gamma_j = \pi j / 40$ (shown by circles on the left). The values of j are specified at the curves. In Figure 3, the temperature for different moments of time $t_j = lj / 20$ is presented (the values of j are specified at the curves).

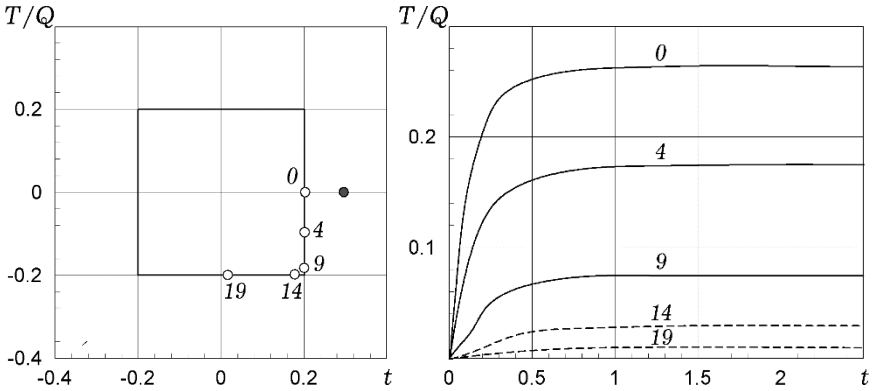


Fig. 2. The shape of domain (on the left) and the distribution of temperature in some points of the plate with square opening (on the right)

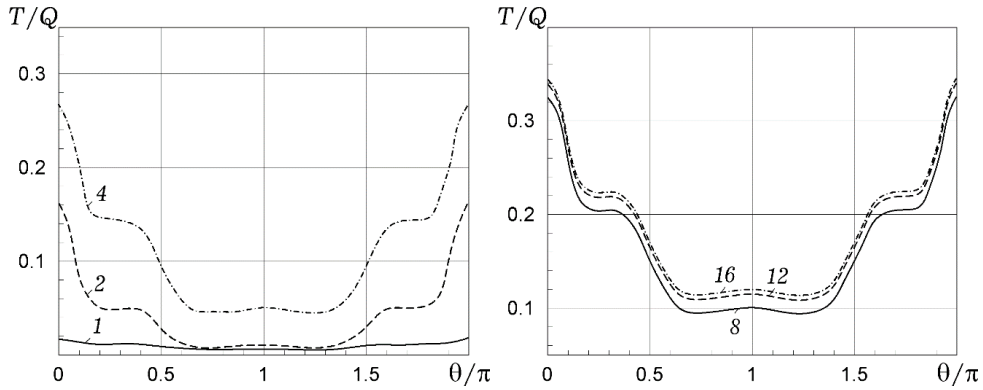


Fig. 3. Temperature fields on the boundary of the plate in different moments of time

5.2. Computation of Non-Stationary Temperature Fields in a Plate with Thermal Emission under Heating by a Surface Heat-Flux

The stationary problems for thermally-insulated plates subjected to a heat-flux at the points of infinity are quite popular in the literature (see [9], for instance). To obtain a similar limiting case of the

stationary problem for an unbounded plate with no thermal emission, let as consider a strip $-H < y < H$ with an opening of small diameter. Let the strip undergoes the action of heating flux

$$\lambda \frac{\partial T}{\partial y}\bigg|_{y=\pm H} = q_0 g(t) \tag{35}$$

on its limiting planes, meanwhile the curvilinear surface is assumed to be under the conditions of Newtonian heat exchange with the surrounding of zero temperature. Here $g(t)$ is a given function. The temperature of plate at the initial moment of time is assumed to be zero. The thermal emissions from the plane surfaces and the surface of the opening are different.

We represent the temperature in the form of superposition of two constituents, $T_c = T_n + T$, where the first constituent is the temperature in the simply-connected plate (found in an explicit form), and the second one is the shifting solution allowing for the satisfaction of boundary conditions on the boundary of the opening (found by means of the proposed algorithm).

We implemented the computation for the strip with elliptic opening, whose semiaxes are 0.2*H* and 0.3*H*. In Figure 4, the time-variation of the temperature, normalized by $Q = q_0 H / \lambda$, is depicted at the points of boundary corresponding to the values of parameter γ (which appears in the description of the boundary, $x = r_1 \cos\gamma$, $y = r_2 \sin\gamma$) at $\gamma = \gamma_j$, $j = 1 \div 80$. The values $c = 3$ and $l / H^2 = 6 \div 10$ have been used in the inversion formula under 20 – 40 terms in the involved series and 40 – 80 grid points in the solution of the integral equations to keep the computational error within 1%; $H\alpha / \lambda = 0.0001$ and $\chi^* = \chi^2 H^2 = 0.003$.

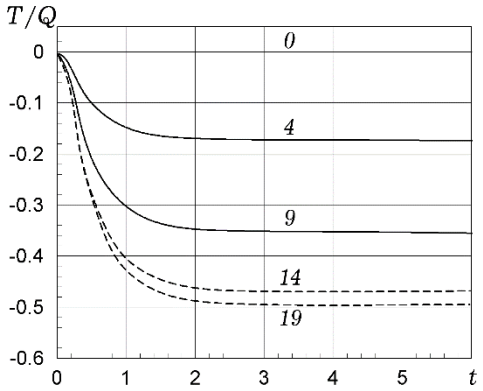


Fig. 4. Distribution of the temperature versus time at the boundary points of the elliptic opening with the axes ratio 2/3 for $l = 6H^2$ *(the numbers at the curves present the values of j)*

The numerical analysis showed that it is reasonable to take $c \approx 3.0$ and l should be twice greater than the value at which the temperature on the boundary is almost equal to the asymptotic one. When solving the integral equations of Helmholtz problems, the accuracy in 99% has been achieved by taking about 80 grid points. In the inversion formula, the error of computation falls within 1% when having 20 to 40 terms in the Fourier series. It is worth noting that the aforementioned errors in determination of the Laplace origin-functions did not provide any significant error in computation of the original for the temperature.

Summary. In this paper, we proposed an approach to the solution of the non-stationary heat-conduction problems, which is based upon the Laplace integral transformation and refined formulas

of its numerical inversion with account for the asymptotic values of the temperature for great values of the time-coordinate. The ill-posedness of this problem has been removed by means of the proposed regularization technique consisting in the acceleration of the series convergence owing to the know values of the original temperature at the initial moment of time. The solutions of boundary-value problems (formulated for the Helmholtz equations) for the image-function are constructed by making use of the boundary-integral equations method. The computational results showed the high accuracy of our technique, the stability of the refined inversion formula, its applicability for two- and three-dimensional problems in multiply-connected solids. This approach can be efficiently used for computation of the thermal stresses in the mentioned solids**.**

References

[1] C. A. Brebbia, J. Telles, and L. Wrobel, Boundary Element Techniques, Theory and Applications in Engineering, Springer-Verlag, Berlin, NY, 1984.

[2] C. A. Brebbia and S. Walker, Boundary Element Techniques in Engineering, Butterworths, London, Boston, 1980.

[3] V. A. Ditkin and A. P. Pudnikov, Integral Transforms and Operational Calculus, Oxford, New York, 1965.

[4] H. S. Carslaw and J. C. Jaeger, Conduction of Heat in Solids, Clarendon Press, Oxford, 1959.

[5] R. M. Kushnir, V. M. Maksymovych, and T. Ya. Solyar, Determination of Nonstationary Temperatures with the Help of Improved Formulas of the Inverse Laplace Transformation, *Mater. Sci.*, 38, No. 2, 2002, pp. 172-184.

[6] V. M. Maksymovich and T. Ya. Solyar, Refined Formulas for Determination of the Inverse Laplace Transform Using Fourier Series and their Use in Problems of Heat Conduction, *J. Eng. Phys. Thermophys*., 75, No. 3, 2002, pp. 648-650.

[7] V. M. Maksymovych and T. Ya. Solyar, Method of Mechanical Quadratures for Solving Integral Equations of Thermoelasticity for Plates with Heat Exchange, *J. Math. Sci.*, 174, No. 3, 2011, pp. 387-399.

[8] Ya. S. Pidstryhach and Yu. M. Kolyano, Unsteady Temperature Fields and Stresses in Thin Plates, Naukova Dumka, Kiev, 1972 [in Russian].

[9] G. N. Savin, Stresses Concentration Around Holes, New York, Pergamon Press, 1961.

[10] A. N. Tikhonov and A. A. Samarskii, Equations of Mathematical Physics, Oxford: Pergamon, 1963.

[11] R. G. Campos and F. M. Díaz, Quadrature Formulas for the Laplace and Mellin Transform Analytic-Element Method for Transient Porous-media Flow, *BIT Numer. Math.*, 49, No. 3, 2009, pp. 477-486.

[12] B. Davis and B. Martin, Numerical Inversion of the Laplace Transform: Survey and Comparison of Methods, *J. Computat. Physics*, 33, No. 1, 1979, pp. 1-32.

[13] K. L. Kuhlman and S. P.Neuman, Laplace-Transform Analytic-Element Method for Transient Porous-Media Flow, *J. Eng. Math*., 64, No. 2, 2009, pp. 113-130.

[14] M. Bonnet, Equations Integrales et Elements de Frontiere. Applications en Mecanique des Solides et des Fluides, CNRS Editions, Editions Eyrolles, 1995.

[15] M. Levesque, M. D. Gilchris, N. Bouleau, K. Derrien, and D. Baptiste, Numerical Inversion of the Laplace-Carson Transform Applied to Homogenization of Randomly Reinforced Linear Viscoelastic Media, *Comput. Mechanics*, 40, No. 4, 2007, pp. 771-789.

Modeling Curvilinear Motion of Tracked Vehicle with the Dual-Flux Electromechanical Turning Mechanism

Dmitriy Volontsevich[1, a], Duong Sy Hiep[2]

1 – Doctor of Technical Sciences, Professor, Transport Machine Building Faculty, National Technical University "Kharkov Polytechnic Institute", Kharkov, Ukraine.

2 – Graduate student, Transport Machine Building Faculty, National Technical University "Kharkov Polytechnic Institute", Kharkov, Ukraine.

a – vdo_khpi@ukr.net

DOI **10.13140/RG.2.1.4361.8960**

Keywords: tracked vehicle, dual-flux turning mechanism, electric drive in the turning mechanism, numerical simulation.

ABSTRACT. Tens of thousands of old tracked vehicles with no ergonomic and ineffective the turning mechanisms are exploited in the world. Light multipurpose tracked transporter-tractor MTLB – is one of these machines, which is equipped with mechanical dual-flux turning mechanisms. These turning mechanisms are controlled by levers instead of a steering wheel and in the turning the part of the kinetic energy is converted to heat by friction mechanisms. This article analyzes the problems of the installation of electric drive in the mechanical dual-flux turning mechanisms of tracked vehicles. Previously, by the authors of this article were published materials, which by the analytical methods investigated the possibility of using the electric drive in the dual-flux turning mechanisms on the example of the light multipurpose tracked transporter-tractor MTLB. To solve this problem, the authors proposed an algorithm and a program that allow by numerical modeling techniques make the parametric optimization of the turning mechanisms and use them to assess their effectiveness. In contrast to the analytical determination of the trajectory of movement of the machine numerical simulation make possible to calculate trajectory considering real-slipping and skidding of caterpillar tracks. In the next publication is planned to bring the results of the comparative modeling of the entry process in the turning of light multipurpose tracked transporter-tractor MTLB with the standard mechanical and two selected scheme of the electromechanical dual-flux turning mechanisms.

Introduction. Previously, by the authors of this article were published materials, which investigated the possibility of using the electric drive in a dual-flux turning mechanisms on the example of the light multipurpose tracked transporter-tractor MTLB.

On the basis of the research it was concluded that, in carrying out the shallow modernization of the tractor transmission the installation and use of electric motors in the traction mode in mechanisms of turning at this stage of Ukrainian electric drive development is impractical. Calculations have shown that to maintain the turning speed indicators on heavy soils without mechanical branch in the turning mechanisms must be installed electric motors with capacity of at least 40 kW for each side. Installation of these motors requires installation of a much more powerful generator and more capacious batteries. As a result, the desired increase in mobility and controllability machines without a substantial increase in engine power, fuel consumption, weighting machine and its rise in price will not be possible.

Thus, it was decided to leave for further consideration two options of the use of electric drive in the dual-flux turning mechanisms:

– with one motor and the sun gears of the summation planetary rows different sides, rotating in opposite directions (Fig. 1);

– with two motors while maintaining the mechanical branch in the turning mechanisms (Fig. 2).

Mathematical models and algorithms to simulate the behavior of the tracked vehicles have been

designed with all three of the above options turning mechanisms for a detailed study of controllability of caterpillar multipurpose transporter-tractor with the proposed turning mechanisms and its comparison with the controllability of basic machine (Fig. 3).

The initial data for modeling. For modeling were used geometric, kinematic, power, weight and inertia characteristics caterpillar multipurpose transporter-tractor MT-LB [5]. Below in Tables 1 and 2 shows the numerical values of the machine parameters and of soils, that were used for all three embodiments schemes of the dual-flux turning mechanisms.

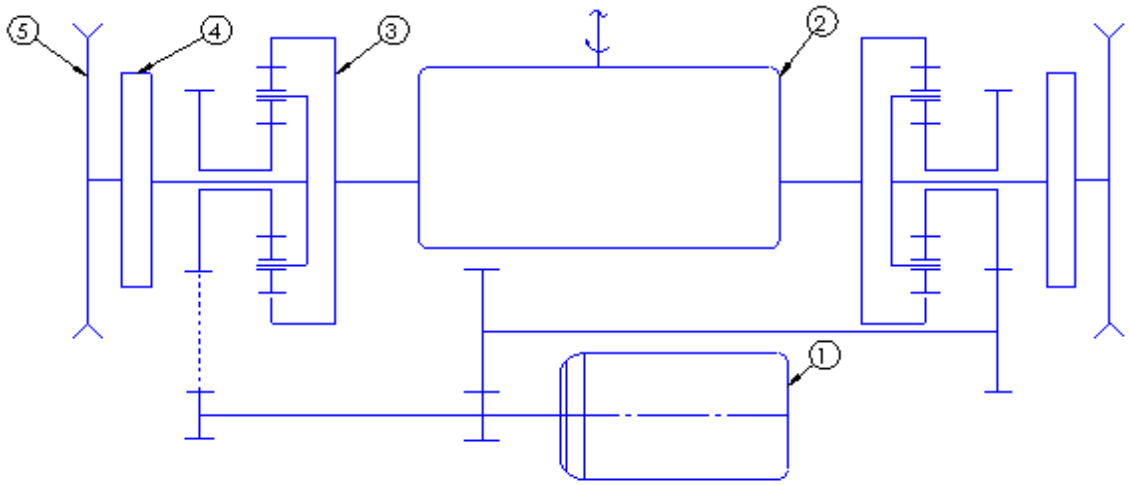


Fig. 1. Kinematic scheme of transmission with one electric motor and the sun gears of the summation planetary rows of different sides, rotating in opposite directions: 1 – Electric drive; 2 – Gearbox; 3 – Summation planetary rows; 4 – Final drives; 5 – Driving wheels

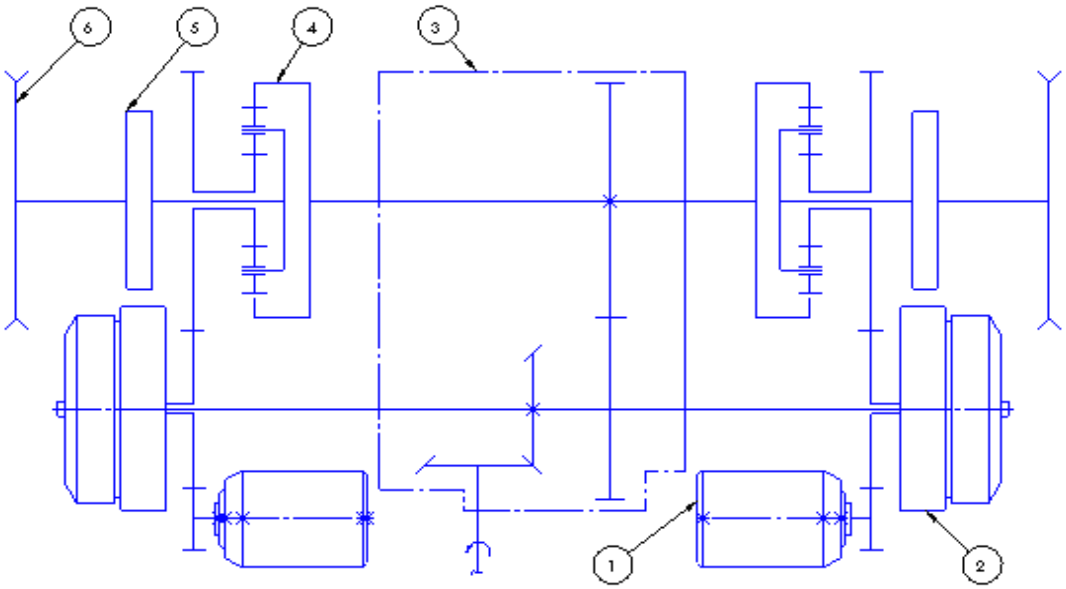


Fig. 2. Kinematic scheme of transmission with two electric motors while maintaining the mechanical branch in the turning mechanisms: 1 – Electric drives; 2 – Native turning mechanisms; 3 – Gearbox; 4 – Summation planetary rows; 5 – Final drives; 6 – Driving wheels

The overall structure of the mathematical model. Mathematical model for the study enter in the turning and curved movement of the light multipurpose tracked transporter-tractor MTLB is based on the integration of the differential equations describing the motion of the perturbed system containing 6 generalized velocities:

– the longitudinal velocity of the machine taking into account skidding (slipping) – v_X;

– the transverse velocity of the side slip of machine – v_Y;

– the angular velocity of rotation of the machine frame about a vertical axis passing through the center of mass – ω_Z;

– the angular velocity of the engine crankshaft – ω_E;

– the angular velocity of rotation of the input link of the lagging mechanism of turning – ω_1;

– the angular velocity of rotation of the input link of the more fast mechanism of turning – ω_2.

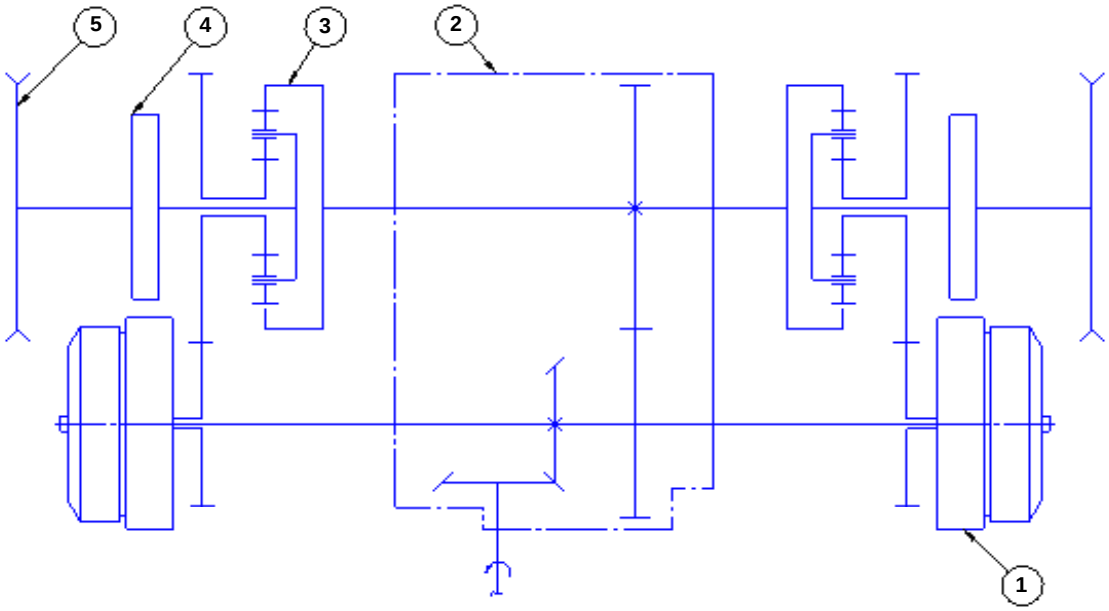


Fig. 3. Kinematic scheme of native transmission of the light multipurpose tracked transporter-tractor MTLB: 1 – Turning mechanisms; 2 – Gearbox; 3 – Summation planetary rows; 4 – Final drives; 5 – Driving wheels

For each of the generalized velocity compiled its differential equations, which are grouped in:

$$\begin{cases} \dfrac{dv_X}{dt} = \dfrac{P_{D1} + P_{D2} - P_{F1} - P_{F2}}{G_M}; \\ \dfrac{dv_Y}{dt} = \dfrac{P_Y - P_{\varphi 1} - P_{\varphi 2}}{G_M}; \\ \dfrac{d\omega_Z}{dt} = \dfrac{0{,}5B\left(P_{D2} - P_{D1}\right) - M_{RR}}{I_Z}; \\ \dfrac{d\omega_E}{dt} = \dfrac{M_E - M_R}{I_E + I_{TR}}; \\ \dfrac{d\omega_1}{dt} = \dfrac{M_{MR1} - M_{R1}}{I_{MR}}; \\ \dfrac{d\omega_2}{dt} = \dfrac{M_{MR2} - M_{R2}}{I_{MR}}. \end{cases} \quad (1)$$

Table 1. Machine parameters

№	Parameter	Value
1.	Machine weight, t	12,5
2.	Engine's type	YaMZ-238V
3.	Engine power, kW (hp)	176 (240)
4.	Engine speed at maximum power, rev/min	2100
5.	Maximum torque, Nm (kgm)	883 (90)
6.	Engine speed at maximum torque mode, rev/min	1250 – 1450
7.	The gear ratio of the input bevel gear	0,905
8.	Gearbox ratio: I II III IV V VI	∞ 3,125 1,500 0,833 0,585 0,435
9.	The internal gear ratio of the summation planetary rows	– 2,41
10.	Gear ratio of final drive	6
11.	The radius of the drive wheel, m	0,265
12.	The width of machines on the track centers, m	2,5
13.	The support caterpillar length, m	3,7
14.	The height of the center of mass, m	1,1
15.	Moment of inertia of the engine with flywheel, kgm^2	4,61
16.	The moment of inertia of the machine in rotation about a vertical axis passing through the center of mass, kgm^2	50000

Table 2. Soils parameters

№	Soil type (road)	f	φ	μ_{max}
1.	Turfy dry clay soil (moisture content <8%)	0,08	0.9	0,9
2.	Dry dirt road on the loam	0,07	0,8	0,8
3.	Plowing on the loam	0,1	0,7	0,7
4.	Wet road on the loam	0,125	0,6	0,35
5.	Snow loose	0,25	0,3	0,3

Here variables are:

P_{D1} and P_{D2} – traction force (braking) on the lagging and more fast sides taking into account the sign, calculated from the coefficients of slipping or skidding;

P_{F1} and P_{F2} – forces of resistance to movement on the lagging and more fast sides based on the redistribution of the normal reactions between the sides in the turning due to centrifugal force P_Y;

P_Y – the centrifugal force generated by the curvilinear motion of the machine;

$P_{\varphi 1}$ and $P_{\varphi 2}$ – cohesion forces caterpillar mover with the ground in the transverse direction (value $P_Y - P_{\varphi 1} - P_{\varphi 2}$ can be positive or zero – the friction force can not be the driving);

M_{RR} – the moment of resistance turning, which depends on the geometrical characteristics of the machine, its weight, the radius of turning and soil characteristics (road);

M_E – engine torque;

M_R – moment of movement resistance reduced to the engine shaft (which depends on P_{F1} and P_{F2});

M_{MR1} and M_{MR2} – torques on the input links of the turning mechanisms of lagging and more fast sides. They depend on the torque in the friction clutches or in the friction brakes for the base transmission and they depend on the torque on the motors of the turning mechanisms if they have electric drive.

M_{R1} and M_{R2} – torques of movement resistance reduced to the input links of the turning mechanisms of lagging and more fast sides, which depends on the P_{F1} и P_{F2}.

Constant values (constants):

G_M – weight (gravity) of the machine;

B – width of machines on the track centers;

I_Z – moment of inertia of the machine in rotation about a vertical axis passing through the center of mass;

I_E – moment of inertia of the engine with flywheel;

I_{TR} – moment of inertia of the rotating parts of the transmission and chassis, reduced to the crankshaft of the engine;

I_{MR} – moment of inertia of the turning mechanism, reduced to its input link.

Assumptions and simplifications. The movement of the machine is considered on level ground.

The coordinate system associated with the machine has the beginning in the center of mass of the machine and the axis: ***OX*** – forward, ***OY*** – to the left, ***OZ*** – up.

Entrance to the turning and movement in turning is considered in a selected gear ratio without switching in the gearbox.

The engine is considered working on the external characteristic with the full fuel feed.

Transmission work is only considered at a high speed range of the presence of two power flows through the transmission and the turning mechanism.

Malleable shafts and other drivetrain components are not taken into account.

When the command to transfer frictional controls to the ON state in the base transmission is assumed that the friction torque increases linearly from zero to a maximum value of 0.5 s.

The turning is always seen in the same direction (to the left) and, accordingly, is not considered right and left side, and more fast and a lagging side.

The model of diesel engine YaMZ-238V. Since the operation of the engine is considered only at full fuel feed, the engine simulation is made possible by the Leiderman's formula:

$$N_e = N_{e\max}\left[a\frac{\omega}{\omega_N} + b\left(\frac{\omega}{\omega_N}\right)^2 - c\left(\frac{\omega}{\omega_N}\right)^3\right], \quad (2)$$

where $N_{e\max}$ =176 kWt – the maximum effective power of the engine when the crankshaft rotational speed $\omega_N = \frac{\pi \cdot 2100}{30} = 219{,}9\,\text{s}^{-1}$;

$a = 0{,}49;\ b = 1{,}7;\ c = 1{,}19$ – coefficients for the Leiderman's formula YAMZ-238V;

ω – crankshaft rotational speed. In the area of regulatory power characteristics decreases linearly from $N_{e\max}$ to 0 for $\omega = 240\,\text{s}^{-1}$.

Accordingly, it is possible to write the formula for the transition to the free torque:

$$M_E = \frac{N_e - a_\Delta\left(\frac{\omega}{\omega_N}\right)^3 N_{e\max}}{\omega},$$

where $a_\Delta = 0{,}14$ – power loss factor for fan cooling system.

To simulate the behavior of the engine at varying load **module "engine"** has been developed, input parameter for which each step of the integration is the current value of the rotation speed of the engine crankshaft ω_E.

The output parameter is the actual value of the free torque M_E, which is supplied from the engine into the transmission.

Model of curvilinear motion of a tracked vehicle on the terrain. To model the curvilinear motion of a tracked vehicle on the terrain were used depending listed in [6].

For this purpose, the module "Rotate" has been developed, input parameters for which on each step of the integration are the current values of the following generalized velocities:

– the longitudinal velocity of the machine taking into account skidding (slipping) – v_X;

– the transverse velocity of the side slip of machine – v_Y;

– the angular velocity of rotation of the machine frame about a vertical axis passing through the center of mass – ω_Z;

– the angular velocity of the engine crankshaft – ω_E;

– the angular velocity of rotation of the input link of the lagging mechanism of turning – ω_1;

– the angular velocity of rotation of the input link of the more fast mechanism of turning – ω_2,

as well as the gear ratio in the gearbox and characteristics road (soil) in which make machine movement.

Given the linear v_X and angular ω_Z velocities of the body of the machine calculates the actual speed of longitudinal movement of the chassis for lagging and for more fast sides relative to the support surface:

$$V_1 = v_X - \omega_Z \frac{B}{2} \text{ and } V_2 = v_X + \omega_Z \frac{B}{2}.$$

Further, for $\omega_Z \neq 0$ determined a central turning radius and turning radius on the sides:

$$R_C = \frac{v_X}{\omega_Z},\ R_1 = \frac{v_X}{\omega_Z} - \frac{B}{2} \text{ and } R_2 = \frac{v_X}{\omega_Z} + \frac{B}{2}.$$

Knowing the turning radius of the machine, we can determine the actual drag coefficient of the turning μ on a given road (terrain) and the centrifugal force P_Y generated by turning:

$$\mu = \frac{\mu_{\max}}{0{,}85 + 0{,}15 \cdot R_2 / B},$$

where $\mu_{\max}$ – maximum drag coefficient of the turning corresponding to turn around stopped caterpillars.

$$P_Y = \frac{G_M v_X^2}{R_C}.$$

Knowing the centrifugal force P_Y and the actual drag coefficient of the turning μ we determine the absolute χ and relative χ_0 bias of the pole of turning:

$$\chi = \frac{P_Y}{\mu G_M} \text{ and } \chi_0 = \frac{2\chi}{L}.$$

If we get $\chi_0 > 1$, then we equate it to $\chi_0 = 1$ and recalculate the actual drag coefficient of the turning μ:

$$\mu = \frac{P_Y}{G_M}.$$

When finally determined the actual drag coefficient of the turning, we find the torque of resistance to turning:

$$M_{RR} = 0{,}25\mu G_M L\left(1+\chi_0^2\right).$$

In view of the rotational speeds of the engine crankshaft ω_E and of the input links of the mechanism of turning ω_1 and ω_2, and the gear ratio of transmission we determine the drive wheels speed for lagging and for more fast sides:

$$\omega_{DW1} = \frac{\left(\omega_1 / i_{MR} + (\omega_E k_S)/(i_{GB} i_{IG})\right)/(k_S+1)}{i_{FD}};$$

$$\omega_{DW2} = \frac{\left(\omega_2 / i_{MR} + (\omega_E k_S)/(i_{GB} i_{IG})\right)/(k_S+1)}{i_{FD}}.$$

Here: k_S – internal gear ratio of the summation planetary rows; i_{GB} – the gear ratio of the gearbox at the selected level; i_{IG} – the gear ratio of the input bevel gear; i_{MR} – the gear ratio of the turning mechanism from the input link to the sun gear of the summing planetary row; i_{FD} – gear ratio of final drive.

Accordingly, the speed of rewinding caterpillar tracks on the sides will be:

$$V_{T1} = \omega_{DW1} R_{DW} \text{ and } V_{T2} = \omega_{DW2} R_{DW},$$

where R_{DW} – drive wheel radius.

Knowing the speed of rewinding the caterpillar tracks, we find the efficiency of caterpillar tracks separately on the sides η_{cat1} and η_{cat2} as well as the coefficients of slipping (skidding) σ_1 and σ_2:

$$\eta_{cat1} = 0{,}95 - 0{,}018 \cdot V_{T1};\ \eta_{cat2} = 0{,}95 - 0{,}018 \cdot V_{T2};\ \sigma_1 = \frac{V_{T1} - V_1}{V_{T1}} \text{ and } \sigma_2 = \frac{V_{T2} - V_2}{V_{T2}}.$$

Knowing the centrifugal force P_Y, we define a longitudinal component of the centrifugal force P_X and the actual normal reaction under the caterpillar tracks N_1 and N_2, taking into account the redistribution of weight due to a lateral centrifugal force P_Y:

$$P_X = \frac{P_Y \chi}{R_C};\ N_1 = \frac{G_M}{2} - \frac{P_Y h_C}{B} \text{ and } N_2 = \frac{G_M}{2} + \frac{P_Y h_C}{B}.$$

Here h_C – the height of the center masses.

In the process of calculating the values N_1 and N_2 need to be monitored, to satisfy the conditions $N_1 \geq 0$ and $N_2 \leq G_M$ that are responsible for the lack of overturn machine.

Knowing the actual normal reaction under the caterpillar tracks N_1 and N_2, to determine the maximum forces of adhesion caterpillar mover with road (terrain) $P_{\varphi 1}$, $P_{\varphi 2}$ and total resistance to movement P_{F1}, P_{F2} under the boards:

$$P_{\varphi 1} = N_1 \varphi;\ P_{\varphi 2} = N_2 \varphi;\ P_{F1} = N_1 f + \frac{0{,}65 F_{\max} v_X^2 + P_X}{2} \text{ and } P_{F2} = N_2 f + \frac{0{,}65 F_{\max} v_X^2 + P_X}{2}.$$

Here, φ – the coefficient of adhesion caterpillar mover with road (terrain); f – coefficient of resistance to movement; $F_{\max}$ – the maximum cross-sectional area of the machine.

Knowing the factors slipping (skidding) σ_1, σ_2, we can determine the traction force (braking) on the lagging P_{D1} and on the more fast P_{D2} boards with sign:

$$P_{D1} = \frac{\sigma_1}{0{,}3} R_{\varphi 1}, \text{ if } \sigma_1 > 0{,}3, \text{ then } P_{D1} = R_{\varphi 1}; \text{ if } \sigma_1 < -0{,}3, \text{ then } P_{D1} = -R_{\varphi 1};$$

$$P_{D2} = \frac{\sigma_2}{0{,}3} R_{\varphi 2}, \text{ if } \sigma_2 > 0{,}3, \text{ then } P_{D2} = R_{\varphi 2}; \text{ if } \sigma_2 < -0{,}3, \text{ then } P_{D2} = -R_{\varphi 2}.$$

Knowing traction force (braking) on the lagging P_{D1} and on the more fast P_{D2} boards, define the torques of engine load M_R and the turning mechanisms M_{R1}, M_{R2}:

$$M_R = \frac{M_{GB} + M_{FMR1} + M_{FMR2}}{i_{IG} \eta_{IG}}. \quad (3)$$

Here, i_{IG} and η_{IG} – gear ratio and efficiency of the input bevel gear;

M_{FMR1} and M_{FMR2} – torques on the input links of the lagging and of the more fast turning mechanisms, depending on the friction torque on the friction clutches of the base transmission ($M_{FMR1} = M_{FMR2} = 0$ for the turning mechanism with one electric motor);

M_{GB} – load torque on the input shaft of the gearbox, is given by:

$$M_{GB} = \frac{2(P_{D1} + P_{D2}) R_{DW} k_S}{i_{FD} i_{GB} (k_S + 1)(\eta_{cat1} + \eta_{cat2}) \eta_{FD} \eta_S \eta_{GB}}, \text{ if } P_{D2} > P_{D1} > 0 \text{ and}$$

$$M_{GB} = \frac{R_{DW} k_S}{i_{FD} i_{GB} (k_S + 1)} \left(\frac{P_{D2}}{\eta_{cat2} \eta_{FD} \eta_S \eta_{GB}} + P_{D1} \eta_{cat1} \eta_{FD} \eta_S \eta_{GB} \right), \text{ if } P_{D2} > 0 \text{ and } P_{D1} \le 0.$$

The load on the turning mechanisms M_{R1}, M_{R2} is calculated according to the formulas

$$M_{R2} = \frac{P_{D2} R_{DW}}{i_{FD} i_{GB} (k_S + 1) i_{MR} \eta_{cat2} \eta_{FD} \eta_S \eta_{MR}};$$

$$M_{R1} = \frac{P_{D1} R_{DW}}{i_{FD} i_{GB} (k_S + 1) i_{MR} \eta_{cat1} \eta_{FD} \eta_S \eta_{MR}}, \text{ if } P_{D1} > 0 \text{ and}$$

$$M_{R1} = \frac{P_{D1} R_{DW} \eta_{cat1} \eta_{FD} \eta_S \eta_{MR}}{i_{FD} i_{GB} (k_S + 1) i_{MR}}, \text{ if } P_{D1} \le 0.$$

As a result, the output parameters of the module are:

P_{D1} and P_{D2} – the traction force (braking) on the lagging and on the more fast boards with sign;

P_{F1} and P_{F2} – the forces of total resistance to movement on the lagging and on the more fast boards;

P_Y – the centrifugal force, generated by the curvilinear motion of the machine;

$P_{\varphi 1}$ and $P_{\varphi 2}$ – the maximum forces of adhesion caterpillar mover with road (terrain);

M_{RR} – torque resistance to the turning;

M_R – torque resistance to the motion, is reduced to the crank shaft of the engine;

M_{R1} and M_{R2} – torques resistance to the motion, is reduced to the input links of the turning mechanisms of the lagging and of the more fast boards.

Model of the dual-flux turning mechanism.

Three modules have been developed to simulate the operation of a dual-flux turning mechanisms:

– "The turning mechanism with one electric motor and the sun gears of the summation planetary rows of different sides, rotating in opposite directions" (fig. 1);
– "The turning mechanism with two electric motors operating in braking mode while maintaining the mechanical branch in the turning mechanisms" (fig. 2);
– "The mechanical turning mechanism (base machine)" (fig. 3).

The input parameters for all modules at each step of the integration are the current values of the generalized velocities of rotation of the input links of the lagging ω_1 and more fast ω_2 the turning mechanisms, as well as the angular velocity of the engine crankshaft ω_E for all modules except the first (fig. 1).

For the mechanical turning mechanism and the turning mechanism with two electric motors on more fast board the friction clutch of the turning mechanism is always enabled. This allows us to eliminate the last equation of the system (1) and to express the angular velocity of rotation of the input link of the more fast turning mechanism ω_2 through the angular velocity of the engine crankshaft ω_E:

$$\omega_2 = \frac{\omega_E}{i_{IG}}.$$

When calculating the load on the engine (3) value M_{FMR2} of friction torque determined by the load torque of the friction clutch considering the sign $M_{FMR2} = M_{R2}$. If these schemes considered the linear motion from the system (1) is deleted and the penultimate equation and $\omega_1 = \omega_2$ and the

respectively $M_{FMR1} = M_{R1}$. When turning with a free radius for the mechanical turning mechanism of the lagging board the friction clutch is switched off $M_{FMR1} = 0$ and the angular velocity ω_1 is determined by integration of the penultimate equation of the system (1).

For the mechanical turning mechanisms when developing fixed turning radius on the lagging board after the clutch is turned off the brake is turned on. Within 0.5 seconds the negative friction torque M_{MR1} increases linearly in absolute value to its maximum value and is kept so until $\omega_1 = 0$. After this, the penultimate equation of the system (1) is excluded from the integration process.

Asynchronous electric motor is switched as a generator for the turning mechanisms with two electric motors on the lagging board. In this case $M_{FMR1} = 0$ and $M_{MR1} = M_{EM1} < 0$. This mode continues until the $\omega_1 = 0$. After this the turning mechanism is placed on the friction brake and the penultimate equation of the system (1) is excluded from the integration process.

For the turning mechanism with one electric motor and the sun gears of the summation planetary rows of different sides, rotating in opposite directions (fig. 1) the last two equations are replaced by one:

$$\frac{d\omega_{EM}}{dt} = \frac{M_{EM} - M_{R2} + M_{R1}}{I^*_{MR}}.$$

Here I^*_{MR} – moment of inertia of the turning mechanism comprising two boards and one electric motor is reduced to the electric motor shaft.

The torque of asynchronous motor M_{EM} (fig. 4, [7]) with frequency adjustment (fig. 5, [7]) determined depending on the speed of its shaft by a generalized characterization (fig. 6).

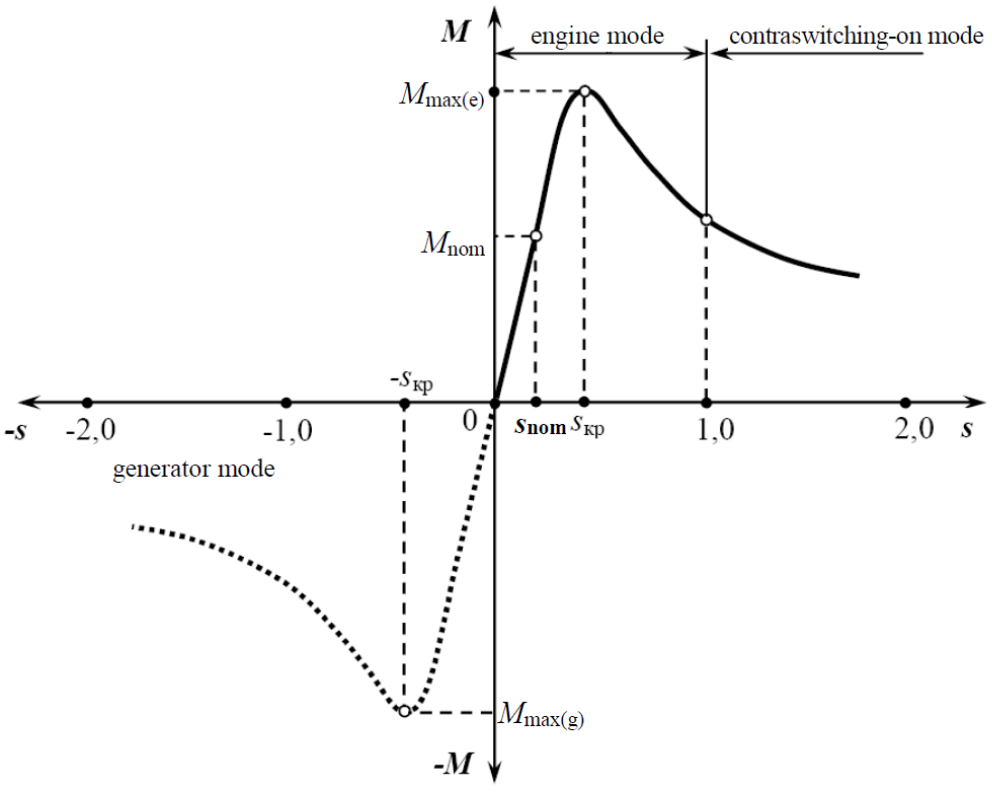


Fig. 4. Mechanical characteristics of asynchronous motor, depending on the slipping s

Asynchronous motor, developed to drive the motor-wheel armored personnel carrier (State enterprise "Kharkov Machine Building Design Bureau named after A.A. Morozov") with a nominal power of 45 kW at a shaft speed of 3150 rev / min (330 s^{-1}) was adopted as a basis for calculations. Maximum torque in the traction mode of the engine was limited by the current force and overheating of the value of 230 Nm. An electric motor is switching to constant power mode when $\omega_X = 195{,}6\ s^{-1}$. The required reduction in the basic power an electric motor is achieved fold reduction in the axial dimension of the engine, in which only changed in proportion to the torque without changing the speed characteristics.

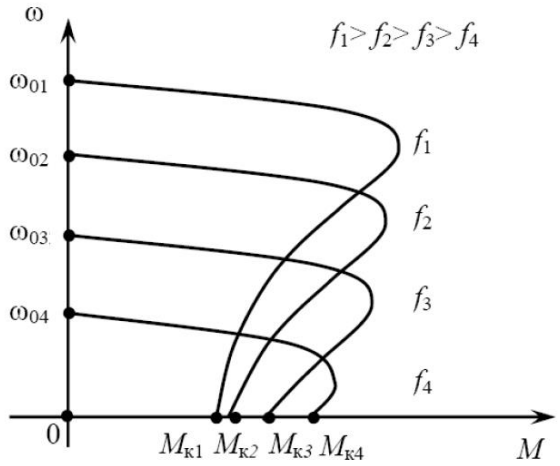


Fig. 5. Mechanical characteristics of the asynchronous motor with frequency speed control

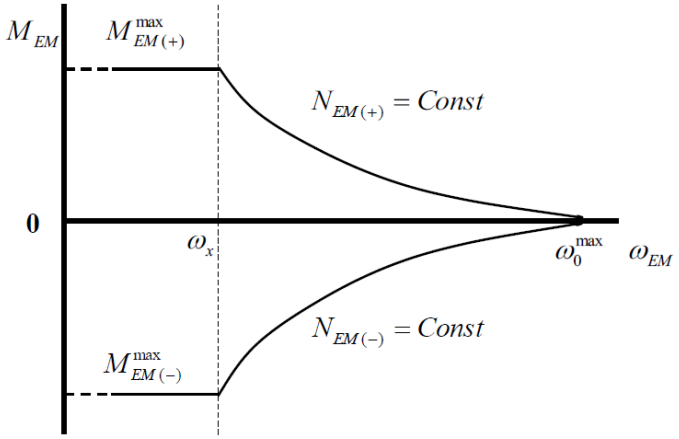


Fig. 6. The dependence of the traction (braking) of the electric motor of the turning mechanism from its speed of rotation of the armature with the management system

Central integration unit. The central integrating unit is a classic solver module for integration of differential equations by the Runge-Kutta method with constant or variable pitch. In this module, formed the right parts of the differential equations describing the behavior of dynamic system considering changes in its structure in the process. In the module following initial data is entered:

– counting time;

– the integration step in fractions of a second and the desired accuracy;

– a list of print parameters to file of the calculate results;

– the type of the dual-flux turning mechanism (one of the three according to fig. 1–3);

– mode of transmission (number of the gear);

– the type of road (terrain), on which machine is moving;

– the initial conditions for each of the differential equations;

– sequence diagram switching of the turning mechanisms.

From the central unit in the desired sequence caused all the previously described blocks for the correct formation of the right parts of differential equations. Then, considering accepted initial conditions or the results of the previous step the differential equations is integrating and the account of the results is written to disc.

Summary. As a result of this work was to create a tool with which on the example of light multipurpose tracked transporter-tractor MTLB became possible to simulate the curvilinear motion of the machine on a horizontal surface with different characteristics and different schemes of the dual-flux turning mechanisms.

In contrast to the analytical determination of the trajectory of movement of the machine numerical simulation make possible to calculate trajectory considering real-slipping and skidding of caterpillar tracks.

In the next publication is planned to bring the results of the comparative modeling of the entry process in the turning of light multipurpose tracked transporter-tractor MTLB with the standard mechanical and two selected scheme of the electromechanical dual-flux turning mechanisms.

References

[1] Volontsevich D.O., Medvedev N.G., Duong Sy Hiep. Estimation of the required power of the dual-flux turning mechanism of a tracked vehicle. // Visnyk NTU "KhPI", Zbirnyk naukovykh prats'. Seriya: Transportne mashynobuduvannya. – Kharkiv: NTU «KhPI», – 2014. –№22(1065). – P. 73–83.

[2] Volontsevich D.O., Medvedev N.G., Duong Sy Hiep. Determination of mechanical parameters of the electric dual-flux turning mechanism of a tracked vehicle. // Mekhanika ta mashynobuduvannya. – 2014. – №1. – P. 51 – 57.

[3] Volontsevich D.O., Duong Sy Hiep. Justification of the choice the drive electric motor for the dual-flux electromechanical turning mechanism of a tracked vehicle // Visnyk NTU "KhPI", Zbirnyk naukovykh prats'. Seriya: Transportne mashynobuduvannya. – Kharkiv: NTU «KhPI», 2015. – № 43 (1152). – P. 151-156.

[4] Duong Sy Hiep, Volontsevich Dmitriy. Research of possibility of electromechanical turning mechanism creating for tracked vehicle as first step to hybrid transmission // Machines, technologies, materials: International journal. (Scientific technical union of mechanical engineering: Sofia, Bulgaria). – 2015. – №9. – P. 55-59.

[5] Light multipurpose tracked transporter-tractor: Technical description / Under general editorship of A.F. Belousov // Voennoe izdatelstvo Ministerstva oboronyi SSSR. – 1969. – 483 pp.

[6] Zabavnikov N.A. Fundamentals of the theory of transport tracked vehicles. –M.: Mashinostroenie, 1975. –448 pp.

[7] Hnatov A.V., Arhun Shch.V., Trunova I.S. Theory of electric drive vehicles: Textbook / – Kh.: KhNADU, 2015. – 292 pp.

A Fast Algorithm to Solve Nonlinear Hypersingular Integral Equations Arising in a Crack Problem

M.R. Capobianco[1], G. Criscuolo[2,a]

1 – Istituto per le Applicazioni del Calcolo "Mauro Picone" - CNR, Sede di Napoli, Via Pietro Castellino 111, 80131 Napoli, Italy e-mail: mariarosaria.capobianco@cnr.it

2 – Dipartimento di Matematica e Applicazioni, Università degli Studi di Napoli ``Federico II", Complesso Monte Sant'Angelo, Edificio T, Via Cintia, 80126 Napoli, Italy

a – giuliana.criscuolo@unina.it



DOI **10.13140/RG.2.1.5051.5605**

Keywords: nonlinear hypersingular integral equation, collocation method, Newton method, GMRES algorithm.

ABSTRACT. A fast algorithm related to the generalized minimal residual algorithm (GMRES) is proposed to approximate solution of a nonlinear hypersingular integral equation arising in a crack problem. At first, a collocation method is proposed and developed in weighted Sobolev space. Then, the Newton-Kantorovjch method is used for solving the obtained system of nonlinear equations.

Introduction. In several applications in mechanics, electrodynamics, aerodynamics, we have to deal with hypersingular integral equations (HSIEs). Therefore, an active development of numerical methods for solving such equations is very interesting in modern numerical analysis.

Among the numerous works devoted to developing efficient numerical schemes for approximate solution of singular and hypersingular integral equations, we mention [2]-[11], [15], and the references cited therein. In particular, many problems in fracture mechanics give rise to the nonlinear hypersingular integral equations (see for example [17], [19], [21]). Nevertheless, approximate solution methods for these latter equations are less elaborated although their increasing interest. Among the papers devoted to these approximate methods we recall [3], [4], [7], [9], [16], [19]. The problem to solve $\nabla^2 u = 0$ inside a bounded region Ω with a nonlinear boundary condition, $\partial u/\partial n + g(x;u) = f(x)$ for all x on the boundary of Ω, is reduced in [16] to a hypersingular boundary integral equation using the normal derivative of the standard Green representation. This nonlinear integral equation is solved using Newton's method and a spline-based Galerkin method. A collocation method for approximate solution of nonlinear hypersingular integro-differential equation

$$\sum_{k=0}^{m} a_k\left(t, x^{(k)}(t)\right) + \sum_{k=0}^{l} \int_{\gamma} \frac{h_k(t,\tau,x^{(k)}(\tau))}{(\tau - t)^p} d\tau = f(t), \qquad p\epsilon\{1,2,\dots\},$$

With

$$\int_{\gamma} x^{(k)}(t) t^{-k-1}\, dt = 0, \qquad k = 0,1,\dots,\nu, \qquad \nu = \max\{m,l\},$$

is developed and justified in [4]. Here γ is a unit ball with center at the origin, Collocation with piecewise constant functions has been examined in [3] for nonlinear hypersingular equations as

$$a\big(t,x(t)\big)+\int_{-1}^{1}\frac{h\big(t,x(\tau)\big)}{(\tau-t)^2}d\tau=f(t).$$

A numerical approach based on an iterative technique and Sinc quadrature has been proposed in [19] to estimate a solution of nonlinear functional integro-differential equations with an integral boundary condition. In [7], [9] an approximate method for solving a hypersingular of the Prandtl type is considered

$$-\frac{\varepsilon}{\pi}\int_{-1}^{1}\frac{v(t)}{(t-x)^2}dt+\gamma\big(x,v(x)\big)=f(x),\quad |x|<1, \tag{1}$$

where $0<\varepsilon\leq 1$, and $v(x)$ is an unknown function satisfying some boundary conditions.

The collocation method with Chebyshev nodes of the second kind was developed for approximate solution of (1). Its justification was given in the Sobolev space. The Newton-Kantorovich method was used for solving the obtained system of nonlinear equations. In order to compute efficiently a solution for (1) in this paper we use the results of [7] and [9] to realize a fast algorithm related to GMRES (generalized minimal residual algorithm). The outline of the paper is as follows. In the next section, starting from a significant application of hypersingular integral equations, we collect the results on the mapping properties needed here for the involved operator. In Section 3 the collocation and the Newton-Kantorovich method and respective results from [7], [9] are presented, which are necessary for designing and investigating the fast algorithm studied in Section 4. Finally, in Section 5 we present some numerical results confirming the theoretical ones.

Nonlinear HSIEs for formulation of bridged straight crack.

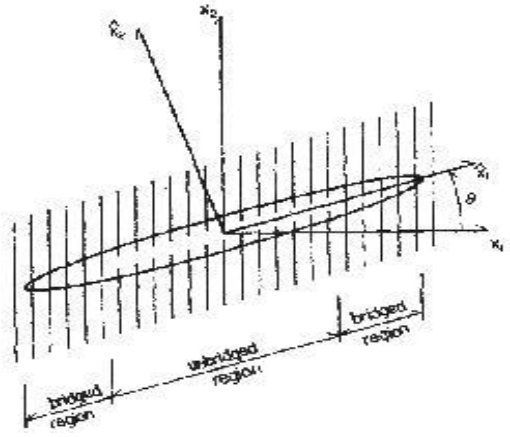


Fig. 1. A partially bridged straight crack in a unidirectionally fiber reinforced composite

Figure 1 shows a partially bridged straight crack along the $\hat{x}_1$-axis which makes an angle θ with the x_1-axis normal to the plane of the material symmetry. We assume that the bridging forces, $\hat{p}_i$, i=1,2, are explicit functions of $\hat{x}_1$ and of the crack opening displacement $\hat{u}_i$, i=1,2, i.e.

$$\hat{p}_i(\hat{x}_1)=K_0 f_i\big(\hat{x}_1,\hat{u}_1(\hat{x}_1),\hat{u}_2(\hat{x}_1)\big),\qquad i=1,2.$$

were K_0 is a dimensional parameter to normalize the bridging forces, and f_i, i=1,2, are dimensionless functions representing the dependence of the stresses in the bridging fibers or ligaments on the location and on the crack opening displacement.

By a suitable choice of these functions, a broad class of partially or fully bridged crack problems in composites can be examined. In particular, we consider the specific cases of possible bridging force variation

$$\hat{p}_i(\hat{x}_1) = -K_0 g(\hat{x}_1)\hat{u}_i(\hat{x}_1), \qquad i = 1,2, \tag{2}$$

$$\hat{p}_i(\hat{x}_1) = -K_0 g_i(\hat{x}_1)\sqrt{\hat{u}(\hat{x}_1)}, \qquad i = 1,2, \qquad \hat{u} = \sqrt{\hat{u}_{1+}^2 \hat{u}_2^2}, \tag{3}$$

In both cases, by a suitable choice of the function g or g_i, a large number of interesting problems can be solved. If (2) is true then the relate crack problems can be formulated by a linear HSIE. On the other hand, for unidirectionally fiber reinforced ceramics with continuous fibers, an estimate of the effective bridging forces suggests a square root relation between the crack opening displacement and the bridging forces. In this case the equilibrium equation can rewritten as

$$-\int_{-1}^{1} \frac{v(\xi)}{(\xi-\chi)^2} d\xi + \sqrt{l}\Lambda(\chi)\sqrt{v(\chi)} = \Psi(\chi), \qquad \chi \in (-1,1), \tag{4}$$

where $\chi = \hat{x}_1/c, v(\chi) = \hat{u}_2(\hat{x}_1), l = c/c_0, c_0 = E_m/K_0, c$ being the half-width of the crack.

Here E_mis the Young's modulus of the matrix material of unidirectionally reinforce composite. Further, the function Ψ depends on a possible variable traction, while the function Λ is related to $g_i, i = 1,2$ in (3). In (4) the integral is to be understood in the sense of the Hadamard finite part. Although the concept of finite-part or hypersingular integral goes back to Hadamard, in the last years the number of papers devoted to hypersingular boundary integral equations, published mainly in engineering journals, has suddenly increased. Suitable numerical methods for computing such integrals can be found for instance in [12-14]. The parameter l defines the magnitude of the nonlinear term in (4): for cracks of about $200\mu m$, $l < 1$for SiC/glass ceramics; $l > 1$ for carbon/glass ceramics. When the crack is of order of a millimeter, then $l \gg 1$.

The solvability of a nonlinear HSIE. In the sequel we will refer to the integral equation (1) assuming that the unknown function v satisfies the boundary conditions $v(\pm 1) = 0$. In agreement with previous remarks, this type of strongly integral equations can be used effectively to model problems in fracture mechanics. Assuming that the solution has an endpoint behavior of the form $\varphi(x) = \sqrt{1-x^2}$, it is convenient to represent $v(x)$ as $v(x) = \varphi(x)u(x)$. Thus, the integral equation in (1) can be rewritten as the following equation

$$-\frac{\varepsilon}{\pi}\int_{-1}^{1} \frac{\varphi(t)u(t)}{(t-x)^2} dt + \gamma\big(x, \varphi(x)u(x)\big) = f(x), \qquad |x| < 1, \tag{5}$$

where $u(x)$ is the unknown function. We are interested in the class of problems for which $\gamma(x, v)$ is a monotone function with respect to v, i.e.

$$[v_1 - v_2][\gamma(x, v_1) - \gamma(x, v_2)] \leq 0, \qquad |x| \leq 1, \qquad v_1, v_2 \in \mathbb{R}.$$

As examples, in the literature $\gamma(x,v)$ is chosen as follows

$$\gamma(x,v)=\Gamma(x)v, \qquad |x|\le 1,\ v\in\mathbb{R},$$

And

$$\gamma(x,v)=\Gamma(x)\sqrt{|v|}sgn(v), \qquad |x|\le 1, \qquad v\in\mathbb{R},$$

where $\Gamma(x)>0, |x|\le 1$. Both cases occur in the analysis of relatively long crack in unidirectionally reinforced ceramics (cfr. (2), (3)). By p_n^{φ} we denote the normalized Chebyshev polynomial of the second kind

$$p_n^{\varphi}(\cos s)=\sqrt{\frac{2}{\pi}}\frac{sin(n+1)s}{\sin s}, \qquad n=0,1,\dots,$$

and by $\boldsymbol{L}_{\varphi}^2$ the real Hilbert space of all square integrable functions u: $(-1,1)\to\mathbb{R}$ with respect to the weight function φ equipped with the inner product

$$<u,v>_{\varphi}:=\int_{-1}^{1}u(x)v(x)\varphi(x)dx=\sum_{n=0}^{\infty}<u,p_n^{\varphi}>_{\varphi}<v,p_n^{\varphi}>_{\varphi}, \qquad u,v\in\boldsymbol{L}_{\varphi}^2.$$

We consider equation (5) in the pair $\boldsymbol{X}\to\boldsymbol{X}^*$ of the real Banach space $\boldsymbol{X}=\boldsymbol{L}_{\varphi}^{2,\frac{1}{2}}$and its dual space $\boldsymbol{X}^*=\boldsymbol{L}_{\varphi}^{2,-\frac{1}{2}}$with respect to the dual product

$$<u,v>=<u,v>_{\varphi}=\sum_{n=0}^{\infty}<u,p_n^{\varphi}>_{\varphi}<v,p_n^{\varphi}>_{\varphi}, \qquad u\in\boldsymbol{X},v\in\boldsymbol{X}^*,$$

where, for $s\ge 0,\boldsymbol{L}_{\varphi}^{2,s}$ is the subspace of $\boldsymbol{L}_{\varphi}^2$ of all $u\in\ \boldsymbol{L}_{\varphi}^2$ for which

$$\|\ u\ \|_{\varphi,s}=\sqrt{\sum_{n=0}^{\infty}(n+1)^{2s}\left|<u,p_n^{\varphi}>\right|^2}<\infty,$$

and $\boldsymbol{L}_{\varphi}^{2,-s}:=(\boldsymbol{L}_{\varphi}^{2,s})^*$. The space $\boldsymbol{L}_{\varphi}^{2,s}$ is equipped with the inner product

$$< u, v >_{\varphi} := \sum_{n=0}^{\infty} (n+1)^{2s} < u, p_n^{\varphi} >_{\varphi} < v, p_n^{\varphi} >_{\varphi} , \qquad u, v \in \boldsymbol{L}_{\varphi}^{2,s}.$$

If we define the operators

$$(Vu)(x) := -\frac{1}{\pi} \int_{-1}^{1} \frac{\varphi(y)u(y)}{(y-x)^2} dy = -\frac{1}{\pi} \frac{d}{dx} \int_{-1}^{1} \frac{\varphi(y)u(y)}{y-x} dy,$$

$$(Fu)(x) := \gamma\big(x, \varphi(x)u(x)\big),$$

$$Au := \varepsilon Vu + Fu,$$

we can rewrite equation (5) in the equivalent operator form

$$Au = f.$$

We remark that the hypersingular operator $V: \boldsymbol{L}_{\varphi}^{2,\frac{1}{2}} \to \boldsymbol{L}_{\varphi}^{2,-\frac{1}{2}}$ is an isometrical isomorphism satisfying

$$Vu = \sum_{n=0}^{\infty} (1+n) < u, p_n^{\varphi} >_{\varphi} p_n^{\varphi} ,$$

(see [6]). In particular,

$$Vp_n^{\varphi} = (1+n)p_n^{\varphi}, \qquad n = 0,1, \dots \dots \dots (invariance\ property).$$

With respect to the function $\gamma: [-1,1] \times \mathbb{R} \to \mathbb{R}$, we can assume

a) $[g_1 - g_2][\gamma(x, g_1) - \gamma(x, g_2)] \geq 0, \qquad |x| \leq 1, \quad g_1, g_2 \in \mathbb{R};$

b) $|\gamma(x, g_1) - \gamma(x, g_2| \leq \nu(x)|g_1 - g_2|^{\alpha}, \qquad |x| \leq 1,\ g_1, g_2 \in \mathbb{R}, for\ some\ 0 < \alpha \leq 1,\ where|$

$$c_{\alpha} := \int_{-1}^{1} [\nu(x)]^{\frac{2}{1-\alpha}} [\varphi(x)]^{\frac{1+\alpha}{1-\alpha}} dx < \infty, \qquad 0 < \alpha < 1,$$

$$c_1 := sup_{x \in [-1,1]} \{|\nu(x)|\varphi(x)\} < \infty,$$

and $\gamma(,,0) \in \boldsymbol{L}_{\varphi.}^{2}$

Then, about the solvability of (5) we can state the following:

Theorem 1 (see Corollary 2.5 in [7]) Let the assumptions a) and b) be fulfilled. Moreover, let $f \in \boldsymbol{L}_{\varphi}^{2,s}$ for some $s > 0$. If $u \in \boldsymbol{L}_{\varphi}^{2,1}$ implies $F(u) \in \boldsymbol{L}_{\varphi}^{2,s}$, then the unique solution $u^* \in \boldsymbol{X}$ of equation (5) belongs to $\boldsymbol{L}_{\varphi}^{2,s+1}$.

Approximate solution of (5).

Collocation method. Denote by $x_{n,k}^{\varphi} = \cos\frac{k\pi}{n+1}$, $\mathrm{k} = 1,2,\dots,\mathrm{n}$, the zeros of the *n*th orthogonal Chebyshev polynomial of the second kind p_n^{φ}, Let L_n^{φ} be the Lagrange interpolation operator onto the space $\boldsymbol{X}_n$ of all algebraic polynomials of degree less than *n*, with respect to the nodes $x_{n,k}^{\varphi}, k = 1,2,\dots,n$, i.e. $L_n^{\varphi}(\mathrm{f}, x_{n,k}^{\varphi}) = f(x_{n,k}^{\varphi}), k = 1,2,,,,n.$ We look for an approximate solution $u_n \in \boldsymbol{X}_n$ to the solution of (5) by solving the collocation equations

$$A_n(u_n) \coloneqq \varepsilon V(u_n) + F_n(u_n) = L_n^{\varphi}(\mathrm{f}), \qquad u_n \in \boldsymbol{X}_n, \tag{6}$$

Where

$$F_n(u_n) \coloneqq L_n^{\varphi}(F(u_n)).$$

The following theorem on the convergence of the collocation methods holds true.

Theorem 2. (see Theorem 3.2 in [7]) Consider equation (5) for a function $f\colon(-1,1) \to \mathbb{C}$. Assume that the conditions a) and b) are satisfied. Then the equations (6) have a unique solution $u_n^* \in \boldsymbol{X}_n$, If the solution $u^* \in \boldsymbol{X}$ of (5) belongs to $\boldsymbol{L}_{\varphi}^{2,s+1}$ for some $s > \frac{1}{2}$, then the solution u_n^* converges in $\boldsymbol{X}$ to u^*, and

$$\| u_n^* - u^* \|_{\varphi,\frac{1}{2}} \leq const\, n^{-s} \| u^* \|_{\varphi,s+1.} \tag{7}$$

Moreover, if we assume that there is an $r \geq \frac{1}{2}$ such that $< F_n(u_n) - F_n(v_n), u_n - v_n >_{\varphi,r} \geq 0$, $u_n, v_n \in \boldsymbol{X}_n$, $n \geq n_0$, and $s \geq r - \frac{1}{2}$, then

$$\| u_n^* - u^* \|_{\varphi,r+\frac{1}{2}} \leq const\, n^{r-\frac{1}{2}-s} \| u^* \|_{\varphi,s+1,}$$

where the constant does not depend on *n*, ε *and* u^*.

Newton-Kantorovich method. To solve the nonlinear collocation equations (6) we apply the Newton-Kantorovich method. To achieve this, we make the following assumptions

(c) $\gamma(x,g)$possesses a partial derivative $\gamma_g(x,g)$ continuous with respect to$g \in \mathbb{R}$ for all $x \in [-1,1]$, such that ,

$$\gamma_g(x,g) \geq 0, \qquad x \in [-1,1], \quad g \in \mathbb{R},$$

And

$$L \coloneqq \sup_{(x,g)\in[-1,1]\times\mathbb{R}} \left[\varphi(x)\gamma_g(x,g)\right] < \infty.$$

Moreover, $\gamma(x,0) \in \boldsymbol{L}_{\varphi}^{2}$.

(d) $\left|\gamma_g(x,\varphi u_1) - \gamma_g(x,\varphi u_2)\right| \le \lambda(x)|\varphi(x)|^{\eta}|u_1 - u_2|^{\eta}$, where $0 < \eta \le 1$ and $\lambda(x)$ is such that

$$L_0 = \sup_{x\in[-1,1]} [\varphi(x)\lambda(x)] < \infty.$$

(e) $f \in \boldsymbol{L}_{\varphi}^{2,s}$ and $u \in \boldsymbol{L}_{\varphi}^{2,1}$ implies $F(u) \in \boldsymbol{L}_{\varphi}^{2,s}$, for some $s > \frac{1}{2}$.

The last assumption guarantees the applicability of the operator L_n^{φ} in the subsequent (8).
We define

$$\left(F_g\left(u^{(i)}\right)u\right)(x) = \gamma_g\left(x, \varphi(x)u^{(i)}(x)\right)\varphi(x)u(x),$$

And

$$F_n'\left(u_n^{(i)}\right)u_n \coloneqq L_n^{\varphi}F_g\left(u_n^{(i)}\right)u_n.$$

The Newton method is described by the following sequence of equations

$$L_n^{\varphi}\left[\varepsilon V\Delta u_n^{(i)} + F_g u_n^{(i)}\Delta u_n^{(i)}\right] = L_n^{\varphi}\left[f - \varepsilon V u_n^{(i)} - F(u_n^{(i)})\right], \tag{8}$$

with $u_n^{(i+1)} = u_n^{(i)} + \Delta u_n^{(i)}, i = 0,1,2,\ldots$, and $u_n^{(i+1)}, u_n^{(i)}, \Delta u_n^{(i)} \in \boldsymbol{X}_n$. Thus,

$$u_n^{(i+1)} = \sum_{j=0}^{n-1} c_{n,j}^{(i+1)} p_j^{\varphi}(x), \qquad u_n^{(i)} = \sum_{j=0}^{n-1} c_{n,j}^{(i)} p_j^{\varphi}(x), \qquad \Delta u_n^{(i)} = \sum_{j=0}^{n-1} \Delta c_{n,j}^{(i)} p_j^{\varphi}(x).$$

The equations (8) are equivalent to

$$\varepsilon V\Delta u_n^{(i)} + F_n'\left(u_n^{(i)}\right)\Delta u_n^{(i)} = L_n^{\varphi}\left[f - \varepsilon V u_n^{(i)} - F(u_n^{(i)})\right]. \tag{9}$$

If we define the following operator

$$A_n u_n \coloneqq \varepsilon V u_n + F_n(u_n) - L_n^{\varphi} f,$$

and its Frechet-derivative $u_n^{(i)} \in \boldsymbol{X}_n$

$$A_n'\left(u_n^{(i)}\right)u_n \coloneqq \varepsilon V u_n + F_n'\left(u_n^{(i)}\right)u_n, \qquad u_n \in \boldsymbol{X}_n,$$

we can rewrite equations (9) in the equivalent operator form

$$A_n'\left(u_n^{(i)}\right)\left(\Delta u_n^{(i)}\right) + A_n\left(u_n^{(i)}\right) = 0, \qquad u_n^{(i+1)} = u_n^{(i)} + \Delta u_n^{(i)},\ i = 0,1,2,\ldots. \tag{10}$$

Due to the invariance property, we have that equations (10) are equivalent to

$$\sum_{j=0}^{n-1} \Delta c_{n,j}^{(i)}[\varepsilon(j+1)p_j^{\varphi}(x_{n,k}^{\varphi}) + \gamma_g(x_{n,k}^{\varphi}, \varphi(x_{n,k}^{\varphi})\sum_{s=0}^{n-1} c_{n,s}^{(i)} p_s^{\varphi}(x_{n,k}^{\varphi}))\varphi(x_{n,k}^{\varphi})p_j^{\varphi}]$$
$$= -\varepsilon\sum_{s=0}^{n-1}(s+1)c_{n,s}^{(i)} p_s^{\varphi}(x_{n,k}^{\varphi}) - \gamma(x_{n,k}^{\varphi}, \varphi(x_{n,k}^{\varphi})\sum_{t=0}^{n-1} c_{n,t}^{(i)} p_t^{\varphi}(x_{n,k}^{\varphi})) + f(x_{n,k}^{\varphi}),$$

$k = 1,2,\ldots,,n, \quad c_{n,j}^{(i+1)} = c_{n,j}^{(i)} + \Delta c_{n,j}^{(i)}$.

For each fixed *n*, we start from an initial approximation $u_n^{(0)}$. Thus, starting from $\left[c_{n,j}^{(0)}\right]_{j=0}^{n-1}$ we compute $\left[\Delta c_{n,j}^{(i)}\right]_{j=0}^{n-1}$, and then

$$\left[c_{n,j}^{(i+1)}\right]_{j=0}^{n-1} = \left[c_{n,j}^{(i)}\right]_{j=0}^{n-1} + \left[\Delta c_{n,j}^{(i)}\right]_{j=0}^{n-1}.$$

When $\left\|u_n^{(i^*)} - u_n^{(i^*-1)}\right\|_{\varphi,\frac{1}{2}}$ is less or equal to a suitable accuracy, we take the polynomial

$$u_n^{(i^*)}(x) = \sum_{j=0}^{n-1} c_{n,j}^{(i^*)} p_j^{\varphi}(x),$$

as approximation of the solution u_n^* of (5).

Let $\boldsymbol{X}_n^S \coloneqq (\boldsymbol{X}_n, \|, \|_{\varphi,S})$, Then, the following theorem proves the convergence of the proposed Newton method to solve (5).

Theorem 3. (see Theorem 4.8 in [9]) We suppose that assumptions (c) and (d) are fulfilled. Then, for all $n \in \mathbb{N}$, the equation $A_n(u_n) = 0,$ has an unique solution $u_n^* \in \boldsymbol{X}_n^{1/2}$. Moreover, there exists a

$\delta > 0$ such that the sequence $\left\{u_n^{(i)}\right\}_{i=0}^{\infty}$ defined by (10) converges in the norm of $\boldsymbol{X}_n^{1/2}$ to the solution u_n^* for each initial approximation $u_n^{(0)}$ satisfying $\left\| u_n^{(0)} - u_n^* \right\|_{\varphi,\frac{1}{2}} \leq \delta$. Further, there exists a constant M dependent on n and η but not on i and $u_n^{(0)} \in U_{\boldsymbol{X}_n^{1/2}}(u_n^*, \delta) := \left\{u \in \boldsymbol{X}_n^{1/2} : \|u - u_n^*\| < \delta\right\}$ such that

$$\left\|u_n^{(i)} - u_n^*\right\|_{\varphi,\frac{1}{2}} \leq M \left\|u_n^{(i-1)} - u_n^*\right\|_{\varphi,\frac{1}{2}}^{1+\eta},$$

and

$$\left\|u_n^{(i)} - u_n^*\right\|_{\varphi,\frac{1}{2}} \leq M^{\frac{(1+\eta)^i - 1}{\eta}} \delta^{(1+\eta)^i}.$$

Moreover, if condition (e) is fulfilled then the sequence $\{u_n^*\}$ converges in the norm of $\boldsymbol{L}_{\varphi}^{2,\frac{1}{2}}$ to the solution $u^* \in \boldsymbol{L}_{\varphi}^{2,\frac{1}{2}}$ of equation (5) where (7) holds.

A fast algorithm based on GMRES. In this section we discuss the applicability of the generalized minimal residual method (GMRES) to the solution of linear systems of equations occurring in the application of collocation by Newton-Kantorovich method to the numerical solution of nonlinear HSIEs. The GMRES method is one of the most popular iterative schemes for large linear system of equations with a square nonsingular matrix. This iterative method approximates the solution of the system by the vector in a Krilov subspace with minimal residual. The Arnoldi iteration is used to find this vector. The GMRES and its suitable variants were subsequently proposed for ill-posed problems [1]. Moreover, in [18] GMRES method was successfully applied to singular integral equations of Cauchy type. Given a regular matrix $A \in \mathbb{R}^{n\times n}$ and a vector $b \in \mathbb{R}^n$, we have to solve the system

$$Ax = b.$$

The basic idea of the Krylov subspace methods consists in minimizing the residual $b - Ax$ for $x = x_0 + \xi$, where

$$\xi \in \mathbf{K}_m(A, \rho_0) = span\{\rho_0, A\rho_0, \dots, A^{m-1}\rho_0\},$$

and $\rho_0 = b - Ax_0$ (see [20]). In the sequel we give the numerical results (i.e., the number of iteration steps necessary to obtain a prescribed accuracy) for a particular subspace method, described shortly as follows. The GMRES (generalized minimal residual) algorithm minimizes the Euclidean norm $\|b - Ax\|$. This is equivalent to find $x_m = x_0 + \xi_m, \xi_m \in \mathbf{K}_m(A, \rho_0)$ such that $b - Ax_m \perp A\mathbf{K}_m(A, \rho_0)$. Using Arnoldi's procedure with the modified Gram-Schmidt algorithm to compute an orthonormal basis in $\mathbf{K}_m(A, \rho_0)$, it leads to the following algorithm, in which $tol > 0$ define the prescribed accuracy.

1. *Start:* Choose x_0 nd compute $\rho_0 = b - Ax_0$ and $v_1 = \rho_0/\|\rho_0\|$; $m = 0$;
2. *Iterate:*
 $m = m + 1$; $\bar{v} = Av_m$;
 For $i = 1,2, \dots, m$; $h_{i,m} = < \bar{v}, v_i >$; $\bar{v} = \bar{v} - h_{i,m}\, v_i$;
 $h_{m+1,m} = \|\bar{v}\|$; $v_{m+1} = \bar{v}/h_{m+1,m}$;

3. *The approximate solution:*
 $x_m = x_0 + V_m y_{m,}$ where and minimizes $\|\rho e_1 - \widetilde{H}_m y\|, y \in \mathbb{R}^m$, with $\rho = \|r_0\|, e_1 = (1{,}00, \dots, 0)^T$ the first vector in the standard basis in $\mathbb{R}^{m+1}$, and

$$\begin{bmatrix} h_{1,1} & h_{1,2} & \cdots & h_{1,m} \\ h_{2,1} & h_{2,2} & \cdots & h_{2,m} \\ . & \ddots & . & \vdots \\ . & . & \ddots & h_{m,m} \\ 0 & . & . & h_{m+1,m} \end{bmatrix};$$

4. *Restart:* Compute $r_m = b - Ax_m$; if $\|r_m\| \le tol\| r_0\|$ then stop;
 else take $x_0 = x_m, v_1 = r_m/\|r_m\|$ and go to 2.

We remark that to solve the least squares problem of the third step of the previous algorithm, plane rotations can be used to get a QR-factorization of $\widetilde{H}_m$, $i.e., Q_m\widetilde{H}_m = R_m, Q_m = (Q_m^{-1})^T \in \mathbb{R}^{m+1,m+1}$. This factorization is updated at each iteration step and the norm of the minimal residual is computed by the last component of $\rho Q_m e_1$. At every iteration, a matrix-vector product Av_mmust be computed. This costs about n^2 floating-point operations for general dense matrices of size n but the cost can decrease for particular matrix. In addition to the matrix-vector product, $\mathcal{O}(nm)$ floating-point operations must be computed at the *m*th iteration. Remark that in our situation $L_n^{\varphi}V = U_n^T D_n U_n$, where $D_n = diag[1{,}2, \dots, n]$and $U_n = \left[p_j^{\varphi}(x_{n,k}^{\varphi})\right]_{j=0,\dots,n-1,k=1,\dots,n}$. The matrix U_n can be written as $U_n = \widehat{U}_n\widehat{D}_n^{-1}$, with

$$\widehat{U}_n = \sqrt{\frac{2}{\pi}}\left[\sin\frac{jk\pi}{n+1}\right]_{j,k=1,\dots,n}, \qquad and\ \widehat{D}_n = diag\left[\sin\frac{k\pi}{n+1}\right]_{k=1,\dots,n}.$$

The matrix $\widehat{U}_n$ can be applied to a vector with $\mathcal{O}(n\log n)$ computational complexity.

Numerical tests. In this section we give some numerical results obtained using the algorithm described in the previous section. All computations reported in this section were carried out in double precision. Let us consider an example of nonlinear hypersingular integral equation of form (5) together with the Newton-Kantorovich method described before and the Krylov subspace method (GMRES). We choose tol equal to 10^{-3}. In the tables we collect the the number *m* of iterations (equal to the dimension of the Krylov space in the last step) necessary to achieve this accuracy. For all computations the initial guess is equal to the vector $x_0 = [1, \dots, 1]^T$.

Example 1. Let us consider equation (5) with

$$\gamma\big(x, \varphi(x)u(x)\big) = \frac{1}{2}\arctan\big(\varphi(x)u(x)\big),$$

and the right hand side

$$f(x) = \frac{\varepsilon}{\pi}\left[6x + \frac{3x^3 - 2x}{\sqrt{1-x^2}}\log\left(\frac{2 - x^2 + 2\sqrt{1-x^2}}{x^2}\right)\right] + \frac{1}{2}arctan\left(x|x|\sqrt{1-x^2}\right).$$

Then, the exact solution is $u(x) = x|x|$. Moreover, $u \in \boldsymbol{L}_{\varphi}^{2,\frac{5}{2}-\sigma}$ and $f \in \boldsymbol{L}_{\varphi}^{2,\frac{3}{2}-\sigma}, \sigma > 0$. Since the exact solution is known, we can compute $u_n^{(i^*)}$ in some points belonging to [0,1] in order to evaluate

$$norm := \left\| u_n^{(i^*)} - u^* \right\|_{\varphi,\frac{1}{2}}.$$

The following Tables show the numerical results of the Newton-Kantorovich method and the GMRES algorithm for this test equation in relation to different values of ε. In both tables stepsNK and stepsG denote the number of the steps of the Newton-Kantorovich method and the GMRES algorithm, respectively. In particular, Table 1 shows the comparison in the evaluation of the norm. Here normNK and normG denote the norms evaluated by the Newton-Kantorovich method and the GMRES algorithm, respectively. Taking into account that $u(0{,}25) = 0{,}0625$, where u denotes the solution of the nonlinear HSIE, Table 2 shows the approximate solution $u_n^{(i^*)}$NK and $u_n^{(i^*)}$G at the point $x = 0{,}25$ obtained by the Newton-Kantorovich method and the GMRES algorithm, respectively.

Example 2. Let us consider equation (5) with

$$\gamma\big(x, \varphi(x)u(x)\big) = \frac{1}{2}\arctan\big(\varphi(x)u(x)\big),$$

and the right hand side

$$f(x) = \cos(x).$$

In this case $f \in \boldsymbol{L}_{\varphi}^{2,s}$ for all $s > 0$ and we do not know the exact solution. Therefore, the following Tables 3-5 show the numerical results of the Newton-Kantorovich method and the GMRES algorithm for this test equation in relation to different values of εand for $x = 0, x = 0{,}5$ and $x = 1$, respectively. In all tables stepsNK and stepsG denote the number of the steps of the Newton-Kantorovich method and the GMRES algorithm, respectively, when we obtain the same approximate value for the unknown solution with the Newton-Kantorovich method and the GMRES algorithm with almost the same number of steps.

Table 1. Newton-Kantorovich method and GMRES algorithm

ε	n	Steps NK	Norm NK	m	Steps G	Norm G
0,01	32	5	0,769D-03	15	7	0,893D-03
0,1		4	0,864D-03		5	0,917D-03
0,25		4	0,891D-03		4	0,921D-03
0,5		4	0,904D-03		4	0,919D-03
1		4	0,911D-03		4	0,919D-03
0,01	64	5	0,203D-03	18	7	0,230D-03
0,1		4	0,227D-03		5	0,236D-03
0,25		4	0,231D-03		4	0,241D-03
0,5		4	0,233D-03		4	0,234D-03
1		4	0,234D-03		4	0,238D-03
0,01	128	5	0,536D-04	25	7	0,653D-04
0,1		4	0,585D-04		5	0,614D-04
0,25		4	0,592D-04		4	0,796D-04
0,5		4	0,595D-04		4	0,668D-04
1		4	0,596D-04		4	0,642D-04

Table 2. Newton-Kantorovich method and GMRES algorithm x=0,25

ε	n	Steps NK	$u_n^{(i^*)}$NK	m	Steps G	$u_n^{(i^*)}$ G
0,01	32	5	0,06239	15	7	0,06238
0,1		4	0,06247		5	0,06236
0,25		4	0,06237		4	0,06235
0,5		4	0,06236		4	0,06235
1		4	0,06235		4	0,06235
0,01	64	5	0,06247	18	7	0,06248
0,1		4	0,06247		5	0,06247
0,25		4	0,06247		4	0,06246
0,5		4	0,06247		4	0,06246
1,		4	0,06247		4	0,06247
0,01	128	5	0,06250	25	7	0,06250
0,1		4	0,06250		5	0,06250
0,25		4	0,06250		4	0,06250
0,5		4	0,06250		4	0,06250
1		4	0,06250		4	0,06250

Table 3. Newton-Kantorovich method and GMRES algorithm (x=0)

ε	n	Steps NK	$u_n^{(i^*)}$NK=$u_n^{(i^*)}$ G	m	Steps G
0,01	8	8	17,5	6	8
	16	8	17,56	9	8
	32	8	17,563	12	8
	64	8	17,5634	16	8
0,1	8	6	3,17	6	6
	16	6	3,173	7	6
	32	6	3,17384	10	6
	64	6	3,1738477	25	5
0,25	8	5	1,72	5	5
	16	5	1,7292	8	5
	32	5	1,72925	11	5
	64	5	1,729252	25	4
0,5	8	5	1,084	6	4
	16	5	1,0844	8	4
	32	5	1,084428	18	4
	64	5	1,0844287	30	4
1	8	4	0,658	6	4
	16	4	0,65813	10	4
	32	4	0,65133	20	3
	64	4	0,6581337	32	3

Table 4. Newton-Kantorovich method and GMRES algorithm (x=0,5)

ε	n	Steps NK	$u_n^{(i^*)}$NK=$u_n^{(i^*)}$ G	m	Steps G
0,01	8	8	14,1	6	8
	16	8	14,158	9	8
	32	8	14,158	12	8
	64	8	14,15840	18	8
0,1	8	6	2,91	6	6
	16	6	2,9204	7	6
	32	6	2,92043	12	6
	64	6	2,920434	25	5
0,25	8	5	1,63	5	5
	16	5	1,6390	8	5
	32	5	1,6389	11	5
	64	5	1,6390001	25	4
0,5	8	5	1,03	6	4
	16	5	1,03913	8	4
	32	5	1,039130	18	4
	64	5	1,039130	24	4
1	8	4	0,6325	6	4
	16	4	0,632593	10	4
	32	4	0,632593	20	3
	64	4	0,63259338	32	3

Table 5. Newton-Kantorovich method and GMRES algorithm (x=1)

ε	n	Steps NK	$u_n^{(i^*)}$NK=$u_n^{(i^*)}$ G	m	Steps G
0,01	8	8	7,75	6	8
	16	8	9,11	9	8
	32	8	10,	12	8
	64	8	10,4	16	8
0,1	8	6	2,66	6	6
	16	6	2,80	7	6
	32	6	2,84	10	6
	64	6	2,85	25	5
0,25	8	5	1,54	5	5
	16	5	1,55	8	5
	32	5	1,58	11	5
	64	5	1,58	25	4
0,5	8	5	0,968	6	4
	16	5	0,978	8	4
	32	5	0,981	18	4
	64	5	0,982	30	4
1	8	4	0,577	6	4
	16	4	0,579	10	4
	32	4	0,580	20	3
	64	4	0,580	32	3

Summary. In the paper we present the mathematical model of a partially bridged straight crack in a unidirectionally fiber reinforced composite in terms of a nonlinear hypersingular integral equation.

We treat this nonlinear integral equation numerically using a collocation method, and applying at the resulting nonlinear collocation equations the Newton method. Moreover, we use GMRES to obtain a fast algorithm. As confirmed in our numerical tests, we show the applicability and the computational gain of the generalized minimal residual method (GMRES) to the solution of linear systems of equations occurring in the application of collocation by Newton-Kantorovich method to the numerical solution of nonlinear HSIEs (5).

Acknowledgment

This work was supported by the CNR MATHTECH Project.

References

[1] M. Besellalij, L. Reichel, H. Sadok, Some properties of range restricted GMRES methods, J. Comp. and Apl. Math. 290 (2015), 310 - 318. DOI 10.1016/j.cam.2015.05.008

[2] I.V. Boykov, E.S. Ventsel, A.I, Boykova, An approximate solution of hypersingular integral equations, Appl. Numer. Math. 60 (2010), 607 - 628. DOI 10.1016/j.apnum.2010.03.003

[3] I.V. Boykov, V.A, Roudnev, E.S. Ventsel, A.I. Boykova, An approximate solution of nonlinear hypersingular integral equations, Appl. Num. Math. 86 (2014), 1 - 21. DOI 10.1016/j.apnum.2014.07.002

[4] I.V. Boykov, J.F, Zakharova, Approximate solution of hypersingular integral equation, Rep. High. Educ. Inst. Phys. Math. Sci., 1 (2010), 80 - 91 (In Russian).

[5] M.R. Capobianco, G. Criscuolo, Numerical solution of a singular integral equation with Cauchy kernel in the plane contact problem, Quart. Appl. Math. 69 (2011), 79 - 89. DOI 10.1090/S0033-569X-2010-01231-3

[6] M.R. Capobianco, G. Criscuolo, P. Junghanns, A fast algorithm for Prandtl's integro-differential equation, ROLLS Symposium (Leipzig, 1996), J. Comput. Appl. Math. 77 (1997), 103 - 128.

[7] M.R. Capobianco, G. Criscuolo, P. Junghanns, On the numerical solution of a nonlinear integral equation of Prandtl's type, Recent advances in operator theory and its applications, 53 - 79, Oper. Theory Adv. Appl., 160, Birkhäuser, Basel, 2005.

[8] M.R. Capobianco, G. Criscuolo, P. Junghanns, On the numerical solution of a hypersingular integral equation with fixed singularities, Recent advances in operator theory and applications, 95 - 116, Oper. Theory Adv. Appl., 187, Birkhäuser, Basel, 2009.

[9] M.R. Capobianco, G. Criscuolo, P. Junghanns, Newton methods for a class of nonlinear hypersingular integral equations, Numer. Algorithms 55 (2010), 205 - 221. DOI 10.1007/s11075-010-9387-8

[10] M.R. Capobianco, G. Criscuolo, P. Junghanns, U. Luther, Uniform convergence of the collocation method for Prandtl's integro-differential equation, Papers in honour of David Elliott on the occasion of his sixty-fifth birthday, ANZIAM J. 42 (2000), 151 - 168.

[11] Z. Chen, Y. Zhou, A new method for solving hypersingular integral equations of the first kind, Appl. Math. Lett. 24 (2011), 636 - 641. DOI 10.1016/j.aml.2010.11.028

[12] G. Criscuolo, A new algorithm for Cauchy principal value and Hadamard finite-part integrals, J. Comput. and Appl. Math. 78 (1997), 255 - 275.

[13] G. Criscuolo, A note on a paper: "Error estimates in the numerical evaluation of some BEM singular integrals" by G. Mastroianni and G. Monegato, Math. Comp. 73 (2004), 243 - 250.

[14] G. Criscuolo, Numerical evaluation of certain strongly singular integrals, IMA J. Num. Anal. 34 (2014), 651 - 674. DOI 10.1093/imanum/drt017

[15] H. Feng, X. Zhang, J. Li, Numerical solution of a certain hypersingular integral equation of the first kind, BIT 51 (2011), 609 – 630. DOI 10.1007/s10543-010-0305-1

[16] M. Ganesh, O. Steinbach, The numerical solution of a nonlinear hypersingula boundary integral equations, J. Comput. Appl. Math. 131 (2001), 267 - 280.

[17] A. Gil, S. Samko, On a hypersingular equation of a problem for a crack in elastic media, Fract. Calc. Appl. Anal. 13 (2010), 1 - 8.

[18] P. Junghanns, K. Rost, Krylov subspace methods for Cauchy singular integral equations, Facta Universitatis, Ser. Math. Inform. 19 (2004), 93-108.

[19] R. Mollapourasl, An efficient numerical scheme for a non linear integro-differential equations with an integral boundary, Appl. Math. and Comp. 248 (2014), 8 - 17. DOI 10.1016/j.amc.2014.09.088

[20] Y. Saad, Iterative Methods for Sparse Linear System, Second Edition, Society for Industrial and Applied Mathematics, Philadelphia, PA, 2003.

[21] S. Samko, On a 3D-hypersingular equation of a problem for a crack, Fract. Calc. Appl. Anal. 14 (2011), 19 - 30.

A Virtual Stage-Gate Approach to Developing Injection Moulds for Polymer-Based Drug-Delivery Systems

Juster H.[1,a], Steinbichler G.[1]

1 – Institute of Polymer Injection Moulding and Process Automation, Johannes Kepler University, Linz, Austria

a – herwig.juster@gmail.com

DOI **10.13140/RG.2.1.3533.9923**

Keywords: mold design, drug delivery systems, stage-gate process, filling simulation.

ABSTRACT. This paper presents a stage-gate procedure for designing a polymer injection mould for the production of tablet-shaped drug-delivery systems and virtual analysis of the effects of temperature, shear rate and pressure during the filling phase. The approach, its theoretical background, methods and stages are presented and discussed. The mould was designed using the commercial computer-aided design software ProEngineer. The filling phase was analyzed by means of the commercial finite-volume analysis software package Sigmasoft, Version 5.0.1. The results show that our stage-gate approach can be used to investigate moulds in terms of processing conditions in the virtual domain, which enables more accurate mould design for pharmaceutical drug-delivery systems.

Introduction. Pharmaceutical drugs with poor solubility in water have been a centre of academic and industrial attention over recent decades. Research in this area has shown that solubility can be improved by using hydrophilic polymers as carrier matrices for Active Pharmaceutical Ingredients (APIs) to form a solid dispersion system [1]. Such systems can be created using the Hot Melt Extrusion (HME) technique [2]. The standard tableting process requires two steps: first granulation and then tablet pressing. In the case of HME, this means that pelletizing (forming 2 mm pellets) is followed by grinding to powder and, subsequently, tablets can be pressed [3].

A one-stop procedure that increases the solubility of poorly soluble drugs may be possible using the polymer injection moulding technique. Clearly, a key element in polymer injection moulding is the mould, whose configuration and design elements must be optimized for a specific production process.

There is an increasing demand in industry for accurate moulds and their production process in the virtual domain. At the same time, the polymer injection mould is poised to enter new fields, such as the pharmaceutical industry. Basic design strategies that allow simple modification and adaption to given design and process criteria are therefore paramount.

In general, the product development process for polymer parts can be divided, according to the VDI-guideline 2222, into three phases: designing, outlining and finishing phase [4]. The presented stage-gate procedure allows to precise the outlining phase in a virtual domain and helping to reach the finishing phase faster.

Designing a mould for a standard thermoplastic part requires some important factors to be taken into consideration, including mould size, overall number of cavities, cavity layouts, runner and gating systems, shrinkage and the ejection system [4].

In the design process of an injection mould for drug delivery systems, some additional factors must be taken into account, namely temperature gradients, mechanical stress as a result of shear rates and residence times of the melt. These parameters influence the miscibility of the drug in the molten carrier phase [5].

We present an approach in which a basic mould design is developed based on experience from previous design studies [6], in particular the choice of hot-runner system to be used as a starting point for the study. There are three conceptual stages and gates in the design procedure (Figure 1):

1) Design stage: Filling simulation of the drug delivery specimen. The hot-runner system and injection machine nozzle are not taken into consideration. Characterization and implementation of all important material data, such as viscosity and volume changes as functions of pressure and temperature, and thermal data (heat capacity, heat transfer).

a. Design gate: Determination of a process window with the following parameters: maximum filling pressure, shear rates and temperature.

2) Process stage: The simulation is extended to include the hot-runner system and the machine nozzle. A multi-cycle analysis is performed to reproduce a real-world production scenario.

a. Process gate: Update of the process window with the following parameters: maximum filling pressure, shear rates and temperature. Additionally, the residence time in the mould is analysed. The optimal filling time is determined.

3) Critical process conditions stage: Filling simulation with the optimal filling time and extension of the process to include the maximum allowed residence time in the injection mould system (plasticizer unit and mould)

a. Critical process gate: Aside from the process factors investigated, a virtual process window that includes the residence time of the allover system can be defined.

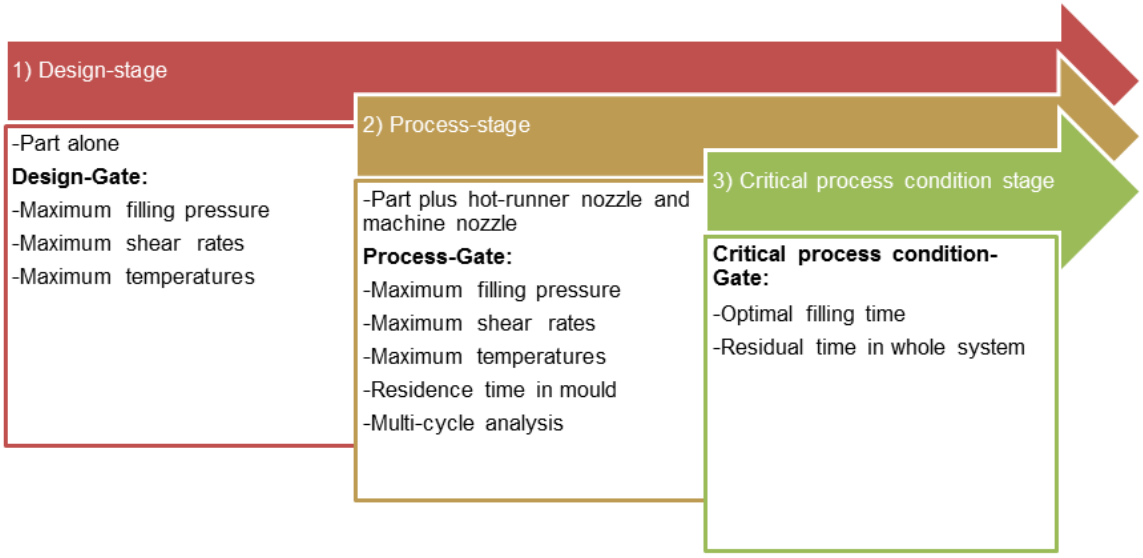


Fig. 1. Three-stage-gate approach for obtaining the optimal process window for a polymer injection moulding process

Design of the drug delivery specimen. The tablet specimen and its dimensions, which are typical of tablet-shaped drug delivery systems, are shown in Figure 2. The part has an overall length of 80 mm and a thickness of 10 mm. Each tablet has a diameter of 13 mm and a thickness of 4 mm, and is connected to the runner (thickness of 5 mm) via side-edge pinpoint gating. Balancing is realized simply with a radial feed system (star distributor). One injection moulding cycle yields six tablets, which have a total weight of 3.5 g; the runner has a weight of 2.9 g.

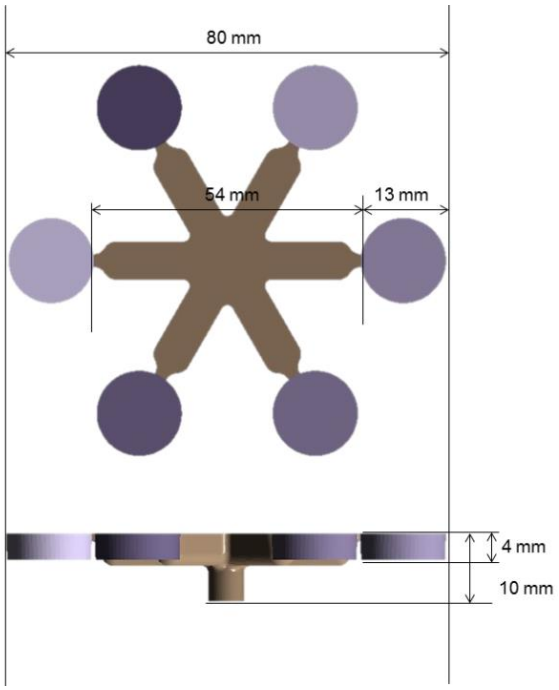


Fig. 2. Drug delivery tablet specimen: six tablets are produced in one injection moulding cycle (shot weight: 6.4 g)

Design of the polymer injection mould for the drug delivery specimen. This section deals with the design aspects and other considerations of the mould. Figure 3 shows the cross section of the designed mould, which consists of two plates. The hot-runner nozzle and a pressure transducer are placed in the manifold backing plate. The six tablet-shaped cavities and the runner are located in the movable platen of the mould. The tablets and the runner are ejected by a central anchor and six ejection pins (each with a diameter of 10 mm) in the movable platen. The cooling lines are placed in the movable half in parallel to the tablets that a homogenous heat transfer can be ensured. The distance to the tablets is 7 mm and the cooling media is water (30°C). The cooling lines have a constant diameter of 7 mm. In the fixed mould half, a nearly quadratic cooling line (diameter of 7 mm) is placed to enable the heat transfer of the top part of the tablets.

Hot-runner system. The star distributor is gated centrally to the hot-runner using an open torpedo-shaped nozzle. The optimal diameter of the hot-runner torpedo tip was determined by means of virtual design using numerical methods [7]. This study included the investigation of the diameter as a function of gate freeze time, shear rate and volume flow rates. Furthermore, symmetric heat removal dissipation of the mould and the tablet parts was taken into account. The hot-runner system must ensure uniform distribution of temperature loads and stresses in the mould. The study concluded that a diameter of 3 mm is optimal for the boundary conditions investigated (Figure 4). The torpedo can be designed based on published examples [8].

Injection moulding machine. The basic data for process simulations were obtained from an all-electric injection moulding machine of the e-mac 50/50 (Engel Austria GmbH, Austria) type with a clamping force of 500 kN and a reciprocating-screw plasticizing unit fitted with an 18 mm three-section screw. This injection moulding machine has a maximum specific injection moulding pressure of 2400 bar, which was used as a boundary condition in our study.

Material system. Kollidon® VA 64 100 wt%. The vinylpyrrolidone-vinyl acetate copolymer [9] Kollidon® VA 64 polymer was obtained from BASF SE (Ludwigshafen, Germany). Figure 5 shows structure and repeat unit of the Kollidon® VA 64 monomer.

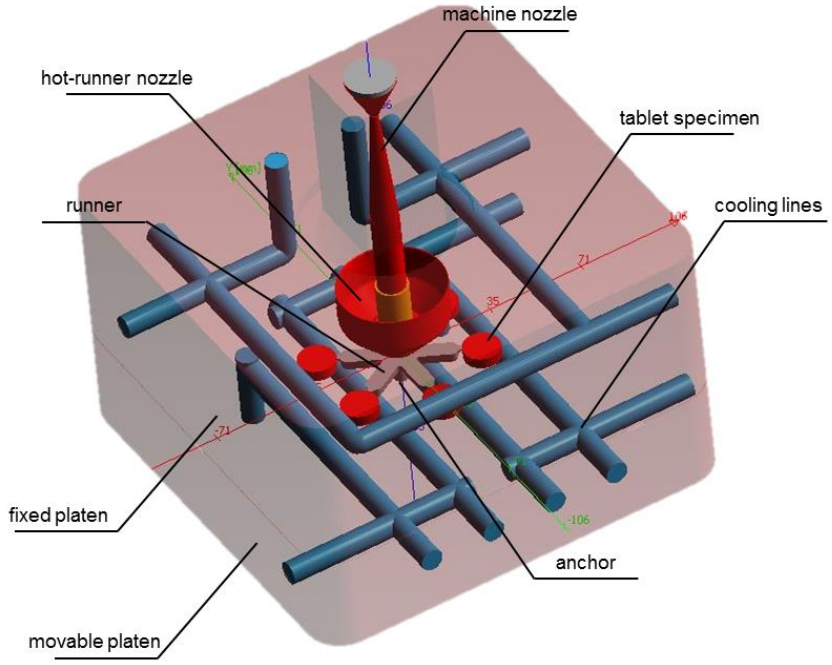


Fig.3. 3D solid model of the mould: drug delivery specimen with central star distributor and a central hot-runner nozzle (length: 245 mm; wide: 245mm; height: 215 mm)

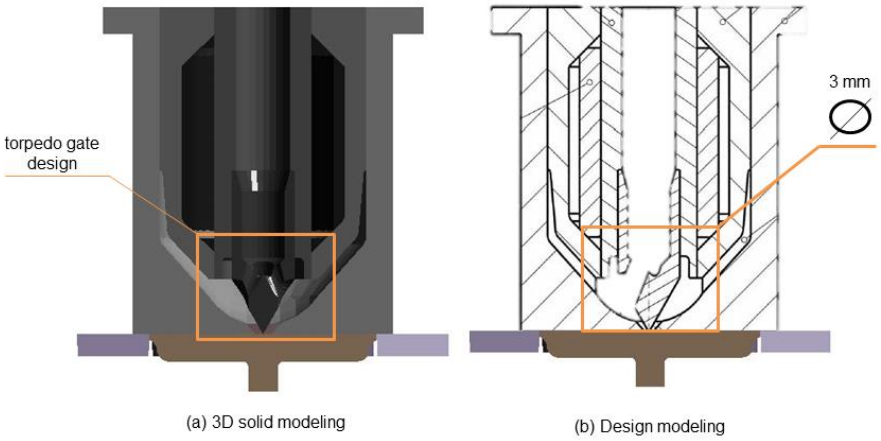


Fig.4. 3D solid model and design model of the hot-runner nozzle with a 3 mm wide tip.

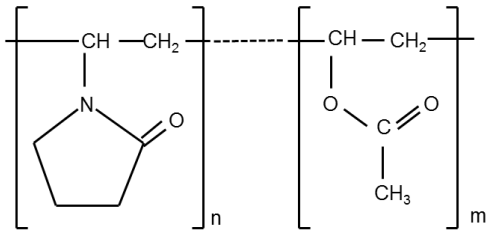


Fig.5. Kollidon® VA 64 polymer, used as a drug carrier matrix system [9]

Enhancing the bioavailability of poorly soluble drugs is the main purpose of this polymeric system. The glass transition temperature is in the area of 80°C [9], which enables processing at melt temperatures of 150°C.

Kollidon® VA 64 90 wt% – Fenofibrate 10 wt%. At Research Center Pharmaceutical Engineering GmbH (Graz, Austria), a drug delivery system was formed by compounding Kollidon® with fenofibrate (Figure 6). Fenofibrate is used to reduce the concentration of the low-density lipoprotein in the human body, and served as a model API in our case. The melting point of fenofibrate is at 80°C.

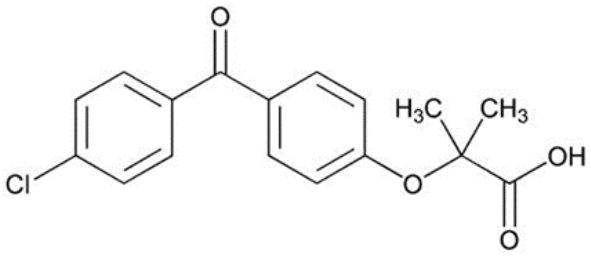


Fig.6. Fenofibrate as a representative lipoprotein-reducing active ingredient, used as a model drug in our study

Characterization of the materials. Simulating a solid dispersion in a fluid simulation requires both rheological and thermal characterization of the material systems. Further, we obtained data on relevant material properties such as shear viscosity, thermal conductivity and pvT behaviour, and converted them into a virtual material data set for simulation. Viscosity data were obtained using high-pressure viscosity and rotational viscosity analysis. The shear thinning behaviour of the polymer-API system was modelled using the Cross-WLF model (Equations 1 and 2); the resulting coefficients are listed in Table 1. We decided to apply the Cross-WLF model to include effects of pressure dependencies of the polymer-API system.

$$\eta(T,\dot{\gamma},p) = \frac{\eta_0(T,p)}{1+\left(\frac{\eta_0(T,p)\cdot\dot{\gamma}}{D_4}\right)^{1-n}}, \tag{1}$$

$$\eta_0(T,p) = D_1 \cdot e^{\frac{A_1(T-D_2-D_3\cdot p)}{A_2+T-D_2}}. \tag{2}$$

Table 1. Material coefficients for the Cross-WLF material model

Material system			**Kollidon 90 wt%– Fenofibrate 10 wt**	**Kollidon 100 wt%**
Factor describing the temperature dependency	A1	[/]	123.79	138.81
Factor describing the temperature dependency	A2	[K]	1000	1000
Cross exponent	n	[/]	0.4545	0.5633
Viscosity at reference temperature	D1	[Pa·s]	2446.2002	20825.61
Reference temperature	D2	[°C]	150	160
Factor describing the pressure dependency	D3	[K/bar]	0.011	0.011
Transition shear stress	D4	[Pa]	140096.6	82306.80

Numerical (CFD) methods. The process phases of an injection moulding cycle (filling, holding pressure and cooling) were simulated with Sigmasoft 5.0.1 (SIGMA Engineering GmbH, Aachen). This virtual injection moulding program is based on solving the Navier-Stokes equations [11]. It can consider all parts of a mould, including mould plates, slides, ejector pins, air gaps, cooling lines and heater elements. Consequently, a successful simulation requires estimation of all necessary boundary conditions.

Results of the design stage and gate. In order to obtain a process window at the end of the design stage, three process parameters were chosen: inlet pressure, shear rate and melt temperature. Each parameter requires a boundary condition, which represents the limit of a possible process window (Table 2).

Table 2. Boundary conditions for the specific filling pressure, shear rates and melt temperature

Boundary condition	**Critical value**
injection pressure	2400 bar
mechanical (especially shear) stress rates	15000 s^{-1}
melt temperature	180 °C

The filling of the part is a function of a predefined filling time, which changed with each simulation. In total, seven filling time steps (from 0.5 s to 2s) at two melt temperatures (150°C and 170°C) were investigated.

A separate study was carried out to obtain the critical mechanical stresses on an injection moulding machine during processing of a solid dispersion system [10]. A visible molar mass reduction of the Soluplus® polymer was correlated to a shear-rate level of 30000 s^{-1}. The critical shear rate was set to 15000 s^{-1}, which corresponds to a safety margin of a factor of two. Before the boundary conditions of [10] could be used, a material consistency study was performed due to the fact that Kollidon® was used in this study. The consistency study covered the comparison of the Cross-WLF material parameters. The deviation of the cross exponent between Kollidon® and Soluplus® is with 5% in an acceptable range. Moreover, the pvt-behaviour and heat transfer modelling was verified to ensure a transfer of the shear rate boundary condition. Furthermore, the material exhibits thermal degradation above a melt temperature of 180 °C [12].

Figure 7 shows inlet pressure, shear rate and temperature as functions of different filling steps. For the inlet pressure analysis, the two melt temperatures (150 °C and 170 °C) and the critical pressure level of the injection moulding machine are plotted to show the effect of filling time on the inlet pressure. The pressure course for a melt temperature of 170 °C decreases from 100 bar to finally 10 bar when the end of the filling time has been reached after two seconds. The pressure course for a melt temperature of 150 °C exhibits no such drop. Here, the temperature dependency of Kollidon® is shown which allows reducing the necessary inlet pressure with increasing filling times only with a certain melt temperature. In terms of shear rate, the curves for both melt temperatures show similar levels at the beginning (8000 s^{-1} and 10000 s^{-1} for 150 °C and 170 °C, respectively, at 0.5 s) and a decrease to 2000 s^{-1} within 2 s. As a consequence of this viscous shear heating, a critical point is reached where the curve for a melt temperature of 170 °C crosses the specified temperature limit of 180 °C.

Figure 8 plots selected parameters (inlet pressure, shear rates and melt temperature) of the Kollidon 90 wt% – Fenofibrate 10 wt% material system, whose curve progressions deviate from those of the Kollidon 100 wt% system. An API content of 10 wt % leads to lower inlet pressures, especially for a melt temperature of 170 °C. The shear rates for both processing temperatures thus reach the same levels, and the temperature increase due to shear heating is smaller.

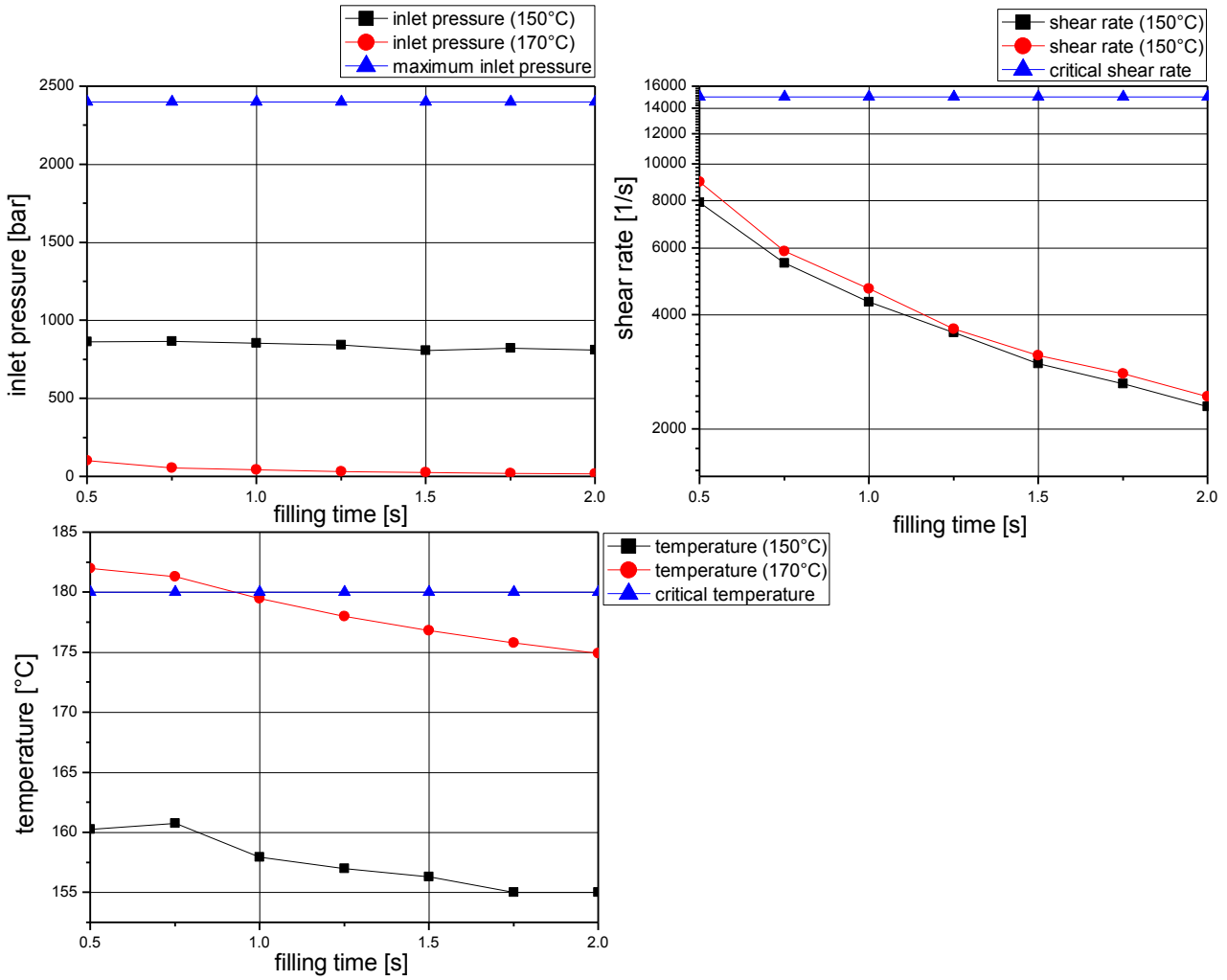


Fig. 7. Simulation results of the design stage of Kollidon VA 64 100 wt%: inlet pressure, shear rates and melt temperature

Information obtained by analyzing the filling of the specimen enriches the process window analysis. The data triple (inlet pressure, shear rates and temperature) values are necessary to find the process window limits. Figure 9 compares the process window of both material systems: The possible process window is wider for the system containing Fenofibrate than for that containing only the polymer. The optimal process quadrant, indicated by a filled green circle, is located in the range of lower melt temperatures and lower filling times.

Results of the Process stage and gate. Given the result of the design gate, we investigated only the material system with API content in the process stage. The basic model, which consists only of the drug delivery specimen, was extended to include the hot-runner system and the machine nozzle. Furthermore, a multi-cycle analysis of the extended model with mould was conducted. This step is essential to render the production environment more realistic. The study was carried out using the same filling steps and boundary conditions as described in section 3.

Figure 10 shows the inlet pressures, shear rates and temperature increases as functions of the filling times. We noticed that, compared to the design stage, the pressure levels and the shear rate levels increased by 100 % and up to 20 %, respectively. Modelling a more accurate system led to these expected results.

Figure 11 presents the process window as a function of filling time and melt temperature. Compared to the design stage, the process window is narrower and provides more accurate results for the real production process. We defined the numerical centre of the window as the processing optimum.

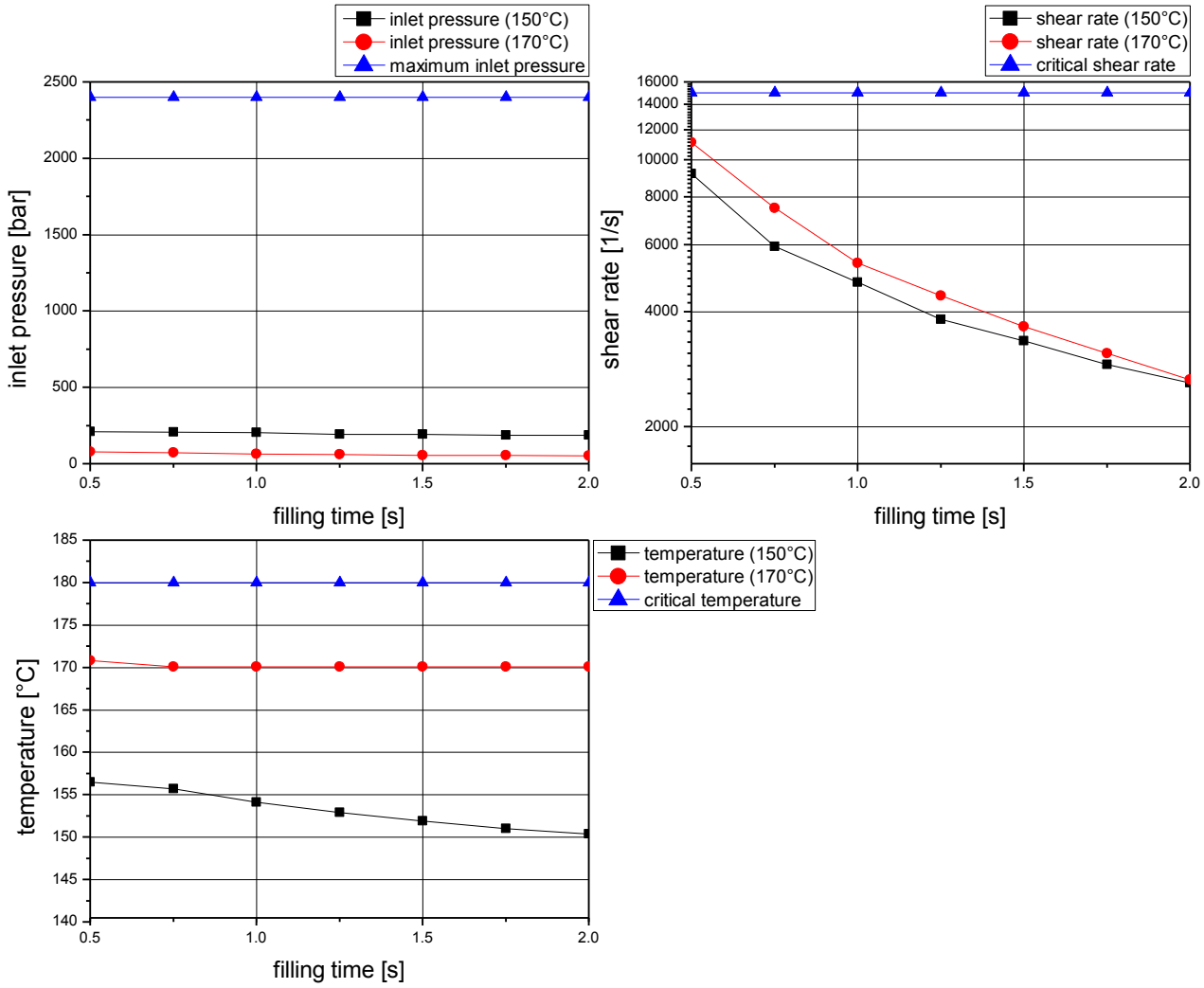


Fig. 8. Simulation results of the design stage of Kollidon VA 64 90 wt% -Fenofibrate 10 wt%: inlet pressure, shear rates and melt temperature

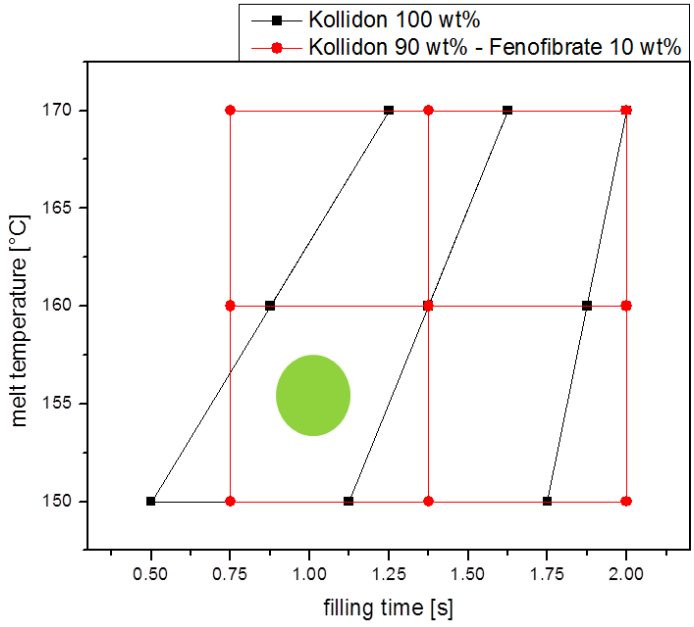


Fig. 9. Comparison of the design-stage process windows: Kollidon 100% wt (black line) and Kollidon 90 wt% – Fenofibrate 10 wt% (red line)

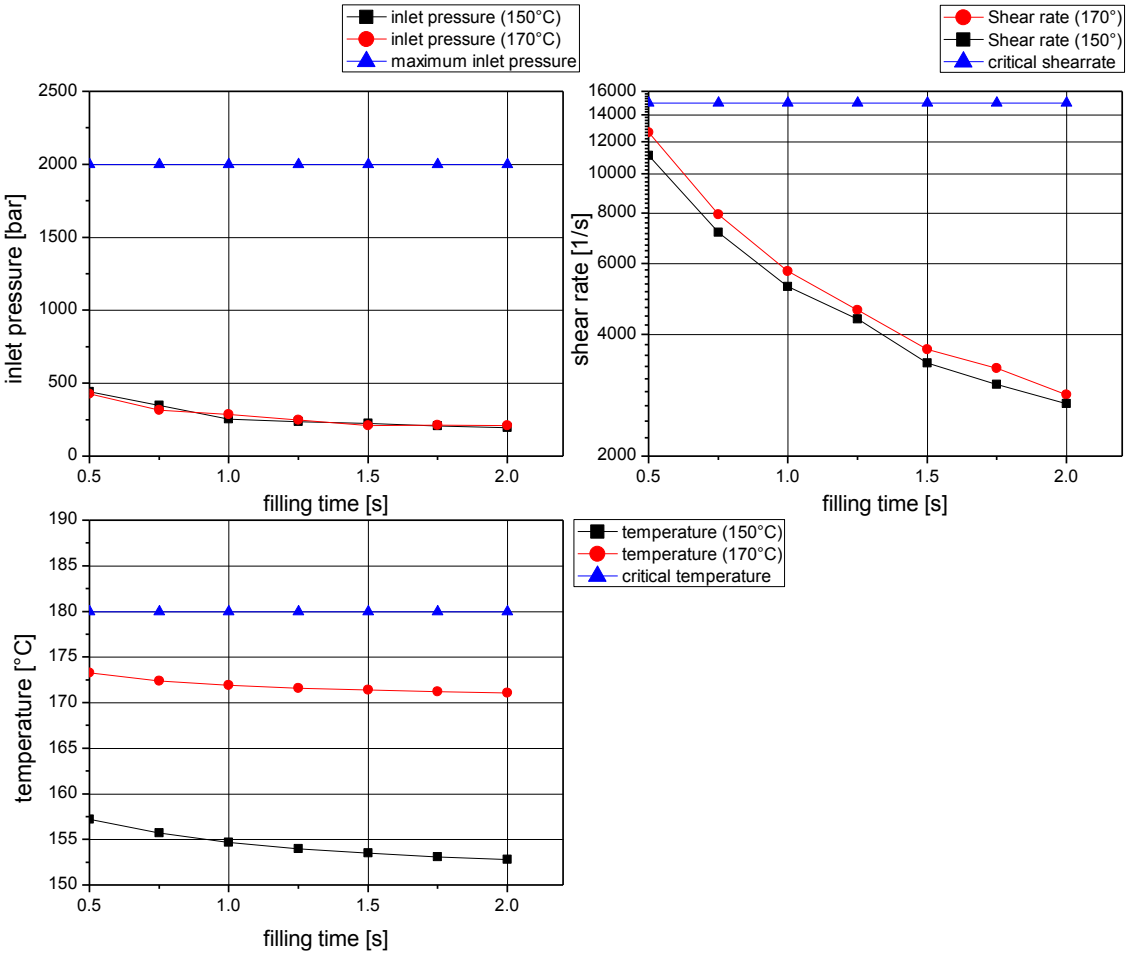


Fig. 10. Simulation results of the process stage of Kollidon VA 64 90 wt% -Fenofibrate 10 wt%: inlet pressure, shear rates and melt temperature

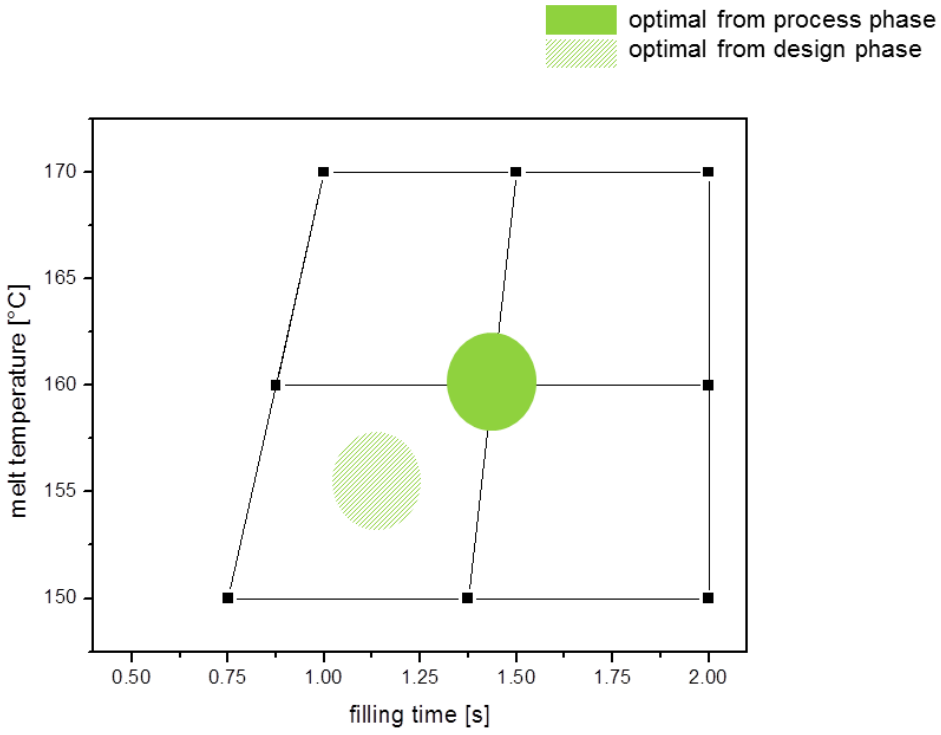


Fig. 11. Process window of the process stage of the Kollidon 90 wt% – Fenofibrate 10 wt% material system

Multi-cycle analysis. A multi-cycle analysis provided several advantages in our case. Calculating the heat distribution across the mould after multiple cycles was the main use of this analysis. In our study, the mould temperature prediction for the filling phase was more accurate when a multi-step procedure rather than a single production cycle was used, as this allowed colder and hotter regions within the mould to be better understood. Moreover, using a hot-runner system leads to an increase in the mould temperature over multiple cycles; this additional information can be used to decide whether the hot-runner is sufficiently insulated from the rest of the mould.

Figure 12 shows the results of the multi-cycle analysis for melt temperatures of 150 °C and 170 °C. The analysis consists of 20 cycles that are simulated with the mould already filled, and the thermal exchange between polymer and mould is calculated. The heat flow information is stored and serves as a starting boundary condition for the next cycle. Since cycle 21 includes the filling phase and the thermal exchange between polymer and mould, a decrease in heat flow is noticeable. As a result, 16 cycles are necessary to reach a thermal equilibrium, which defines the production window for good-quality parts. However, the most salient result of our study is the difference in heat flow between the two processing temperatures: Processing of Kollidon with API at 170 °C leads to a doubling of the heat flow and energy stored in the mould compared to processing at 150 ºC. Thus, we conclude that the lower processing temperature is preferable in terms of energy consumption and lifetime of the mould.

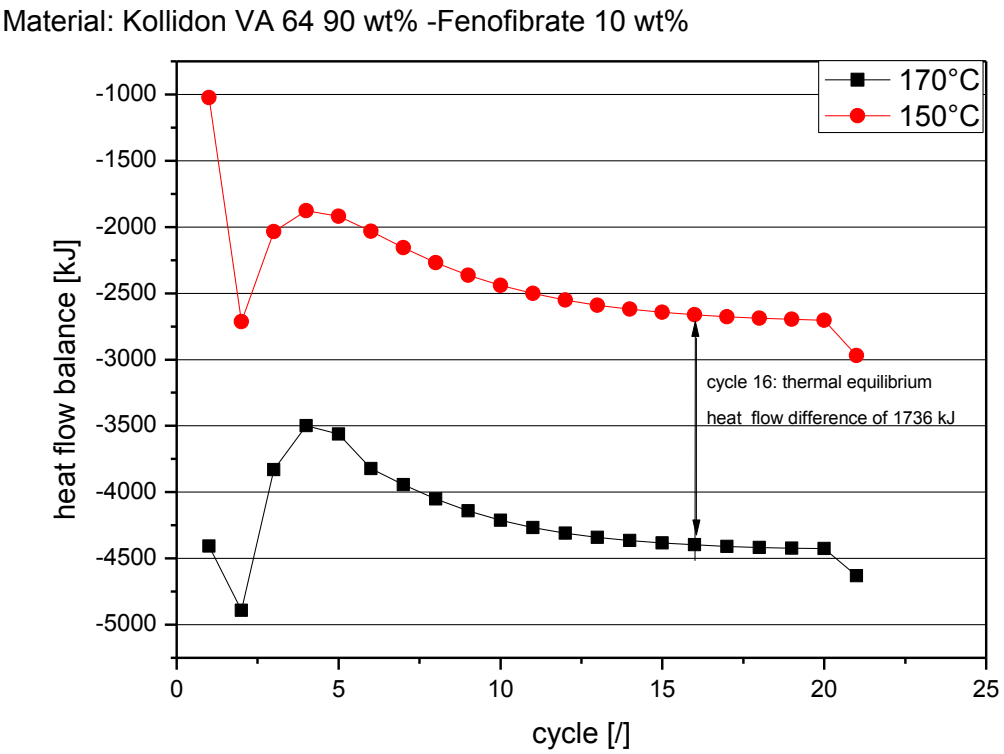


Fig. 12. Multi-cycle analysis of the Kollidon 90 wt% – Fenofibrate 10 wt% material system

Results of the critical process-conditions stage. The third stage of this study focused on filling simulations with optimal filling time. Expanding the process simulation to include the maximum allowed residence time in the injection mould system (plasticizer unit and mould) is key at this stage.

Up to this point we have considered only the filling phase and modified the injection mould accordingly. For a residence time analysis, the simulation process needs to include also the packing and the cooling phases. A boundary condition for the end of solidification was defined at 80 °C. Ejecting is possible when the specimen temperature falls below 80 °C (Figure 13). The mould temperature was kept at 30 °C during the whole process. For the Kollidon-API material system, the optimal filling time of the specimen is 1.375 s, which corresponds to production cycle times of 31.4

s and 34.4 s for melt temperatures of 150 ºC and 170 °C, respectively. Calculating the residence time in the mould includes estimating the turnover volume of the hot-runner system. Since our hot-runner system has a turnover of 1.8, two production cycles are necessary to completely replace the polymer-API melt in the hot-runner system. To include the plasticizer unit in the residence time study, the screw volumes of 18 mm reciprocating screws with length-to-diameter ratios of 20 and 24 were estimated. Dividing the specimen volume by the screw volume and multiplexing it with the production cycle time yielded the residence time in the plasticizer unit, the result of which are shown in Figure 14. The residence time in a pharmaceutical compounding process is usually around three minutes. In our study, this value was chosen as the boundary condition for producing drug delivery specimen in order to minimize degradation of the polymer or the API during the whole injection moulding process. Our results show minimum residence time distributions of 4.22 minutes (melt temperature: 150 °C; plasticizer unit: 20D) and 4.62 minutes (melt temperature: 150°C; plasticizer unit: 24D). Clearly, the limit of three minutes was exceeded (by 40 %), and the process must be optimized towards meeting this criterion.

One way of optimization the residence time is by estimating the maximal cooling time and mould temperature. The calculation was performed using the melt temperature of 150 °C and 170 °C and a plasticizer unit of 20D and 24D. The results are shown in Table 4.

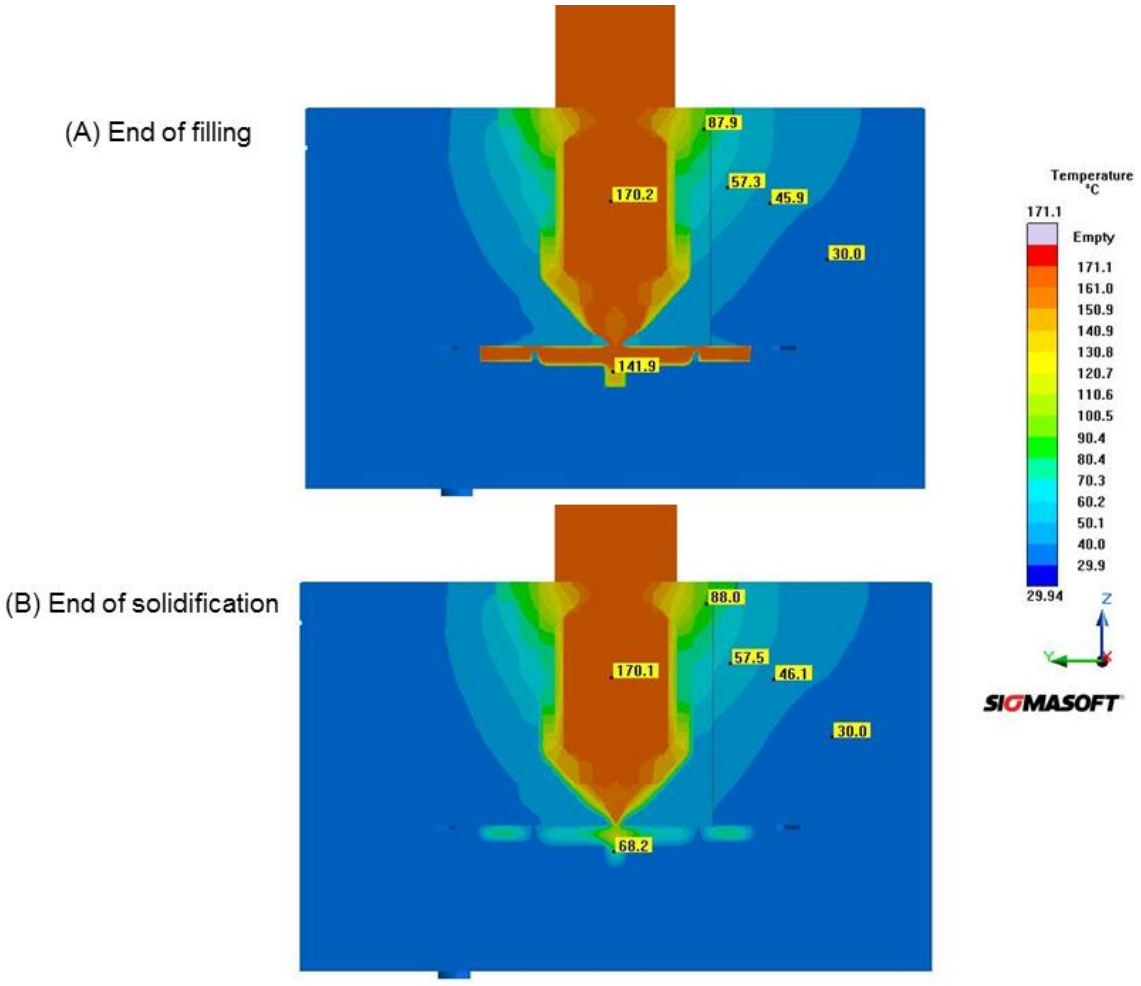


Fig.13. Temperature distributions: (A) end of specimen filling and (B) end of solidification process (Melt temperature: 170°C)

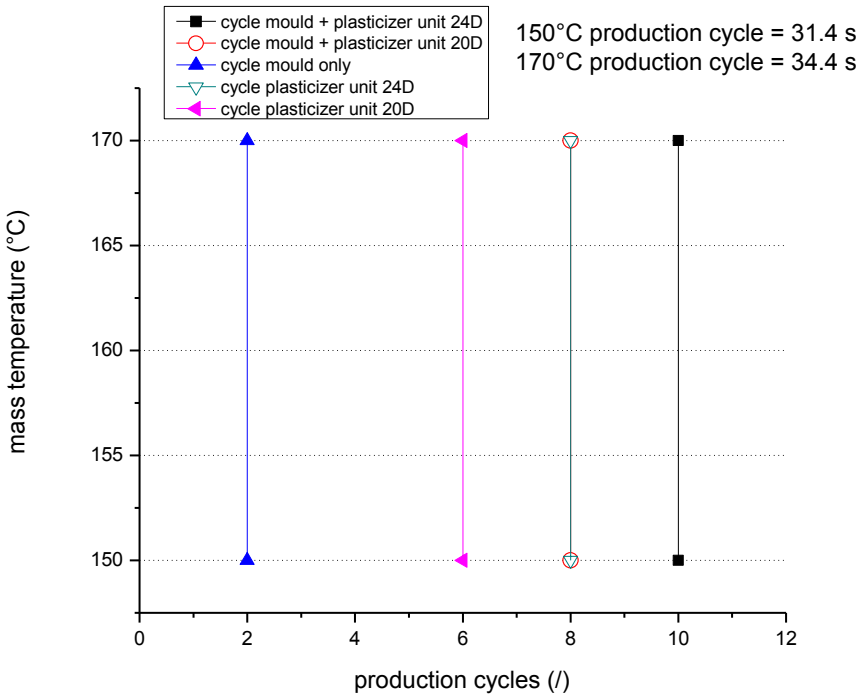


Fig. 14. Residence times of the Kollidon 90 wt% - Fenofibrate 10 wt% system for the mould, plasticizer unit and the whole processing system

Table 3. Results of the residence time simulations

Melt temperature	*Mould*	*Plasticizer unit*	*Residence time*
[°C]	*[/]*	*[L/D]*	*[min]*
150	*Drug delivery specimen with hot runner system*	*24D*	*4.85*
150		*20D*	*4.22*
170		*24D*	*5.32*
170		*20D*	*4.62*

Table 4. Results of the optimized residence time calculations

Melt temperature	*Plasticizer unit*	*Estimated mould temperature*	*Permitted cycle time*	*Residence time*
[°C]	*[L/D]*	*[°C]*	*[s]*	*[s]*
150	*24D*	*20*	*19*	*180*
150	*20D*	*20*	*22*	*180*
170	*24D*	*20*	*19*	*180*
170	*20D*	*20*	*22*	*180*

Summary. The presented stage-gate process made it possible in the virtual domain to optimize the design of a mould and identify its process window for a specific drug delivery application. The stage-

gate process we developed increases knowledge, especially about processing parameters such as inlet pressures, shear rates and temperature gradients for different predefined filling times.

Stage-gate analysis of the mould design provides a better understanding of the influence of API in a polymer carrier. A plasticizing effect of the drug was observed, which resulted in lower injection pressure rates but higher mechanical stresses.

Each of the three gates enabled clear decisions to be made on the results and on what was to be taken into account in further stages. Furthermore, a multi-cycle analysis helped to understand the heat flows in the mould over a production period of 20 cycles.

Combining the stage-gate process with criteria from the pharmaceutical industry, in particular maximum residence time and maximum temperature, renders this approach a useful engineering tool in designing moulds for poorly soluble drug delivery systems. The criteria must be defined at the beginning of the process, since modifying them becomes harder from one stage to the next; changing the criteria remains possible, but results in inaccurate process windows.

We believe that this stage-gate design approach will reduce development times and be a helpful tool in other areas in which polymer injection moulding will gain a foothold in the future.

Acknowledgments. The authors wish to thank DI Tobias Mansfeld (Senior Engineer and Sales, Sigma Engineering GmbH, Aachen, Germany) for scientific support in all phases of the study.

The authors wish to express their thanks to Dr. Eggenreich (RCPE GmbH, Graz, Austria) and Dr. Koscher (RCPE GmbH, Graz, Austria) for supplying the material data, and to the Austrian Research Fund (FFG) for financial support.

References

[1] K. Dhirendra, S. Lewis, N. Udupa, et al., Solid Dispersions: A Review, Pakistan Journal of Pharmaceutical Sciences, 22, 2009, p. 234-246, DOI 10.13040/IJPSR.0975-8232.4(6).2094-05

[2] J. Breitenbach, Melt extrusion: from process to drug delivery technology, European Journal of Pharmaceutics and Biopharmaceutics, 54, 2002, p. 107-117, DOI 10.5402/2012/436763

[3] M.A. Repka, S.K. Battu, S.B. Upadhye, et al., Pharmaceutical applications of hot-melt extrusion: part II, Drug development and Industrial Pharmacy 33, 2007, p. 1043-1057, DOI 10.1080/03639040701525627

[4] G. Menges, P. Mohren, How to make injection molds, Carl Hanser Verlag, p.129, 1993, DOI 10.3139/9783446401808

[5] S. Shah, S. Maddineni, J. Lu et al., Melt extrusion with poorly soluble drugs, International Journal of Pharmaceutics, 453, 2013, p.233-252, DOI 10.1016/j.ijpharm.2012.08.034

[6] T. Distlbacher, Design and Simulation of an prototype injection mold for drug delivery systems, Bachelor Thesis, Johannes Kepler University, Linz, 2013

[7] H. Juster, G. Steinbichler, Multi-Cycle hot runner simulation of a polymer drug delivery system by numerical (CFD) methods, Sigmasoft International User Meeting, 2014

[8] P. Unger, Heißkanaltechnik, Carl Hanser Verlag, 2004, DOI 10.3139/9783446401327

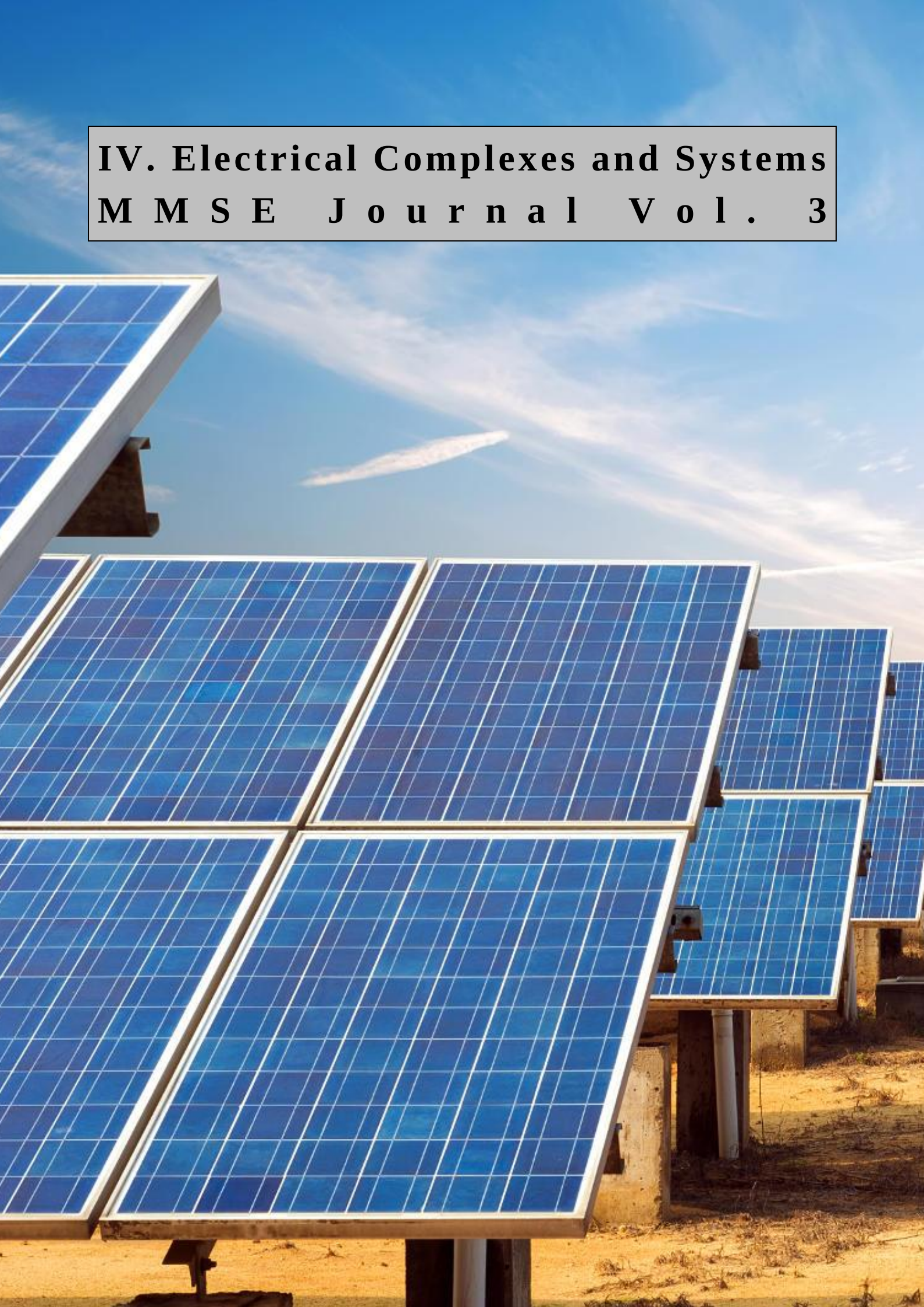
[9] N.N, Technical information: Kollidon VA 64, 2008

[10] SIGMA Engineering GmbH, Manual: Sigmasoft Version 5, 2012

[11] S. Wetzlmair, Untersuchung von Molmassenänderungen beim Spritzgießen pharmazeutischer Darreichungsformen, Bachelor Thesis, Johannes Kepler University, Linz, 2015

[12] K. Kolter, M. Karl, A. Gryczke, Hot-melt extrusion with BASF Pharma Polymers: Extrusion Compendium, 2012

IV. Electrical Complexes and Systems
MMSE Journal Vol. 3



Secondary Power Resources of the Fuel and Energy Complex in Ukraine

Shkrabets F.P.[1], Berdnyk V.V.[2]

1 – Head of the Department of Renewable Energy, professor, National Mining University, Dnepropetrovsk, Ukraine

2 – Postgraduate, the Department of Renewable Energy, National Mining University, Dnepropetrovsk, Ukraine



DOI **10.13140/RG.2.1.2970.7921**

Keywords: secondary sources of energy, coal mines, heat electropower stations, diesel power plants, coal methane, power generation.

ABSTRACT. This article describes the types of secondary energy resources that occur during or as a result of mining or of technological processes at metallurgical, coke and chemical enterprises. The research of opportunities to use them directly at industrial enterprises, in case when an energy resource or the energy generated "is not a commodity" was carried out. To generate electricity from secondary sources, the use of diesel power plants and gas–turbine facilities was offered. The values of investments in the construction of thermal power plants (TPP) based on different types of secondary energy resources were calculated. Tentative capacities of power plants, which utilize the energy of secondary sources were also computed. The figures used for assessing the release and use of secondary energy resources were given. The necessity of using secondary sources of energy to reduce harmful effects on the environment was emphasized.

Introduction. World coal production totals 2.025 billion tons per year (4033 mines). This results in nearly 6 bln tons of solid, liquid and gaseous waste being formed, which is about 3 tons per 1 ton of coal (including dump waste product of 2.5 tons). In underground coal mining, specific output of the rock hoisted onto the surface of the mine constitutes about 0.3 tons per 1 ton of coal. Actually combustible mass in the coal industry is only 20% of the rock mass. As follows, in order to preserve fossil fuel resources the number of which is steadily decreasing in the world and the use of which produces more harmful effect on the environment, one should try to use all their potential. The use of waste, or so–called secondary energy resources (SER), formed during the coal mining, will reduce the harmful effects on the environment and increase the energy potential of Ukraine.

Research objective. Unprofitability of mines associated with the high cost of coal production, large overheads and a complex environmental situation in these regions are considered to be main problems of coal mining enterprises in Ukraine.

1. Coalbed methane. In coal mining, the methane emitted from coal seams can be used as fuel for energy production. The potential of this energy source is immense. Eco–efficiency of methane combustion is high. However, minimum of methane emitted is currently in use. Methane, a primary component of natural gas emitted during the formation of coal is an explosive gas. To ensure the maintenance of methane concentration in mines below the explosive level, the staff must carry out the ventilation of shaft or divert methane to the surface. Coal Mine Methane (CM) refers to methane emitted during coal bed development [1]. Now CM is a potential energy source that can provide electricity and heat, and such an efficient use prevents the flow of it into the atmosphere and reduces the greenhouse effect, because the greenhouse activity of carbon dioxide (CO_2) obtained by burning methane, is 20 times less than greenhouse effect of the gas itself.

Methane obtained in mine development is only 8 % of the total methane emitted due to human activities. CMM can be used for power generation, in boiler houses for heating the residential sector, in gas–fueled vehicles, as motor fuels, in various industrial processes. Mainly, methane is used to produce electricity and heat in mines. In a number of mines, it is insufficient to ventilate only, that is why a special decontamination process precedes the development of mines and is held during their

operation. Degassing is carried out both from the surface through vertical shafts and through boreholes drilled in coal seams. The content of methane in degasification boreholes sometimes exceeds 90 %.

Given the magnitude of these energy resources in Ukraine, the proportion of fuel and energy balance in the country can be significantly affected by the use of coal bed methane, of combustible gas from small gas pools, from condensate and oil–gas fields, of associated gas and combustible gases of anthropogenic (industrial) origin. In addition, changes in the legislative regulations of Ukraine, in particular, direct or indirect promotion of the use of local fuel and energy resources, can enlarge on the list of potential energy sources.

Resources of coal bed methane in coal basins of Ukraine are estimated at 2.5–3.0 trillion. m^3. According to American experts, these resources only in Donbass reach 25 trillion m^3 [1]. Most of the methane is emitted into the atmosphere through the systems of degassing (so called "the captured methane"), of ventilation, it is desorbed from coal and coal stone after its mining and processing. As estimated, at 1 ton of coal extraction on average 10–12 m^3 of methane is emitted. In some fields in Donbass, specific content of methane in coal is up to 500 m^3/t.

In mines and mining towns, only the captured methane is restricted in use. In case of coal mining at 100 mln t/year, annual resources of coal bed methane emitted from coal and discharged into the atmosphere can be estimated at 1.0–1.2 bln. m^3. In case of 50 % utilization of these resources, up to 1.5–1.8 bln KW·h of electricity per year can be generated, which corresponds to 300–400 MW of electrical capacity. For the generation of electricity, gas–turbine installation (GTI) of serial production made by production associations (PA)"Zarya", "Motor–Sich" or mass production diesel power plants of Pervomaysk diesel plant and Malyshev plant (Kharkiv) can be employed, as they have been updated to use coal bed methane and have passed the relevant tests. The most effective use of coal methane is the development of power generation facilities directly in the mines (associations), when the energy resource (methane) and the generated energy are not considered as a commodity. Thus, at the same time, in addition to electricity, completely consumed by the mine or its departments, it is reasonable to utilize the discharged heat power, i.e. the generating facility is to operate as a Heat Electropower Station (HES). Taking into account local conditions, the electrical power of such HES can range from 25 kW to 2.5 MW or even 6 MW. Methane relates to greenhouse gas emissions [2]. In addition, methane is also an ozone–depleting gas, and hence, the use of coal bed methane would have beneficial effect on the environment in Ukraine, and the setting up of "emissions trading" in accordance with the Kyoto Protocol can be a source of foreign currency and foreign investments inflow.

Capital investments in the construction of HES on coal bed methane make up 800–1200 USA dollars/kW·h subject to their capacity and the payback period is of less than 5 years [2]. In the construction of thermal/heat power station, which are to be owned by mines and mine management administration (energy is not a commodity), the investment payback period will take less than 4 years. The urgency for accelerated construction and operation of HES on coal methane stems from the necessity of improving safety in coal mining. The high mortality rate of accidents in mines almost exclusively is associated with explosions of desorbed methane, which creates explosive mixtures with air in the mine area [1]. Given the plans of the President of Ukraine to improve the safety of coal production and considering the availability of equipment for power plants (stationary and even mobile) operating on coal bed methane, it is required to intensify the construction of HES to ensure that by 2017 they will be put into operation with a total capacity of 300 MW. Initially these HES is to be based on current systems of degassing the mines. In the future, it is necessary to take on proactive degasification of coal fields from the surface and only afterwards, start mining operations in coal faces or construction of mines. With the projected increase in coal production in Ukraine, the total capacity of thermal power stations working on coal bed methane can be brought to 1000 MW within the 2020.

2. Combustible gases of small gas, condensed gas deposits and oil–gas condensate fields and associated–dissolved gas. At present, these energy resources are hardly used due to small cross sections of wells, difficulties in their re–activation, lack of the equipment required, low pressures, small reserves, unprofitable supply into the overall system of gas transport, etc. [1]. To ensure the use of this energy source, it is important that a program design provides for manufacture of special equipment for processing raw materials on–site to extract useful liquid oil products, and combustible gas that remains after processing must be used taking into account the technologies of generating the energy for local needs via station or mobile HES . The equipment for such HES (diesel and gas turbine power plant) is available, and it is approved for the use on such gases. These resources are located in eight regions of Ukraine. Gas reserves in all these regions account for about 30.0 bln m^3. Almost half of these reserves are concentrated in Kharkiv. Among the other areas, Lviv region is also noticeable for substantial reserves of gas. In total, there are 39 small fields where 70 wells have been drilled and preserved. Gradually, with the expansion of exploration for oil and gas, new fields and wells will be worked out.

The construction of HES on gas of small deposits should be carried out primarily on the basis of diesel power stations [2]. Specific capital investments in the construction of the HES will amount to 800–1200 USA dollars / kW. Overall development of gas resources in small fields (i.e. the construction of power plants and equipment for the extraction of liquid petroleum fractions) will increase profitability and yield of the respective companies. Recoupment of capital investment depends on specific conditions and can last for 4–7 years.

Given available gas resources in small fields and the associated gas of refining, perspective use of these resources, lack of experience in establishing and operating the enterprises aimed at an integrated use of such resources, and a number of other factors, it is reasonable to set a goal and have built such HES by 2017 with a total electric capacity of at least 100 MW, and then get a total capacity of 400–500 MW by 2020.

3. Combustible gases of industrial origin. In industrial processes of steel, coke and chemical enterprises, such gases occur as by–products [3]. Among these secondary energy resources the biggest are of coke gas, the annual output of which is estimated at 5.2 million tons, blast–furnace – 4.8 million tons, ferroalloy – 0.15 million tons and combustible gases of chemical industry – 0,75 million tons. Total annual output of energy of these resources is estimated at 11 million tons. The bulk of these energy sources, especially coke oven and blast furnace gas is used as fuel in industrial processes at metallurgical and coke enterprises. However, the potential of these gases as a resource is still left unused within the territory of enterprises, and to transport them outwards the enterprise, it is economically impractical and technically difficult. In this situation, economically viable, cost–effective option is to use the existing surplus of these gases on–site of their generation for HES based on GTI [4].

Although the installation of such facilities is to be in accordance with the original design decisions on the development and manufacture of special machinery, nevertheless their cost–effectiveness is supposed to be high. In particular, in some cases, specific investments in the construction of HES based gas turbines using coke oven gas might not exceed 500 $USA/kW, and the payback period of capital investment will take about one year. Taking into account such favorable economic indicators, the development of these secondary energy resources by no later than 2018 is anticipated. Given the amount of the part of industrial gases, which is currently not in use by companies, one can schedule for the construction of HES with a total capacity of 700–800 MW at such plants. In this case, the relevant decision of the government should provide funding from the budget, funds for energy saving efficiency and / or concessional loans of banks. The implementation of these tasks can contribute to the establishment of taxes on the imported fuel and the introduction of "emissions trading" as far as greenhouse gases are concerned.

The main objective in the design of power facilities is to determine methane emission volumes, duration and stability of emissions [4]. Like in the energy sector, for the drive of generators, both

gas–piston engines (GPE) and gas turbines (GT) can be used. The range is the same: with the capacity of above 10 MW, the use of turbine is more appropriate. The advantage of GPE is higher efficiency whenever the methane content is at least 25 %, whereas the turbine can be used at a lower methane concentration.

Methane of lower concentrations (less than 1 %) from the ventilation shafts is also used in power plants, serving as the air for combustion, which increases the efficiency.

4. Gas emissions from industrial plants as SER. The development of energy, industry, transport, chemicals and petrochemicals leads to rapidly increasing consumption of air used as a raw material in the process of oxidation [3]. Chemical, petrochemical, food, pharmaceutical and other industries consume large quantities of clean air and emit huge amounts of exhaust gas and oxygen–contaminated ventilation air.

Perspective is the method of air purification from trace contaminants, i.e. integration of power and chemical complexes [4]. The possibility of combining these processes is achieved by the use of the exhaust air from industrial enterprises as an oxidizer, for example in boiler furnaces. In this case, purification of air pollution from toxic contaminants at a lower cost is provided, and the need for consumption of clean air in order to oxidize the fuel is eliminated.

5. Secondary thermal energy. In their current state, thermal SER are generally used in industry. The largest share is concentrated in such sectors of the economy as metallurgy, chemistry, petrochemistry, and to some extent, in engineering. Heat SER are utilized in evaporation cooling systems of large industrial units, in waste–heat boilers, in systems of utilization the evaporation or condensation, in upcast and downcast systems and many others. Utilization of thermal SER can significantly reduce the need for fuel and improve the economic performance of the final product in general and in particular. The largest share of utilization systems is geographically bound to the areas of heavy industry concentration. In recent years, rates of utilization levels as for thermal SER decreased due to the reasons for the general decline in industrial production, leading to the underload or shutdown of many powerful technological units – the original sources of SER. The equipment of utilization systems of thermal SER requires substantial renovation and modernization. With thermal SER, about 8 million Gcal / y of the final heat consumption is provided, accounting for about 3.0% of the total demand for heat and about 65.5% of the provision in 1990. Since the heat SER are consumed usually near the place of generation, there are no extensive heat networks and heat losses do not exceed 3 % [3, 4].

6. **Gas–expansion machines and generating units** for using the potential energy of natural gas of high pressure of gas mains. In Ukraine, there is a network of gas mains. Gas is pumped under pressure created by compressor stations. Drive units of compressors consume up to 7 % of the pumped gas. For pumping natural gas through pipelines over long distances, it is pressurized by compressors, the pressure in the transport line being increased. The pressure in the pipelines is maintained within 50–70 atmospheres. For consumers, such a high pressure is unacceptable. Therefore, in the field of gas consumption on the highway, the diversion is made to the distribution stations, where the gas pressure drops to 6–12 atmospheres at first, and then, at the distribution points (belonging to large customers and municipal enterprises–retailers), it is reduced to a maximum of three atmospheres. This pressure drop can be used by turbine units (expanders) and makes possible to recover some of the energy consumed by the drive of compressors. Hence, green energy is used, i.e. natural gas pressure drop.

The efficiency of power generation technology using expanders is 4 – 5 times higher than of current thermal power plants. Expander–generator sets with the capacity of 1 to 30 MW have been developed. Nowadays, a turbine expander is estimated by experts as one of the promising turbine products with a large sales market. And the market demand is the highest for capacity range of 1.5 – 6.0 MW [5].

7. Use of mine water energy. The coal industry is characterized by availability of renewable energy sources, which include the heat of mine water, of ventilation emissions, of sewage and household waste dumps [6]. As researched, at mining enterprises, about half of mine water discharged is neutral

with an average temperature of 20 °C. The ground water disposal aimed at preventing the flooding in coal mines is a widespread practice. With this water, a huge amount of energy of a low potential that can be utilized is dispersed into the environment.

On the other hand, there are many mines where every year the problem of heat provision is exacerbated. The old boiler equipment wears out, resulting in a large number of enterprises facing the lack of heat. When using such equipment in winter, the entire amount of the air supplied to the mine is not heated up to the required temperature, there are emergency shutdowns of main ventilating fans that lead to downtime in mines, coal production losses. To reconstruct the existing boiler room and to buy the necessary equipment for the boiler, there are no sufficient funds. In this case, the conventional heat energy (generated by burning solid fuels) causes irreparable harms to the environment and thus, unfavorable changes in the environment occur.

8. The indicators used to measure the output and utilization of SVR: SER utilization factor (1) – the figure represents the ratio of actual (planned) generation to the output of SER:

$$K_1^u = \frac{Q_u}{Q_{out}}, \tag{1}$$

where Q_{out} – is the output of SER [kWh]. The amount of energy generated by secondary energy resources produced during the manufacturing process in the given technological assembly per unit of time; Q_u – energy generation by SER [kWh].

The amount of energy obtained from using SER in a rendering plant. Energy generation differs from its output by the magnitude of heat losses in a rendering plant. There may be the economically expedient, the planned and the actual power generation. This indicator is used if there are no restrictions on the end–temperature potential, as in case of cooling the heating furnaces.

Utilization factor (2) – the ratio, which shows how the heat consumed by the utilizer–boiler relates to the heat of the fuel burned in the furnace. For example, as for open–hearth furnace (OHF):

$$K_2^u = 0{,}143\left(\frac{\alpha_{sp}}{q_{\text{out}}}\right)\cdot 1{,}16, \tag{2}$$

where α_{sp} – the specific production of steam by the utilizer–boiler per melting 1 ton of steel, [MWh/t]; q_{out} – specific consumption of fuel per 1 ton of melted steel, [toe / t].

The ratio can be used to compare the SER use by similar in design and technology assemblies. This indicator can not be used to characterize complex and varied processes (e.g., in non–ferrnous industry).

Utilization factor in general terms (3) is calculated as the ratio of actual (planned) economy of fuel provided by SER use to the possible (or economically expedient) one:

$$K_3^u = \frac{B_u}{B_{out}} \tag{3}$$

where B_u – the actual fuel economy due to the use of SER, i.e. the amount of primary fuel, which is saved as the result of SER use [toe]; B_{out} – possible (or economically feasible) fuel economy, [toe]. Utilization factor is used when the fuel consumption is planned.

The efficiency coefficient of utilization units (4), which represents the ratio of energy generation per unit of material being processed is:

$$K_4^u = \frac{Q_u}{\alpha_{out}\mathrm{N}} \tag{4}$$

where N – the performance of the unit, t/year.

Summary. The benefits of the use of such secondary energy resources as coal bed methane, associated gas, etc. directly at the objects themselves (mines, industrial enterprises) in the case of construction of local HES plants based on diesel power stations or gas turbine installations have been emphasized. In such cases, secondary energy resources and electricity generated by them will not be a commodity, they will be used for their own needs only, and this will reduce the payback period for utilization units. The factors have been given, by which one can assess the rate of SER usage, compare SER utilization factor of similar in design and technology units, as well as determine the effectiveness of utilization units.

Since the cost of fuel resources increases each year, the technologies of processing the secondary energy resources directly at the objects themselves are relevant in these days; the utilization of secondary energy sources will significantly reduce greenhouse gas emissions into the environment.

References

[1] Aleksandrov I. A. (2001). The possibility of using alternative energy sources in Ukraine and Donbass. *Energosberezhenie №5*, P. 15–21.

[2] Shuklin L. I. (2001). Independent energy supply on the basis of secondary and low–potential energy resources. *Energosberezhenie №6*, P. 14–16.

[3] Rihter L. A. (2008). Secondary energy resources of ferrous metallurgy, and their use. «*Vysshaya shkola»,* 328 pp.

[4] Tolochko A. I. (2001). Protecting the environment from emissions of the ferrous industry. «*Metallurgiya»,* 95 pp.

[5] Gataullina A. R. (2012). Overpressure energy utilization of transported gas in compressed–gas engine generator sets. *Sbornik trudov XVIII Vserossiyskoy nauchno–tehnicheskoy konferentsii «Energetika: effektivnost, nadezhnost, bezopasnost»,* P. 171–174.

[6] Chemeris I. F. (2006). The use of the energy potential of the mine ventilation stream. *Geotehnicheskaya mehanika: Mezhved. sb. nauch. tr. Vyp. 67,* P. 359–370.



VI. Power Supply Technologies
MMSE Journal Vol. 3

Monitoring of the Thermal State of Induction Motors with Low Quality Power Supply

Girnik A.S. [1] & Fedyanin A.L[1]

1 – Department of Electrotechnical complexes and materials, Tomsk Polytechnic University, Tomsk, Russia



DOI **10.13140/RG.2.1.1637.3520**

Keywords: monitoring, thermal, unbalance, rotor.

ABSTRACT. An innovative technological system that provides the control process of the induction motors thermal state, when exposed to unbalanced supply voltage or power supply which can have the presence of higher harmonics frequencies and with the presence of technological defects in the rotor winding. The monitoring system calculates the temperature of the stator and the rotor on the basis of transfer functions, which take into account the impact of individual factors of low quality power supply. The calculation of the thermal state can occur in real-time.

Introduction. The system providing control of an overheat of asynchronous engines at influence of asymmetrical feeding pressure with presence of the higher time harmonics and in the presence of technological defects of a winding of a rotor is developed.

Topicality. Recently, upon failure of the auxiliary electrical machines (AEM) on electric because of the influence of various unfavorable factors [1]. These factors include:

1) unbalance power supply;

2) the presence of higher harmonics frequencies;

3) poor quality of manufacturing rotor.

This is particularly a problem for auxiliary motors, working on locomotives. This is confirmed by statistics of failures caused by auxiliary machines.

Solution. In this paper we consider a universal monitoring system, which allows to control the overheating of induction motor based on measurements of phase voltages and currents. Unbalanced power usually causes additional losses in the stator and rotor induction motor. These losses lead to overheating and reduce the life of stator winding insulation.

Already, there are ways to control the state of induction motors, using information about the consumed currents. For example a way to monitor the condition of the rotor and stator currents [2], [3], [4]. Existing methods do not give a complete picture is the thermal state of the engine, based on current consumption. Especially if it is necessary to take into account factors such as unbalanced and sinusoidal voltage, as well as the presence of defects in the rotor shaft.

This system allows to take into account such factors.

Figure 1 shows a block diagram of a monitoring system consisting of the measurement circuit and the microprocessor unit (MPU) with appropriate software (SW). The circuit comprises sensor measurements of phase voltages Dn1, Dn2, Dn3 and current sensor analog-digital converter ADC. LPA Software, created by the system software NI LabVIEW [5]. The algorithm of the system is as follows. With sensors Dn1, Dn2, Dn3 removed and the values of phase voltages. In the ADC, they are converted into digital form and transmitted to the MPU. Here, these voltages are processed in order to isolate the input from the following harmonics: main (first), third, fifth and seventh. For the first harmonic it is also determined and the initial phase angles for all three phases. According to

Theorem Fortescue [6], any asymmetric system can be decomposed into three symmetrical - a system of positive sequence, negative and zero. With this in mind, for the first harmonic is the definition of each of these sequences. To top the third, fifth and seventh, these sequences are not determined, since they usually make up a relatively small part of the fundamental and significant impact on the non-uniformity of thermal heating of stator. These harmonics are more strongly affect the thermal state of the rotor due to the guidance in it more of EMF with increased frequency.

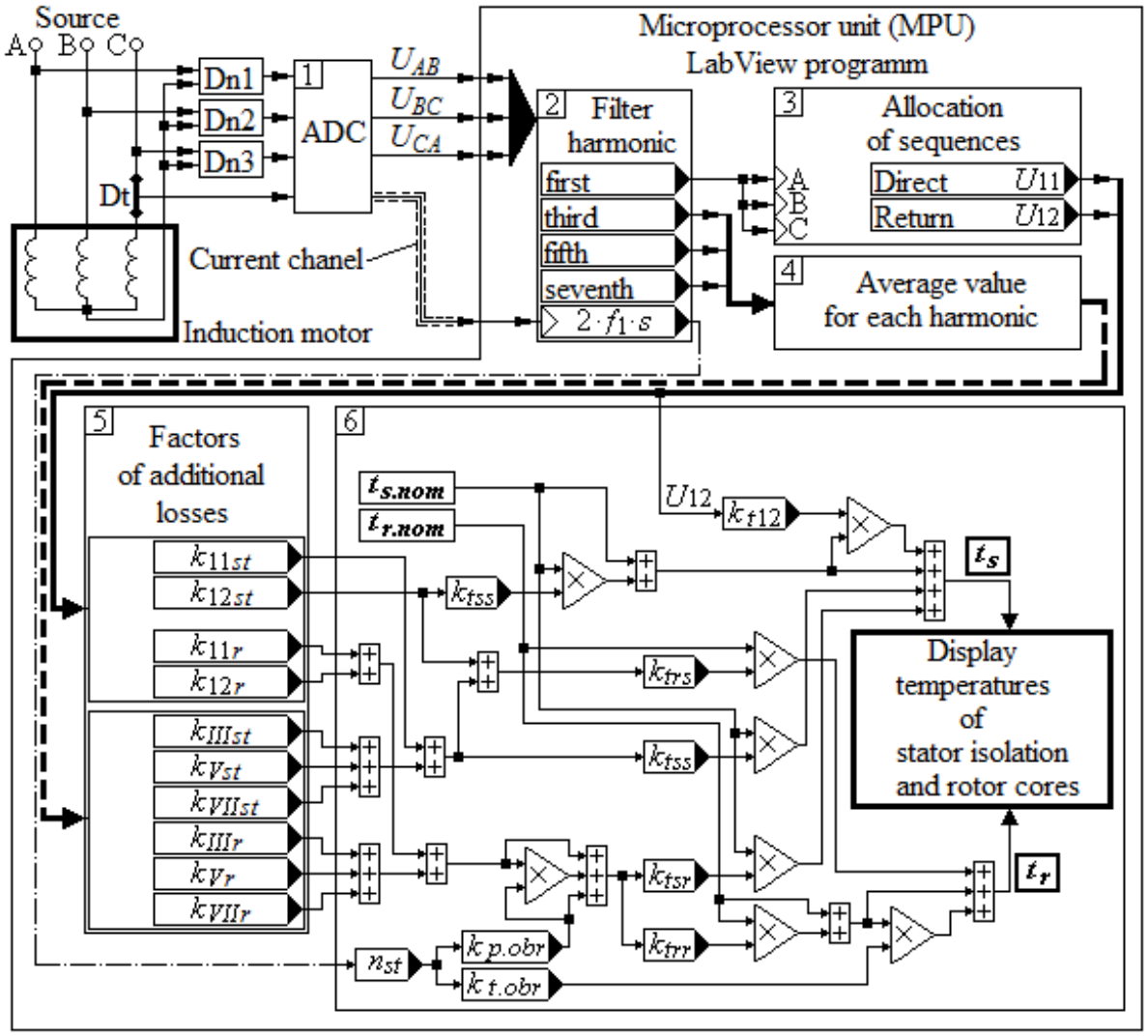


Fig. 1. The block diagram of the monitoring system of the induction motor

However, the asymmetry of these harmonics is practically no effect on the uneven heating of the rotor. For the higher harmonics in the phase voltages are determined by the average value of their units. The frequency of the induced EMF of these harmonics can be expressed by the formula $fv=f_1 \cdot (s-1 \pm v)$, where f_1 - frequency of the basic harmonic (50 Hz), s - sliding, v - number of the higher harmonic. The sign «+» at a symbol «v» testifies that the field from the higher harmonic of feeding pressure rotates in the same party, as the basic field, a sign «-» - in return.

According to studies, it was found that each sequence of three-phase voltage system in its own influence on the occurrence of additional losses in the motor. Thus:

• The level of positive sequence voltage affects the uniform change in the phases of the stator and rotor currents.

• The increase in pressure of return sequence leads to a warp of currents in stator and on increase total stator losses. Besides, this pressure leads to occurrence electromotive power and a current in a rotor with the doubled frequency (the second harmonic) in relation to frequency of feeding pressure, and, hence, to additional losses of a rotor.

On this basis following factors of additional losses in stator and rotor are calculated:

k_{11st} и k_{11r} – coefficients of the additional losses in the stator and the rotor under the influence of positive sequence voltage;

k_{12st} и k_{12r} – coefficients of the additional losses in the stator and the rotor under the influence of negative sequence voltage;

k_{10st} – coefficient of the additional losses in the stator under the influence of zero-sequence voltage;

k_{IIIst} and k_{IIIr} – Coefficients of the additional losses in the stator and the rotor under the influence of the third harmonic voltage;

k_{Vst} and k_{Vr} - coefficient of the additional losses in the stator and the rotor under the influence of the fifth harmonic voltage;

k_{VIIst} and k_{VIIr} – coefficient of the additional losses in the stator and the rotor under the influence of the seventh harmonic voltage.

These coefficients are calculated by dividing the loss of electric heating the engine with the appropriate power factor influencing the loss obtained in the nominal mode of the machine. Heating is the loss of the engine to find the sum of products of the electric resistance of a particular section of the square of the current flowing through it. Accordingly, the currents are calculated using a mathematical model of an induction motor in phase coordinates. The model was constructed based on the basic relations [7] and implemented in a software package MATLAB 7.

Below are the results of calculations of the coefficients for the auxiliary motor NVA-55, has the following options: synchronous speed 1500 rev/min, the active resistance of stator and rotor phase R_1=0.045Ω and R'_2=0.064Ω; inductance of the field scattering phase stator and rotor $L_{\sigma 1}$=0.00038H and $L'_{\sigma 2}$=0.0005H; mutual inductance of phases stator and rotor L_m=0.01H; number of phases of a rotor m_2=38; number of pairs poles p=2; the moment of inertia of a rotor together with the inertia moment moving mechanism J=1 Kg·m^2; nominal 3-phase supply voltage 380/220V, 50Hz. Scheme winding connection - "Star". These parameters were determined using the method [8].

Figure 2 shows the dependence of the coefficients of the additional losses from the line voltage levels, negative and zero sequences, as well as the level of the higher harmonic frequencies.

Further, based on the coefficients of the additional losses are calculated coefficients of the additional temperature in relative units. The auxiliary motor NVA-55 [9] to isolate the stator temperature at rated speed is 140 ˚ C for the rotor shaft 145 ˚C. These coefficients depend on the additional losses in the stator kps and rotor kpr designated as:

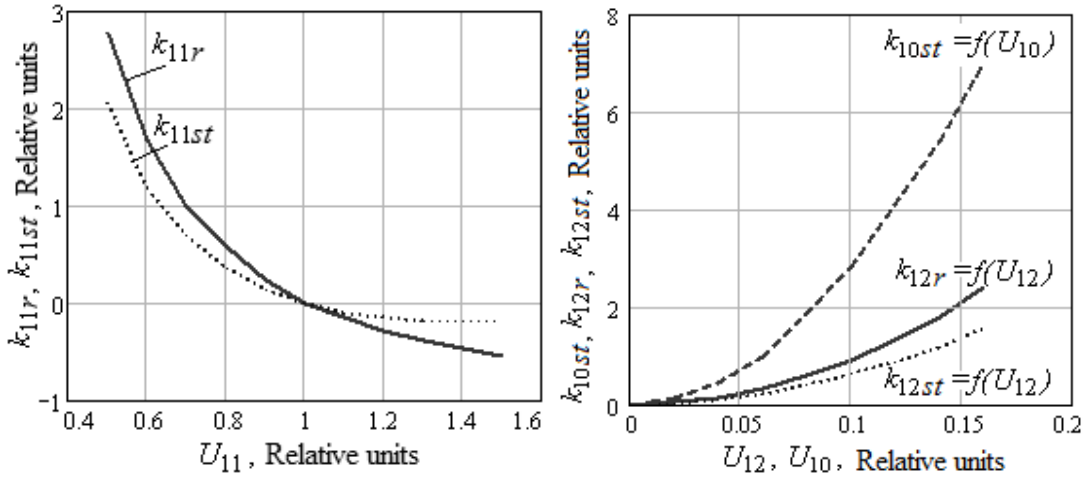
k_{tss} – additional temperature coefficient of the stator insulation under the influence of additional losses in the stator. It uses the transfer function, shown as in fig. 1;

k_{trs} – additional temperature coefficient of the rotor shaft under the influence of additional losses in the stator. Transfer function on fig. 1;

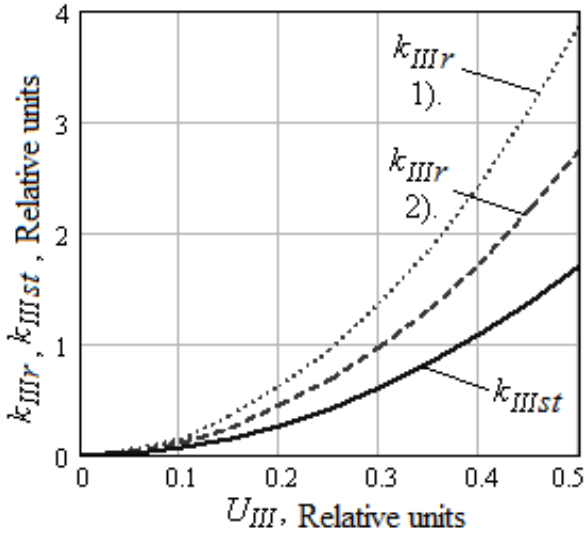
k_{trr} – additional temperature coefficient of the rotor shaft under the influence of additional losses in the rotor. Transfer function on fig. 1;

k_{tsr} – additional temperature coefficient of the stator insulation under the influence of additional losses in the rotor. Transfer function on fig. 1.

Values of factors of additional temperature in relative units are resulted on fig. 3.



(a) *(b)*



(c)

Fig. 2. The coefficients of the additional losses in relative units, 1 *- the field of higher temporal harmonic rotates in the opposite direction with respect to the main field,* 2 *- time the field of higher harmonic rotates in the same direction as the main*

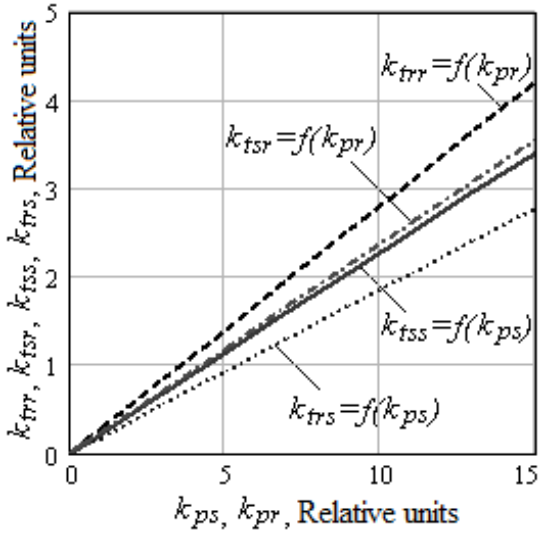


Fig. 3. The coefficients of the additional temperature in relative units

These values were obtained using a software package ELCUT [10] as follows:

• k_{tss} obtained from the experiments of change of the additional losses in the stator at a constant losses in the rotor;

• k_{trs} as well as ktss, the temperature calculated for the rotor;

• k_{trr} obtained from the experiments changing the ditional losses in the rotor at a constant loss in the stator;

• k_{tsr} as well as ktrr, the temperature calculated for the stator.

ELCUT software product designed to simulate the thermal fields of electromechanical transducer finite element method. The necessary input data for calculation of specific losses were attributable to the unit volume of an area, the properties of the surfaces of heat and thermal conductivity of the materials motor parts.

It should be noted that the above factors added temperature calculated taking into account the fact that the total losses, they have caused, are uniformly distributed on the stator and rotor. This was achieved using the data in the calculation of equivalent current losses in all three phases, as a result of which, the total losses are losses in the non-uniform current load. And finally to more accurately determine the actual temperature of the stator insulation, using special coefficients, called the bias temperature coefficients (see figure 4). These coefficients were derived from the calculated data using the program ELCUT.

In addition to the above listed, for the calculation of the possible change in temperature of the rotor bars under the influence of their workmanship, is the display of the stator current frequency harmonics $2 \cdot f_1 \cdot s$ using a current sensor Dt is made. This current Is.д.c increases with the number of defective rods (figure 5b). On the schedule value of this current in relative units in relation to actual value of a current of the first harmonic in a phase means.

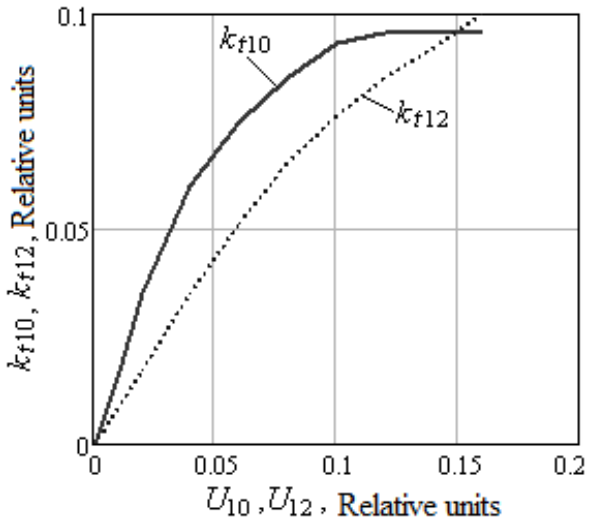
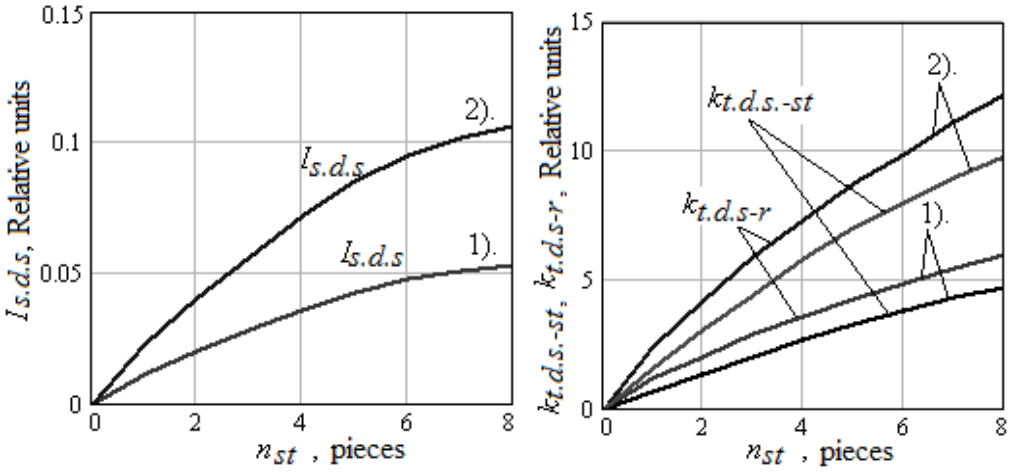


Fig. 4. The coefficients of the conditional bias temperature uniform in relative units from the actual to the stator losses caused by the zero voltage U_{10} and U_{12} reverse sequences.

The principle indication is based on the fact that the rotor bars with defective system of currents become unbalanced and there will be negative sequence current, which induces in the stator winding additional EMF, which leads to the pulsation of the stator current with a frequency $2 \cdot f_1 \cdot s$. The magnitude of this current can be judged on the degree of damage to the engine from overheating, defective areas of the rotor bars.



(a) *(b)*

Fig. 5. Depending on the presence of faulty rotor bars: a - coefficients of the additional stator temperature kt.d.s-st and a rotor kt.d.s-r; – a current stator frequency $2 \cdot f_1 \cdot s$*; 1 – a case when the section of transition of a defective site of a core is reduced in 9 times;* 2 *- too at the reduced section of transition in* 16 *times.*

It should be noted that the decrease in area under different sections of the transition of the defective part of the bar, the additional temperature increase by approximately the same time, how much current is increased frequency of $2 \cdot f_1 \cdot s$ (figure 5). This proportion is very easy to harp on this current one could judge the overheated motor. The resulting coefficients allow calculating the temperature of the stator insulation of the rotor shaft *ts* and *tr* using their nominal temperature and rotor $t_{s.nom}$ and $t_{r.nom}$. The values obtained are compared with the maximum allowable temperature, above which the operation of the motor is an emergency.

Summary. The developed system of monitoring of induction motors with low quality power supply allows you to quickly calculate the heating of the stator and rotor windings during operation and the signal reaches the limit temperature. Calculations were carried out by the example of an asynchronous auxiliary engine NVA-55 is installed on the locomotive 2ЭС5К "Ermak" [11]. Feature of the proposed monitoring system is not necessary to install temperature sensors in the motor. By determining the temperature produced by indirect means of system. For implementation of this algorithm is sufficient to calculate a single sample pre-factors for the particular motor and enter them into the memory of the microprocessor unit. After this, the monitoring system can operate in real time for optimum performance of motor.

References

[1] Ivanov-Smolenskij A.V. Electric cars, vol. 1. Publishing house MEI, 2004, p. 652.

[2] Howard W Penrose, Ph.D. “Motor current signature analysis and interpretation”. General Manager ALL-TEST Pro A Division of BJM Corp 123 Spencer Plain Rd Old Saybrook, CT 06475, 2004.

[3] William T.Thomson, Mark Fenger. “Development of a tool to detect faults in induction motors via current signature analysis”. IEEE Industry Application Magazine July, August 2001.

[4] William T. Thomson. “Motor current signature analysis to detect faults in induction motor drives-fundamentals, data interpretation, and industrial case histories”. AMEC Upstream Oil & gas, Nigg, Aberdeen, Scotland, 2003.

[5] Suranov A.Y. LabVIEW 8.20 Function Reference. DMK Press, 2007, p. 536.

[6] Voldek A.I. Electrical machines. Energy, 1978, p. 832.

[7] Designing of electric cars / Under the editorship of I.P.Kopylov. The Higher school, 2002, p. 757.

[8] Goldberg O.D. Tests on electric cars. The Higher school, 2000, p. 255.

[9] Specifications. “Asynchronous type of NVA”. NPO NEVZ, VelNII, 1999, p. 28.

[10] Server support of elkat program. [Online]. Available: http://elcut.ru

[11] Assistant locomotive drivers. [Online]. Available: http://pomogala.ru/wiki/ermak.html



VII. Environmental Safety

MMSE Journal Vol. 3

Nasal Bone Fractures In Children And Adolescents.

Patient Demographics, Etiology of The Fracture and Evaluation of Plain Film Radiography as a Diagnostic Method in Children's Clinical University Hospital

Marks Ronis[1], Linda Veidere[1], Daiga Marnauza[1], Lana Micko[1], Lasma Bidina[1], Janis Sokolovs[2]

1 – Riga Stradins University, Faculty of Medicine, Latvia

2 – Children's Clinical University Hospital, Department of Otorhinolaryngology, Latvia



DOI **10.13140/RG.2.1.4639.4001**

Keywords: otorhinolaryngology, nasal, trauma, pediatrics, x-ray

ABSTRACT. Nasal bones are the second most common site of fractures in the craniofacial area in pediatric population. Nasal fractures are less common in very young children mostly due to underdeveloped nasal bones and other factors. Nasal bone fractures can be diagnosed clinically. Plain film radiographs are not indicated if an uncomplicated fracture is suspected. They may be difficult to interpret and have low specificity and sensitivity.

Aim. To retrospectively collect data of patients admitted to the Children's Clinical University Hospital, Otorhinolaryngology department with the diagnosis „Fracture of nasal bones" S02.2 (ICD-10) from 01.01.2012 to 31.12.2014. To obtain descriptive statistics concerning pediatric patients. Also, to evaluate if the plain film x-ray is a necessity when diagnosing nasal bone fractures and its impact on the decision for surgical reduction of the fracture.

Results. During the time period of three years given above there were 153 patients admitted to the ENT department with diagnosis S02.2. Among those 120 (78,4%) were male and 33 (21,6%) were female. Most patients, 103, were 13 to 17 years old. The etiology of trauma was obtained from 89 (58,2%) patients' histories. Convincingly the most common cause was sports trauma in 43. Statistical analysis showed no statistically significant connection (p=0,296) between the positive findings of nasal bone fractures and the decision to perform a reduction of the fracture. However, it showed a statistically significant association (p<0,05) between deformity of the nose and the decision to perform the reduction.

Conclusions. Based on the descriptive statistics a risk group of nasal bone fracture patients in pediatric population can be outlined – boys who do contact sports in their early teenage years. As to plain film radiography it is safe to conclude that it is unreliable for the evaluation of nasal fractures in children. Furthermore, this study showed, that the decision for the surgical reduction of the fracture can be based on the results of a thorough patient examination and the fact that the patient presents with a visual deformity of the nose.

Introduction. Nasal bones are the second most common site of fractures in the maxillofacial area in pediatric population [1, 2]. Still the incidence is much lower than in adults. In adolescence, a nasal bone fracture pattern more closely resembles that of adults [3]. In very young children, however, nasal fractures are less common mostly due to underdeveloped nasal bones and less prominent nasal pyramid [4]. Therefore prevalence of pediatric nasal bone fractures increases progressively with increasing age. Two peaks have been observed in the frequency of such fractures: The first, at the age of 6–7 years, is associated with the beginning of school attendance [9]. The second, at 12–14 years, is related to increased physical activity and participation in sports during puberty and adolescence [9,12]. In pediatric patients sports and falls are the major causes of isolated nasal bone fractures. There is a marked preponderance of boys in the worldwide pediatric population affected by facial fractures, with the male-to-female ratio ranging from 1.1:1 to 8.5:1, depending on the study [9, 10, 12]. The predominance of boys is attributed mainly to the fact that their physical activity is more intense and more hazardous than that of girls.

To properly treat nasal bone fracture it is important to evaluate and diagnose it by physical or radiologic examination. In general, these fractures can be diagnosed by clinically identifying crepitus and

tenderness [5]. If an uncomplicated nasal fracture is suspected, plain film radiography is rarely indicated [6]. Previous studies show that plain radiography yields negative results in 25 % of patients who required surgical intervention [7]. A study by de Lacey found that plain films had a 66 % false-positive reading as a result of the misinterpretation of normal suture lines, vascular indentation lines, or developmental thinning of the nasal bones (8). Plain radiographs of the nose in pediatric patients are especially difficult to interpret because of possible growth plate fractures and cartilaginous injuries [9, 10]. Due to low sensitivity of plain x-ray imaging, its' efficiency in clinical decision making has become controversial [11] (Figure 1). Over the course of 3 years, at least 136 nasal bone radiographs in multiple projections have been ordered in Children's Clinical University Hospital mostly due to possible legal matters but also because of patients' parents' concerns about the required reduction of the fracture without what they believe to be a critical step in diagnosing – nasal bone x-ray.

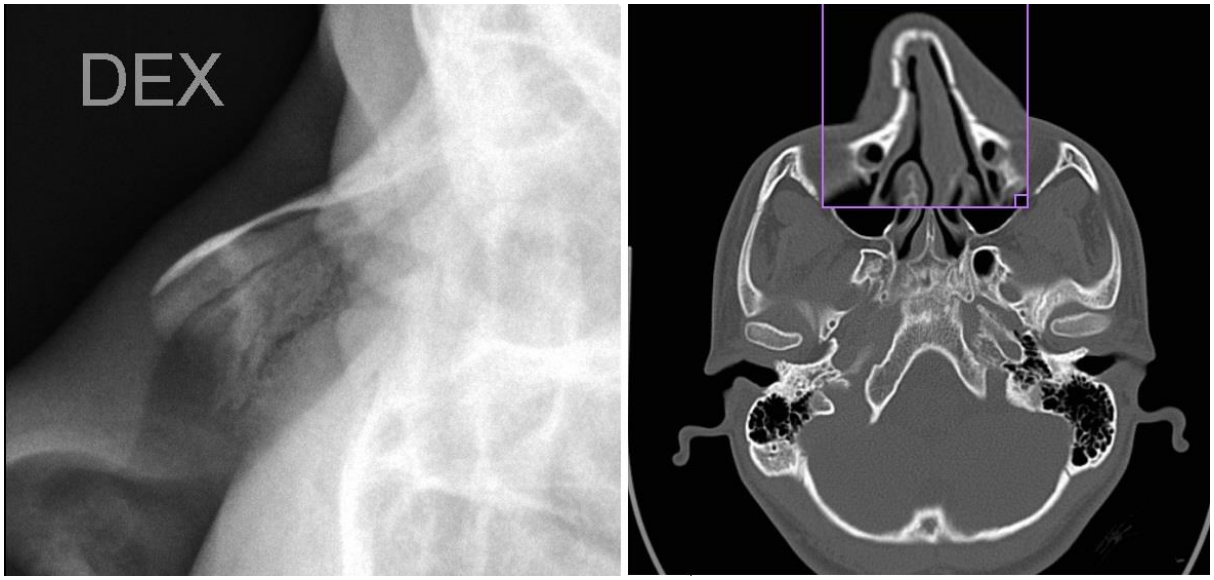


Fig. 1. On the left: a plain film radiograph of the right nasal bone of a patient from this study. Note the seamingly normal appearance of the nasal bone. On the right: a head CT scan of the same patient, performed on the same day as the radiograph. Note the fracture of the right nasal bone with a slight dislocation (white arrow)

Aim. The aim of this study was to identify the characteristics in the demographics of pediatric patients with nasal bone fractures and find the most common causes of the trauma to further establish possible risk groups.

The second objective was to evaluate whether plain film radiography is a crucial diagnostic procedure, which further determines the necessity of a reduction of the fracture in children presenting with nasal trauma in Children's Clinical University Hospital.

Materials and Methods. Using a retrospective study design records of 153 patients admitted to the Children's Clinical University Hospital (Riga, Latvia) department of otolaryngology with the diagnosis „Fracture of nasal bones" S02.2 (ICD-10) from 01.01.2012 to 31.12.2014 were studied. Data was gathered using patient data from Children's Clinical University Hospital's information system "Andromeda". Statistical analyses were performed using IBM SPSS Statistics ver. 22 software. $p<0,05$ was considered statistically significant.

Descriptive statistics concerning patients' age, gender, month in which the trauma occurred, etiology of the trauma were obtained. Patients were sorted into three age groups: preschool children (less than 7 years old), primary school children (7 to 12 years old) and teenagers (13 years and older). Depending on the etiology of the trauma, patients were categorized into five groups: traffic accident,

sports trauma, domestic trauma (including accidental falls), fight without criminal character between peers and fight with criminal character (including domestic abuse, beating by a group of people, assault on the street by a stranger). χ^2 test was applied to determine if there was a statistically significant difference between the etiology of the nasal bone fracture in different age groups.

Cross tabulation with χ^2 test was used to determine if there was any connection between positive radiologic findings and treated patient rate as well as between visual deformity of the nose on initial physical exam and treated patient rate.

Results. A total of 153 patients' records were selected for further analysis. Patients were from 2 to 17 years old with the mean age at the moment of nasal bone fracture of 13.21 years (±3,45). 120 (78.4 %) patients were male and 33 (21.6 %) were female. Most frequently, the trauma occurred in April and March (20 and 19 cases respectively). The mean duration of hospital stay was 3,42 days (± 1.98).

The precise etiology of trauma was obtained from 89 (58,2%) patients' histories (Figure 2) due to lack of specific information about the trauma in some cases. The most common cause was sports injury in 43 cases. Comparing the cause of trauma in two separate age groups: teenagers in which the majority of the traumas occurred (103 cases) and primary school children revealed that the most common type of trauma in both groups was sports trauma followed by fights among peers without criminal character for teenagers and household trauma for primary school children (Figure 3). Pearson's χ^2 test revealed that there is statistically significant difference in nasal bone fracture causes between these groups. There were only 7 patients in the preschool group of which only one record specified the cause of trauma therefore this group was excluded from statistical analysis. It is worth pointing out that while the male/female ratio stayed similar in both the preschool and primary school children 1.9:1, in teenage group the number of males tripled while the number of female patients stayed the same resulting in a male/female ratio of 5.9:1.

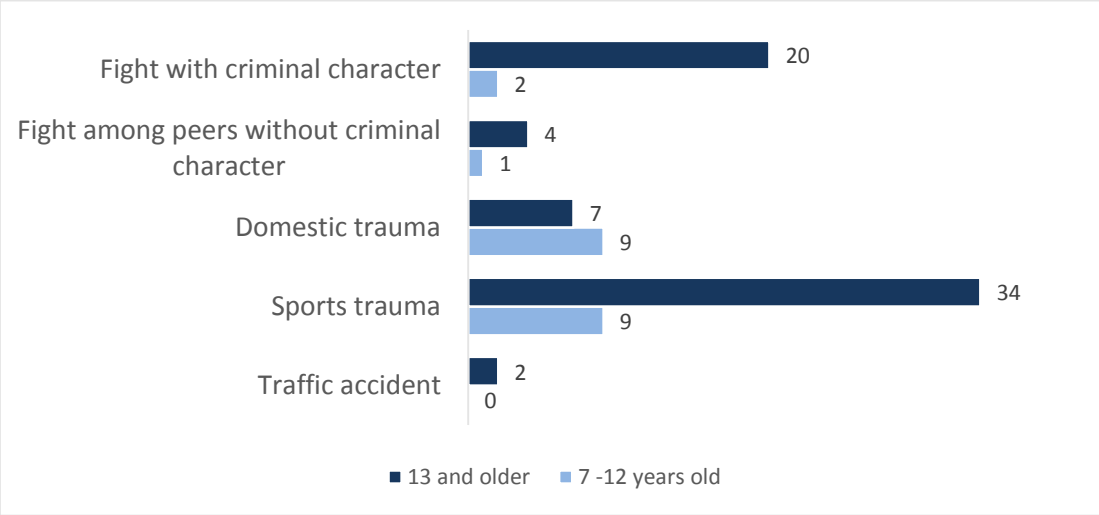


Fig. 2. The causes of nasal bone fractures in teenage and primary school age groups

136 (88.9 %) patients underwent plain film radiography of nasal bones in at least 2 projections. 6 of these patients had diagnostic imaging done outside Children's Clinical University Hospital and there was no official radiologist's conclusion in the records. Due to this fact only the rest 130 patients were selected for further analysis of which 92 had a confirmed nasal bone fracture on plain film radiographs, while the rest 38 had no confirmation of fracture using this imaging modality.

Out of all patients 114 had a mention of visual deformity of the nose on the initial clinical examination by an otorhinolaryngologist at Children's Clinical University Hospital while 9 patients did not present with a visual deformity and 30 patients had no data concerning the visual appearance of the nose.

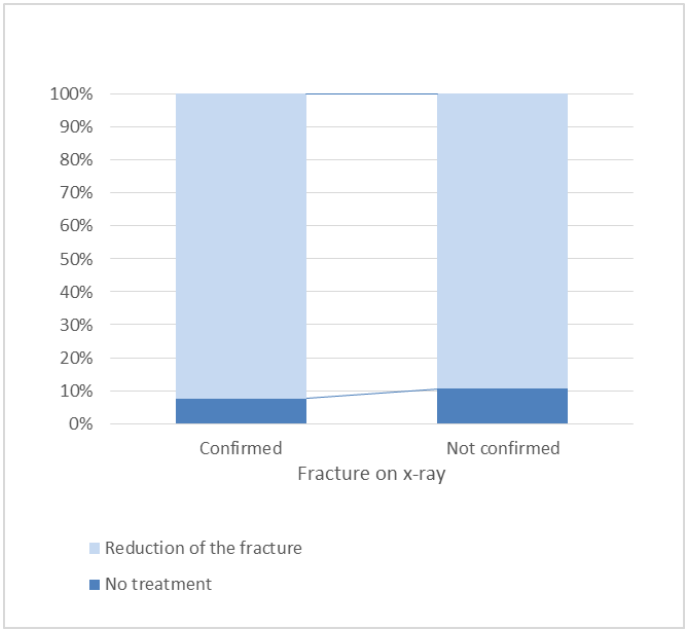


Fig. 3. Even on graphical presentation of the data there is only a slightly noticeable difference between the patients who had a confirmed fracture on the x-ray and those who did not

The statistical analysis of Pearson's χ^2 showed that there is no statistically significant connection ($p=0,296$) between the positive findings of nasal bone fractures and the decision to perform a reduction of the fracture (Figure 4). However, it showed a statistically significant association ($p<0,05$) between deformity of the nose and the decision to perform the reduction (Figure 5).

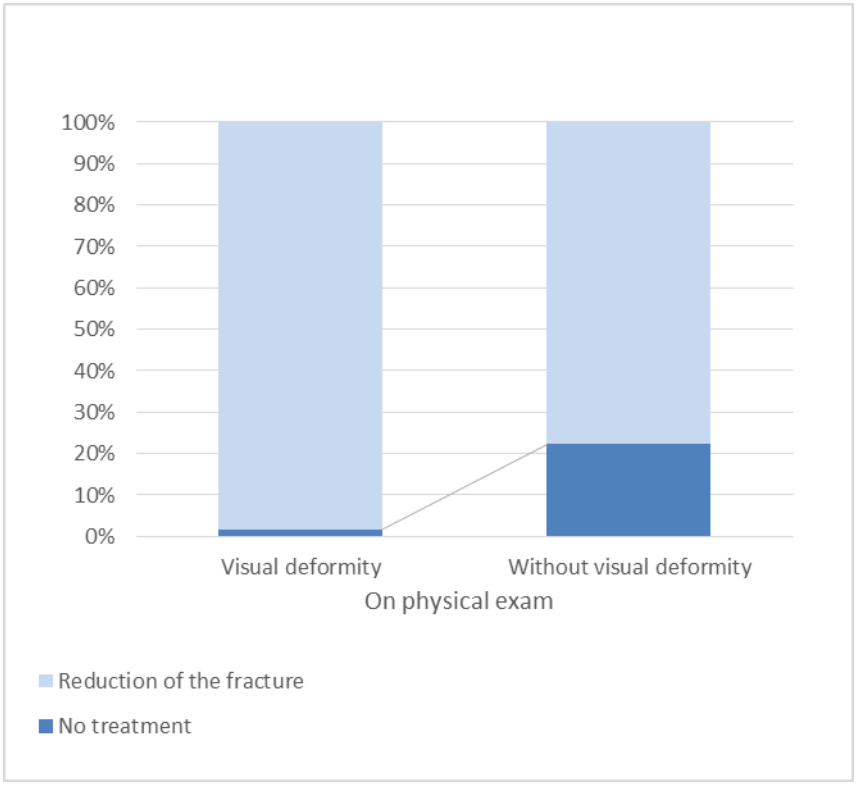


Fig. 4. The difference, unlike in Fig. 3, is visible when comparing those with visual deformity of the nose after trauma with those who had no deformity

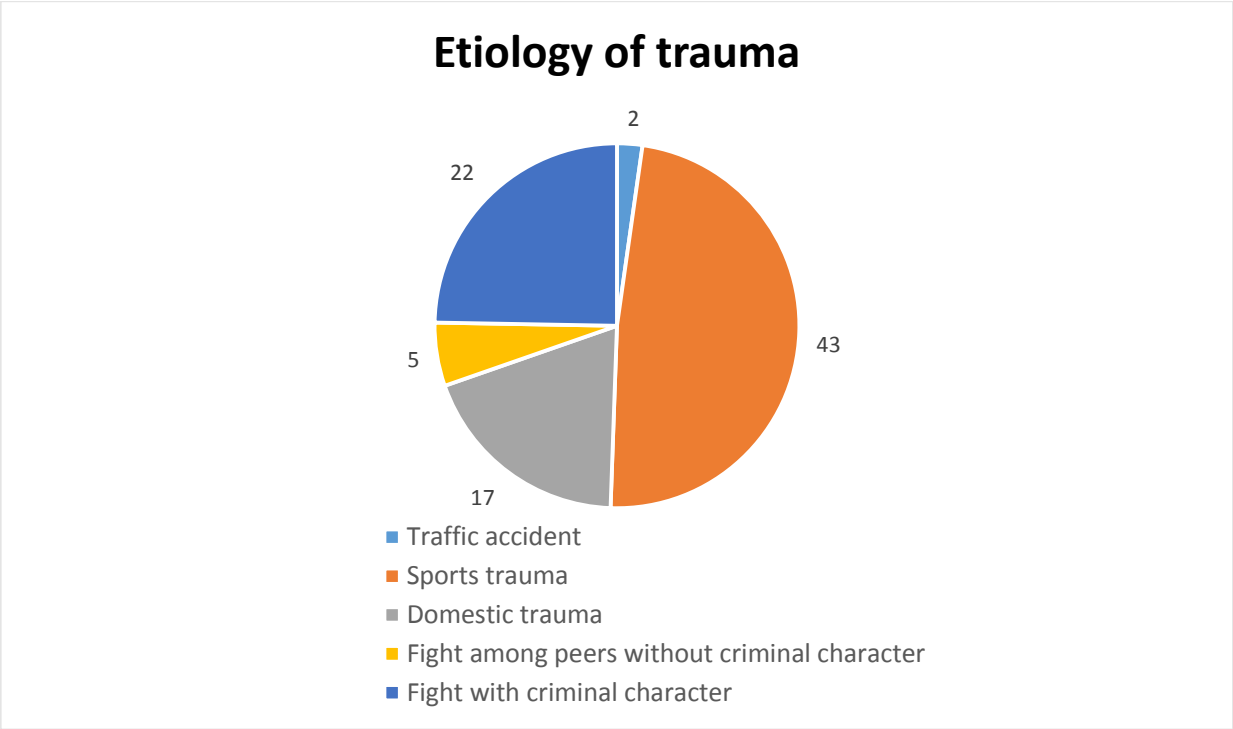


Fig. 5. Etiology of trauma

Discussion. Male patients are at higher risk of nasal bone fractures, especially in their teenage years. In puberty fights among peers with resulting nasal trauma are common among males, however trauma acquired during sports activities such as football, basketball and martial arts, all of which can be described as contact sports, remains the number one cause of nasal bone fractures in the teenage portion of the pediatric population. The high number of male patients is what brings this age group to have the most cases. The number of female patients does not change much with age and the relative increase in the primary school group could be explained with the fact that they start school and are left without the attention of adults more frequently. This could also be true in accordance to males in the primary school group as this is the age at which most parents decide that their children should also do after school activities of which sport is the most popular. Nasal bone fractures in preschool children were rare. There are some limitations to this study in case of etiology because only 89 records contained precise description of how the trauma occurred, especially in younger children. Also, this study showed very small number of patients in the traffic accident etiology group, this may be due to the fact that these patients have polytrauma and are treated in other departments of the hospital with an otorhinolaryngologist as a consult. To sum up, demographic data (predominance of male patients and patient number increase with age) and trauma etiology (sports trauma as the most common) corresponds with the tendencies given in existing literature and studies [9, 10, 12] – the small incidence peak at the start of school attendance and the bigger peak in teenage years during puberty (Figure 6).

This study shows that plain film radiography has little or no role in clinician's decision to perform reduction of the nasal bone fracture. Several patients with positive findings on x-ray examination have been left untreated, while some of those who had no signs of fracture on the x-ray images still underwent the reduction of the fracture. The diagnosis "fracture of nasal bones" remains mostly dependent on the findings on the initial examination by an otorhinolaryngologist. The most significant finding being the visual deformity of the nose, which in many cases indicates the necessity to perform a reduction of the fracture. Over the course of 3 years at least 136 nasal bone radiographs have been done in Children's Clinical University Hospital. The government's funding for this procedure is 4 euro and 15 euro-cents per projection. That makes at least 564.40 euro in total for a method that is reported to be only 72 % sensitive and 73 % specific [13].

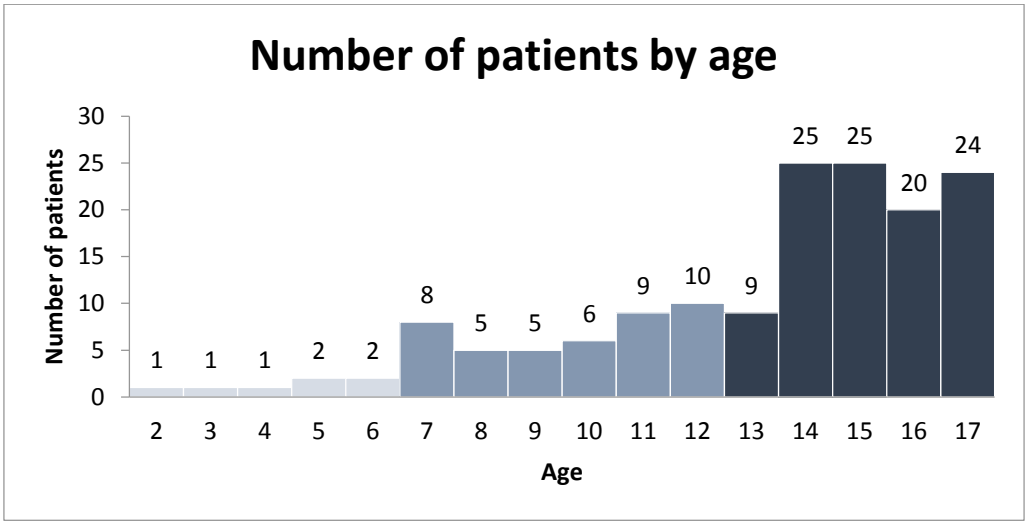


Fig. 6. Incidence of nasal bone fractures by age. Notice the small peak of incidence at 7 years and the big peak at the onset of puberty at 14 years

However, due to legal matters it is still important to confirm nasal bone fractures using diagnostic imaging. Computer tomography (CT) is a great alternative for detecting nasal bone fractures with sensitivity and specificity near 100 % [13, 14]. Yet, ordering a CT scan for younger children often requires sedation or general anesthesia. Additionally there are risks of radiation-induced leukemia and brain cancer with CT head scans [15]. In this study 12 patients underwent a CT head scan ordered by a neurologist on account of neurologic symptoms such as severe headache or short loss of consciousness after the trauma. Unfortunately, the sample size of these patients was too small to yield any statistically correct results concerning the accuracy of CT in the diagnosis of nasal bone fractures. The CT scan confirmed nasal bone fractures in 9 patients.

In the past decade, the use of high-resolution ultrasonography (HRUS) in detecting nasal bone fractures has emerged. There have been numerous publications comparing HRUS to plain film radiography and CT in all of which the specificity and sensitivity of HRUS was near 100 %. Another advantage of HRUS is that it is radiation free and doesn't require the patient to be completely still during examination [13, 16, 17]. Taking into account the poor performance of plain x-ray imaging shown in this study and the radiation hazards and complexity of performing CT head scans in younger children, authors suggest that a new study should be conducted using HRUS as a diagnostic procedure in nasal bone fractures alongside plain film radiography. This would help to bring a safer and more precise imaging modality into everyday practice.

Summary. A risk group of nasal bone fracture patients in pediatric population can be outlined; they are predominantly males 7 to 17 years of age with a peak of incidence at the time of puberty. Children, including females, who do contact sports, are at higher risk of nasal bone fracture. These fractures are very rare in children less than 7 years of age.

It is safe to conclude that plain film radiography is unreliable for the evaluation of nasal fractures in children. Furthermore, this study showed, that the decision for the reduction of the fracture can be based on a thorough otorhinolaryngologist's examination and the fact that the patient presents with a visual deformity of the nose.

References

[1] Muñante-Cárdenas J.L., Olate S., Asprino L., et al: Pattern and treatment of facial trauma in pediatric and adolescent patients. J. Craniofac. Surg. 2011; 22: pp. 1251-1255.

[2] Imahara S.D., Hopper R.A., Wang J., et al: Patterns and outcomes of pediatric facial fractures in the United States: a survey of the National Trauma Data Bank. J. Am. Coll. Surg. 2008; 207: pp. 710-716.

[3] Lee D.H., Jang Y.H. Pediatric nasal bone fractures: Does delayed treatment really lead to adverse outcomes? Int. J. Pediatr. Otorhinolaryngol. 2013; 77: pp. 726-731.

[4] Desrosiers A.E., and Thaller S.R.: Pediatric nasal fractures: evaluation and management. J. Craniofac. Surg. 2011; 22: pp. 1327-1329.

[5] Han D.S., Han Y.S., Park J.H. A new approach to the treatment of nasal bone fracture: radiologic classification of nasal bone fractures and its clinical application. J. Oral Maxillofac. Surg. 2011; 69: pp. 2841-2847.

[6] Kucik C.J., Clenney T., Phelan J. Management of acute nasal fractures. Am. Fam. Physician. 2004; 70: pp. 1315-1320.

[7] Damman F. Imaging of paranasal sinuses today. Radiologe 2007; 7: pp. 576, 578-583.

[8] de Lacey G.J., Wignall B.K., Hussain S., Reidy J.R. The radiology of nasal injuries: problems of interpretation and clinical relevance. *Br J Radiol.* 1977; 50:412-4.

[9] Zimmermann C.E., Troulis M.J., Kaban L.B. Pediatric facial fractures: recent advances in prevention, diagnosis and management. Int. J Oral Maxillofac Surg 2006;35(1):2–13

[10] Holland A.J., Broome C., Steinberg A., Cass D.T. Facial fractures in children. Pediatr Emerg Care. 2001;17(3):157–160.

[11] Gurkov R., Clevert D., Krause E. Sonography versus plain X-rays in diagnosis of nasal fracture. Am. J. Rhinol. 2008;22: 613-616.

[12] Ferreira P.C., Amarante J.M., Silva P.N., et al. Retrospective study of 1251 maxillofacial fractures in children and adolescents. Plast. Reconstr. Surg. 2005; 115: 1500–1508.

[13] Mohammadi A, Ghasemi-Rad M. Nasal bone fracture--ultrasonography or computed tomography? Med. Ultrason. 2011;13: 292-295.

[14] Hwang K., You S.H., Kim S.G., Lee S.I. Analysis of nasal bone fractures; a six-year study of 503 patients. J Craniofac Surg. 2006;17(2):261–4.

[15] Miglioretti D.L., Johnson E, Williams A. The Use of Computed Tomography in Pediatrics and the Associated Radiation Exposure and Estimated Cancer Risk. JAMA Pediatrics. 2013; 167: 700-707.

[16] Lee M.H., Cha J.G., Hong H.S., Lee J.S., Park S.J., Paik S.H., Lee H.K. Comparison of high-resolution ultrasonography and computed tomography in the diagnosis of nasal fractures. J. Ultrasound. Med. 2009; 28:717-23.

[17] Adeyemo W.L., Akadiri O.A. A systematic review of the diagnostic role of ultrasonography in maxillofacial fractures. Int. J Oral Maxillofac Surg. 2011; 40:655-661.

New Basis Points of Geodetic Stations for Landslide Monitoring

V. Riabchii[1], M. Tregub[2], O. Yankin[1]

1 – National University «Lviv Polytechnics», Lviv, Ukraine

2 – State Higher Education Institution «National Mining University», Dnipropetrovsk, Ukraine



DOI **10.13140/RG.2.1.1874.6001**

Keywords: basis points, landslide processes, local geodetic network, recalculation of coordinates, the coordinate system.

ABSTRACT. The results of mathematical processing of modern geodetic observations of landslide processes in Dnipropetrovsk on points of observation stations in case of lost basis points are presented. Previous observations were conducted in 1993 using classic geodetic instruments. To provide the required accuracy of observations the local geodetic coordinate system was developed. There were two basis points; using laser range equipment the distance between them was measured with accuracy higher than 0.001 m. New observations were conducted in 2015 using GNSS-technologies and satellite observations in static mode because the traditional methods were impossible to use as the mutual visibility between basis points was lost. The biggest problem in current monitoring was the loss of basis points of monitoring stations. Some suggestions as for choosing the most stable points of network were made. Such points were defined according to previous observations; and the new method of determining the "temporary" basis points by comparing the lengths of lines between points of observation is offered. There were chosen three most stable points with minimal length disparity. Using such method we have transformed satellite observations from WGS-84 to local coordinate system established at the territory of landslide. Such method could be used in case of lost basis points and with considerable number of rather stable observation points. At the same time, we suggest setting the basis points as far from the landslide observation stations as possible. For further observations, we suggest using GNSS-technologies in static mode and setting the new basis points. To improve the accuracy, the observations on basis points will be combined with GNSS and other ground observations.

Introduction. The use of local geodetic networks to monitor landslides has some advantages over the use of public or state ones, especially in cases where precision of information is very important. Local geodetic network is usually created for observation of engineering structures or natural objects. Some of them were created at the time when the GNSS systems were not in use. The application of modern satellite systems is problematic in one local geodetic network and the most significant problem is the comparison of results measured during previous observations without satellite instruments.

It is especially significant when the primary basis points have been destroyed but you need to perform repeated geodetic measurements, and for various reasons, there is no mutual visibility between points of observation, while most of measurements can only be performed using GNSS-receivers. Also, without taking into account the results of previous long-term observations it might be inappropriate and provide incomplete characteristics of the landslide.

Analysis of recent research and publications concerning the problem. There are some modern publications dwelling on the methods of geodetic observations for establishment of geodynamic networks. The publication by Dyshlyk A. [1] is devoted to the methods of geodynamic observations of soil mass of Sudak fortress. The authors have systematized the implementation of methods of geodynamic observations by the accuracy of their methods. There is an example of construction of geodynamic network for observations at the Sudak fortress.

Zuska A. [2] investigated landslide processes in Dnipropetrovsk, including in the area of «Sokil». The findings of the study made the basis for modelling the soil mass changes over time, as of mid-1990.

Works by Tyschuk M. [3] indicate the importance of sharing disparate observations, which is reflected in five papers.

The paper by Khoda O. [4] features monitoring by using GNSS equipment. The author researched the factors that significantly affect the accuracy of measurements, and developed proposals for forecasting the relevant factors. He also suggested the program campaigning GPS-observations on geodynamic polygons to study local deformation of the landslide.

There are many other very important works on the research topic by the following experts Voitenko S., Savchuk S., Trevoho I., Tretyak K., Chernyaha P. etc., however there was no research dedicated to the problem of new observations using GNSS methods when the basis points of local network are lost.

Aim of research. The aim of this research is to determine the methods of selection of new "temporary" starting points by comparing the lengths of lines between points of observation on the results of modern geodetic observations using GNSS equipment for the monitoring of natural landslides in Dnipropetrovsk. This task is dedicated to the problem when the primary basis points of observation stations are not protected.

The main material. Observation of landslides on natural landslide "Sokil" in Dnepropetrovsk were provided by the Department of Geodesy of the National Mining University during 1984-1993. The last series of observations was conducted in autumn 1993. Fig. 1 shows general view of observation points and Fig. 2 – the layout of observation points stations in this area.

To perform the research, the researchers designed the network of microtriangulation, polygonometry and height observation points by using geometric levelling of 2nd class. Additionally, on the slopes of landslide there were set the sedimentary soil rapper, but as of autumn 1993 they were almost lost. The starting points of this network were 16 and 20. The observations were performed in cycles twice a year.

To suspend the landslide in the relevant territory, a retaining wall and drainage systems were built. On this wall, observation points were also established. The shift of the observation points allowed talking about reducing the shear process in general.



Fig. 1. General view of points of tracking station on the section " Sokil "

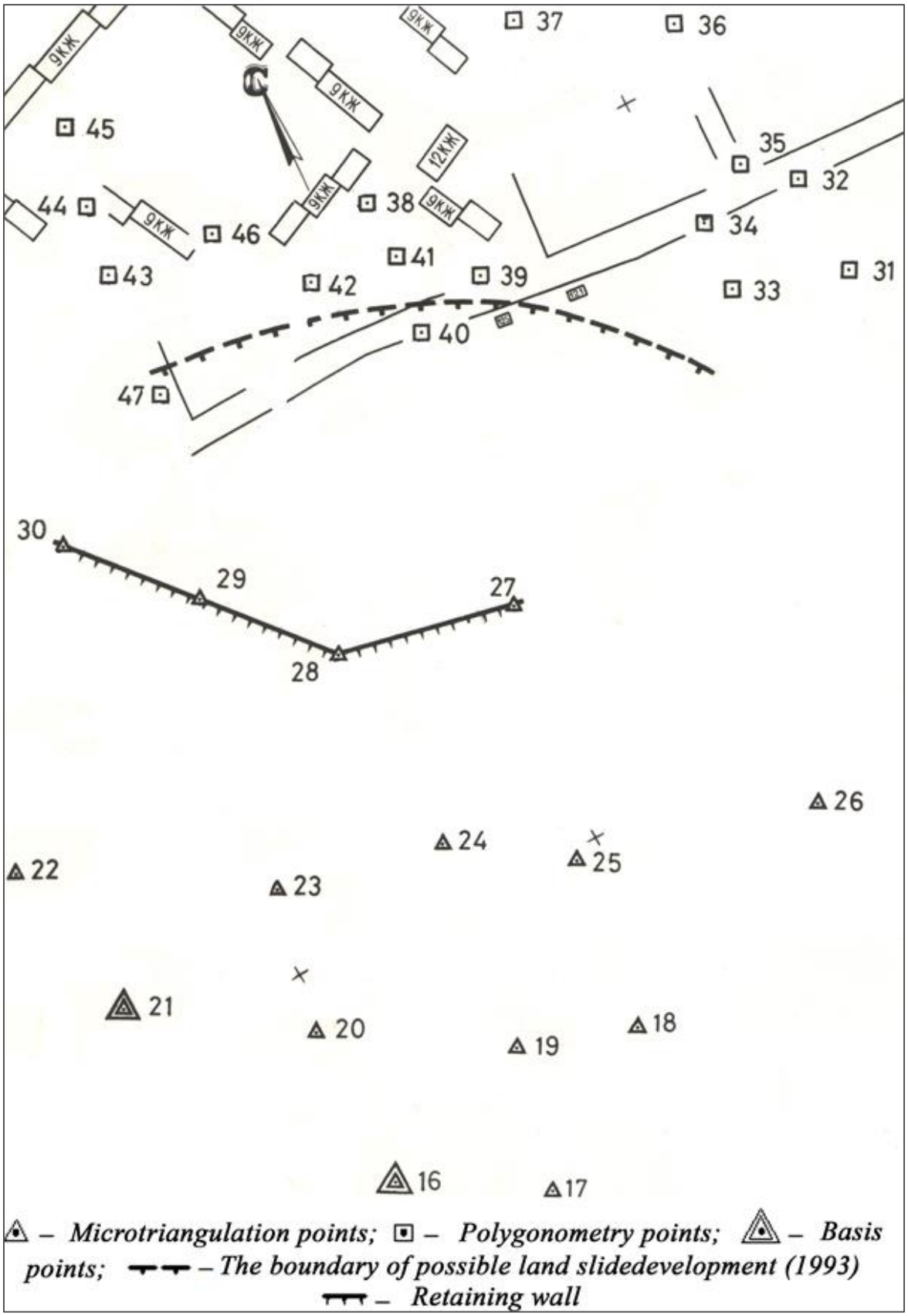


Fig. 2. Scheme of observation station points on the section " Sokil " (Autumn 1993)

In April 2015 the survey at the following areas was made. According to the results of the survey it was established that only the stations shown in Fig. 3 were saved and possible to use.



Fig. 3. Scheme of points available on the section of observation station "Sokil" (Spring 2015)

Station 28 on the retaining wall is not completely preserved, except for its base. Stations 22, 23 and 24 are lost as a result of the widening of the ravine. Stations 16, 17, 20 and 21 are destroyed as a result of human activity.

To receive the results that can be compared with previous cycles of observations the most important was to recalculate the current observations to the local coordinate system. The ideal solution of the problem could be the use of the basis points of previous network 21 - 16, but they were destroyed. Every possible combination of basis points from those remaining were analysed, and the most stable items were selected according to the results of existing geodetic observations from 1984 to 1993. The new basis points are 18, 19 and 41.

The summary of the results of plotted coordinates and elevations of points on the first and the last five cycles with their differences are shown in the table 1. According to the results of geodetic observations of last (seventeenth) cycle in 1993 compared with previous observations, it was established that these points almost did not change their position.

Table 1. Results of planned and altitudinal displacement of points 18, 19, 41

№ point / cycle	Coordinates of points, m			The deviation from previous, mm			The planned shift, mm	The spatial shift, mm
	X	Y	H	X	Y	H		
18/1	83.642	375.013	134.045					
18/13	83.711	375.050	134.040				-	-
18/14	83.722	375.061	134.040	11	11	0	15.6	15.6
18/15	83.731	375.059	134.040	9	-2	0	9.2	9.2
18/16	-	-	134.044	-	-	4	-	-
18/17	-	-	134.045	-	-	1	-	-
19/1	103.024	301.505	136.652					
19/13	103.027	301.506	135.650				-	-
19/14	103.030	301.512	135.649	3	6	-1	6.7	6.8
19/15	103.038	301.509	135.651	8	-3	2	8.5	8.8
19/16	-	-	135.649	-	-	-2	-	-
19/17	103.032	301.506	135.654	-6	-3	5	6.7	8.4
41/1	574.703	432.351	129.944					
41/13	574.691	432.373	129.942				-	-
41/14	574.703	432.362	129.945	12	-11	3	16.3	16.6
41/15	574.701	432.365	129.943	-2	3	-2	3.6	4.1
41/16	-	-	129.945	-	-	2	-	-
41/17	574.738	432.366	129.946	37	1	1	37.0	37.0

In May 2015, observations on saved points of the station "Sokil" were performed by the professors of the Department of Geodesy. The base receiver was installed at point 41, where it worked for the cycle at all observation points. Observations on other points were performed by rapid static method. Time of observations on points ranged from 25 to 35 minutes depending on the geometry of the satellites constellation.

Using the Topcontools software, the coordinates of all observation points were transformed from WGS 84 to the local coordinate system, which was the base for geodetic monitoring of landslides in the past.

The choice of new basis points was performed in the following order. First, the results of GNSS observations in spring 2015 were used to calculate lengths of lines between all points of observation. Then there were calculated the same length of lines according to the results of the last cycle of observations in autumn of 1993. After that the lengths of all lines were compared. The results of this comparison are presented in Table 2 and Fig. 4.

As can be seen from Table 1 and Fig. 4, of all possible lengths of lines between points of observation the distances between points 41, 18 and 19 have the least changed.

As point 41 and points 18 and 19 are located on different sides of the ravine and they are stabile we can use them to make the transformation. But, as can be seen from differences in lengths between other points, landslides are still continuing.

Table 2. Comparison of distances between points of observation stations

N of lengths	Distance from the results of GNSS observations, m	Distance based on observations of last cycle in 1993, m	The difference between the distances, m
18 – 19	76.025	76.043	-0.018
18 – 26	174.262	174.883	-0.621
18 – 27	269.190	269.830	-0.640
18 – 30	460.741	460.938	-0.197
19 – 26	236.679	237.425	-0.746
19 – 27	270.647	271.096	-0.449
19 – 30	415.245	415.481	-0.236
27 – 30	279.698	278.852	0.846
41 – 18	494.322	494.340	-0.018
41 – 19	489.482	489.521	-0.039
41 – 26	424.258	424.652	-0.394
41 – 27	225.232	224.585	0.647
41 – 30	269.867	269.664	0.203

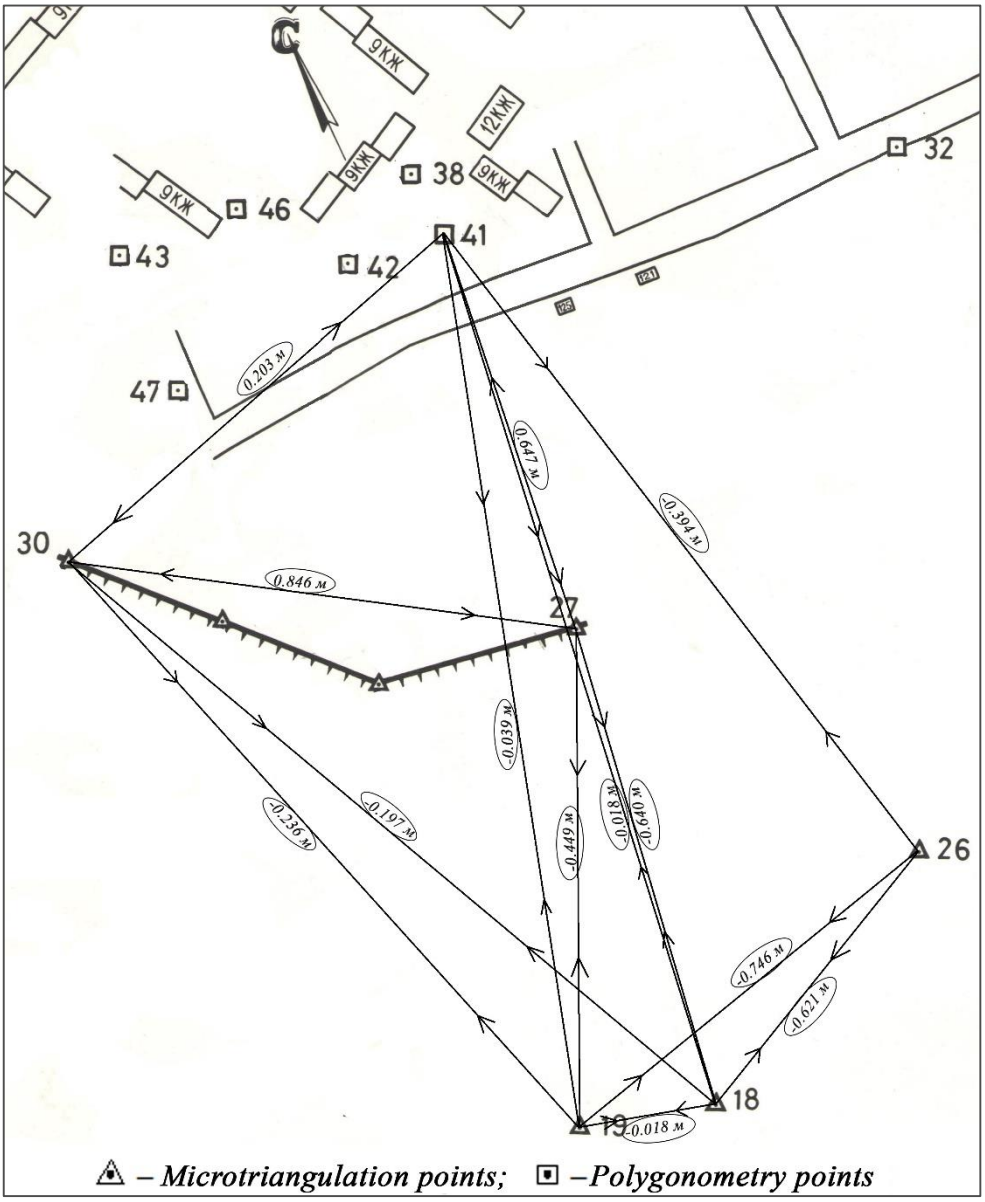


Fig. 4. Directions and changes in distances in the network on the section "Sokil " (Spring 2015)

Conclusions and proposals. Summarizing the information above, the following conclusions can be reached.

1. If the starting points of local geodetic network observations are lost, in order to select new starting points it is proposed to use the method comparing lengths of lines between all points of observation.

2. Application of this method allows using the observations of previous years.

3. To reduce the risks of losing basis points we suggest setting the basis points away from the landslide area. The key demand for new basis points is mutual visibility to provide GNSS and ground observations using all stations.

Further research is aimed at creating a base outside the landslide area, to be set in the state geodetic network UCS 2000 and local coordinate system of Dnipropetrovsk city. Also it is recommended to carry out repeated observations using multifrequency and multisystem GNSS-receivers.

References

[1] Dyshlyk, A., & Markov, S. (2010). Geodynamic observation of soil mass and attractions of Sudak fortress. *Modern Achievements of Geodetic Science and Industry, 1*(19), P 140-145.

[2] Zuska, A. (2014). *The kinematic model of landslide slopes*. Dnipropetrovsk, Ukraine: NMU, 140 P.

[3] Tyschuk, M., & Hozhyy, A. (2015). Private stations for combined astronomical, geodetic and geophysical observations in Stepanivtsi. *Modern Achievements of Geodetic Science and Industry, 1*(29), P 44-47.

[4] Khoda, O. (n.d.). *Observation of satellites of global positioning system (GPS) for geodynamic and ionospheric studies in Ukraine*. Abstract of thesis for the degree of Cand. Sc. for specials. 01.03.01 - astrometry and celestial mechanics, 18 P.

IX. Economics & Management
MMSE Journal Vol. 3



The Current State of Taxation and Regulation of Land Plot Size of Industrial Areas in Ukraine

M.A. Malashevskyy [1], L.V. Melnyk [2,a]

1 – candidate of engineering sciences, associate professor, Head of the Land Resources department of the Institute of Advanced Education Kyiv National University of Construction and Architecture, Kyiv, Ukraine

2 – post-graduate student of Kyiv National University of Construction and Architecture, Kyiv, Ukraine

a – l-melnyk@ukr.net



DOI **10.13140/RG.2.1.4083.3685**

Keywords: industrial facility, excess area, taxation.

ABSTRACT. An analysis of the domestic legal and regulatory framework for land taxation has been performed. The ratio of industry land within the land resources of Ukraine has been investigated. The legal basis for determination of land plot areas necessary for implementation of industrial activities has been considered. The legal regime of industry land has been investigated. The conclusion of the need for improvement of methods for determining excess areas for taxation purposes has been made and optimization of land use in populated areas.

Introduction. According to the Constitution of Ukraine [1], land is national wealth and it should be under special state protection. Solving the problem of exaction of payments for land, under conditions of market-based economy development, has been and remains especially important. The issue of exaction of payments for land is closely related to accounting of land plots, completeness and accuracy of which depends on local governments, authorities and land management agencies.

By today, the extremely important question of forming an effective tax system in Ukraine remains unresolved. The problem of taxation must be approached holistically, taking into account both critically assimilated foreign experience and domestic features and distinct perspectives and courses of development. Lack of perspectives, vagueness of priorities, objectives and implementation mechanisms, in circumstances where there are no developed institutions of the democratic, law-governed state and civil society, makes it impossible to build a socially oriented economy in the country.

According to the statistical reporting of the Public Service of Ukraine on Geodesy, Cartography and Cadastre of quantitative land accounting [2] the land reserves of Ukraine as of 01.01.2016 is distributed as follows:

- agricultural land - 70.8 %;
- forests and other wooded areas - 17.6 %;
- built-up land - 4.2 %;
- open bog covered areas - 1.6 %;
- open dry land with special plant formation - 0.0003 %;
- open land without plant formation or with little plant formation (stony areas, sands, ravines, etc.) – 1.7 %;
- water (areas covered with surface water) – 4.0 %.

Based on the results of the research conducted, it has been found that built-up land occupies most of the territory within populated areas – 2550.4 thousand ha, representing 4.2 % of the territory of Ukraine. Since the land used for transport and communication, is mainly located outside the populated areas, the largest territory within the populated areas is occupied by lands of residential and public construction – 769.4 thousand ha or 1.3%, and by industrial land – 224.1 thousand ha or 0.4 % of the entire territory of the country (Fig. 1).

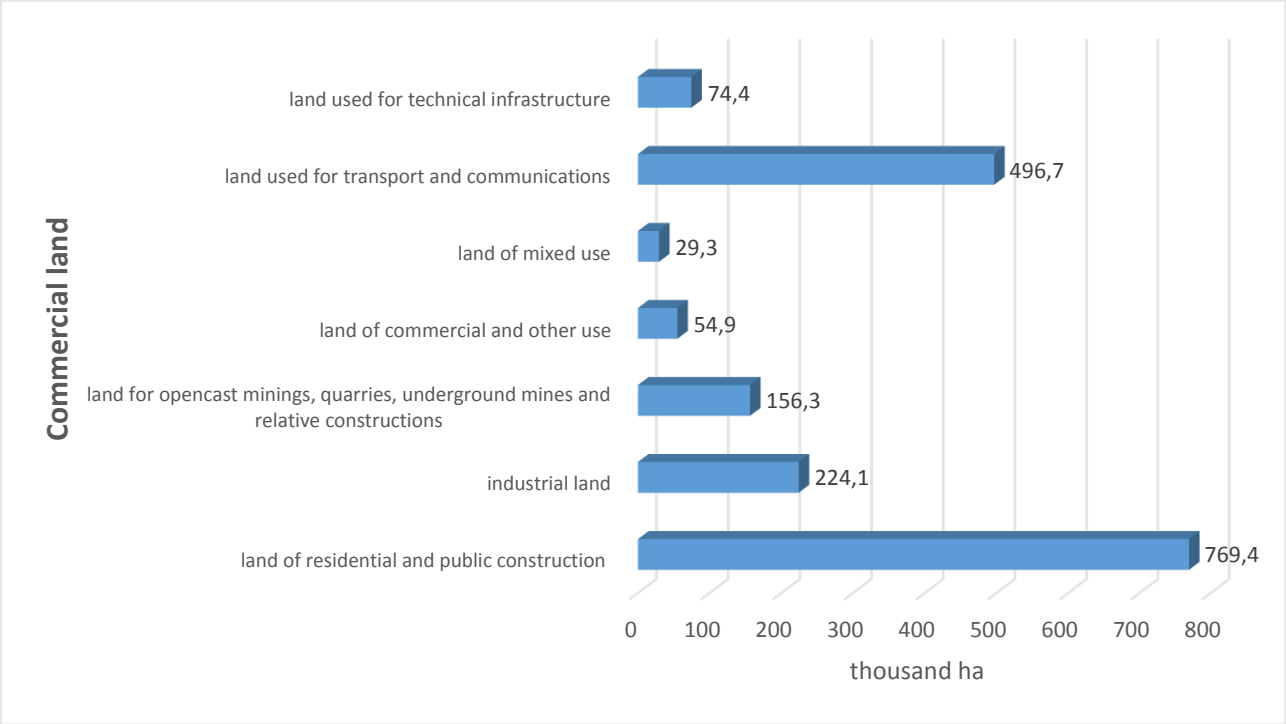


Fig. 1 Distribution of the built-up land by the type of major commercial lands and economic activities as of January 1, 2015

The research of Rozumkov Center [3] has revealed the uneven regional distribution of the built-up land across the country. The Carpathian region and Polissya have the most balanced inhabitable environment where non-agricultural land use ranges within 40-63% of the total land area of the regions. Thus, only 3-5 % of the territory is built-up in the Carpathian Region and Polissya, whereas in the Dnipropetrovsk Region there is 6% of built-up land and in the Donetsk Region- 7,4% of built-up land (Fig. 2).

As for the residential development land, there are standards of land plot areas justification for an apartment building, which is based on methodical approaches on the basis of standardization in the field of urban planning. The following scientists conducted these studies: Sulima-Samuylo G.D., Malashevskyy M.A., Mosiychuk Y.A., Berova P.I. [4]

To implement the state policy on creation of condominium associations, the Ministry of Regional Development and Housing and Communal Services has developed the guidance [4], which has adjusted basic methods for determining land plots areas of apartment buildings on the basis of urban planning conditions.

The main method of the existing built-up environment area distribution is a method that involves the distribution of a residential area of a neighbourhood and determining a separate apartment building land plot as a share of the residential area in proportion to the number of inhabitants of the house. The legal basis of the method is the regulation of a residential area per capita, which is established in the

Public construction codes. However, for industrial land there are only land allotment norms for newly established enterprises.

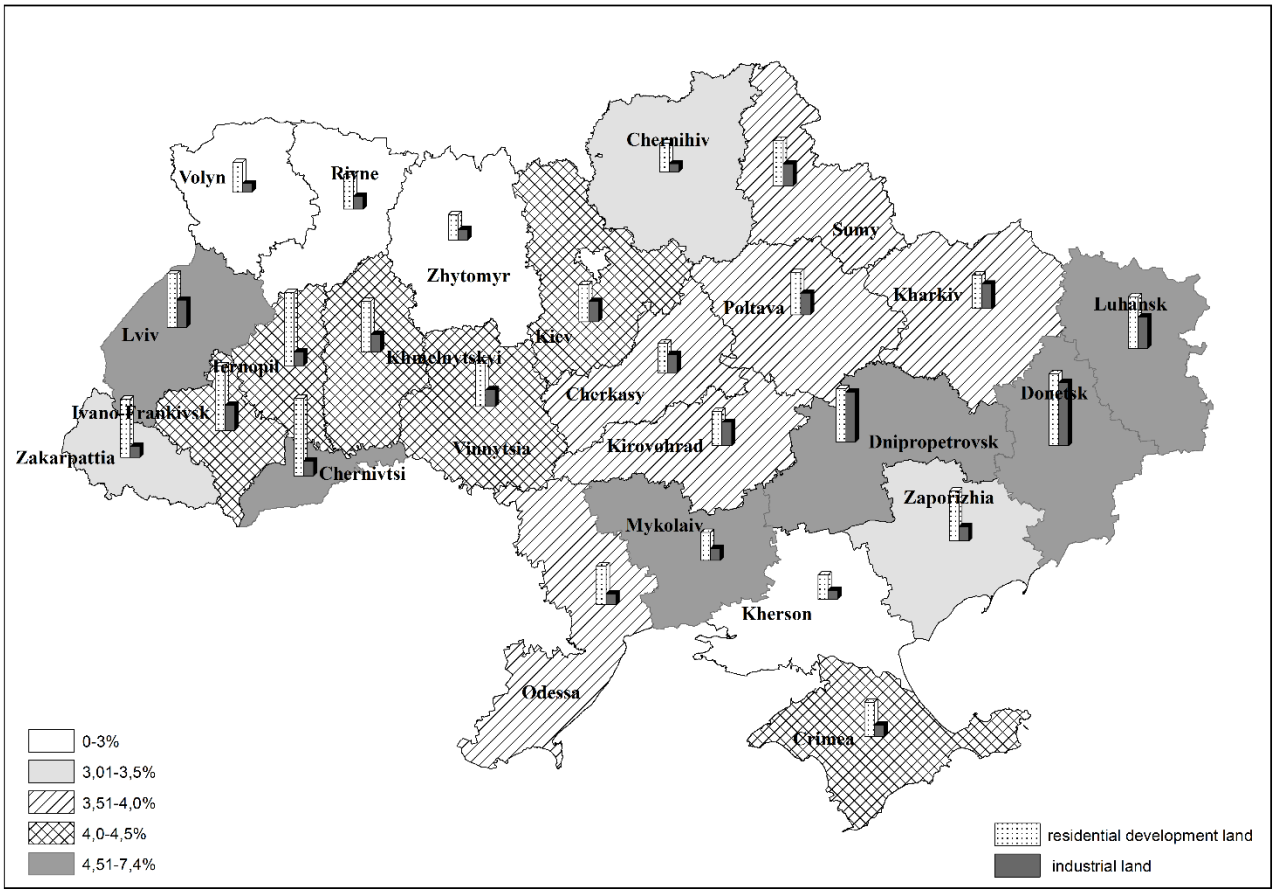


Fig. 2 Map of built-up land in the regions of Ukraine [3] (% of the total land area of the region)

In the Payments for Land Act of Ukraine [6], which was valid until 01.01.2011, there was a provision which stated that the part of land plots' areas, given to enterprises, institutions and organizations (other than agricultural land), which exceeds the allocation limits, should be taxed above quota. However, this rule did not have a practical implementation, since there is no well-defined mechanism for determining the regulatory area.

Ukraine inherited large industrial facilities from the USSR that have reserved large areas that are redundant and not used in full. The development of methods for determining excess areas, especially for industrial facilities in cities, will optimize land use in localities.

The existing legislation of Ukraine in the sphere of land regulation is not yet fully focused on the issues of payments for land.

The problem lies in the lack of an appropriate mechanism of normative legal and business regulation of determining the required and excess area that is needed for the operation of an industrial facility.

The regulatory area of land under industrial facility is determined according to health standards and regulations II-89-80 "General Layouts for Industrial Enterprises" [7]. There have been changes in technological processes, equipment and the need in some industries altogether since the date of adoption of the document, so the development of approaches that provide a means of calculating the area of land for productive activities is a key issue.

According to Articles 13 and 14 of The Constitution of Ukraine [1], the land lying within the territory of Ukraine is the property of the Ukrainian people and is the main national wealth that is under special

state protection. The property right to land is guaranteed. This right is acquired and exercised by the citizens, legal persons and the State only in accordance with the law.

The use of land in Ukraine is fee-based. Payments for land are levied in the form of land tax or rent, which is determined by the monetary value of this land. Tax amount for the land, the monetary value of which was not estimated, was previously determined in the manner, specified by the Payments for Land Act of Ukraine" [6]. This Law used to define the size and manner of payment for usage of land resources, as well as responsibilities of taxpayers and control over correctness of calculation and collection of land tax. Now the specifics of exaction of payments for land are defined in Chapter XIII of The Tax Code of Ukraine, which entered into force on 01.01.11 [8].

There are differences between the no longer valid Payments for Land Act of Ukraine [6] and the current Tax Code of Ukraine [8], this applies to both design and content of the text.

The Tax Code of Ukraine [8] states that payments for land combine two mandatory payments - land tax and rent for land plots of the state and municipal property.

The lands of industry, transport, communications, energy, defence and of other purposes are an independent category of lands within the land resources of Ukraine. They cover an area of 223.2 thousand hectares, accounting for 0.4% of the total area of the state's territory (Fig. 1) [2].

In accordance with paragraph 1 of Article 65 of The Land Code of Ukraine [9], the lands of industry, transport, communications, energy and defence and of other purposes are defined as the lands granted in the prescribed manner to enterprises, institutions and organizations for the corresponding activity.

Their legal regime is determined by regulatory requirements, which are concentrated in The Land Code of Ukraine [9] and a number of other regulations. Most of the legal rules, governing the legal regime of these lands, are enshrined in freestanding instruments, devoted mainly to special activities of certain enterprises, institutions and organizations, including The Air Code, The State Border, The Defence of Ukraine, The Transportation, The Communication, The Rail Transport, The Pipeline Transport, The Electric Power Industry and The Road Transport Acts of Ukraine.

The legal regime of all types (subcategories) of the specified lands is based on common principles: national and public importance of the category, which these lands belong to; special tasks of usage of such lands.

The main feature of their legal regime is ensuring of balanced environmentally sustainable land use in the operation of a variety of non-agricultural facilities. As for the features of legal regulation of usage and protection of certain land types that belong to this category, they are based on specifics of their purpose [10].

Land plots that belong to this category of land are characterized by a diversified purposiveness and legal regime. Meanwhile, it is agreed under the law in legal doctrine to provide common features of legal regime of land for industry, transport, communications, energy, and defence and for other purposes. In particular:

– all land plots in this category have a special non-agricultural purpose, which allows to compendiously call this category of land in professional literature – lands of special non-agricultural purpose;

– size of relevant plots is determined on the basis of standards, approved in the established procedure (for typical facilities - railways, roads, power lines, airports, pipelines, etc.) or projects, approved in the established procedure (for non-standard facilities – industrial enterprise, etc.) that, however, are also developed in accordance with certain standards. This allows distinguishing such specific feature of land for non-agricultural purposes, as size normalization of relevant plots;

In most sectors of economy, lands are used inefficiently, due to imperfect regulations, low-level design, and technical solutions. The regulations of land allotment for the needs of industry, transport and energy are 2.5-2.7 times higher, than those accepted in Western European countries.

Internal and external zoning of land for special non-agricultural purposes is carried out. So, for example, sanitary protection zones, where home construction activity and housing is prohibited, are set around potentially harmful objects, and exclusion zones are set around potentially vulnerable facilities, and so on.

In certain cases, the areas designated for special non-agricultural purposes, may be not assigned as separate plots at all. Specifically it is referred to the land plots designated to locate some linear objects (communications, power lines, and underground pipelines). Although a separate plot of land for the location of such object is not allotted, the location of the object causes significant changes to the regime of the corresponding area, in particular, exclusion and sanitary protection zone is set. The applicable land servitude can be set.

In most cases, legislation has no rules for determining legal regime of land plots that concomitantly cover the features of several types of industry, transport, communications, energy, defence lands and lands of other purposes (e.g., land at intersection of line networks).

Formulation of the concept of "industry land" is contained in paragraph 1 of Article 66 of The Land Code of Ukraine: "1. Industrial lands are the lands granted for placement and operation of the main, auxiliary and ancillary buildings of industrial, mining, transport and other enterprises, their access roads, utilities, administrative and residential buildings and other structures" [9].

According to paragraph 3 of Article 66 of The Land Code of Ukraine: "3. Size of land plots provided for these purposes, shall be determined in accordance with the approved in the established procedure state standards and design documentation, and land plots allotment shall be based on the sequence of their development" [9].

Size and internal zoning of land plots of industrial enterprises is defined by project documentation based on sanitary norms and regulations II-89-80 "General Layouts for Industrial Enterprises" [7] that, in particular, establish standards for minimum site development density, which affects the area of land required, allow for functional zoning "based on technological linkages, sanitation and fire protection requirements, cargo turnover and means of transport" (par. 3.3., etc.), determine the configuration of buildings (par. 3.22.), the distance between buildings (paragraphs 3.25., 3.26., Tables 1-4, etc.) and so on.

In particular, par. 3.8. of norms and regulations provides for allocation of the following zones on the site of an enterprise: (a) offsite area (outside a fence or conventional boarders of an enterprise), (b) production zone, (c) auxiliary zone, (d) storage area.

Within a production area the following zones are allocated (e) civic center, (f) enterprise grounds, (g) common objects of auxiliary departments and facilities.

Zoning is allowed to be specified taking into account specific conditions of an enterprise.

External zoning of lands adjacent to industrial enterprises' plots, such as setting sanitary protection zones around enterprises, is carried out on the basis of the State Sanitary Regulations of Planning and Building of Settlements approved by The Ministry of Healthcare of Ukraine from 19.06.1996 № 173 [11] (replaced the Sanitary Norms 245-71 "Sanitary Norms of Design of Industrial Enterprises", approved by the State Committee of the Council of Ministers of the USSR on Construction on 05/11/1971 [12]).

There are 5 hazard classes of enterprises that are determined in accordance with the Sanitary Classification of Enterprises, Productions and Constructions (Annex 4 to Regulations [11]) (class I means the most dangerous enterprises, productions and constructions), according to which a sanitary protection zone is from 50 to 3000 m.

The law does not provide for restrictions on a circle of persons who may have industry land on the right of ownership or usage (paragraph 2 of Article 66 of The Land Code of Ukraine [9]).

During the "Soviet era" there was a practice of placement of industrial enterprises on lands that were allocated for the usage by other land users - on railroad and highways precincts and even on agricultural lands (this refers to inter-collective farm enterprises). Their land usage was not documented in any way, which nowadays generates multitude conflicts and disagreements. [11]

The use of land in Ukraine is fee-based. Payments for land are levied in the form of land tax or rent, which is determined depending on the monetary value of this land.

Summary. The part of land plots' areas given to enterprises, institutions and organizations (other than agricultural land), that exceeds the allocation limits, should be used effectively. However, there is no well-defined mechanism for determining of the regulatory area for facilities. Solving this problem will increase the rational area of settlements, improve the land use system and increase the country's budget revenues.

References

[1] The Constitution of Ukraine (1996). Verkhovna Rada of Ukraine; Supreme Council of Ukraine (VVR), 1996, № 254k/96-VR, art. 14. Available at: http://zakon3.rada.gov.ua/laws/show/254к/96-вр.

[2] Land Fund of Ukraine as of January 1st, 2015 and the dynamics of its changes compared to the data as of January 1st, 2014. Information Derzhheokadastru. Available at: http://land.gov.ua/info/zemelnyi-fond-ukrainy-stanom-na-1-sichnia-2015-roku-ta-dynamika-ioho-zmin-v-porivnianni-z-danymy-na-1-sichnia-2014-roku/

[3] State land policy in Ukraine: state and development strategy (2009). - National Security and Defence, 3, 72. Available at: http://www.razumkov.org.ua/ukr/journal.php?y=2009&cat=146

[4] Sulima-Samuylo, G. D., Malashevskyy, M. A., Mosiychuk, Y. A., Berova, P. I. (2014). Approaches to taxation of housing development excessive land area. Urban construction and land-use planning magazine, 53, 320–238.

[5] DSTU-H B B.2.2-9:2013 Guidelines for the distribution of neighborhood areas to determine the adjoining area for a multifamily building (2013). Kyiv, Ministry of Regional Development Construction and Housing and Communal Services Of Ukraine 2013. Available at: http://otipb.at.ua/load/dstu_n_b_b_2_2_9_2013_nastanova_shhodo_rozpodilu_teritorij_mikrorajoniv_dlja_viznachennja_pribudinkovikh_teritorij_bagatokvartirnoji_zabudovi/23-1-0-4316

[6] On Land Law of Ukraine (1992). Verkhovna Rada of Ukraine; Supreme Council of Ukraine (VVR), 1992, № 2535-XII, art. 20. Available at: http://zakon4.rada.gov.ua/laws/show/2535-12

[7] SNIP II-89-80. Master plans of industrial enterprises (1981). Moscow: Stroyizdat. Available at: http://www.budinfo.org.ua/doc/1810233/SNiP-II-89-80-Generalni-plani-promislovikh-pidpriiemstv/

[8] Tax Code of Ukraine (2012). Verkhovna Rada of Ukraine; Supreme Council of Ukraine (VVR), 2012, № 2755-VI. Available at: http://zakon4.rada.gov.ua/laws/show/2755-17

[9] Land Code of Ukraine (2002). Verkhovna Rada of Ukraine; Supreme Council of Ukraine (VVR), 2002, № 3-4, art. 27. Available at: http://zakon4.rada.gov.ua/laws/show/2768-14

[10] Miroshnichenko A.M. Legal order of lands of industry, transport, communications, energy, defense and other use. Available at: http://www.pandia.ru/text/77/191/15740.php

[11] State sanitary rules of planning and development of human settlements (1996). Ministry of Health of Ukraine 1996, №173. Available at: http://zakon5.rada.gov.ua/laws/show/z0379-96

[12] SNIP 245-71. Sanitary regulations of industrial enterprises designing (1971). Moscow : State Committee of the Council of Ministers for Construction, 1972. Available at: http://document.ua/sanitarnye-normy-proektirovanija-promyshlennyh-predprijatii-nor3142.html

X. Philosophy of Research and Education

M M S E J o u r n a l V o l . 3

Physics and Optics in Dante's Divine Comedy

Amelia Carolina Sparavigna[1]

1 – Department of Applied Science and Technology, Politecnico di Torino, Italy

DOI **10.13140/RG.2.1.3509.0965**

ABSTRACT. The Divine Comedy is a poem of Dante Alighieri representing, allegorically, the journey of a soul towards God, in the framework of Dante's metaphysics of the divine light. However, besides metaphysics, we can find in the poem several passages concerning the natural phenomena. Here we discuss some them, in order to investigate Dante's knowledge of Physics and, in particular, of Optics.

Keywords: Medieval Science, History of Science, History of Optics

1. Introduction. Dante Alighieri was one of the most educated persons of his time. He knew deeply the logic, physics and metaphysics of Aristotle. The theology came to him from the thought of Albert the Great and Thomas Aquinas, that Dante, in his Divine Comedy poem, places among the "Wise Spirits" in the Heaven of the Sun [1]. He also knew very well the classic literature and the Neoplatonic thought. As Thomas Aquinas, Dante aimed that his listeners were practicing philosophy, but the poet was teaching through a poetry in Vulgar, rather than through a prose in Latin. Dante's philosophy, which is present in his poem, the Divine Comedy, was supported by a metaphysics, that we can define as a metaphysics of the Light of Divine Love [2]. In such a manner, when Dante in his allegorical journey comes to the Empyreum, a region beyond physical existence, the highest place of his medieval cosmology, the Comedy presents its "sense of a complete harmonization of divine light, divine love, and divine life" [3]. Besides metaphysics, we can find in Dante's poem several passages concerning the natural phenomena. Here we discuss some of them, in order to investigate Dante's knowledge of Physics and, in particular, of Optics. Reference [4] helps us in investigating the Divine Comedy to evidence these points.

2. The journey in the realms of afterlife. The Divine Comedy, Divina Commedia, is the poem written by Dante Alighieri, from approximately 1308 and his death in 1321. This poem is an allegorical journey in the realms of afterlife, based on the vision of the world of medieval Western Europe. In the poem written in the first person, Dante describes his journey through Hell and Purgatory, and then his rise through Heavens, up to the Empyreum and the vision of God. This travel is representing allegorically a soul's journey towards the Divine Love of God.

The Comedy is composed of 14,233 lines, divided into three Cantiche: Inferno (Hell), Purgatorio (Purgatory), and Paradiso (Paradise). In the first canto, the prologue of the poem, Dante is in a dark wood, where he meets the Roman poet Virgilio. In the third canto, Dante and Virgilio enter the Hell. Virgilio guides Dante through Hell and Purgatory; Beatrice, Dante's ideal woman, is leading him through the Paradise.

The structure of the three realms is given in a numerical pattern of 9 plus 1, for a total of 10. There are nine circles of Inferno, and Lucifer is contained at its bottom, which is the center of the Earth. We have nine rings around the Mount Purgatory, and the Garden of Eden at its top. Then, Dante finds the 9 'cieli' (heavens), the nine celestial spheres of Paradise, crowned with the Empyreum, and God, the radiating point of Light. In each of the circles, rings and spheres, Dante and his Guides meet different characters, because each of these places is concerning a different sin or virtue. Here in the Figure 1 a sketch of Dante's world.

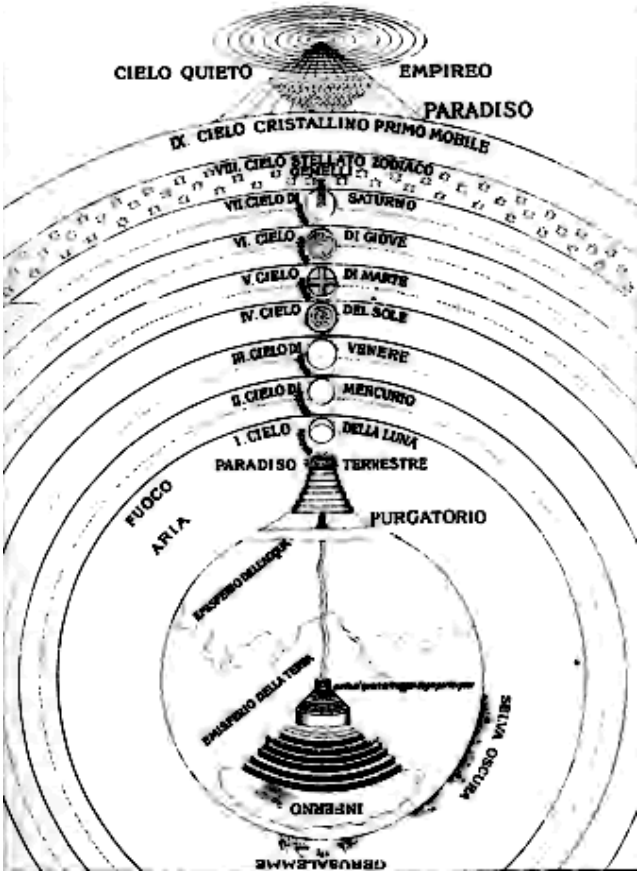


Fig. 1. The world of Divine Comedy, as shown by Michelangelo Caetani, duca di Sermoneta, in his book "La materia della Divina commedia di Dante Alighieri dichiarata in VI tavole", Passerini G.L. editor, 1921.

3. Gravitation, motion and time. In a previous paper [5], we have discussed some of medieval physics concerning gravitation and the form of the world. Except for a few isolated cases, dictated by a religious aversion to the ancient philosophy, to the medieval Europe, the world was a sphere. But there was a problem that arose some discussions, and this was the existence of Antipodes. Do they exist? Are they inhabited? Can we reach them?

This issue was considered by Dante Alighieri in depicting the realms of afterlife. The Earth is a sphere having at its center Lucifer, who dug the Hell with his fall. Dante and his guide Virgil, go down following the "gironi" of Hell, reaching the center of the Earth, and then rise to the Earth surface at the Antipodes where they find the Mountain of Purgatory. When Dante is passing the center of the Earth, Virgil tells him that this is *"l punto al qual si traggon d'ogni parte i pesi", "the point to which things heavy draw from every side", (Inferno, Canto XXXIV).* To Dante, the gravitation was a power applied to any mass, of which he knew, given its spherical symmetry, the direction towards the center of the Earth, that was also the center of the Universe. Therefore, the gravitation was the principle that constrained the Medieval model of universe, composed of many spheres, to rotate about the center of the world.

Using this simple theory of gravitation, Dante was able to solve another quite relevant question of his time. In 1320, in the church of St. Helena in Verona, Dante discussed the question about the two elements of water and earth; with geometric, hydraulic and cosmographic reasons, he showed that the circumference of water is not larger than that of earth, according to the nature of gravity [4]. Let us stress that the medieval scholars had not the concept of force and then could not formulate a law such as that of the universal gravitation, first proposed by Newton in the Philosophiæ Naturalis Principia

Mathematica, published in 1687. Dante's cosmology was a medieval cosmology, with nine heavens having the as their common center. Above the starry heaven, there is the crystalline heaven of Primum Mobile, the "first moved", linking God and the universe. The existence of the Primo Mobile depends on nothing else than light and love of God.

"La natura del mondo, che quieta / il mezzo e tutto l'altro move, / quindi comincia come da sua meta; / e questo cielo non ha altro dove / che la mente divina, in che s'accende / l'amor che il volge e la virtù ch'ei piove." (Paradiso, XXVIII, 106-111).

"The nature of that motion, which keeps quiet / The centre and all the rest about it moves, / From hence begins as from its starting point. /And in this heaven there is no other Where / Than in the Mind Divine, wherein is kindled / The love that turns it, and the power it rains." (Longfellow's translation)

Time has its origin from the motion of this heaven, as Beatrice tells to Dante:

"E come il tempo tegna in cotal testo / Le sue radici e ne li altri le fronde, / omai a te può esser manifesto." (Paradiso, XXVIII, 118-120).

"And in what manner time in such a pot / May have its roots, and in the rest its leaves, / Now unto thee can manifest be made." (Longfellow's translation)

4. Astronomical passages. In the Divine Comedy, Dante was often referring to astronomical phenomena, to mark the time of his journey in the afterlife's realms. And then, in the poem, there are many passages about astronomy [6]: let us remember just two of them. One is the reference to the polar stars: in the Hell, Dante encounters Ulysses. The Greek hero describes to Dante his last voyage, undertaken by him and his old comrades, beyond the Pillars of Hercules. Ulysses is heading towards the Southern Hemisphere. He sees the stars of the other hemisphere and those of the Boreal pole that no more rise above the horizon. He sailed for five lunar months and then he saw a mountain, indistinct for the distance. This is the Antipodean mountain: Ulysses, however, does not get it because a strong whirlwind does sink the ship. The sea closed over him and his companions.

"Tutte le stelle già de l'altro polo / vedea la notte, e 'l nostro tanto basso, / che non surgea fuor del marin suolo. / Cinque volte racceso e tante casso / lo lume era di sotto da la luna, / poi che 'ntrati eravam nell'alto passo, / quando n'apparve una montagna, bruna / per la distanza, e parvemi alta tanto / quanto veduta non avea alcuna." (Inferno, XXVI, 127-135).

"Already all the stars of the other pole / the night beheld, and ours so very low / it did not rise above the ocean floor. / Five times rekindled and as many quenched / had been the splendour underneath the moon, / since we had entered into the deep pass, / when there appeared to us a mountain, dim / from distance, and it seemed to me so high / as I had never any one beheld." (Longfellow's translation)

However, Dante is on a very different journey, and therefore he arrives to the conical mountain of Purgatory, made by terraces that rise to the Earthly Paradise.

In the Eleventh Canto of Purgatory, Dante alludes to the precession of the equinoxes in the following manner.

"Che voce avrai tu più, se vecchia scindi / da te la carne, che se fossi morto / anzi che tu lasciassi il "pappo" e 'l "dindi", / pria che passin mill'anni? ch'è più corto / spazio a l'etterno, ch'un muover di ciglia / al cerchio che più tardi in cielo è torto." (Purgatorio, XI, 103-108).

"What fame shalt thou have more, if old peel off / from thee thy flesh, than if thou hadst been dead / before thou left the 'pappo' and the 'dindi,' / ere pass a thousand years? which is a shorter / space to the eterne, than twinkling of an eye / unto the circle that in heaven wheels slowest." (Longfellow's translation)

5. Dante's Physics. Astronomy was one of the arts of the Quadrivium and then had a very important part in medieval culture. And then, it is not surprising to find it in Dante's works. Physics was a part of the philosophy of Nature. We can ask ourselves if Dante is also referring to it in his Comedy; the answer is positive. For our investigation of Dante's physics, we find a huge help in a book written in 1804 by Giovanni Bottagisio [4]. Bottagisio was a landowner with a passion for Dante's works that led him to write a work on the scientific aspects of the Divine Comedy. Among physics, Giovanni Bottagisio considers optics and atmospheric phenomena, but also the behavior of animals and human biology.

As Bottagisio tells in his introduction [4], "To my best knowledge, no one had considered so far to make an "anatomy" of Dante's poem, to learn about the physics that he discussed in very gentle and seemly way. Only Benedetto Varchi, in a lecture about the generation of the human body, had reviewed a corresponding passage (Purgatory, XXV)". The mathematician and poet Giuseppe Torelli in a letter to Abbot Clemente Sibiliati, professor at the University of Padova, exhibited and explained a physical passage (Purgatory, XV) on the reflection of the light that strikes the surface of water, or a mirror. Besides these two examples, no one preceded Bottagisio. He picked up from the three poems of the Comedy, twenty or more passages, regarding physical things, omitting those concerning astronomy, already discussed by other scholars, in order to understand the physics that Dante was knowing.

According to Bottagisio, Dante was a theologian, a metaphysician and a moralist; but he was also a "poet of physics", who described in verse some natural and scientific phenomena in a graceful manner. Following Giovanni Boccaccio, Bottagisio tells us that Dante had Brunetto Latini as his teacher of physics. Dante studied and disputed in public about physical phenomena even in Paris, where he went after his exile from Florence. Let us see some passages that Bottagisio had discussed in his book.

6. Optics. Let us start with geometrical optics. In the Purgatory, Dante uses a similitude from the reflection of light.

"Come quando dall'acqua o dallo specchio / salta lo raggio all'opposita parte, / salendo su, per lo modo parecchio / a quel che scende, e tanto si diparte, / dal cader della pietra, in igual tratta, / si come mostra esperienza e arte: / cosi mi parve da luce rifratta / ivi dinanzi a me esser percosso. (Purgatorio, XV, 16-23).

"As when from off the water, or a mirror, / the sunbeam leaps unto the opposite side, / ascending upward in the selfsame measure / that it descends, and deviates as far / from falling of a stone in line direct, / as demonstrate experiment and art, / so it appeared to me that by a light / refracted there before me I was smitten." (Longfellow's translation)

Dante is telling that the light of an angel, who appeared to him, hits him in the face as the ray of light, descending from the sun, hits the surface of water, or a mirror, and is reflected to the other side. It is coming out on the same way that it went down, that is, forming equal angles on both sides. Therefore, the reflected ray departs with an angle equal to the incidence angle, "dal cader della pietra", from the "falling of a stone", that is, from the line perpendicular to the reflecting surface, "as experience and art are demonstrating". The perpendicular line is called the "falling of a stone" by the ancient scholars; Bottagisio tells that this metaphor was used by Albertus Magnus.

Dante tells that the law of reflection was proved by "experience" and "art", and then we can imagine, as Bottagisio is telling, that Dante had saw some instruments designed to make experiments of geometrical optics. Let us note that the "refracted light" in this Dante's passage is actually a "reflected light"; Dante was using the language of ancient physics, which was not using two different terms for reflection and refraction. We can find the same use of term "refraction" in Robert Grosseteste's works on optics [7, 8]. According to the Poet, to prove the laws of optics, besides the experience, the Latin "experimentum", we need also the "art", which at Dante's time was known as "catottrica" [9].

It remains to establish the scientific sources that Dante knew and used in the Comedy and also in his Convivio. According to [10], the scientific observations were often derived from encyclopedic

compilations. For his astrological knowledge, Dante used the Liber de aggregatione scientiae stellarum of Alfraganus and the Sphera written by John Sacrobosco. Moreover, the interest of Dante for optics and physics and for the metaphysics of light may indicate a possible relationship with Bartholomew of Bologna [10], who was influenced by Robert Grosseteste. Bartholomew of Bologna, who died about 1294, was an Italian Franciscan scholastic philosopher, follower of John Pecham [11]. Among his works we find the Tractatus de Luce, on optics and the metaphysics of light. Already about 1290, several chapters of the Tractatus de Luce were reported by the Franciscan Servasanto da Faenza, in his work De Exemplis naturalium [12]. In Bartholemew's work, we can find an Oxonian origin of his luministic theory. In the Tractatus de Luce, this theory appears as a natural aesthetic legacy, an aesthetic legacy that in Dante is quite clear. The Tractatus de Luce gives evidence of the Oxonian influence either through explicit references to Robert Grosseteste's work, readable in it, either through the clear symptoms of a lesson entirely absorbed by Dante and rendered in his Convivio [12-14].

7. In the light of the Moon. Dante's Paradiso begins at the top of Mount Purgatory. After ascending through the sphere of fire, believed to exist in the earth's upper atmosphere (Canto I), Beatrice leads Dante through the nine celestial spheres of Heavens, to the Empyreum. The nine spheres are concentric, as in the standard medieval geocentric model of cosmology, derived from Ptolemy. The Empyreum is immaterial. In the Canto II of Paradiso, Dante is in the sphere, or heaven, of the Moon.

In the heaven of the Moon, Dante finds a wonderful place that attracts all his attention. Beatrice, that can read his mind, summons the poet to direct his mind to God in gratitude for having reached the heaven of the Moon. Then Dante describes his feelings: he seems to be wrapped in a cloud which is shining like a diamond hit by the sun. The moon welcomes Beatrice and Dante within herself, without opening, like the surface of the water when it is receiving a ray of light. On the Earth, tells Dante, we cannot understand how a solid body can penetrate into another solid body, without suffering any change.

"Pareva a me che nube ne coprisse / lucida, spessa, solida e pulita, / quasi adamante che lo sol ferisse. / Per entro se' l'eterna margherita / ne ricevette, com'acqua recepe / raggio di luce, permeando unita. / S'io era corpo, e qui non si concepe / com'una dimensione altra patio, / ch'essere convien se corpo in corpo repe, / accender ne dovria più il disio / di veder quella essenza in che si vede / come nostra natura e Dio s'unio." (Paradiso, Canto II, 30-42).

"It seemed to me a cloud encompassed us, / luminous, dense, consolidate and bright / as adamant on which the sun is striking. / Into itself did the eternal pearl / receive us, even as water doth receive / a ray of light, remaining still unbroken. / If I was body, and we here conceive not / how one dimension tolerates another, / which needs must be if body enter body, / more the desire should be enkindled in us / that essence to behold, wherein is seen / how God and our own nature were united." (Longfellow's translation)

What is the nature of the light, material or immaterial? I think this was the question that Dante was considering, when he was writing these words on a ray of light passing through a medium.

This light further increases the desire for reaching the highest Heaven. After thanking God, Dante asks Beatrice to explain the phenomenon of the dark spots of the Moon. He believes that these spots depend on the different density of this celestial body. But Beatrice confutes his argument, by an experiment. The experiment is on the role of distance, between an observed and surfaces reflecting the light. We can take three mirrors, placed at unequal distances from a light source; we will see them equally resplendent.

"Da questa instanza può deliberarti / esperienza, se giammai la provi, / ch'essere suol fonte ai rivi di vostra arti. / Tre specchi prenderai; e due rimovi / da te d'un modo, e l'altro più rimosso / tr'ambo li primi gli occhi tuoi ritrovi. / Rivolto ad essi fa, che dopo il dosso / ti stea un lume, che i tre specchi accenda, / e torni a te da tutti ripercosso. / Benché nel quanto tanto non si stenda / la vista più lontana, li vedrai / come convien, ch'egualmente risplenda." (Paradiso II, v. 89-105).

"From this reply experiment will free thee / if e'er thou try it, which is wont to be / the fountain to the rivers of your arts. / Three mirrors shalt thou take, and two remove / alike from thee, the other more remote / between the former two shall meet thine eyes. / Turned towards these, cause that behind thy back / be placed a light, illuming the three mirrors / and coming back to thee by all reflected. / Though in its quantity be not so ample / the image most remote, there shalt thou see / how it perforce is equally resplendent." (Longfellow's translation).

Bottagisio explains that the distance is not changing the quality of the light reflected by the three mirrors. Ottavio Fabrizio Mossotti (Italian physicist, 1791-1863, known for the Clausius–Mossotti relation), in a letter to the Editor of Bottagisio's book, has a relevant observation about this experiment [15]. "It seems to me that Dante, by the experiment of the three mirrors, wanted to point out the principle that flat surfaces, which emit or are illuminated in equal degree, appear to have the same brightness at any distance they are placed. This happens because the size of their image and the amount of light that receives the eye from each point are both decreasing as the inverse of the square of the distance. Therefore, there is a compensation, and each element of equal apparent extension of the image is always represented by the same amount of light reaching the eye at any distance you observe the surface. ... (The light source must be supposed to be at a large distance, comparatively to that at which the mirrors are between them). ... The theoretical principle of Dante is right, and for that time had to be a sublime truth and not common knowledge".

Mossotti's brightness is the ratio of the light reaching the eye to the apparent size of the object. These both diminish with the square of the distance, so the brightness remains constant.

After proposing the experiment with the three mirrors, Beatrice continues with her explanation, which becomes more metaphysical: the brightness of the celestial bodies varies as the force of virtue varies from star to star. This virtue is the heavenly power, that we can find in Grosseteste's metaphysics of light too [16].

The motion and the influence of the spheres depend on angelic intelligences, as the ability of using the hammer depends on the mind of the blacksmith; like in the human body where we have a soul, which is one, but manifests itself in the different organs to perform different functions, we have the angelic intelligence from the eight heaven that unfolds from heaven to heaven and is manifested in different forms, merging with the different matter of the various stars. From this reason, it comes the change in brightness from star to star and then also the spots of the Moon.

Bottagisio is also remarking that the Pythagoreans, and also the mathematician Christian Wolff in his Elements of Astronomy, have considered the spots of the Moon being seas, lakes and ponds, which reverberate the rays they receive from the sun, most of them being absorbed. Let us note that Dante, through Beatrice's words, is summoning the use of an "experimentum". The same we can find, for example, in the works of Robert Grosseteste (1175-1253), considered the founder of the scientific thought in the medieval Oxford. The Grosseteste's "experimentum" of his medieval physics, like that of Dante, was obviously different from an experiment of modern physics; it was referring to a thought experiment (Gedankenexperiment) or the experience of a related natural phenomenon.

8. The rainbow. Robert Grosseteste wrote on reflection and refraction in his treatise entitled De Iride (on Rainbow) [7,8], where, after a discussion on the propagation of light he proposed his explanation of such natural phenomenon. Then, the rainbow was a subject of physics. In the Divine Comedy, we find the rainbow too:

"E come l'aere, quand'è ben piorno, / Per l'altrui raggio, che 'n sé si riflette, / Di diversi color si mostra adorno." (Purgatorio XXV, v. 91-93).

"And even as the air, when full of rain, / By alien rays that are therein reflected, / With divers colours shows itself adorned." (Longfellow's translation).

In fact, if we imagine that the meaning of Dante's reflection was that of a refraction, it seems that the poet was in agreement to Grosseteste, who told that it is "necessary that the rainbow is created by the

refraction of the sun's rays by the humidity carried by the cloud" in its convexity [7]. "Necesse est ergo, quod iris fiat per fractionem radiorum solis in roratione nubis convexae" [8]. Also the double rainbow is present in the Dante's Comedy, with the second rainbow being the image of the first reflected by the cloud.

"Come si volgon, per tenera nube, / Du' archi paralleli e concolori, / Quando Giunone a sua ancella jube, / Nascendo di quel d'entro quel di fuori." (Paradiso, XII, 10-13).

"And as are spanned athwart a tender cloud / Two rainbows parallel and like in colour, / When Juno to her handmaid gives command, / The one without born of the one within." (Longfellow's translation).

These Dante's passages on rainbow are reinforcing what we have previously told on the scientific treatises that he knew. May be, he had not a direct knowledge of Grosseteste's works, but in the Divine Comedy we can see some of the Oxonian theory of light rendered in poetry.

References

[1] Lansing, R. (2011). The Dante Encyclopedia, Routledge. ISBN 1136849726, 9781136849725.

[2] Sparavigna, A. C. (2014). Using Time Series and Graphs in the Analysis of Dante's Divine Comedy. International Journal of Sciences, 3(12), 33-40. DOI: 10.18483/ijSci.605.

[3] Bainbridge Webster, J., & Torrance, I. (2007). The Oxford Handbook of Systematic Theology, OUP Oxford.

[4] Bottagisio, G. (1894). Osservazioni sopra la fisica del poema di Dante, Nuova edizione del testo del 1807, a cura di G.L. Passerini, Città di Castello, S. Lapi.

[5] Sparavigna, A. C. (2013). From Rome to the Antipodes: The Medieval Form of the World. International Journal of Literature and Arts, 1(2), 16-25. DOI: 10.11648/j.ijla.20130102.11.

[6] Orr, M.A. (1913). Dante and the Early Astronomers, London: Gall and Inglis.

[7] Sparavigna, A.C. (2013). On the Rainbow, a Robert Grosseteste's Treatise on Optics. International Journal of Sciences, 2(9), 108-113. DOI: 10.18483/ijSci.296.

[8] Sparavigna, A.C. (2012). Translation and discussion of the De Iride, a treatise on optics by Robert Grosseteste. arXiv preprint arXiv:1211.5961.

[9] Dante Alighieri. La Divina Commedia, col commento di G. Biagioli, Napoli, Puzziello Libraio Editore, 1838. Vol.2, Pagina 202.

[10] Vasoli, C. (2012). Dante Alighieri, in "Il Contributo italiano alla storia del Pensiero: Filosofia", Istituto dell' Enciclopedia Italiana, www.treccani.it.

[11] Vv. Aa. (2016). Bartholomew of Bologna, Wikipedia.

[12] Guidubaldi, E. (1970). Bartolomeo da Bologna, 1970, in VV.AA. Enciclopedia Dantesca, vol.1, Istituto della Enciclopedia Italiana, Roma, pp.526-527.

[13] Olschki, L. (1933). Il Canto XXX del Paradiso, Il Giornale Dantesco, XXXVI.

[14] Mocan, M. (2007) La trasparenza e il riflesso: sull'alta fantasia in Dante e nel pensiero medievale, Pearson Italia S.p.a.

[15] Mossotti, G.F. (1894). Illustrazioni astronomiche a tre luoghi della Divina Commedia, Collezione di Opuscoli danteschi inediti e rari, diretta da G.L. Passerini, Volume Settimo, Città di castello, S. Lapi Tipografo-Editore.

[16] Sparavigna, A.C. (2014). Robert Grosseteste's Thought on Light and Form of the World, International Journal of Sciences, 3(4):54-62 DOI: 10.18483/ijSci.486.

A Matlab Toolbox For Grey Clustering Probability Model Of Postgraduate's Innovative Ability

Xiao-qing Tang[1,a]

1 – School of Mathematics & information, Shanghai Lixin University of Commerce, Shanghai, 201620 China

a – tangxiaoqing5168@163.com


DOI **10.13140/RG.2.1.1682.6004**

Keywords: grey clustering, probability model, Matlab toolbox

ABSTRACT. In this article, we propose a new grey clustering probability model. That is, grey whiteness function is the probability when score in the clustering. And the weight is the proportion of the thresholds. As an illustrative example, we use the toolboxes developed for carrying on an analysis of the test scores of postgraduate's ability on innovation. The evaluation process successfully shows that the toolboxes are fairly convenient, quite efficient.

1. Introduction. In this article, we develop an evaluation Matlab toolbox based on grey clustering probability model. We all know that postgraduate degree is the highest education degree, and innovation is one of its most important tasks. So, it is important to accurate evaluate the innovative ability of postgraduate. Because that there are so many factors influencing innovative ability, such as innovative thinking, knowledge accumulation, innovative environment, and so on. Traditionally, when using the statistical method in analyzing an issue, the summation method has mostly been used to get an average value, and the standard deviation method can only be used to reach a simple conclusion [1]. In past research in this field, most of them are qualitative analysis, only a few quantitative analysis using old conventional method and which has many weak points [2]. And it is known that software plays an important role in our life, because it will not only cause significant effects in a real operation system, but also it will make the results more convincing and practical. MATLAB is commercial mathematics software of U.S. MathWorks company, it is much more simple and convenient by using MATLAB than by using C or Fortran language. Now MATLAB is a foundation of the software research training in a university, so we use it to develop the grey clustering evaluation toolbox.

After comprehensive consideration, we think that the postgraduate's innovative ability index system including six first class indexes, that is, innovative spirit, innovative thinking, knowledge accumulation, innovative environment, research practice, research results[3]. And each first class index has some second class indexes as Table 1 shown. Without loss generality, we set that total score is 100, and the first index (innovative spirit) score is 15, it is to say, each of the three second class index score is 5;the second index (innovative thinking) score is 20, each of the two second class index score is 10;and the third index(knowledge accumulation) score is the same as the second index; the fourth index (innovative environment) score is 15, and academic environment score is 8 and infrastructure score is 7; the fifth index (research practice) and the sixth (research results) is the same as the fourth index.

This article is organized as follows. Section 1 is the purpose and introduction. Section 2 is the mathematical model and section 3 is the development of toolbox. Section 4 is a real example. Section 5 is the conclusion and discussion. We use software Matlab 7.0 in this article.

2. Mathematical model. We suppose there are *n* evaluation objects, *m* evaluation indexes and *l* grey clustering [4]. And $a_{ij}(1 \le i \le n; 1 \le j \le m)$ is the score of the *i*-th object at the *j*-th index; $\mu_{jk}(1 \le j \le m; 1 \le k \le l)$ is the threshold of the *j*-th index at the *k*-th level grey clustering, and the order is $\mu_{j1} \ge \mu_{j2} \ge \cdots \mu_{jl}$.

Table. 1 evaluation index system for postgraduate's innovative ability

First class index	Second class index
innovative spirit	skepticism
	innovative consciousness
	spirit of devoting to science
innovative thinking	thinking differently
	thinking migration
knowledge accumulation	theoretical buildup
	professional skills
innovative environment	academic environment
	infrastructure
research practice	practice willingness
	practice ability
research results	published paper number
	as a member or organizer research

Definition 1 let $a_1, a_2, \cdots, a_n$ are the statistical objects; $b_1, b_2, \cdots, b_m$ are the statistical indexes [5]. $f_1, f_2, \cdots, f_l$ are the grey whiteness functions and where $n, m, l \in N$, and $a_{ij}(1 \le i \le n; 1 \le j \le m)$ are the sample values for the objects.

For example, we think there are four grades for postgraduate's innovative ability, they are diminishing as **excellent, good, middle** and **weak**.

2.1. Grey whiteness function. Assume $f(x)$ is a linear monotonic function of x and x is the grey number, $f(x) \in [0,1]$. Then $f(x)$ is called the whitenization weight function, and will be divided into four levels.

Definition 2. Assume in grey clustering system, because of various factors and errors, random variables, evaluation criterions are normally distribution as $N(\mu_{jk}, \sigma_{jk}^2), (j = 1,2,\cdots,m; k = 1,2,\cdots,l)$, where μ_{jk} is the threshold of the *j*-th index at *k*-th level grey clustering, and σ_{jk}^2 is the variance.

The first grey clustering (excellent) whiteness function is

$$f_{j1}(a_{ij}) = \begin{cases} 1 & a_{ij} \geq \mu_{j1} \\ 2[1-\Phi(\dfrac{\mu_{j1}-a_{ij}}{\sigma_{j1}})] & a_{ij} < \mu_{j1} \end{cases} \tag{1}$$

We set above function based on maximum likelihood estimation of probability [6 – 10]. So, when score is more than μ_{j1}, f_{j1} should be the maximum, then $f_{j1}=1$; when $a_{ij} < \mu_{j1}$, the nearer of a_{ij} to μ_{j1}, the bigger f_{j1} whiteness function value, therefore we set the function

$$P(X < a_{ij}) + P(X > 2\mu_{j1} - a_{ij}) = 2[1-\Phi(\frac{\mu_{j1}-a_{ij}}{\sigma_{j1}})],$$

where $\Phi(x) = \int_{-\infty}^{x} \frac{1}{\sqrt{2\pi}} e^{-\frac{t^2}{2}} dt$.

The second grey clustering (good) whiteness function is

$$f_{j2}(a_{ij}) = \begin{cases} 2[1-\Phi(\dfrac{a_{ij}-\mu_{j2}}{\sigma_{j2}})] & a_{ij} \geq \mu_{j2} \\ 2[1-\Phi(\dfrac{\mu_{j2}-a_{ij}}{\sigma_{j2}})] & a_{ij} < \mu_{j2} \end{cases} \tag{2}$$

The third grey clustering(middle) whiteness function is

$$f_{j3}(a_{ij}) = \begin{cases} 2[1-\Phi(\dfrac{a_{ij}-\mu_{j3}}{\sigma_{j3}})] & a_{ij} \geq \mu_{j3} \\ 2[1-\Phi(\dfrac{\mu_{j3}-a_{ij}}{\sigma_{j3}})] & a_{ij} < \mu_{j3} \end{cases} \tag{3}$$

The fourth grey clustering (weak) whiteness function is

$$f_{j4}(a_{ij}) = \begin{cases} 0 & a_{ij} \geq \mu_{j1} \\ 2[1-\Phi(\dfrac{a_{ij}-\mu_{j4}}{\sigma_{j4}})] & \mu_{j4} \leq a_{ij} < \mu_{j1} \\ 1 & a_{ij} < \mu_{j4} \end{cases} \tag{4}$$

The figure of this four whiteness functions is shown as following Fig 1.

2.2. The grey clustering weight

$$\eta_{jk} = \frac{\mu_{jk}}{\sum_{j=1}^{m} \mu_{jk}}, (1 \le j \le m; 1 \le k \le l) \tag{5}$$

It is the weight of the *j*-th index belongs to the *k*-th grey clustering.

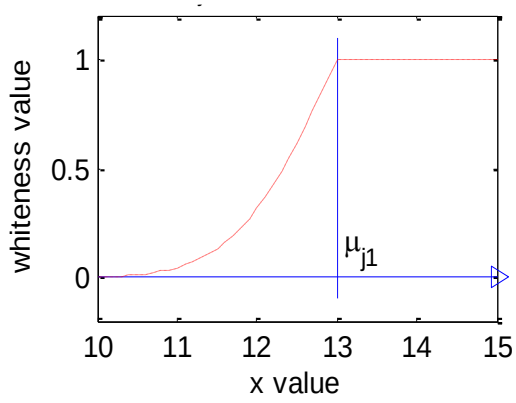


Fig. 1. $f_{j1(x)}$ *whithess function*

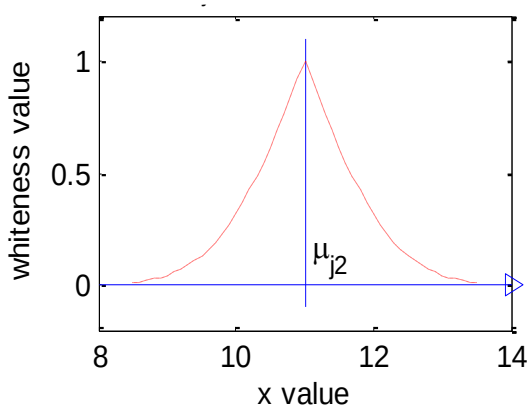


Fig. 2. $f_{j2(x)}$ *whithess function*

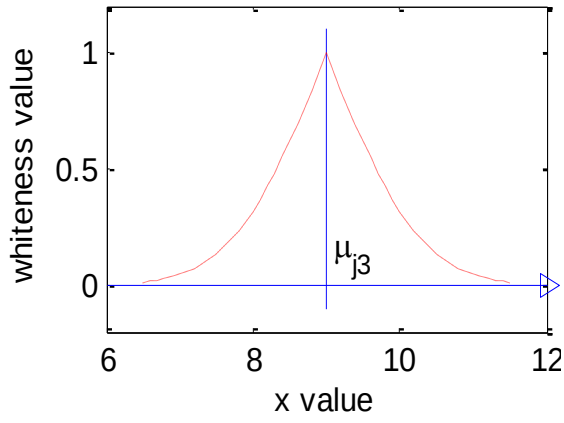


Fig. 3. $f_{j3(x)}$ *whithess function*

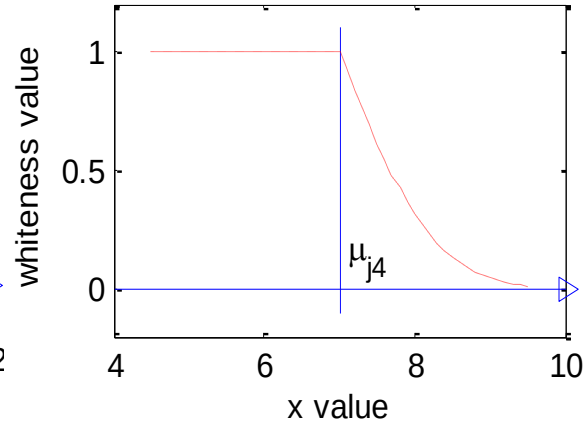


Fig. 4. $f_{j4(x)}$ *whithess function*

2.3. Grey clustering likely coefficients

$$\theta_{ik} = \sum_{j=1}^{m} f_{jk}(a_{ij})\eta_{jk}, (i = 1,2,\cdots n; k = 1,2,\cdots, l) \tag{6}$$

Therefore, we can calculate each component of the *i*-th vector (object), which is the likely coefficient of *k*-th level. Then we will think it belongs to *k*-th level if the *k*-th component is the maximum among all those four components.

3. The development of toolbox. As we know that, Matlab has been very convenient and practical software for researchers. It is very easy to be operated due to its wide coverage. Matlab not only has many functions, but also it allows the user to develop their own calculation functions and integrate

them into the toolbox. It is also very convenient to process graphs with Matlab, and the graphs can be displayed as soon as the data are input into the Matlab system. And, there are many other toolboxes in Matlab for convenient operation with special calculations for users of different application domains, it will be very convenient to develop related software with Matlab as the core. The users can develop new toolboxes according to their own research topics with Matlab as the base.

3.1. The characteristic of the toolbox. In this article, we developed two toolboxes, the whole structure of toolbox is shown in Fig.5.

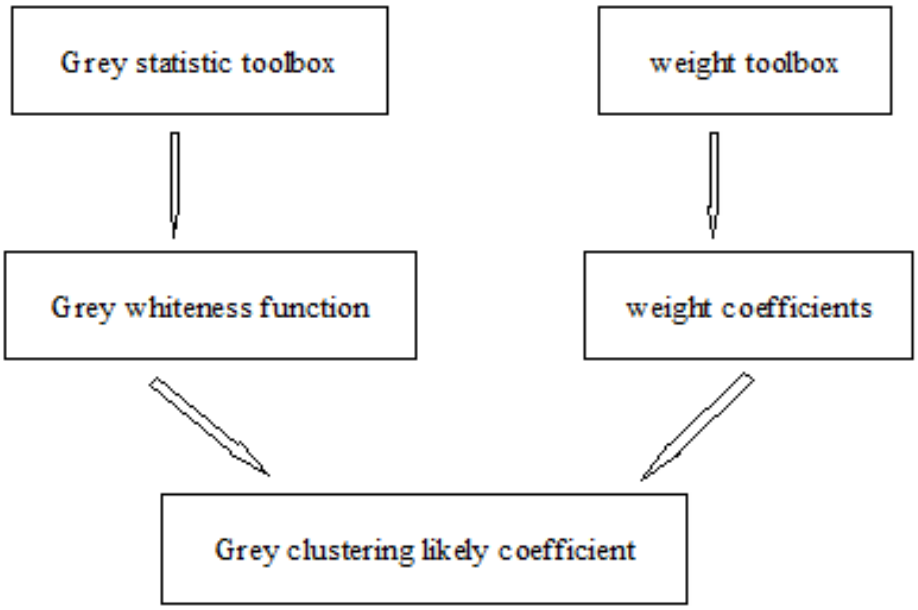


Fig. 5. Structure of our toolbox

3.2. The computer and software requirements

(1) windows 2000 or upgrade version.

(2) computer screen at least 1024*768.

(3) Matlab 6.0 or upgrade version.

3.3. The operation of grey clustering statistic toolbox

(1) start the toolbox.

(2) Matlab system

(i)Input the data of students score: $A=[a_{11},a_{12},\cdots,a_{1m};a_{21},\cdots,a_{2m};\cdots;a_{n1},\cdots,a_{nm}]$,

Where $a_{ij}(1\le i\le n;1\le j\le m)$ is the target score.

(ii)Input the data of threshold matrix: $B=[\mu_{jk}]_{m\times l}$.

Following Fig. 6 is the whiteness function value of the first student, also we can get the others calculation results.

```
f1 =

    1.0000    0.0027    0.0000         0
    0.3173    0.3173    0.0027    0.0000
    0.3173    0.3173    0.0027    0.0000
    1.0000    0.0027    0.0000         0
    0.0455    1.0000    0.0455    0.0001
    1.0000    0.0455    0.0001    0.0000
```

Fig. 6. The whiteness function value of the first student

3.4. The operation of weight toolbox

(1) start the toolbox.

(2) Matlab system, input the data of threshold matrix: $B = [\mu_{jk}]_{m\times l}$, following Fig. 7 is the screenshot of toolbox running result.

```
The element type "name" must be terminated by the matching end-tag "</name>".
Could not parse the file: d:\matlab7\toolbox\ccslink\ccslink\info.xml

mu =

    85    73    61    49


nu =

    0.1529    0.1507    0.1475    0.1429
    0.2000    0.2055    0.2131    0.2245
    0.2118    0.2192    0.2295    0.2449
    0.1412    0.1370    0.1311    0.1224
    0.1529    0.1507    0.1475    0.1429
    0.1412    0.1370    0.1311    0.1224

>>
```

Fig. 7. T screenshot of toolbox running result

4. Example

4.1. There are 5 postgraduates and their score as Table 2 shown.

Table 2. Score of the postgraduates' innovative ability

object / index	Student 1	Student 2	Student 3	Student 4	Student 5
innovative spirit	14	12	8	13	8
innovative thinking	16	14	13	17	15
knowledge accumulation	17	13	12	18	11
innovative environment	13	10	10	14	5
research practice	11	11	10	12	6
innovative environment	12	12	8	12	7
total	83	72	61	86	52

So we can get the score matrix as following;

$$A=\begin{Bmatrix} 14 & 16 & 17 & 13 & 11 & 12 \\ 12 & 14 & 13 & 10 & 11 & 12 \\ 8 & 13 & 12 & 10 & 10 & 8 \\ 13 & 17 & 18 & 14 & 12 & 12 \\ 8 & 15 & 11 & 5 & 6 & 7 \end{Bmatrix}$$

Then we determine the classification threshold value of each index as Table 3 shown.

Table 3. Threshold of classifying the grey clustering level

index	Grey clustering			
	excellent	good	middle	weak
innovative spirit	≥13	11	9	<7
innovative thinking	≥17	15	13	<11
knowledge accumulation	≥18	16	14	<12
innovative environment	≥12	10	8	<6
research practice	≥13	11	9	<7
research results	≥12	10	8	<6

So we get the threshold matrix as following

$$B=\begin{Bmatrix} 13 & 11 & 9 & 7 \\ 17 & 15 & 13 & 11 \\ 18 & 16 & 14 & 12 \\ 12 & 10 & 8 & 6 \\ 13 & 11 & 9 & 7 \\ 12 & 10 & 8 & 6 \end{Bmatrix}$$

4.2. The calculate results

4.2.1. According to grey statistic toolbox, we can get the results of 5 students whiteness function value, here we illustrate the results of student 1 which is shown as Table 4 (here we set all $\sigma_{ij}=1$).

Because of the space saving, we don't write about others student calculation results.

Table 4. Student 1 whiteness function value

index	Grey clustering			
	excellent	good	middle	weak
innovative spirit	1.0000	0.0027	0.0000	0
innovative thinking	0.3173	0.3173	0.0027	0.0000
knowledge accumulation	0.3173	0.3173	0.0027	0.0000
innovative environment	1.0000	0.0027	0.0000	0
research practice	0.0455	1.0000	0.0455	0.0001
research results	1.0000	0.0455	0.0001	0.0000

4.2.2. According to weight toolbox, the results of weight coefficients matrix is shown as Table 5.

Table 5. Weight coefficients value

index	Grey clustering			
	excellent	good	middle	weak
innovative spirit	0.1529	0.1507	0.1475	0.1429
innovative thinking	0.2000	0.2055	0.2131	0.2245
knowledge accumulation	0.2118	0.2192	0.2295	0.2449
innovative environment	0.1412	0.1370	0.1311	0.1224
research practice	0.1529	0.1507	0.1475	0.1429
research results	0.1412	0.1370	0.1311	0.1224

4.2.3. So we can get the last results of every students' grey clustering likelihood coefficients as following Table 6 shows:

Table 6. Students likely coefficients value

object	Grey clustering likelihood coefficient				Likely level
	excellent	good	middle	weak	
(Student 1) θ_1	0.5729	0.2924	0.0079	0.0000	excellent
(Student 2) θ_2	0.2036	0.4075	0.1535	0.0783	good
(Student 3) θ_3	0.0069	0.2008	0.4543	0.3064	middle
(Student 4) θ_4	0.1416	0.0802	0.0004	0.0000	excellent
(Student 5) θ_5	0.0091	0.2063	0.0995	0.5944	weak

We can see that the first component is the biggest among 4 components, so we can say that **student 1** belongs to the level of ***excellent***.

Also we can see that the second component is the biggest among 4 components, so we can say that **student 2** belongs to the level of ***good***.

We can see that the third component is the biggest among 4 components, so we can say that **student 3** belongs to the level of ***middle***.

We can see that the first component is the biggest among 4 components, so we can say that **student 4** belongs to the level of ***excellent***.

We can see that the fourth component is the biggest among 4 components, so we can say that **student 5** belongs to the level of ***weak***.

The above inference is obviously consistent with people's intuition, especial consistent with their total scores.

And those results can be shown in Figure 5.

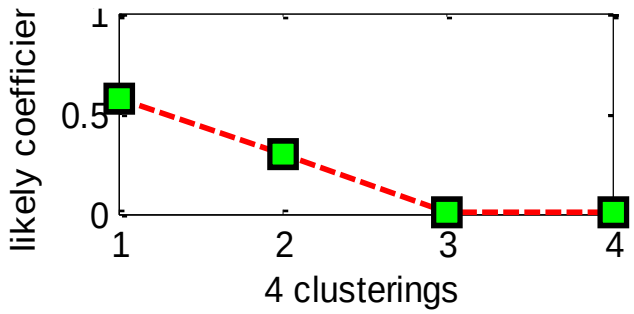


Fig. 8. The first student likeliest clustering

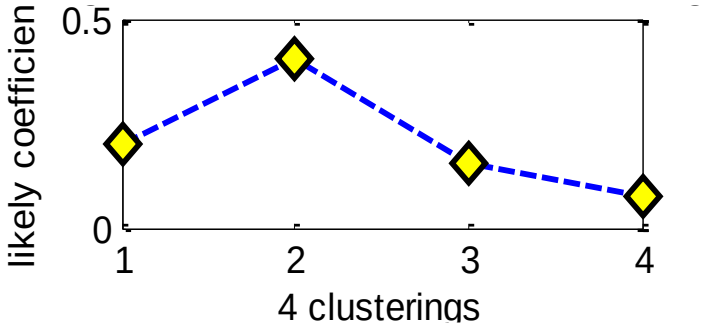


Fig. 9. The second student likeliest clustering

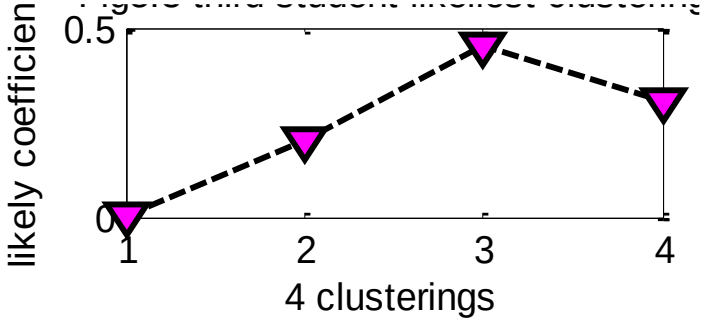


Fig. 10. The third student likeliest clustering

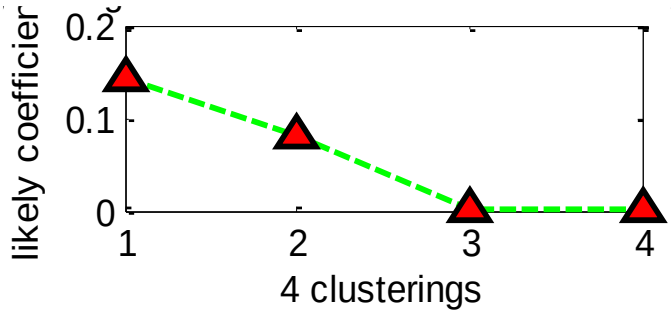


Fig. 11. The fourth student likeliest clustering

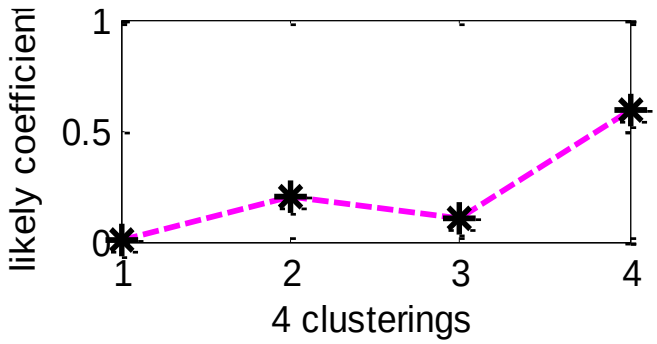


Fig. 12. The fifth student likeliest clustering

Summary. We make toolbox with software Matlab7.0, and it is efficient and convenient in processing data and graphs [11-13]. It has the following academic implications.

1. To make a designer thoroughly understands the whole essential meaning in grey statistics probability, our method can accurately deduce the grey level of every student based on their score

and threshold matrix.

2. It is easy to write and in fact its grammar does not present any difficulty, and it is portable. Also it is user-friendly for human interface, and the total required memory space is quite small.

3. The member of grey clustering level, weight functions and object member can be easily extended to what is wanted.

4. Matlab has more functions than others software and encompasses the convenience and the output expansion.

Although the software computing toolbox of grey statistics and evaluation has been developed [14, 15], our probability model is the newest one. This study presents both theoretical and practical significances, especially in student test score appraisal.

References

[1] Chiang J.L. Statistics, Taipei, Gauli Publisher; 2001.

[2] Wen K.L. Grey systems modeling and prediction, AZ, USA. Yang's Scientific Research Institute; 2004.

[3] Zhao Q.M. The formation and cultivation of innovation ability, Wuhan, Huazhong University of Science and Technology Press; 2002.

[4] Deng J.L. Grey prediction and grey decision-making, Huazhong University of Science and Technology Press; 2002.

[5] Tang X.Q, Wang H.X. Stepwise confidence interval method for finding drug's minimum effective dose in trial. Drug Evaluation Research 2010; 33(1):58-62.

[6] Tang X.Q, Tan M.C. Estimation of simple constrained parameters with EM method. J. Hunan Institute of Engineering 2010; 20(1):61-64.

[7] Tang X.Q, Liu N.Z, Wang H.X. Stepwise confidence interval method for dose-response and effectiveness studies. IEEE 2nd international conference of MACE, 2011, p.679-682.

[8] Tang X.Q, Bai Y.Q, Liu N.Z, Liu Y. Markowitz portfolio model based on random matrix theory. J.Shanghai University (Natural Science) 2013;19(3):293-297.

[9] Tang X.Q. New expected value expansions of rooted graphs. Acta Mathematicae Applicatae Sinica, English Series 2015; 31(1):81-88.

[10] Liu N.Z, Tang X.Q, Wang H.X. On reliability of two probability in regular q-tree rooted graph. J.Southwest China Normal University(Natural Science Edition) 2013;38(12):24-27.

[11] Tang X.Q, Liu N.Z, Wang H.X. The two-variable chromatic polynomial of regular tree study. Acta Mathematicae Applicatae Sinica 2013;36(4):761-768.

[12] Tang X.Q, Liu NZ., Wang H.X. A class of new two-variable chromatic polynomial. J. Lanzhou University(Natural Sciences) 2012;48 (2):106-112.

[13] Liu Y., Tang X.Q. Comparison of some classes of two-variable chromatic polynomials. J. Natural Science of Hunan Normal University 2014; 37(6): 67-72.

[14] Wen K.L. A Matlab toolbox for grey clustering and fuzzy comprehensive evaluation. Advances in Engineering Software 2008; 39: 137-145.

[15] Abdulshahed A.M, Longstaff A.P, Fletcher S, Myers A. Thermal error modeling of machine tools based on ANFIS with fuzzy c-means clustering using a thermal imaging camera. Applied Mathematical Modelling 2015; 39: 1837-1852.

Mechanics, Materials Science & Engineering Journal ©

ISSN 2412-5954

Published by Magnolithe GmbH

Printed by Magnolithe GmbH